Building a mass function and testing gravity using galaxy clusters

by

Ben Hoyle

THE THESIS IS SUBMITTED IN PARTIAL FULFILMENT OF THE REQUIREMENTS FOR THE AWARD OF THE DEGREE OF
DOCTOR OF PHILOSOPHY
OF THE
UNIVERSITY OF PORTSMOUTH

June, 2009

Copyright

Preface

Whilst registered as a candidate for the above degree, I have not been registered for any other research award. The results and conclusions embodied in this thesis are the work of the named candidate and have not been submitted for any other academic award.

To my family and friends

Abstract

With the undertaking of large scale surveys of the cosmos, the field of cosmology has been promoted to a precision discipline where theoretical postulates and experimental results are compared with increasing levels of accuracy.

This thesis examines the role of clusters of galaxies, which are massive gravitationally bound collections of galaxies, as an alternative probe of cosmology through the measurement of the large scale distribution of matter. Other, more popular probes, test the geometry of the Universe and so by combining these probes we can build and test a consistent model of the Universe.

We begin by introducing the theoretical framework and observational data which have shaped our current understanding of the cosmological model of the Universe, and describe how clusters of galaxies can be used to test this "concordance" cosmological model. Cluster of galaxies can only be used as a probe of cosmology if a large number are identified and their masses estimated. The middle chapters of this thesis describes work undertaken to achieve these aims.

We then introduce the datasets used throughout the remainder of the thesis, and describe the creation of the largest sample of X-ray clusters (> 400) compiled to date. X-ray identified clusters are useful because their masses can be theoretically estimated from the X-ray emission whereas optically identified clusters (of which we have $\sim 15,000$) have no such theoretical mass scaling relationship. We continue by measuring the optical properties of the X-ray clusters and find that the total optical luminosity L scales with cluster mass M_{200} with a relationship given by $L \propto M_{200}^{0.73^{+0.30}_{-0.27}}$. This allows us to estimate the masses of the more plentiful optically selected clusters.

Subsequently, we develop an alternative measurement of the masses of optical clusters, using weak gravitational lensing. We find that we are unable to measure the mass of any one cluster using this technique, but by stacking all the clusters, we find an upper limit on mass of $\sim 3.2 \times 10^{15} M_{\odot}$ (where $M_{\odot}$ is solar mass) which agrees with the masses derived from the X-ray.

We then convert the cluster masses to a Cluster Mass Function (hereafter CMF), which is the number of clusters as a function of mass and redshift. After describing how the theoretical CMF

changes with cosmological parameters and models, we compare it with the measured CMF and find that we are able to place interesting independent constraints on cosmology when used alone (e.g. $\sigma_8 = 0.67^{+0.25}_{-0.25}$ assuming flat ΛCDM), and competitive constraints when used in combination with the other, geometric probes of cosmology (e.g. $\Omega_m = 0.20^{+0.04}_{-0.04}$ assuming $\sigma_8 = 0.8$ and $\sigma_8 = 0.73^{+0.05}_{-0.05}$ assuming $\Omega_m = 0.26$). After making an ansatz we are even able to rule out a modified theory of gravity called DGP (Dvali et al., 2000) at high ($3\,\sigma$) significance.

We finish with conclusions, future applications and future work.

Acknowledgements

Firstly I would like to thank Bob Nichol for supervising my Ph.D and always showing infinite enthusiasm for the subject, my results, and any changes of direction during my research. I am also indebted to David Bacon for his patience and guidance, and Robert Crittenden for lengthy and useful discussions. I am thankful to the University of Portsmouth and the Science and Technology Facilities Council which have enabled me to undertake this studentship and allowed me to travel to distant lands for conferences, meetings and to use telescopes. I would also like to thank all of the people at the Institute of Cosmology and Gravitation for promoting an atmosphere of collaboration, and to the administration staff for making life run smoothly. I have also been partially funded by a grant from Google.

This work would not have been possible without data from, and the help of, the XMM Cluster Survey collaboration, especially Kathy Romer, Ed Lloyd-Davies, Chris Miller, Chris Collins and Nicola Mehrtens. I have also drawn extensively from data made available by the Sloan Digital Sky Survey[1]. I would also like to thank past and present members of the ICG who have been there to discuss ideas and to enlighten, including Bjoern Schaeffer, Edd Edmonson, Steven Bamford, Mat Smith, Dan Carson, Jim Cresswell, Tommaso Giannantonio, Elisabetta Majerotto, Antonio Cardoso, Cris Sabiu, Kelly Nock, Lukas Hollenstein, Prina Patel (who also proof read this thesis), and Fabio Silva.

Life at the ICG would not have been half as interesting without the sport partners, teams and social gatherings. Thanks!

Finally I'd like to thank my friends (including all ICG'ers) for making life so much fun and my family for their continued love and support.

[1]Funding for the SDSS and SDSS-II has been provided by the Alfred P. Sloan Foundation, the Participating Institutions, the National Science Foundation, the U.S. Department of Energy, the National Aeronautics and Space Administration, the Japanese Monbukagakusho, the Max Planck Society, and the Higher Education Funding Council for England. The SDSS Web Site is http://www.sdss.org/. The SDSS is managed by the Astrophysical Research Consortium for the Participating Institutions. The Participating Institutions are the American Museum of Natural History, Astrophysical Institute Potsdam, University of Basel, University of Cambridge, Case Western Reserve University, University of Chicago, Drexel University, Fermilab, the Institute for Advanced Study, the Japan Participation Group, Johns Hopkins University, the Joint Institute for Nuclear Astrophysics, the Kavli Institute for Particle Astrophysics and Cosmology, the Korean Scientist Group, the Chinese Academy of Sciences (LAMOST), Los Alamos National Laboratory, the Max-Planck-Institute for Astronomy (MPIA), the Max-Planck-Institute for Astrophysics (MPA), New Mexico State University, Ohio State University, University of Pittsburgh, University of Portsmouth, Princeton University, the United States Naval Observatory, and the University of Washington.

Table of Contents

Chapter 1

Introduction

In this chapter we introduce the "concordance cosmological model" and describe the theoretical and experimental research which has shaped its present form. We discuss the experimental constraints on the concordance cosmological parameters, and describe the place of clusters of galaxies within this framework. We then introduce and describe the basic properties of clusters of galaxies and show how they can be used as alternative probes of cosmology through the construction of the "cluster mass function" (hereafter CMF), and discuss complications which arise while attempting to measure the masses of clusters. We introduce previous work to constrain cosmology using the CMF and show the improvement of parameter constraints by combining cosmological probes. We finish with an overview of the thesis and its goals.

1.1 The current cosmological model

In this section, we present an overview of the current cosmological model, and derive the relevant equations for the remainder of the thesis. We then introduce observations performed to measure the values of the parameters in the cosmological model, and show that the real strength of observational cosmology comes from combining different cosmological probes.

1.1.1 Theoretical cosmology

Modern cosmology has been built by applying the Einstein equations for General Relativity to the Universe as a whole. To do this, we begin with two simplifying assumptions; the Universe is isotropic on large scales, meaning that each direction looks similar to all other directions, and the Universe is homogeneous on large scales, meaning one region of the Universe has very similar properties to all other regions.

The Friedmann, Lemaître, Robertson, Walker metric

The assumptions of homogeneity and isotropy led Friedmann, Lemaître, Robertson, and Walker to write down the most general spherically-symmetric (r, θ, ϕ) metric to describe space-time in

terms of the expansion of the Universe, or the scale factor $a(t)$, and given by,

$$\mathrm{d}s^2 \;=\; -c^2\mathrm{d}t^2 + a(t)^2\left(\frac{\mathrm{d}r^2}{1-Kr^2} + r^2\left(\mathrm{d}\theta^2 + \sin^2\theta\mathrm{d}\phi^2\right)\right)\;, \tag{1.1}$$

where c is the speed of light, t is a time coordinate, K is the curvature of the Universe which is measured to be very close to zero (see §1.1.6), and $\mathrm{d}s$ is an invariant called the "interval". Equation 1.1 can be rewritten in terms of the metric $g_{\mu\nu}$ which contains all the information about the time and space coefficients and written as,

$$\mathrm{d}s^2 \;=\; g_{\mu\nu}\mathrm{d}x^\mu\mathrm{d}x^\nu\;, \tag{1.2}$$

where μ, ν are components such that $\mathrm{d}x^0$ represents a time coordinate and $\mathrm{d}x^1, \mathrm{d}x^2, \mathrm{d}x^3$ represent spatial coordinates.

The Einstein equations

In General Relativity, the Einstein equations describe how the space-time $G^{\mu\nu}$ is curved (using a quantity $R^{\mu\nu}$, see §A.1) by the presence of matter and energy $T^{\mu\nu}$,

$$G^\mu_{\ \nu} \;=\; R^\mu_{\ \nu} - \frac{1}{2}g^\mu_{\ \nu}R \;=\; 8\pi G T^\mu_{\ \nu}\;, \tag{1.3}$$

$$G^\mu_{\ \nu} \;=\; 8\pi G T^\mu_{\ \nu} + \Lambda g^\mu_{\ \nu}\;. \tag{1.4}$$

In the last line, we have inserted a "Cosmological Constant" (Λ), without loss of generality. The Cosmological Constant was first introduced into the Einstein equations by Einstein to accommodate his prejudice for a steady state theory (neither contracting or expanding universe), which he later removed when the expansion of the Universe was observed by Hubble (see §1.1.2). In recent years, Λ has been reintroduced to explain the observed accelerated expansion of the Universe (see §1.1.6) but is poorly motivated from particle physics. A contender for Λ is the "vacuum energy" (the energy of empty space), but the measured value is $10^{\sim 120}$ orders of magnitudes greater than expected. Some modified theories of gravity (see §4.1.1) attempt to explain the observed accelerated expansion of the Universe by adding more complex terms in place of Λ in the Einstein equations (e.g, Carloni et al., 2005), or by introducing new physics which modifies the Einstein equations on large scales (e.g, Dvali et al., 2000). In more general models, Λ is replaced by "dark energy".

The Friedman equations

Inserting Equation 1.1 into the Einstein equations (Equation 1.4) and solving the time-time component ($G^0_{\ 0}$) and the space-space components ($G^i_{\ i}$), yield the Friedmann and acceleration equations, which describe the expansion of the Universe and how the expansion changes with time,

and are given by

$$\left(\frac{\dot{a}}{a}\right)^2 = \frac{8\pi\rho}{3} + \frac{\Lambda}{3} + \frac{K}{a^2}\,, \tag{1.5}$$

$$\frac{\ddot{a}}{a} = -\frac{4\pi G}{3}\left(3p+\rho\right) + \frac{\Lambda}{3}\,. \tag{1.6}$$

where ρ corresponds to the energy densities of the Universe which have pressures p, and a is the scale factor. The addition of Λ in the Einstein equations (Equation 1.4) has resulted in an additive factor in Equation 1.6. If Λ represents a "Cosmological Constant" then at some time the Universe will have evolved (see §1.1.5) such that $\Lambda > 4\pi G\left(3p+\rho\right)/3$, i.e $\ddot{a} > 0$, which results in the accelerated expansion of the Universe, as measured by observations (see §1.1.6).

The fluid equation

To describe the evolution of the material in the Universe, the "fluid equation" is required. The fluid equation is obtained by subtracting Equation 1.6 from the time differential of Equation 1.5 and is given by

$$\dot{\rho} + 3\frac{\dot{a}}{a}\left(p+\rho\right) = 0\,. \tag{1.7}$$

Once the equation of state $w = p/\rho$ is specified for each energy component of the Universe, the evolution of the material in the Universe can be predicted.

The critical density

Equation 1.5 allows a critical density $\rho_c(z)$ to be defined as the density required to produce zero spatial curvature ($K = 0$), and is given by

$$\rho_c(z) = \frac{3H(z)^2}{8\pi G}\,, \tag{1.8}$$

where the Hubble function is $H(z) \equiv \dot{a}/a$. The abundances of different forms of energy density can then be re-written in units of this critical density today,

$$\Omega_r = \frac{\rho_r(z=0)}{\rho_c(z=0)}\,, \Omega_m = \frac{\rho_m(z=0)}{\rho_c(z=0)}\,, \Omega_\Lambda = \frac{\rho_\Lambda(z=0)}{\rho_c(z=0)}\,, \tag{1.9}$$

where the subscripts r, m, Λ correspond to radiation, matter, and the cosmological constant, which are all discussed further in §1.1.5. Combining Equations 1.8 and 1.9 allow the writing of the Hubble function in its usual form of

$$H(z) = H_0\sqrt{\Omega_m(1+z)^3 + \Omega_r(1+z)^4 + \Omega_\Lambda(1+z)^{3(1+w_0)}}\,, \tag{1.10}$$

where H_0 (called the Hubble Constant) is measured by observation (see §1.1.2), and we have allowed the equation of state of dark energy w_0 to be constant. Often we include our lack of

knowledge of H_0 in terms of the unit less parameter h where $h = H_0/(100 \text{ km } s^{-1} \text{ Mpc}^{-1})$. The present day value of the critical density is

$$\rho_c\,(z=0) = 1.88h^2 10^{-26}\,\text{kg m}^{-3}\,, \quad (1.11)$$

$$= 2.78h^{-1}10^{11}\,\text{M}_\odot\,h^3\text{Mpc}^{-3}\,. \quad (1.12)$$

In Equation 1.12 we transformed SI units to those more associated with cosmology (solar mass $M_\odot$, and megaparsec Mpc). We present other cosmological parameters with their SI conversions, seldom found in the literature but invaluable for comparing theory with observations, in Table 1.1. Equation 1.12 suggests that if the Universe is flat, we expect to find around one typical "Milky Way" sized (L_*) galaxy per $h^{-3}\,\text{Mpc}^{-3}$.

Unit conversions			
Measure	Symbol	Value	Unit
Mega parsec	Mpc	3.086×10^{19}	km
Speed of light	c	2.998×10^5	km s^{-1}
		9.714×10^{-15}	Mpc s^{-1}
Solar Mass	$\text{M}_\odot$	1.989×10^{30}	kg
Gravitational constant	G	6.67×10^{-11}	m^3 kg^{-1} s^{-2}
		4.514×10^{-48}	Mpc^3 $\text{M}_\odot{}^{-1}$ s^{-2}
Hubble Constant	H_0	$100h$	km s^{-1} Mpc^{-1}
		$3.24h \times 10^{-18}$	Mpc s^{-1} Mpc^{-1}
Critical density	ρ_c	$1.88h^2 \times 10^{-26}$	kg m^{-3}
		$2.78h^2 \times 10^{11}$	$\text{M}_\odot$ Mpc^{-3}
		$2.78h^{-1} \times 10^{11}$	$\text{M}_\odot$ h^3 Mpc^{-3}

Table 1.1: Some typical cosmological units used throughout the thesis, their abbreviation and values in SI and cosmological units. The inclusion of h contains our lack of knowledge about the true value of the Hubble Constant.

1.1.2 Observational cosmology

In this section we introduce the seeds of modern observational cosmology and continue with a theoretical description of equations which are measurable by observations.

The Hubble law

Modern observational cosmology began with Hubble's discovery that all galaxies were receding from us, and distant galaxies appeared to be receding faster than nearby galaxies (Hubble, 1929). His famous Hubble diagram replicated in Figure 1.1 shows the correlation between the recession velocity of galaxies (measured by spectroscopy) and their distance (measured by the magnitudes

of Cepheid, Novae and Blue stars). He found that distance was directly proportional to recession velocity, with the constant of proportionality now called the Hubble Constant and denoted by H_0.

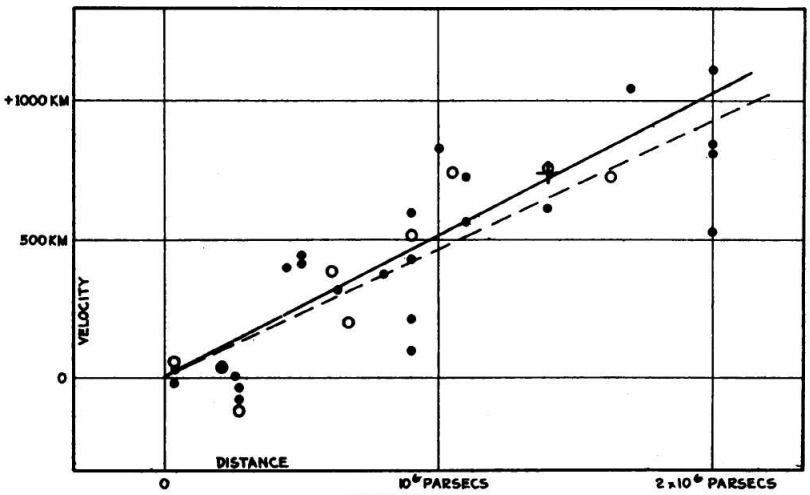

FIGURE 1
Velocity-Distance Relation among Extra-Galactic Nebulae.

Figure 1.1: The original Hubble diagram, showing individual galaxies (or nebulae as they were then known) in black, stacked galaxies in white, with the cross indicating 22 combined galaxies with inaccurate measurements. Credit: Hubble (1929).

The latest measurements of H_0 are given by Dunkley et al. (2009) to be $71.9^{+2.6}_{-2.7}$ km s^{-1} Mpc^{-1} using the Cosmic Microwave Background radiation (see §1.1.6), Riess et al. (2009) to be 74.2 ± 3.6 km s^{-1} Mpc^{-1} using 240 Cepheid stars within recent hosts of SNe Type Ia, which are consistent with older results of 71 ± 8 km s^{-1} Mpc^{-1} by Freedman et al. (2001) using the the The Hubble Space Telescope Key Project[1].

Redshift

The recession velocities measured by Hubble can be quantified using the redshift z, defined as the fractional stretching of the wavelength λ of light emitted at epoch e and observed at epoch o due to the background expansion of the Universe, and is given by,

$$z \equiv \frac{\lambda_0}{\lambda_e} - 1 \,, \tag{1.13}$$

which is related to the scale factor describing the expansion of the Universe by,

$$a = \frac{1}{1+z} \,. \tag{1.14}$$

[1] http://www.ipac.caltech.edu/H0kp/

1.1.3 Distance measures in cosmology

The expansion of space-time necessitates the generalisation of our Euclidean (flat and static) concepts of distances. The proper distance D_P corresponds to the distance between two objects as travelled by a photon and is found by setting $\mathrm{d}D_p^2 = -c^2\mathrm{d}t^2$ in Equation 1.1, and in a flat cosmology has the form,

$$D_P = \frac{c}{H_0}\int_{z_1}^{z_2}\frac{\mathrm{d}z}{(1+z)\,E(z)}\,, \tag{1.15}$$

where $E(z) \equiv H(z)/H_0$. The comoving distance D_C describes the distance between two objects which remains unchanged with the expansion of the Universe, and is found by setting $\mathrm{d}s^2 = 0$ in Equation 1.1. In a flat cosmology D_C is given by,

$$D_C = \frac{c}{H_0}\int_{z_1}^{z_2}\frac{\mathrm{d}z}{E(z)}\,. \tag{1.16}$$

The luminosity distance D_L relates the measured bolometric flux f to the emitted bolometric luminosity L given by,

$$f \equiv \frac{L}{4\pi D_L^2}\,, \tag{1.17}$$

$$= \frac{L}{4\pi D_C^2(1+z)^2}\,, \tag{1.18}$$

where the comoving distance is multiplied by one factor of $(1+z)$ from the loss of energy of the photon being stretched by the expanding universe, and an additional factor of $(1+z)$ from the modification of the photon arrival time. Therefore by comparing Equations 1.17 and 1.18 one obtains $D_L = D_C(1+z)$.

Additionally, the angular diameter distance D_A is defined as the ratio between the apparent size of an object θ transverse to the line of sight and its physical size A. In a flat Universe D_A is given by,

$$\theta \equiv \frac{A}{D_A^2}\,, \tag{1.19}$$

$$= \frac{A}{a^2 D_C^2}\,, \tag{1.20}$$

$$D_A = \frac{D_C}{(1+z)}\,. \tag{1.21}$$

Cosmological probes of geometry

Distance measures can be used as probes of cosmology (see §1.1.6) by comparing the measurement of a known, or theoretically motivated length scale with the redshift at which the length scale is measured. Equation 1.16 demonstrates the correspondence between redshift and distance and forms the basis (through the luminosity distance, angular diameter distance, or comoving

distance) of many probes of geometry.

An alternative cosmological probe is the growth of structure, which describes how the density perturbations in the early Universe evolve with time to form the structures (e.g. filaments, clusters and voids) observed today. We introduce the equations governing the growth of structure in the next section.

1.1.4 The growth of structure

To describe how large scale structures like filaments and clusters of galaxies form out of the perturbations in the initial density field we need to determine how the perturbations δ evolve.

Following Schaefer and Koyama (2008) we write the Hubble function as

$$H(z)^2 = H_0^2\, g(\eta_0), \quad \eta_0 = \frac{8\pi G\rho}{3H_0^2}, \tag{1.22}$$

and then take the time derivative of the Friedmann equation (Equation 1.5) to obtain,

$$\frac{\ddot{a}}{a} \;=\; H_0^2\Big(g(\eta_0) - \frac{3}{2}\eta_0 g'(\eta_0)\Big)\;, \tag{1.23}$$

where $g'(\eta) = \mathrm{d}g(\eta)/\mathrm{d}\eta$. We would like to understand how matter overdensities collapse so we consider a spherically symmetric shell with density ρ_s and radius $r(t)$ related by,

$$r(t)^3 \;=\; \frac{3M}{4\pi\rho_s}. \tag{1.24}$$

Initially the properties of the sphere are given by $r(t) = a(t)r_0$ and $\rho_s = \rho$, and under the assumption that the dynamics of the shell are determined completely by the mass within r, the equation of motion for $r(t)$ is given by

$$\frac{\ddot{r}(t)}{r(t)} \;=\; H_0^2\Big(g(\eta) - \frac{3}{2}\eta g'(\eta)\Big)\;, \tag{1.25}$$

$$\eta \;=\; \frac{8\pi G\rho_s}{3H_0^2}\;. \tag{1.26}$$

We then define an overdensity δ as

$$\delta \;=\; \frac{\rho_s - \rho}{\rho}\;. \tag{1.27}$$

The conservation of mass within the shell (see Equation 1.24) implies $r(t)^3\rho_s = a^3 r_0\rho$. This allows us to write the evolution of δ from Equation 1.25 and is given by,

$$\ddot{\delta} + 2H\dot{\delta} \;=\; 4\pi G\big(g'(\eta_0) + 3\eta_0 g''(\eta_0)\big)\rho\delta\;. \tag{1.28}$$

Variance of the density field

The initial density field was close to smooth with small ($\sim 10^{-5}$, see §1.1.6) perturbations, which collapsed gravitationally (as described by the growth equations) to form the highly peaked density fields observed today. For example, galaxies are $\sim$ 10kpc across and have mass $\sim 10^{11}\,M_{\odot}$ making them approximately a million times more dense than the critical density. To describe the large scale properties of the density field, we calculate its variance σ_R smoothed over some volume (or scale R). Historically $8\,h^{-1}$ Mpc has been chosen as the smoothing scale at which to quantify the variance of the density field and is denoted by σ_8.

1.1.5 The energy components of the Universe

The Universe is composed of differing components of energy density, which are diluted as the Universe expands depending on their equations of state w and given by (with the exception of curvature discussed below),

$$\Omega_i(z) \;=\; \frac{\Omega_i(z=0)}{a^{3(1+w_i)}}\,. \tag{1.29}$$

In this section we introduce the equations of state for each of the energy components in the Universe and describe this dilution as a function of scale factor.

Radiation

The energy component of radiation includes all electromagnetic radiation and relativistic matter (e.g neutrinos) and has $p = \rho/3$ i.e $w = 1/3$. The radiation energy density thus reduces quickly as the Universe expands, given by,

$$\Omega_r(z) \;=\; \frac{\Omega_r(z=0)}{a^4}\,. \tag{1.30}$$

Alternatively, the a^4 factor in the denominator can be thought of as coming from three factors of the expanding space (in each direction), and one factor due to the change in frequency as the photons are redshifted. Today the radiation energy density as measured from the Comic Microwave Background radiation is $\sim 10^{-4}$ smaller than that of matter and dark energy and is therefore often neglected.

Matter

The energy content of the Universe in the form of non-relativistic matter is composed of baryonic matter Ω_b in the form of stars, gas and dust, and non-baryonic or "dark matter" Ω_{DM} whose existence is inferred by observation. Dark matter is unlike ordinary matter because it only interacts through the force of gravity, and is transparent to electromagnetic radiation. It was proposed to explain the measured shapes of galaxy rotation curves and galaxy cluster velocity dispersions. Theoretical particle physics provides possible candidates for dark matter in the form of:

- Weakly Interacting Massive Particles (WIMPs), which are massive particles which only interact through the weak nuclear force and gravity.
- Supersymmetric particles, which are the proposed counterparts of normal baryonic particles, and are detectable only at high energies.
- Axions, which are theoretical particles that couple with photons in the presence of magnetic fields.

In addition to hypothetical particles, dark matter has been postulated to be composed of:

- Massive Astrophysical Compact Halo Objects (MACHOs), which are baryonic massive objects, e.g Black holes, Brown Dwarf stars, which emit little or no light.
- Neutrinos, whose absolute masses have yet to be measured.

Whatever dark matter is, we know that it must be mostly non-relativistic (known as "Cold" Dark Matter or CDM, Blumenthal et al., 1984) otherwise large scale structures could not have collapsed as observed. Non-relativistic matter has close to zero pressure, so the equation of state for matter is $w = 0$. Therefore the total matter energy density $\Omega_m = \Omega_b + \Omega_{DM}$ is diluted simply as the volume in the Universe increases,

$$\Omega_m(z) \quad = \quad \frac{\Omega_m(z=0)}{a^3} \; . \tag{1.31}$$

Dark energy

The energy density of the dark energy, fuelling the accelerated expansion of the Universe (see §1.1.6) is often assumed to be a Cosmological Constant as described in §1.1.1. Solving Equation 1.7 for Λ results in $p = -\rho$, and therefore the Cosmological Constant has an equation of state of $w = -1$, such that the energy density as a function of redshift is given by

$$\Omega_\Lambda(z) \quad = \quad \Omega_\Lambda \; . \tag{1.32}$$

This means that at early times, the energy density from Λ is much smaller than the matter ($\propto 1/a^3$) and radiation ($\propto 1/a^4$), but comes to dominate at late times, as the other components are diluted.

A slightly more general dark energy model allows the equation of state to be a different valued constant; then the evolution is given by,

$$\Omega_\Lambda(z) \quad = \quad \frac{\Omega_\Lambda(z=0)}{a^{3(1+w_0)}} \; . \tag{1.33}$$

In this thesis, we use Λ to refer both to the "Cosmological Constant" and to this more general dark energy model, and will quote the equation of state when different from -1.

Curvature

The curvature of the Universe has been measured to be very close to zero (see §1.1.6). The energy density of curvature Ω_k falls as,

$$\Omega_k = \frac{\Omega_k(z=0)}{a^2}. \tag{1.34}$$

The total energy density

The values of the energy densities have been determined using combinations of cosmological probes, which we introduce and discuss in the next section, and their combined value Ω_{tot} has been found to be,

$$\Omega_{tot} = \Omega_r + \Omega_m + \Omega_\Lambda + \Omega_k \simeq 1 \ . \tag{1.35}$$

Cosmological models which are based on General Relativity and are (dark) matter and dark energy dominated are denoted by ΛCDM, and are discussed further in §1.1.7. In the next section we examine cosmological probes and describe the constraints they can place on cosmological parameters.

1.1.6 Combining cosmological probes

We use cosmological probes to measure the cosmological parameters such as the densities of the energy components of the Universe (described in §1.1.5). We find that the constraining power of any one cosmological probe is generally too small to effectively constrain all cosmological parameters simultaneously, and therefore their true power comes from combining different probes, breaking parameter degeneracies and lessening systematic uncertainties. For example, the Cosmic Microwave Background radiation (hereafter CMB) measures the Universe to be close to spatially flat (i.e. $\Omega_k = 0$), and the Baryon Acoustic Oscillations (hereafter BAO) tell us that the matter content of the Universe is less than $0.4\rho_c$, additionally Supernovae (hereafter SNe) measure the Λ energy content of the Universe to be larger than the matter content. Combining these constraints allows us to build the current concordance cosmological model (see §1.1.7). We discuss these experiments in more detail below.

The Cosmic Microwave Background Radiation

The presence of the CMB is conclusive evidence that the Universe has evolved from a hot ionised state where photons and baryons were strongly coupled (e.g. see Hu and White, 2004). As the early Universe expanded, the photon-baryon plasma cooled and upon reaching ~ 3000K, neutral hydrogen formed allowing the photons to decouple and free stream to us to be seen as the CMB. The CMB has interacted little with matter since decoupling and so provides a detailed picture of how the Universe looked when it was just $\sim 380,000$ years old. The CMB has been redshifted by $z = 1089$ and is detected today in the microwave bands with a temperature of ~ 2.7K.

The CMB was detected serendipitously by Penzias and Wilson in 1965 and later measured by the COsmic Background Explorer[2] (Smoot et al., 1991, hereafter COBE) to be isotropic over the entire sky to one part in 10^5. This remarkable discovery implies that at the time of decoupling, non-causally connected regions of space looked identical. This could be caused by superluminal expansion (in the very early Universe) of a tiny region of space to a size larger than the present observable Universe, a process known as "Inflation" (see Guth, 1997).

Some statistical properties of the CMB are quantified using the temperature power spectrum as a function of angular wavenumber l. The theoretical shape of the temperature power spectrum is related to the energy density of radiation, baryons, and dark matter. By comparing the observed and theoretical temperature power spectra we can use the CMB to constrain cosmological parameters.

The CMB temperature power spectrum has been measured to high precision by the Wilkinson Microwave Anisotropy Probe[3] (hereafter WMAP), and we reproduce their results in Figure 1.2 which show the temperature power spectrum $l(l+1)C_l/2\pi$ as a function of multipole l where $l = \pi/\theta$.

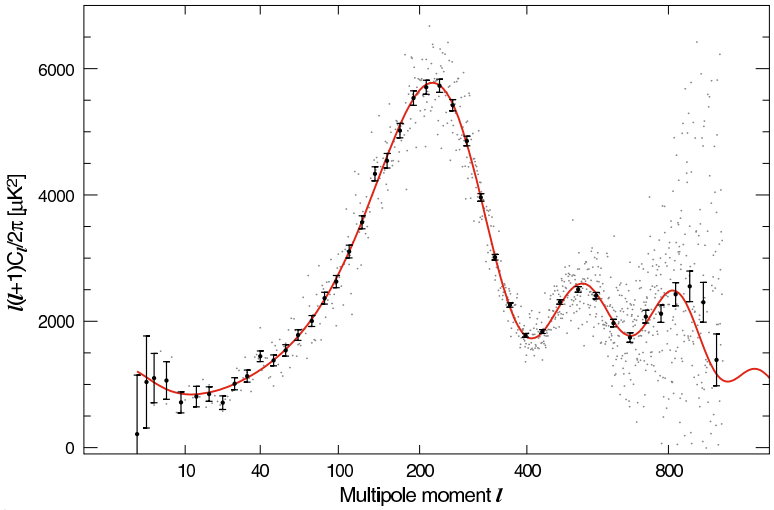

Figure 1.2: The temperature power spectrum $l(l+1)C_l/2\pi$ of the Cosmic Microwave background as a function of increasing multipole l (decreasing scale) as measured by WMAP. Credit: Dunkley et al. (2009).

The location of the first peak in the CMB power spectrum corresponds to the size of the sound horizon at last scattering, and we can measure the distance to the surface of last scattering from the redshift of the CMB, and therefore we have a very accurate measurement of a point on the Hubble diagram (albeit at high redshift), which allows us to probe the geometry of the Universe.

[2] http://aether.lbl.gov/www/projects/cobe/
[3] http://map.gsfc.nasa.gov/

This technique measures the curvature energy density of the Universe to be 0.0001 ± 0.030. The subsequent peaks probe combinations of Ω_r, Ω_b and Ω_m, and the current values for the energy densities of the Universe as measured by WMAP are shown in Table 1.2.

Returning briefly to Figure 1.2, we can see that WMAP has measured the location and shape of the first and second peaks in the temperature power spectrum to high accuracy. The less well constrained third peak (at $l \sim 800$) provides information about the parameter combination $\Omega_m H_0^2$, and is due to be measured by PLANCK[4] which launched on 14/05/2009.

The CMB allows us to test physics in the early Universe ($z = 1089$), but is less sensitive to the late Universe as the photons rarely interact with matter. Exceptions where the weak interaction of the CMB with the Universe is important, are the Integrated Sachs-Wolfe effect (Sachs and Wolfe, 1967) and the Sunyaev-Zeldovich effect (Sunyaev and Zeldovich, 1970).

The Baryon Acoustic Oscillations

The Baryon Acoustic Oscillations occur as pressure waves at the surface of last scattering, as measured by the CMB, form overdensities in the matter density field which seeded the growth of structure through gravitational collapse. This is measured today in galaxy redshift surveys as an overdensity of galaxies at a characteristic comoving scale of $100\,h^{-1}$ Mpc, and used to constrain cosmology through the distance-redshift relationship.

The BAO has been measured by Eisenstein et al. (2005) using $46,748$ Luminous Red Galaxies (hereafter LRGs) from the Sloan Digital Sky Survey (hereafter SDSS, see §2.1.1) with a median redshift of $z = 0.35$. Figure 1.3 shows the measured galaxy cross correlation $\xi(s)$ as a function of comoving separation, with flat theoretical models containing baryons and dark matter (curves with a bump) and baryon free pure dark matter (the bump free curve).

By examining the difference between the peak of the measurement (at $100\,h^{-1}$ Mpc) with the baryon free curve (magenta line) in Figure 1.3, we see that the amplitude of the BAO signal is $< 1\%$ making an accurate measurement only possible with time consuming, expensive wide field spectroscopic surveys, containing many hundreds of thousands of galaxies. Additionally the signal can be distorted by nonlinear effects, such as redshift space distortions caused by peculiar velocities from galaxy clustering (Angulo et al., 2008).

The BAO measurement was repeated with a larger dataset by Percival et al. (2007) using galaxy samples from the SDSS, combined with data from the 2 Degree Field Galaxy Redshift Survey[5] (hereafter 2dFGRS). They measured the BAO scale at $z = 0.35$ using the SDSS Luminous Red

[4] http://www.rssd.esa.int/index.php?project=planck
[5] http://www.mso.anu.edu.au/2dFGRS/

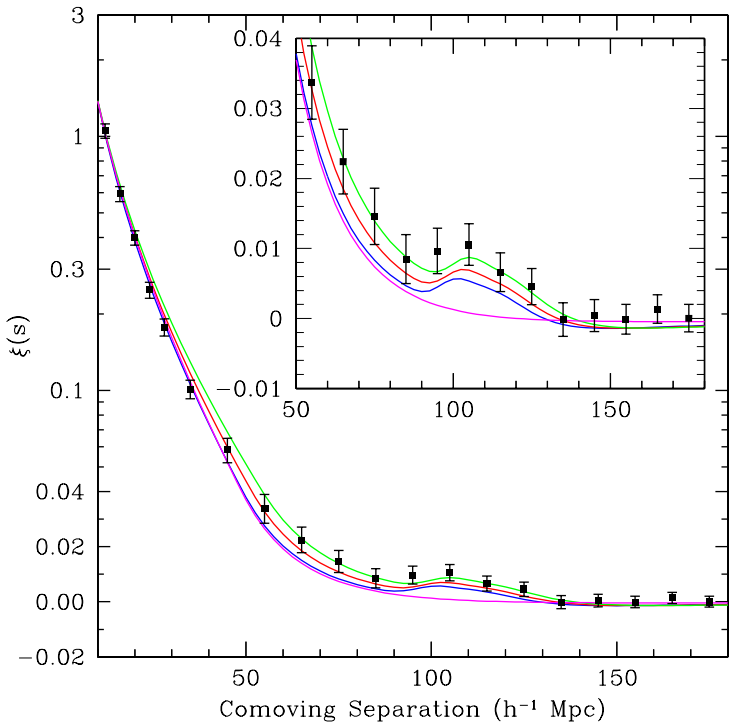

Figure 1.3: The measured galaxy cross correlation $\xi(s)$ as a function of comoving separation, using the SDSS LRGs with a median redshift $z = 0.35$. The coloured lines correspond to theoretical models assuming $\Omega_m h^2 = 0.12, 0.13, 0.14$ (green, red, blue lines) with baryon fraction $\Omega_b = 0.024$, and a baryon free model with $\Omega_m h^2 = 0.105$ (magenta line), within a $w_0 = -1$, ΛCDM. Credit: Eisenstein et al. (2005).

Galaxies (LRGs) and at $z = 0.2$ using the SDSS and 2dFGRS galaxies. The obtained cosmological constraints on Ω_Λ and Ω_m assuming $w_0 = -1$, ΛCDM after being combined with SNe and WMAP are shown in Table 1.2.

Supernovae

Type Ia Supernovae are believed to be accreting white dwarfs which explode upon reaching the Chandrasekhar mass limit (more correctly, the temperature at which fusion occurs), thus emitting a characteristic intrinsic luminosity which can be empirically standardised, potentially making them independent distance estimators i.e "standard candles". They emit $\sim 10^{51}$ergs and are bright enough to outshine their host galaxies allowing them to be detected to high redshifts. Other SNe types are formed by more complicated collapsing processes of different star classes, which produce a range of intrinsic luminosities, making them less standardisable. The observed SNe brightness is proportional to distance, which is compared to the redshift of the SNe (or host galaxy) using a "distance modulus-redshift" diagram. The distance modulus is the observed magnitude minus the standardised intrinsic magnitude and is sensitive to cosmological parameters through the luminosity distance.

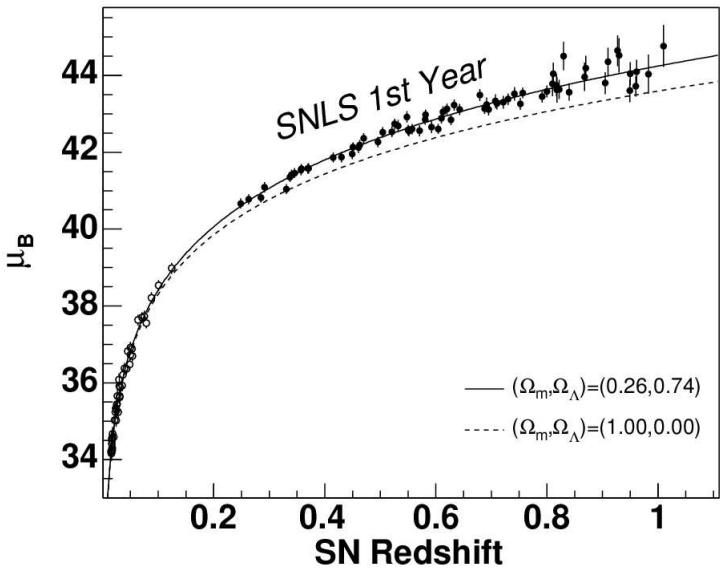

Figure 1.4: The SNe distance modulus μ_B against the SNe spectroscopic redshift using data from the SuperNovae Legacy Survey. Overplotted is an Einstein de-Sitter model (dotted line) and the best fitting ΛCDM model (solid line). Credit: Astier et al. (2006).

In 1998 two teams (Riess et al., 1998; Perlmutter et al., 1999) used SNe Type Ia as distance indicators to measure the expansion of the Universe and concluded that the expansion was accelerating. This could be explained by introducing Λ in the Einstein equations (see Equation 1.4). Figure 1.4 shows the latest measured distance modulus μ_B as a function of redshift with two models ($\Omega_m = 1$ and $\Omega_m = 0.26, \Omega_\Lambda = 0.74$) overplotted. The figure demonstrates that the pure matter model is a poor fit to the data, which prefers a dark energy component. The constraints placeable on Ω_Λ and Ω_m assuming $w_0 = -1$, ΛCDM are shown in Table 1.2.

Supernova are however fraught with theoretical and observation complications. The identification of a SNe Type Ia requires spectroscopic followup, which at high redshift needs large ground based telescopes or expensive space based telescopes. Additionally, for the light curves to be standardised, the SNe must be imaged multiple times within a time frame of a few weeks, preferably before and after the maximum of the emission. Theoretical challenges also exist in the modelling of the complicated explosion and feedback processes. Additionally Howell et al. (2006) has shown that SNe Type Ia may be sub-divided, and so their ability to be standardised has been brought into question.

Geometry and structure

In General Relativity (including ΛCDM, hereafter GR) the geometry of the Universe is completely described by the amount of matter (clusters, filaments and voids) in the Universe (see Equation 1.4). One can infer the structure of the Universe by testing the geometry (with the

CMB, BAO or SNe). Alternatively, one may test *both* the structure and the geometry using different probes, and compare their equivalence. Some modified theories of gravity (which attempt to explain the accelerated expansion of the Universe without dark energy by modifying GR) predict the structure and geometry are separate quantities with their own evolution (e.g. see Song and Koyama, 2009).

We can use clusters of galaxies as such probes of structure which are advantageous in two respects: If the underlying cosmology is GR, clusters provide an independent measure of cosmological parameters with differing sets of systematics to the CMB, BAO and SNe, or if the underlying cosmology is different from GR, clusters will provide a probe of the growth of structure to be used in addition to the probes of geometry to constrain model parameters. We introduce galaxy clusters as cosmological probes below, and in more detail in §1.2. We note that weak lensing probes the combination of growth and structure and can be used to break parameter degeneracies and is introduced in §5.

Galaxy clusters

Clusters of galaxies are the largest gravitationally bound structures and are typically up to a few megaparsecs in extent, containing tens to thousands of galaxies (usually red early type galaxies), and have masses in the range 10^{13} to 10^{15} solar masses.

Galaxy clusters can be used as probes of cosmology by measuring the "cluster mass function" (hereafter CMF), which is the abundance of clusters as a function of mass and redshift, and will be discussed further and derived in §4. Constraining cosmology using the CMF has only recently been achievable, because for the CMF to be constructed, a large number of clusters with measured redshifts must be identified, their levels of completeness understood, and crucially, their masses estimated.

Cluster masses have traditionally been computed using one or more of the following techniques:

- The temperature of the Intra-Cluster Medium (hereafter ICM), a hot diffuse ionised gas. The temperature of the ICM is related to the mass of the cluster halo (Cavaliere and Fusco-Femiano, 1978).
- Gravitational lensing, which measures the distortion of the images of background galaxies due to the cluster halo mass warping space-time (e.g. Dahle, 2007).
- According to the Halo Occupation Distribution, the number of cluster galaxies is related to the cluster mass (e.g. Seljak, 2000).
- The optical luminosity has been shown to trace cluster mass (e.g. Miller et al., 1999).

The primary aims of this thesis are to assign mass estimates to optically identified clusters and then construct the CMF and use it to obtain constraints on cosmological models and parameters.

We describe clusters of galaxies in more detail in §1.2 and discuss complications which arise with the measurement of cluster mass.

Previous work to measure cosmological parameters using the CMF has been undertaken by Vikhlinin et al. (2009) who followed up 37 high redshift $z > 0.55$ X-ray clusters selected from the ROSAT 400 square degree catalogue (see §2.2.1) with CHANDRA[6] to obtain accurate temperature measurements. Additionally included were 49 low redshift $z < 0.25$, clusters selected from the ROSAT All Sky Survey with measured temperatures. They use the X-ray temperature measured in an annulus $(0.15 - 1)R_{500}$ (R_{500} corresponds to the radius of a sphere for which the average density enclosed is $500\rho_c$), as a mass proxy. Assuming a flat ΛCDM with a constant equation of state of dark energy w_0, they constrain the parameter combination $\sigma_8(\Omega_m/0.25)^{0.41} = 0.832 \pm 0.033$ and $w_0 = -1.14 \pm 0.21$ using clusters alone, and break the $\sigma_8 - \Omega_m$ degeneracy using the Cosmic Microwave Background (Dunkley et al., 2009), supernovae (Astier et al., 2006) and Baryon Acoustic Oscillation (Percival et al., 2007) constraints and find $\sigma_8 = 0.786 \pm 0.011, \Omega_m = 0.268 \pm 0.016$, and $w_0 = -0.991 \pm 0.045$.

Using the stacked weak lensing shear signal of background SDSS galaxies (created by Sheldon et al., 2007) around an optical cluster dataset called MaxBCG (see §2.1.7), and using the number of cluster galaxies N_{gal} as a proxy for mass (Johnston et al., 2007) Rozo et al. (2009) fit the measured mass function for cosmological parameters assuming a flat ΛCDM. After marginalising over mass-observable fitting parameters, they constrain $\sigma_8(\Omega_m/0.25)^{0.41} = 0.832 \pm 0.033$, which reduce to $\sigma_8 = 0.807 \pm 0.020$ and $\Omega_m = 0.265 \pm 0.016$ when combined with constraints from the Cosmic Microwave Background (Dunkley et al., 2009).

Figure 1.5 is a reproduction of their results, showing the one and two σ confidence contours in the $\sigma_8 - \Omega_m$ plane, assuming a flat ΛCDM cosmology with $w_0 = -1$, additionally shown are the confidence contours for WMAP (Dunkley et al., 2009) and the combined confidence contours. The parameter confidence contours in Figure 1.5 are seen to improve by $\sim 70\%$ after combining the constraints from clusters with constraints from the CMB.

The limitations of these studies are that they use relativity low number of X-ray luminous clusters (e.g. 86 in Vikhlinin et al., 2009), or divide the cluster sample into subgroups and assign a mass estimates to each subgroup, so the mass of any one cluster is unknown (e.g, Rozo et al., 2009). By contrast, in §3 we use > 400 X-ray identified clusters to determine mass estimates for each of the MaxBCG clusters.

Combining cosmological constraints

We summarise the constraints from all the above probes of cosmology in Table 1.2 and show, where available, the improvement in constraints when combining different datasets. For example

[6] http://chandra.harvard.edu/

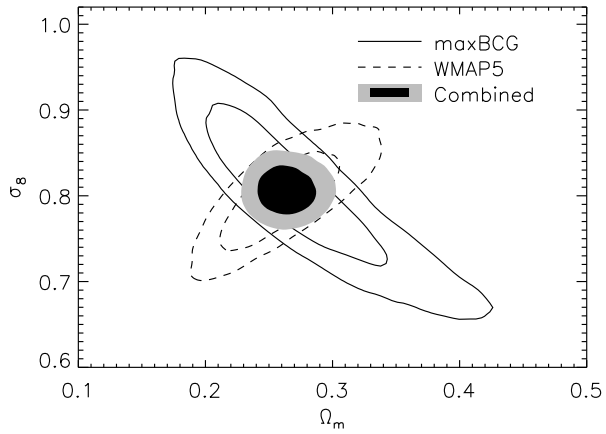

Figure 1.5: A reproduction of Figure 5 of Rozo et al. (2009), showing the one and two σ confidence contours in the $\sigma_8 - \Omega_m$ plane by reconstructing the MaxBCG CMF using weak lensing shear measurements and N_{gal} as a mass proxy. Additionally shown are the confidence contours of WMAP (Dunkley et al., 2009) and the combined contours. Credit: Rozo et al. (2009).

the SNe alone measure Ω_m with an error of 67.7% which is reduced to 7.4% after being combined with the CMB. Generally a single measurement is so poor at constraining cosmological parameters that the results are often published *after* combining with other datasets. A notable exception is the CMB, which measures some parameters very accuractly (but at $z = 1089$).

Measured cosmological parameters						
Tests of geometry						
Probe	Reference	Parameters				
		Ω_b	Ω_{DM}	Ω_Λ	$H_0^\star$	σ_8
CMB	Dunkley et al. (2009)	0.0441 ± 0.003	0.214 ± 0.027	0.742 ± 0.030	$71.9^{+2.6}_{-2.7}$	0.796 ± 0.036
CMB + BAO + SNe	Dunkley et al. (2009)	0.0462 ± 0.002	0.233 ± 0.013	0.721 ± 0.015	70.1 ± 1.3	0.817 ± 0.026
SNe Ia	Astier et al. (2006)	0.31 ± 0.21		0.80 ± 0.31	–	–
SNe Ia + BAO	Astier et al. (2006)	0.27 ± 0.02		0.75 ± 0.08	–	–
BAO + SNe + CMB	Percival et al. (2007)	0.252 ± 0.027		0.743 ± 0.047	–	–
Tests of the growth of structure						
Clusters + CMB	Rozo et al. (2009)	0.265 ± 0.016		$1 - \Omega_m$	–	0.807 ± 0.020

Table 1.2: The values of cosmological parameters as measured by different probes, and their values after being combined with other datasets. * H_0 has units $\mathrm{km\,s^{-1}\,Mpc^{-1}}$.

In §1.1.7 we combine the theoretical framework with the observational data to describe the currently accepted concordance cosmology model.

1.1.7 The concordance cosmological model

After 90 years of research we have a widely tested concordance model for cosmology called Λ (representing dark energy) Cold Dark Matter and abbreviated to ΛCDM, which is constructed by combining theoretical ideas with observational evidence (see Table 1.2) and is composed of:

- Electromagnetic radiation accounting for $< 1\%$ of the total energy density.
- Baryons, in the form of stars, gas, and dust, which accounts for $\sim 4\%$ of the total energy density.
- Non baryonic dark matter, which provides the "missing mass" required to explain the measured shapes of galaxy rotation curves and galaxy cluster velocity dispersions. Dark matter accounts for $\sim 22\%$ of the total energy density of the Universe.
- A dark energy component (Λ) which is required to explain the accelerated expansion of the Universe and accounts for $\sim 74\%$ of the total energy density.

Although ΛCDM is currently poorly motivated theoretically, it predicts all cosmological observations to within experimental errors. To test ΛCDM further we need probes of cosmology which rely on different sets of systematics than those which test geometry (CMB, SNe, and BAO see Table 1.2). As introduced above, clusters provide an independent test of ΛCDM through a measurement of the growth of structure.

Using galaxy clusters in combination with a geometric probe like the CMB, provides an improvement in constraints compared to the combination of purely geometric probes CMB and SNe and BAO (e.g the error on σ_8 reduces from 0.026 using three probes to 0.020 using two probes, see Table 1.2). The developing field of CMF research forms the basis of this thesis, and as such we introduce galaxy clusters in more detail in the next section.

1.2 Clusters of galaxies as probes of cosmology

This section introduces clusters of galaxies as probes of cosmology, through a measurement of the "cluster mass function" (hereafter CMF), which is the abundance of clusters as a function of mass and redshift. The CMF has the potential to constrain the cosmological parameters σ_8, Ω_m and provide independent evidence for Ω_Λ. We reiterate, that for the CMF to be constructed, a large number of clusters must be detected, their redshifts determined and their levels of completeness and purity understood, and their masses measured.

1.2.1 Detecting galaxy clusters

We show a multi-wavelength image of the cluster of galaxies "Abell 0520" (located at RA,DEC $[73.579, 2.947]$ and $z = 0.199$) in Figure 1.6. The galaxies are shown in yellow and stars in white. The X-ray emission (from the Intra Cluster Medium) is represented by the red cloud and the reconstructed weak lensing mass map represented by blue.

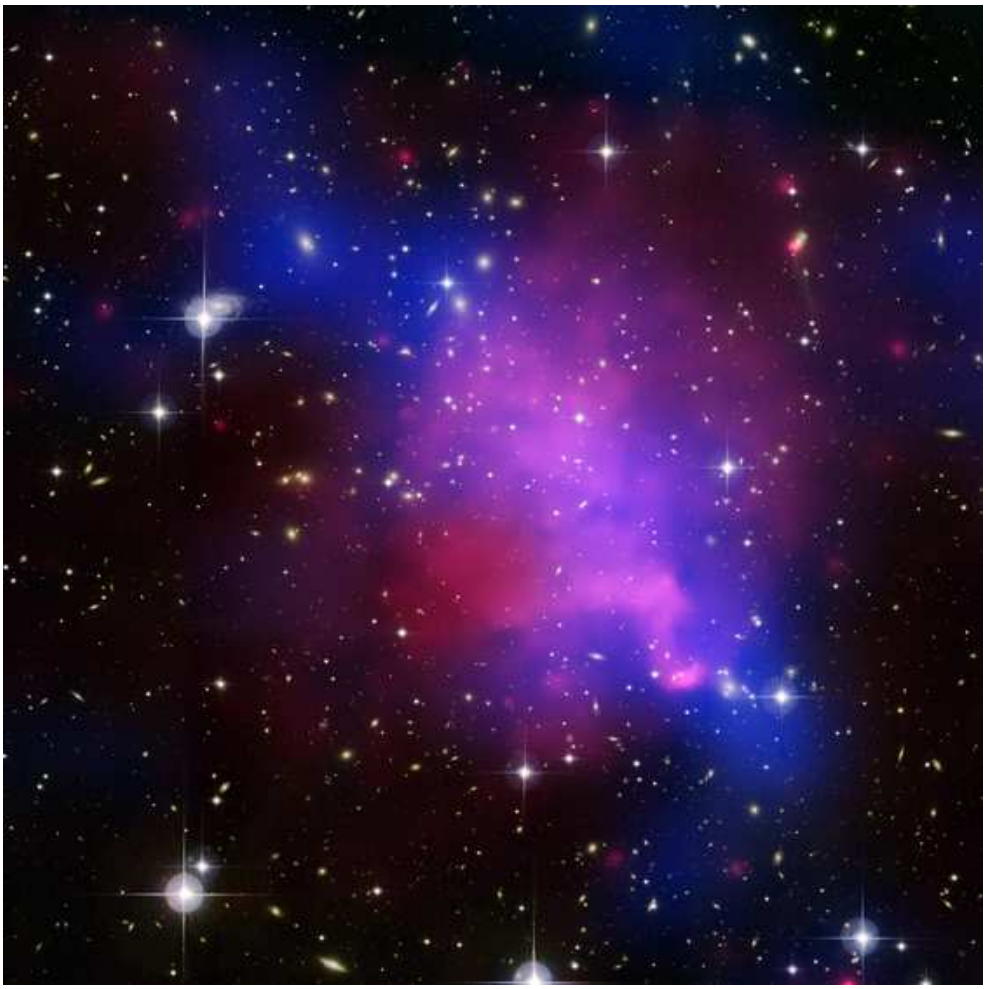

Figure 1.6: A multi-wavelength image of the cluster of galaxies "Abell 0520" (located at RA,DEC $[73.579, 2.947]$ and $z = 0.199$), the image scale is 9.25 arcminutes across. The galaxies are shown in yellow and stars in white. The X-ray emission is represented by the red cloud and the reconstructed weak lensing mass map represented by blue. Credit: X-ray: NASA/CXC/UVic./A.Mahdavi et al. Optical/Lensing: CFHT/UVic./A.Mahdavi et al.

Figure 1.6 demonstrates that clusters emit electromagnetic radiation over a range of wavebands, and as such are commonly detected using:

- X-ray wavelengths, due to the Bremsstrahlung emission of the hot diffusion ionised Intra Cluster Medium (e.g. Ebeling et al., 1998, 2000; Burenin et al., 2006; Romer et al., 1999; Stanford et al., 2006).
- Optical wavelengths, as an overdensity of early type galaxies (e.g. Miller et al., 2005; Koester et al., 2007b), or due to the gravitational distortion of background galaxies (Padmanabhan et al., 2003; McInnes et al., 2009).
- Microwaves, due to an interaction between the Intra Cluster Medium and the CMB (e.g. Bennett et al., 2003).

The detection of clusters using optical and X-ray wavelengths are discussed in more detail in §2. Once large cluster datasets have been compiled their masses must be measured before the CMF can be calculated.

1.2.2 The masses of galaxy clusters

Measuring the masses of clusters of galaxies is imperative if they are to be used to construct the CMF and probe cosmology. This is difficult to achieve for two reasons; the definition and measurement of cluster properties (such as radius) is ambiguous, and mass is not an observable quantity; we address these issues below.

To measure the physical properties of a cluster, such as radius (or volume within which to calculate a mass) they must first be defined. Complications arise because, for example, the radius of a cluster can be measured from the number density of member galaxies, which is inherently problematic because one must decide where the galaxy cluster ends and the background galaxy field begins. This problem may be overcome by adopting certain definitions such as R_{200}, corresponding to the radius at which the mass enclosed is 200 times that of the average density of the Universe (both ρ_c and $\bar{\rho}_m$ are used in the literature) calculated at the redshift of the cluster, or alternatively $R_{\Delta_{VIR}}$ corresponding to the virial radius, which is the radius at which an object contains just enough mass to self collapse. In an Einstein-de Sitter Universe ($\Omega_m = 1$) the virial radius is 178, but is lower and a function of redshift in more general flat cosmologies and given by (Stoehr, 1999),

$$\Delta_{vir} = 9\pi^2\Big(1 + 0.7\big(1 - \Omega_m(z)\big) + \Omega_m(z)^{0.44}\Big) . \tag{1.36}$$

Once physical properties (such as radius) of the cluster are defined and measured, the process to calculate the cluster mass (which is not an observable) can begin.

If a theoretical motivation exists, a cluster observable can be used to measure the cluster mass. For example the X-ray temperature T of the ICM was shown by Cavaliere and Fusco-Femiano (1978) to be related to the cluster mass M by $M \propto T^{1.5}$ (see §3.1.2). Measuring the temperature of the ICM is expensive and difficult to achieve because the X-ray observatories must be placed on satellites, and require long exposure times. Therefore only a few hundred clusters have had their masses estimated using this technique (e.g. see Vikhlinin et al., 2009).

The velocity dispersions of cluster member galaxies can be used to infer the masses of clusters, but requires spectroscopic followup of member galaxies, which is very time consuming, and relies heavily on the assumption that the cluster is relaxed (has not undergone a recent merger e.g. Carlberg et al., 1996).

Additionally, cluster masses of a few tens of clusters have been inferred through the strong and

weak gravitational distortion of images of background galaxies (e.g. Dahle, 2007, and §5), but requires the clusters to be massive and in areas with deep photometry and large numbers of lensed galaxies must have measured redshifts.

The cluster mass may also be inferred empirically, by measuring the relationship between an easily obtained observable (e.g optical luminosity), and an observable which scales with cluster mass (e.g. X-ray temperature, see Miller et al., 1999, and §3).

Studies have also compared the mass estimates from differing techniques applied to the same cluster, for example Wu et al. (1998) complied a list of 20 clusters from the literature with X-ray and velocity dispersion (hereafter VD) mass estimates, 24 clusters with weak gravitational lensing (hereafter WL) mass estimates, and 38 clusters with strong gravitational lensing (hereafter SL) mass estimates. They find the WL and VD mass estimates agree to 8% (with a scatter of 70%), the SL and VD disagree by a factor of 6, the X-ray mass and WL to agree to 3% (with a scatter of 44%) and X-ray mass and SL to differ by a factor of 3. More recently Pedersen and Dahle (2006) measure the scatter in the X-ray mass and WL masses of 30 heterogeneously selected clusters and find consistency to within 20%.

These works show that the consistent measurement of cluster mass is difficult. In this thesis we aim to reduce these uncertainties by using orders of magnitude more clusters than previously possible to quantify the relationship between observables and mass.

1.2.3 The cluster mass function

As further motivation to measure the masses of clusters, we present how the CMF changes with varying cosmological parameters. The CMF is sensitive to cosmology models and parameters through the theoretical description of how matter overdensities collapse to form clusters (see §1.1.4). We calculate the CMF under the assumption that clusters collapse to form ellipsoidal structures (Sheth and Tormen, 2002) and discuss this and alternatives in more detail in §4.2.5.

Figure 1.7 shows the change in the theoretical CMF, calculated at a mass of $10^{14}\ h^{-1}\ M_{\odot}$ as a function of redshift, by changing cosmological parameters away from a fiducial flat $h = 0.7, \Omega_m = 0.3, \sigma_8 = 0.8, w_0 = -1, \Lambda$CDM model shown by the solid line in each figure. We adopt the redshift range $0 < z < 0.3$ in these predictions to mirror the redshift range of the cluster catalogues used in this work (described in §2).

Figure 1.7(a) demonstrates that the theoretical CMF is highly sensitive to σ_8 (the normalisation of the variance of the matter power spectrum, smoothed on a scale of $8\,h^{-1}$ Mpc) with relatively small changes of σ_8 from 0.6 to 1.0 between models, producing a difference ratio of 3.2 at $z = 0.01$ to 5.8 at $z = 0.30$. Figure 1.7(b) shows that the mass function is also sensitive to Ω_m, with a ratio of 3.2 at $z = 0.01$ and 2.8 at $z = 0.30$ when comparing models with $\Omega_m = 0.3$ and

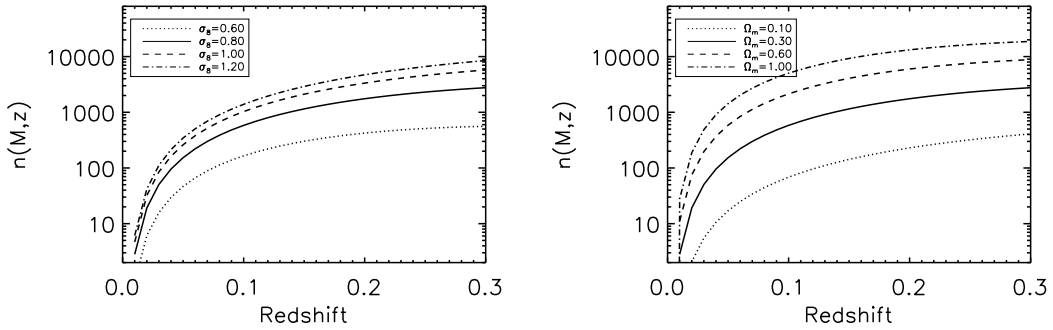

(a) Changing σ_8

(b) Changing Ω_m

Figure 1.7: The theoretical cluster mass function $n(M, z)$ at $10^{14}\ h^{-1}\ M_\odot$ as a function of redshift, while varying cosmological parameters σ_8 (left figure) and Ω_m (right figure), away from a flat fiducial $\Omega_m = 0.3, \sigma_8 = 0.8, w_0 = -1, \Lambda$CDM.

$\Omega_m = 0.6$.

We have shown that clusters of galaxies (through the CMF) can provide a probe of cosmology which is independent of geometry which other probes rely heavily upon (such as CMB, SNe, BAO) and will therefore have different sets of systematics. We have also shown that the definition of a cluster and the measurement of its mass is difficult and because of this clusters have only recently been used to constrain cosmology. The remainder of this thesis is dedicated to measuring the masses of clusters of galaxies in order to compute the CMF and constrain cosmology.

1.3 Summary of the thesis

In this chapter we have introduced some key concepts in observational cosmology and discussed some experimental probes of the cosmological parameters and their findings. We have described the use of galaxy clusters as additional independent probes of cosmology and shown how they can be used to measure the cluster mass function with which to probe cosmology, through a measurement of their number densities and masses.

In §2 we discuss the optical and X-ray datasets used throughout the thesis, and describe work done as part of the XMM Cluster Survey to measure redshifts for a large sample of newly identified X-ray clusters for which temperatures have been measured. Even with this work, there are still two orders of magnitude more optical than X-ray selected clusters.

In §3 we find the X-ray selected clusters which have optical counterparts and after converting the X-ray temperature to a mass, we compare X-ray and optical properties, finding that the summed optical luminosity scales with X-ray derived cluster mass, allowing the assignment of mass to all the optically selected clusters.

We continue in §5 by using an alternative weak lensing mass estimator, called the magnification bias, on the optical cluster catalogues. We introduce and measure the magnification bias and find that our samples are Poisson noise dominated, allowing only the placing of an upper mass limit on the stacked optical clusters. However, using this method we are able to place upper constraints on σ_8 and Ω_m.

In §4 we compare the masses of clusters measured in §3 and §5 and show them to be consistent, and then convert the measured masses to cluster mass functions and compare with theoretical abundance predictions, and find good independent constraints on σ_8 and Ω_m assuming a flat ΛCDM universe.

We conclude and discuss future applications in §6.

Chapter 2

Data catalogues

This chapter introduces the Sloan Digital Sky Survey (hereafter SDSS) and describes the optical catalogues and X-ray catalogues used throughout the thesis. It documents the creation of a Luminous Red Galaxy (hereafter LRG) sample using the latest SDSS data. We then develop a method to estimate redshifts of X-ray clusters using the LRGs, and estimate redshifts for the XMM Cluster Survey (hereafter XCS). We finish with calculations of the purity of the XCS and introduce work to uniformly recalculate luminosities and temperatures for the X-ray cluster catalogues.

2.1 Optical data

The optical data used throughout this thesis are drawn from the Sloan Digital Sky Survey (Abazajian et al., 2008). In the following section we describe the SDSS and derived properties useful to this work. We continue by describing selection criteria for Luminous Red Galaxies and the compilation of a massive LRG sample. Finally spectroscopic and photometric galaxy cluster catalogues and photometric quasar catalogues are introduced.

2.1.1 The Sloan Digital Sky Survey

The original incarnation of the SDSS (York et al., 2000) imaged $8,423$ square degrees of the (mostly) Northern sky and had dedicated spectroscopic follow up of selected targets. This first project ran from 2000-2005 and obtained 5 band imaging of 230 million unique objects. At this stage, the SDSS had obtained spectra for $5,700$ square degrees and $1,048,960$ objects, of which $674,749$ comprised galaxies. SDSS-II was launched in part to complete the spectroscopic coverage and in 2008 had completed the spectroscopic survey footprint obtaining $1,640,960$ unique spectra, of which $929,555$ are galaxies.

The SDSS uses a 2.5 meter (Gunn et al., 2006) telescope at Apache Point Observatory New Mexico. Optical imaging is performed using a 142 mega-pixel CCD camera with a 1.5 square degree field of view and a pixel resolution corresponding to $0.396''$ (Gunn et al., 1998). The five SDSS photometric bands, u, g, r, i, z (Fukugita et al., 1996; Lupton et al., 1999; Hogg et al., 2001) are shown in Figure 1 of Padmanabhan et al. (2005), replicated here as Figure 2.1. Imaging

is taken under good seeing conditions and calibrated using photometry of standard stars measured on a nearby 20 inch telescope (Smith et al., 2002).

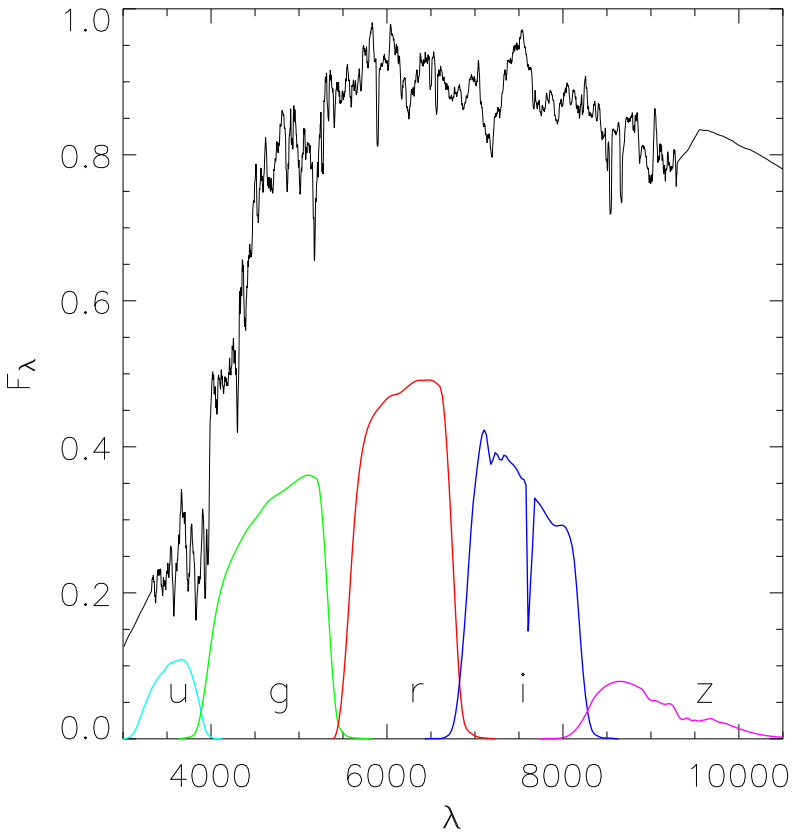

Figure 2.1: The five band SDSS photometric filters. Overplotted is a Luminous Red Galaxy spectra taken from Bruzual and Charlot (2003). The prominent break in the spectrum at 4000Å enables accurate photometric redshifts using the SDSS filters. Credit: Padmanabhan et al. (2005).

Spectroscopic follow up is performed using two spectrographs capable of measuring spectra of 640 targets per observation. Targets are selected dynamically from SDSS imaging and other surveys (e.g. optical counterparts to X-ray selected ROSAT clusters Anderson et al., 2003). Targets include "main sample" galaxies (Strauss et al., 2002), quasars (Richards et al., 2002), LRGs (Eisenstein et al., 2001) and calibrating objects (Stoughton et al., 2002).

Data is publicly available via on-line interfaces. Using the "Navigate"[1] tool, the user can view color images of the sky at a range of magnifications across the footprint of the SDSS. Alternatively, users may use the web accessible "Data Archive Server"[2] and the "Catalog Archive

[1] http://cas.sdss.org/dr7/en/tools/chart/navi.asp
[2] http://das.sdss.org/www/html/

Server"[3] to access spectra, images (in FITS and JPEG formats) and catalogue tables. Additionally "Casjobs"[4] is a web interface to a database back end allowing queries to be run on SDSS data using Structured Query Language. Casjobs holds 18 terabytes of instrument and viewing data, and properties derived by the SDSS pipelines.

The automated SDSS pipelines reduce the imaging correcting for flat fields, sky subtractions and instrument defects. The pipelines use the reduced imaging to measure co-ordinates, shapes and fluxes of all objects. Flags are set depending on the successes of the pipelines to measure the properties of an object. For example, flags identify objects which are well detected at high signal-to-noise (**BINNED1**) or objects which are nearby/behind other astronomical objects and need to be reconstructed after the removal of the neighbour (**DEBLENDED**). The flags checked to ensure clean galaxy samples in this thesis are discussed in §2.1.4.

The measuring and conversion of flux to magnitude is not unique. In the following section we discuss the magnitude systems used in the SDSS and highlight those of interest here.

2.1.2 SDSS magnitudes

This section introduces the SDSS conversion from flux to magnitude and describes the various magnitudes available in the SDSS and the conversion of magnitudes to the AB system.

Luptitudes

The flux from SDSS objects are noise and sky subtracted. For very faint objects, the detected flux f is very small. It is possible for the corrected fluxes to be negative. The traditional method (Pogson, 1856) using $m = -2.5\ \log(f)$ is unable to account for such negative fluxes. A solution was proposed by Lupton et al. (1999), which uses a hyperbolic transformation and is well defined for low and negative fluxes e.g,

$$m \quad = \quad \frac{-2.5}{\ln(10)} \sinh^{-1}\left(\frac{f/f_o}{2b} + \ln(b)\right) , \tag{2.1}$$

where f_0 is the classical flux zero point and b is the sky's typical 1σ noise in a Point Spread Function (hereafter PSF) aperture in $1''$ seeing. As the flux increases past $10f_0$, the Pogson and Lupton magnitudes agree to $< 1\%$.

Fiber magnitudes

Fiber magnitudes are calculated in each band from the total flux within the $3''$ aperture diameter of a spectroscopic fiber.

[3] http://cas.sdss.org/astrodr7/en/
[4] http://casjobs.sdss.org/

PSF magnitudes

The PSF magnitudes are used to describe stars. The star flux and the local spatial flux variations of the PSF around the star are modelled by two Gaussians. The difference between the two Gaussians is the aperture correction. A final aperture correction out to a radius of $7.4''$ is applied from comparisons with standard stars. These corrections reduce the uncertainty in the objects PSF magnitude to < 0.02 even in poor $2''$ seeing conditions.

Petrosian magnitudes

The Petrosian magnitude (Petrosian, 1976; Blanton et al., 2001; Yasuda et al., 2001) is one of the SDSS magnitudes used to measure the flux of galaxies. Unlike stars, galaxies can have irregular flux profiles. To model this behaviour a radius R_p is defined at which the ratio of surface brightness within an annulus at R_p is a fraction of the mean surface brightness within R_p. The SDSS sets this ratio to be 0.2. R_p is measured for each band but only the r band radius R_{p_r} is used in the measurement of the magnitudes in all other bands to ensure comparability. The SDSS define the Petrosian magnitude in each band to be the flux contained within $2R_{p_r}$.

Model magnitudes

In addition to the Petrosian magnitude, the SDSS pipeline measures model magnitudes of galaxies. As the name suggests model magnitudes *model* the surface brightness profiles of galaxies, but there are infinitely many ways to model surface brightness profiles. For computational ease, the SDSS has chosen two models, the "Exponential" profile which has the form of Equation 2.2, and the "de Vaucouleurs" profile shown in Equation 2.3

$$I(r) = I_0\, exp\big(-1.68\,(r/r_e)\big), \tag{2.2}$$

$$I(r) = I_0\, exp\big(-7.67\,(r/r_e)^{1/4}\big), \tag{2.3}$$

where the intensity I is measured as a function of radius r, and r_e, I_0 are measured by the pipeline for each object. The de Vaucouleurs profile is smoothly truncated after $7\,r_e$ to go to zero by $8\,r_e$. The Exponential profile smoothly tends to zero between $3\,r_e$ and $4\,r_e$. The effect of the PSF on the model magnitude is calculated similarly to the PSF magnitude. The locally averaged Gaussian fit to the PSF is removed from a Gaussian PSF convolved with the models. The best fitting surface brightness profile of the two models is used as the model magnitude. The SDSS recommend using the model magnitudes when comparing colours of galaxies because the model magnitudes in each band are calculated using a fixed aperture, calculated in the r band, applied to each band[5].

Cmodel magnitudes

Finally we introduce a composite magnitude or "cmodel" magnitude which is a linear combination of the Exponential and de Vaucouleurs models. The coefficients are chosen to best fit

[5] http://www.sdss.org/dr5/algorithms/photometry.html#which_mags

the galaxy surface brightness profile. There is excellent agreement between cmodel magnitudes and Petrosian magnitudes for galaxies, and between cmodel magnitudes and PSF magnitudes for stars. The scatter between cmodel magnitude and the Petrosian magnitude is lower than the scatter between the model magnitudes and Petrosian magnitude. The cmodel magnitudes are used in the MaxBCG cluster catalogue (see §2.1.7), but we do not use them in this work because of the above recommendation, and the added difficulty in their calculation.

2.1.3 Magnitude corrections

In this section we describe corrections that one needs to make to the SDSS magnitudes before they can be used scientifically.

Extinction corrections

Light travelling through the Milky Way is scattered by dust whose distribution has been measured by Schlegel et al. (1998) and accurate maps produced. The scattering amplitude is as a function of wavelength, with bluer wavelengths being more affected than longer wavelengths. The SDSS do not automatically apply extinction corrections, although they are provided within CasJobs.

K and evolution corrections

To compare the magnitudes of astronomical objects at different redshifts we must apply two corrections which account for the modification of the measured spectrum due to the redshift difference and the evolution of the colour of galaxies with time. The redshift modification moves the entire spectrum towards longer wavelengths as the redshift increases. To account for this correction, a K-correction (denoted by K, e.g see Hogg et al., 2002), is applied to convert the apparent magnitude of a galaxy in a band m_r, at a redshift z_0, to an apparent magnitude m'_r the galaxy would have if it were at a redshift z_1.

The evolution correction describes the change in a galaxy's colours as the galaxy evolves with redshift. To correctly compare galaxies of different redshifts, a knowledge of the evolution of the galaxy stars, or stellar populations, is required. Stellar population models describe the evolution of stars and therefore, galaxy colours. For example, red sequence galaxies become redder as the stellar population ages.

We use the K and evolution correction models for red sequence galaxies of Maraston et al. (2008), and show the corrections as a function of redshift in Figure 2.2. The Maraston et al. (2008) corrections convert the magnitudes of galaxies at a redshift z, to those the galaxies would have, if they were at a redshift $z = 0.3$. The comparison redshift $z = 0.3$ is chosen because it is approximately halfway to the maximum redshift of the LRGs.

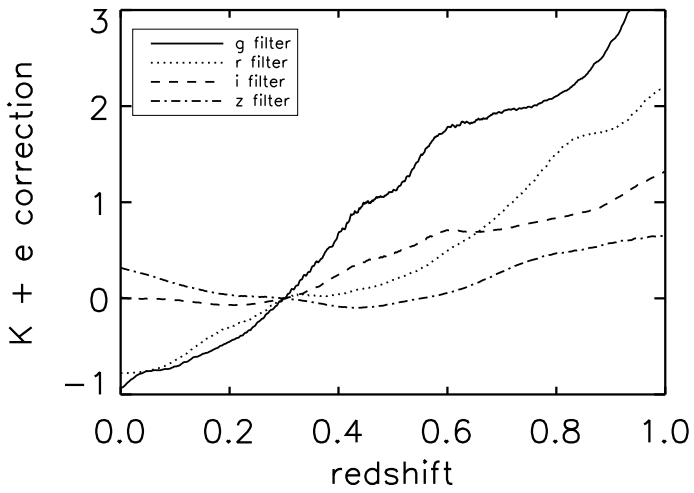

Figure 2.2: The K and evolution e magnitude corrections as a function of redshift using the stellar populations of Maraston et al. (2008). The corrections convert the magnitudes of galaxies at a redshift z, to those the galaxies would have if they were at a redshift $z = 0.3$.

The effect of the K and evolution corrections on the apparent magnitude is given by

$$m_r \quad = \quad M_r + 5\log\left(D_L/10pc\right) + K + e, \tag{2.4}$$

where the absolute magnitude M_r is defined as the true magnitude an object would have if it were 10 parsecs from an observer, and D_L is the luminosity distance.

The Maraston et al. (2008) models are the most accurate galaxy evolution models currently available, because they include the effect of the Asymptotic Giant Branch (hereafter AGB) red stars on the galaxy spectral energy distribution (hereafter SED). The AGB stars constitute only a few percent of the stellar population, but their high luminosity produces observable differences in the galaxy's SED at the red end of the spectrum.

Conversion to the AB system

The SDSS magnitudes are approximately equivalent to the AB system (Oke, 1974; Abazajian et al., 2004), with the current best estimates for the AB offset given by AB$[u, g, r, i, z]$ = SDSS$[u - 0.036, g + 0.012, r + 0.010, i + 0.028, z + 0.040]$ (Blanton and Roweis, 2007). Systematic errors of $[\Delta u, \Delta g, \Delta r, \Delta i, \Delta z] = [0.05, 0.02, 0.02, 0.02, 0.03]$ should be added in quadrature to the quoted SDSS magnitudes (Blanton and Roweis, 2007).

2.1.4 Clean photometry

To use data scientifically it must be robust and have well understood associated errors. In this section we describe the conditions we place on the SDSS photometric data to ensure suitability for subsequent research.

SDSS photometric flags

The SDSS automated pipelines measure and derive fluxes, radii and other object properties. The success of the pipeline to fit properties are indicated by the presence of flags. For example, some flags indicate the detection significance of an object (**BINNED1** meaning objects are detected at $> 5\sigma$ signal-to-noise by the pipeline) or the presence of saturated pixels (**SATURATED** which indicates the number of photons exceeded the maximum amount for a CCD pixel). Checking the value of an object's flags indicate how much the derived properties can be trusted and for objects to be used scientifically, their flag status must be acceptable. The SDSS website[6,7] give flag status guidelines to obtain robust data, and below we describe the flags checked to obtain clean data used in this thesis.

- First the object must be detected by the pipeline, meaning one of **BINNED1**, **BINNED2** or **BINNED4** must be set. **BINNED2** labels objects detected by the pipeline after all **BINNED1** objects have been masked and the image binned in 2x2 pixels. Similarly **BINNED4** indicates the detection of an object by the pipeline after all **BINNED1** & **BINNED2** objects have been masked and the image binned in 4x4 pixels.

- If object features overlap the algorithm identifies and measures the properties of the brightest "parent" object first, which is then removed and the pipeline continues fitting properties to the "child" remnants. The **DEBLEND_NOPEAK** flag shows that after this deblending, the child object does not have a peak.

- The **PEAKCENTER** flag indicates failure of the algorithm to determine the centroid of an object, and is set when faint, ill defined objects are deblended from a brighter source. This flag indicates that the object may not be real.

- If the algorithm is unable to fit a Petrosian radius, the flag **NOPETRO** is highlighted.

- The **NOPROFILE** flag is set if a radial profile in a given band cannot be measured.

- The **NOTCHECKED** and **NOTCHECKED_CENTER** flags indicate that an object has pixels which have not been checked for peaks by the deblender, which can occur in the cores of saturated stars or near a plate edge.

- When the algorithm encounters a bad or saturated pixel, it interpolates the photometry across it, and in the case that the **PSF_FLUX_INTERP** flag is set, over 20% of the PSF flux has been interpolated over.

[6] http://www.sdss.org/dr5/products/catalogs/flgas_detail.html
[7] http://www.astro.princetown.edu/∼rhl/flags

Flag	Hexadecimal identifier	Approx % of objects with flag set
BINNED1	0x0000000010000000	97.55
BINNED2	0x0000000020000000	2.53
BINNED4	0x0000000040000000	0.09
Combined flags I	0x0000000070000000 >0	99.56
PEAKCENTER	0x0000000000000020	0.64
NOPROFILE	0x0000000000000080	0.00
NOPETRO	0x0000000000000100	85.18
NOTCHECKED	0x0000000000080000	1.75
BADSKY	0x0000000000400000	0.00
BAD_COUNTS_ERROR	0x0000010000000000	0.00
PSF_FLUX_INTERP	0x0000800000000000	16.01
DEBLEND_NOPEAK	0x0000400000000000	12.61
NOTCHECKED_CENTER	0x0400000000000000	0.00
Combined flags II	0x0400c100004801a0 =0	11.84

Table 2.1: The SDSS pipeline's success of deriving an objects properties are described by flags which are stored as hexadecimal identifiers. Multiple flags can be simultaneously checked by adding the hexadecimal values. This table shows the flags checked to obtain clean data, their hexadecimal value and the percentage of a selection of $\sim 400,000$ objects, which have the flag set in at least one band.

- If **BAD_COUNTS_ERROR** is flagged the interpolation is so significant that the PSF error should not be believed.
- If the local sky subtraction is poorly measured the reduced flux of an object may be ill defined and the **BADSKY** flag indicates this failure.

The pipeline is run on each of the five photometric bands and flags are set within each band. We check for the presence of the flags across four photometric bands, g, r, i, z; the u band is not checked because it is not used in this work. The flags are stored as hexadecimal numbers and multiple flags can be checked simultaneously by adding their hexadecimal values. The flags, along with their hexadecimal identifiers and the percentage of $\sim 400,000$ randomly selected objects with their set flags are shown in Table 2.1. Additionally shown are the combined "clean" flags and their percentages. We only use objects with "Combined flags I"> 0 and "Combined flags II"$= 0$ in the g, r, i, z bands. The surprisingly high number of objects with the flag **NOPETRO** set is caused by our random selection of all objects along various lines of sight, including many very faint objects for which the Petrosian radius is difficult to measure in each band.

Other clean photometry checks

In addition to the flag checks, other quantities determined by the algorithm can be used to obtain a robust sample. The pipeline determines an object's **type**, which corresponds to whether the pipeline classifies an object to be a star, quasar, LRG etc. We only use objects with **type** $= 3$ corresponding to galaxies, and furthermore discard objects if the pipeline fails to measure model magnitude across either of the g, r, i bands.

2.1.5 Luminous Red Galaxy redshifts

Luminous Red galaxies (hereafter LRGs) are a subclass of galaxies defined by their colours and magnitudes (as highlighted on Figure 2.4), and are found to inhabit the densest regions of the Universe. We concentrate on LRGs here because we use them extensively to locate clusters in §2.2.5, and when identifying cluster member galaxies and measuring total optical luminosity in §3.2.2, and we apply the K+evolution corrections of Maraston et al. (2008) for early type galaxies. We therefore impose constraints upon their selection, in addition to the above flag checks, by using redshift cuts.

The SDSS pipelines calculate the photometric redshifts of LRGs (Abazajian et al., 2008; Csabai et al., 2003, 2007) using the sharp 4000Å break in the spectral energy distribution of the galaxies (e.g. see Figure 2.1). As the break is cosmologically redshifted, so its location can be used to estimate the redshift. Measuring the difference in colours between the different filters e.g, $g - r$ or $r - i$, determines the position of the 4000Å break and therefore the redshift of the galaxy. More accurate spectroscopic redshifts are found by measuring the redshifted positions of spectral emission and absorption lines.

Where available we retrieve both spectroscopic and photometric redshifts, and remove galaxies without spectra if the photometric redshift error is greater than 0.1.

2.1.6 SDSS Luminous Red Galaxies

In this section we describe the LRG sample we have compiled using SDSS data, and various literature definitions of LRG colour selection criteria. The subtle differences between the LRG selection criteria is beyond the scope of this work and we hereby use a very general definition of LRG, encompassing all the works described below. As with all the galaxies used in this work, the selected LRGs are made to comply with the clean photometry flags given in §2.1.4.

High redshift colour selection

To obtain high redshift LRGs, we follow the colour cuts outlined in Padmanabhan et al. (2005) and Collister et al. (2007) applied to SDSS Data Release 7 (hereafter DRX). The Padmanabahn "cut I" returns $849,911$ cleaned LRGs and "cut II" returns $980,436$ LRGs, with an overlap of $31,397$ LRGs between the two cuts. The Collister cuts return $1,920,023$ LRGs of which $744,742$ are in

common with cuts I & II of Padmanabahn. Figure 2.3 is taken from Figure 4 of Collister et al. (2007) and shows the LRG color selection criteria.

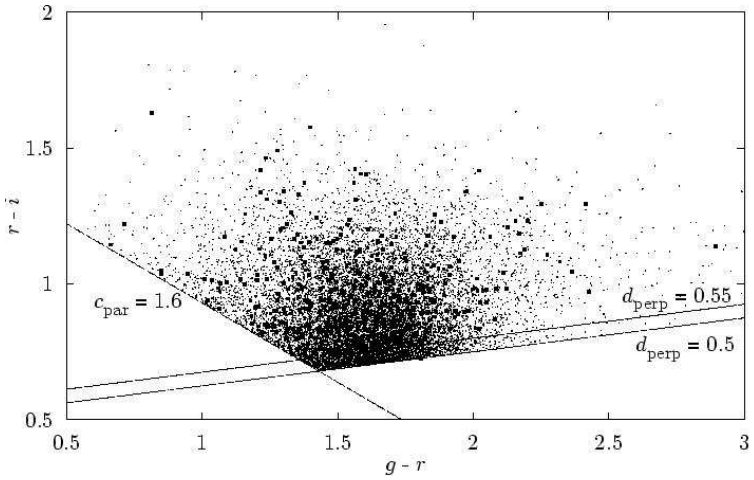

Figure 2.3: The colour distributions of a random selection of LRG candidates as identified by the selection criteria of Collister et al. (2007). Credit: Collister et al. (2007).

Low redshift colour selection

To select low redshift LRGs we use the internal SDSS target selection identifier **TARGET_RED_GALAXY** and **TARGET_RED_GALAXY_II** (Eisenstein et al., 2001), and employ colour cuts suggested by Jim Annis on the SDSS website[8]. We reproduce Figure 11 of Eisenstein et al. (2001) here, as Figure 2.4, which shows how colour cuts separate LRGs from main sample galaxies.

The targeted galaxies total $274,967$ LRGs and the Jim Annis colour cuts return $936,465$ galaxies. There is an overlap of $135,341$ LRGs.

Combining the samples and redshift cuts

We combine the low and high redshift selected LRGs, and place a further cut on the redshift error of $\Delta z < 0.1$, which reduces the sample by a further $1,413,757$. We also remove the very low and high redshift LRGs ($z < 0.005, 1.0 < z$), which reduces further the number of LRGs by $31,000$.

Sample properties

The final combined, cleaned, LRG catalogue has $2,060,318$ LRGs of which 10.9% have spectroscopic redshifts. We compare the photometric and spectroscopic redshifts for 500 randomly selected LRGs in Figure 2.5. We choose to plot galaxies with a photometric redshift error $\Delta z < 0.1$, because the galaxies without spectroscopic redshifts have this constraint imposed upon them. We see that the photometric redshifts are reasonable estimators for the LRG redshift, but they should

[8] http://cas.sdss.org/dr7/en/help/docs/realquery.asp#lrg

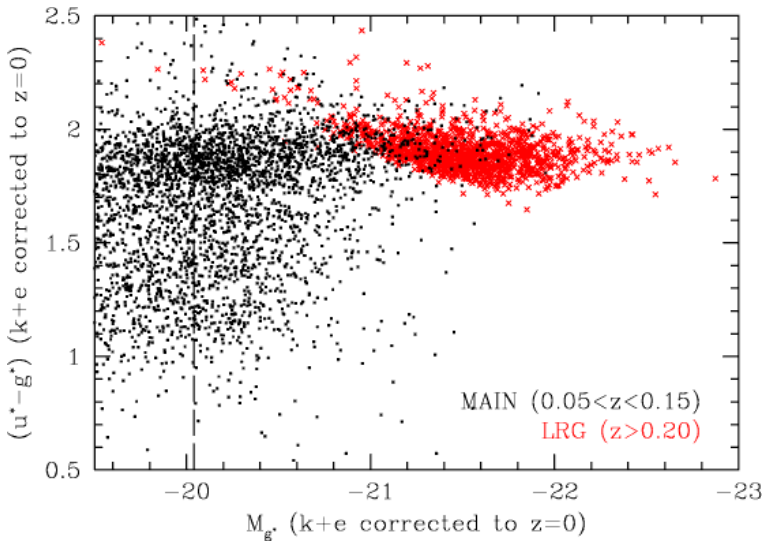

Figure 2.4: Colour plots of LRGs (red crosses) and main sample galaxies (black dots). Credit: Eisenstein et al. (2001).

be used with caution because of occasional catastrophic outliers. An Aitoff projection of the final SDSS DR7 LRG catalogue is shown in Figure 2.6, with Right Ascension (hereafter RA) running east-west, and Declination (hereafter DEC) running north-south.

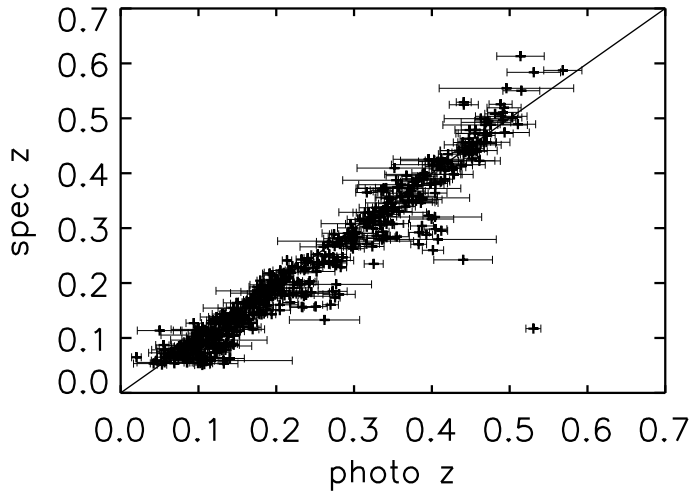

Figure 2.5: A comparison of photometric and spectroscopic redshifts for 500 randomly selected LRGs from the SDSS DR7. Only displayed are LRGs with a photometric redshift error < 0.1 for comparison with cuts applied to LRGs without spectra. Overplotted is the line of equality.

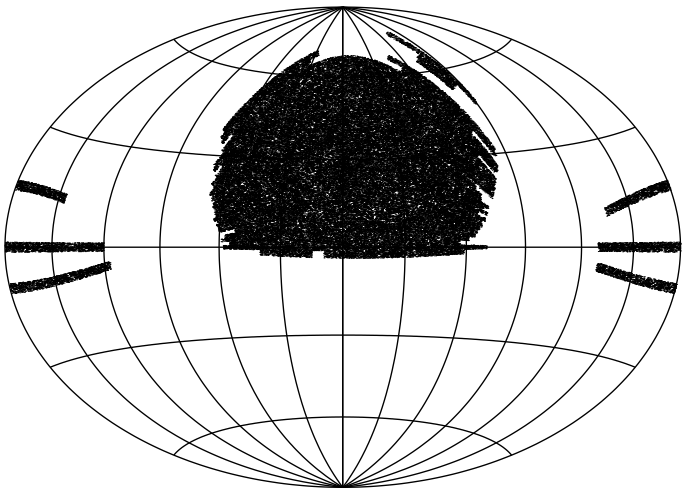

Figure 2.6: An Aitoff projection of the compiled SDSS DR7 LRG catalogue, with Right Ascension running east-west, and Declination running north-south.

2.1.7 The MaxBCG cluster catalogue

The MaxBCG optical cluster catalogue (Koester et al., 2007a, hereafter MaxBCG), identifies groups and clusters by scanning for an overdensity in position and colour space of early type galaxies, and identifying the Brightest Cluster Galaxy (hereafter BCG), which is generally the most luminous LRG. The algorithm and catalogue are discussed in Koester et al. (2007a,b) and briefly described below.

The cluster catalogue is drawn from the SDSS DR5 main sample photometric galaxy catalogue, with colour cuts applied to identify galaxies with colours consistent with early type galaxies spanning the redshift range $0.1 < z < 0.3$. Early type galaxies (or E/S0 galaxies) populate a tight ridge line in colour space, see Figure 2.4. The colour cuts used by the MaxBCG (Equation 2.5) compare the $g - r$ and $r - i$ colours of the modelled BCG, X_{model}, and the galaxy candidate, $X_{candidate}$, at each redshift (z), using

$$\begin{aligned} (g-r)(z)_{model} - \sqrt{\sigma_{err}^2 + 0.15^2} < (g-r)_{candidate} < (g-r)(z)_{model} + \sqrt{\sigma_{err}^2 + 0.15^2}\,, \\ (r-i)(z)_{model} - \sqrt{\sigma_{err}^2 + 0.18^2} < (r-i)_{candidate} < (r-i)(z)_{model} - \sqrt{\sigma_{err}^2 + 0.18^2}\,. \end{aligned} \tag{2.5}$$

The factors 0.15 and 0.18 in Equations 2.5 correspond to three times the width of the early type ridge line, and are included to conservatively select galaxies with colours consistent with early type galaxies. The colour error of the galaxies σ_{err}, is a function of magnitude and aperture (Scranton et al., 2005b). The colour distribution of main sample galaxies with the above cuts consistent with selecting early type galaxies is shown in Figure 1 of Koester et al. (2007a), replicated here in Figure 2.7.

MaxBCG use the SDSS cmodel magnitudes, and are corrected for extinction using the dust maps of Schlegel et al. (1998). Only galaxies brighter than $0.4L_\star$ in the i band are retained to impose a

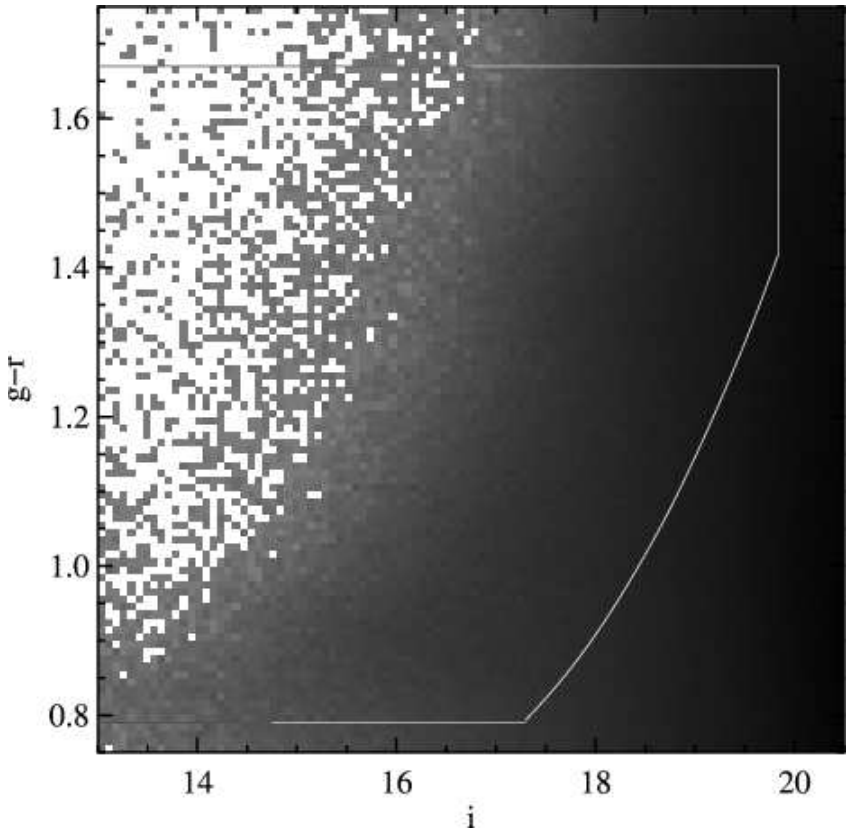

Figure 2.7: The $g - r$ colour of galaxies as a function of i band magnitude. The grey scale is linear in the number of galaxies, and the region enclosed by the overplotted line corresponds to galaxies with colours consistent with E/S0 ridge line galaxies within the redshift $0.1 < z < 0.3$ as used by the MaxBCG. Credit: Koester et al. (2007a).

minimum luminosity threshold across the redshift range of the catalogue, where $L_\star$ is the typical luminosity of the galaxies in SDSS. The galaxies are K-corrected to $z = 0.25$ using the LRG templates of v4.14 of KCORRECT (Blanton and Roweis, 2007) which do not include evolution corrections.

The algorithm determines the likelihood for each galaxy to be near the spatial center of a local galaxy overdensity, and the likelihood that the colours are typical of a BCG at a redshift z. The likelihoods are recomputed over a grid of redshifts from $z = 0.1$ to $z = 0.3$. The maximum likelihood of the redshift scan produces a redshift estimate. The ability of the pipeline to calculate a redshift using a galaxy's colour is demonstrated in Figure 2 of Koester et al. (2007a), replicated here in Figure 2.8, which plots the redshift as a function of $g - r$ for all targeted spectroscopic galaxies. There is a tight linear relationship between spectroscopic redshift and colour for the red galaxies (the upper dark overdensity) with a less well constrained relationship for the lower cloud of bluer galaxies.

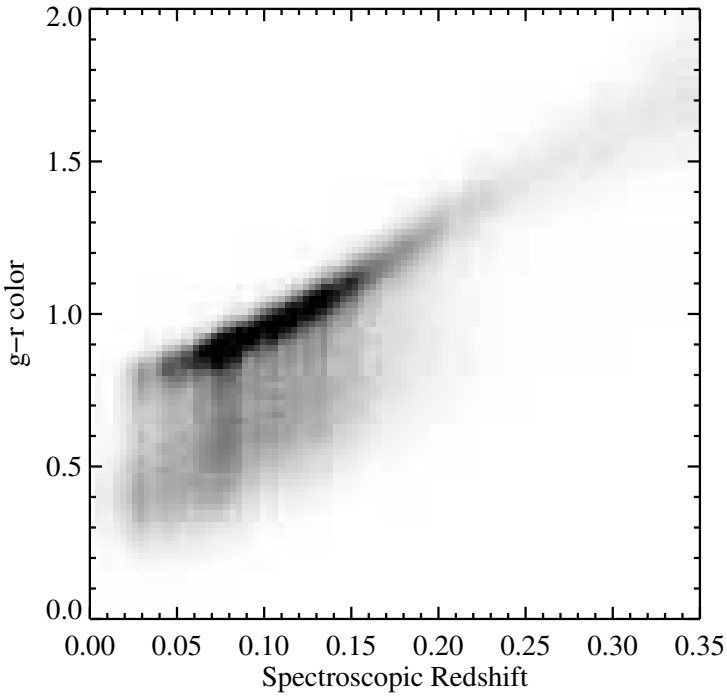

Figure 2.8: A reproduction of Figure 2 of Koester et al. (2007a) showing the spectroscopic redshifts of all targeted galaxies as a function of $g-r$ colour. The E/S0 galaxies form a ridge with a good correlation between colour and redshift which forms the basis of the MaxBCG photometric redshifts. The lower cloud of bluer galaxies has a less well defined relationship between colour and redshift. The grey scale is linear in the number of galaxies at each colour and redshift. Credit: Koester et al. (2007a).

The pipeline subsequently assigns the status of BCG to the galaxy which maximises the likelihood and calculates the number of galaxies within $1h^{-1}$Mpc of the BCG, denoted by Ng. The initial Ng is converted to R_{200} defined here as the radius at which the overdensity of $> 0.4L_\star$ galaxies with an absolute r band magnitude between $-24 \leq M_r \leq -16$ is 200 times that of the average galaxy density (Hansen et al., 2005).

Cluster membership is assigned to all galaxies within R_{200} which have similar ($\pm 2\sigma$) colours in $g-r$ and a similar i magnitude of the BCG. The final number of cluster members is then stored as $Ng^{R_{200}}$. Subsequent clusters are identified by removing this BCG and cluster members from the galaxy catalogue, and the next highest likelihood galaxy identified. This process is iterated until all galaxies are either BCGs or subsumed as cluster members. The final catalogue has an additional cut satisfying $Ng^{R_{200}} \geq 10$, and contains the r and i band luminosities of the BCG and the members, and the galaxy number counts Ng and $Ng^{R_{200}}$. An Aitoff projection of the final MaxBCG catalogue is shown in Figure 2.9.

Completeness and purity are estimated using N-body mock galaxy catalogues (Wechsler et al., 2006) with realistic galaxy properties. To ensure a BCG exists in each cluster within the simulation, the brightest galaxy within the halo is positioned at the bottom of the dark matter potential

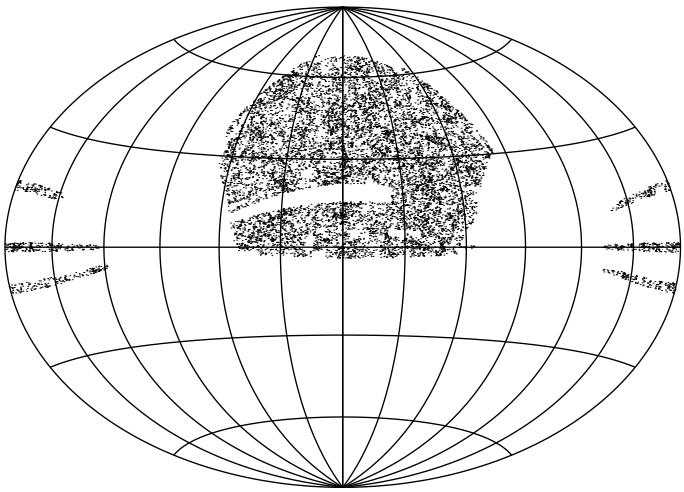

Figure 2.9: An Aitoff projection of the SDSS DR5 MaxBCG cluster catalogue (Koester et al., 2007a).

well.

For each mock cluster detected by the MaxBCG algorithm, the fraction f_c of a cluster's galaxies contained within the most populated dark matter halo is measured. The value of f_c indicates the purity of the cluster finding algorithm. A low value of f_c indicates a false positive detection of a cluster, because the cluster galaxies cannot be clearly associated to one dark matter halo. At $f_c = 0.3$ the purity is $> 90\%$ for $Ng^{R_{200}} > 10$ and $95 - 100\%$ pure for $Ng^{R_{200}} > 20$.

In contrast to purity, one may calculate the completeness using the fraction f_h of galaxy halos found within the cluster halo. If f_h falls below a threshold, the number of identified galaxy halos within the cluster is very low, and therefore the cluster has failed to be detected. At $f_h = 0.3$ the sample is $> 90\%$ complete above $\sim 2 \times 10^{14}\, h^{-1}\, M_\odot$ and $95 - 100\%$ complete above $\sim 3 \times 10^{14}\, h^{-1}\, M_\odot$.

The completeness as a function of mass is shown in Figure 7 of Koester et al. (2007a) and replicated here as Figure 2.10. The final redshift distribution for the MaxBCG clusters is shown in Figure 4 of Koester et al. (2007a) and replicated here as Figure 2.11. Overplotted is the expected number of clusters for a volume limited sample in flat $\Omega_m = 0.3, H_0 = 70\text{kms}^{-1}$ ΛCDM cosmology. We note that the MaxBCG do not have mass estimates, and so the direct comparison of the line with the data is impractical.

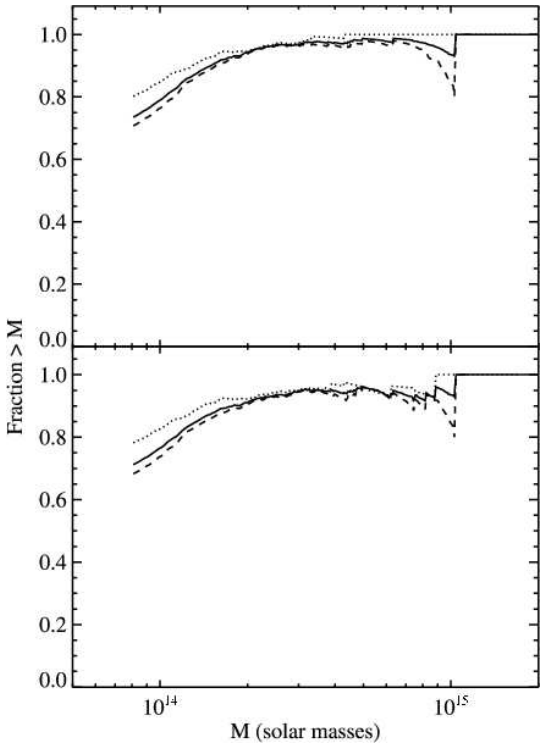

Figure 2.10: *Basic results of completeness tests based on mock catalogs. In each plot the solid line is for the full mock catalog, the dotted lines for halos of 0.1 $< z <$ 0.2 and dashed lines for halos at 0.2 $< z <$ 0.3. The top panel is a completeness plot for a halo matching fraction $f_h = 0.3$, the bottom for $f_h = 0.5$. In each case, a dark matter halo is considered found if a fraction f_h of its red sequence members is found in a single identified cluster.* Credit: Koester et al. (2007a).

2.1.8 The C4 cluster catalogue

The C4 cluster catalogue (Miller et al., 2005) locate clusters using a 7 dimensional position and colour space detection algorithm. The catalogue is drawn from the SDSS DR5 spectra (Miller, private communication) and is an extension of the cluster catalogue based on SDSS DR2 (Miller et al., 2005). The algorithm is described briefly below and we refer to Miller et al. (2005) for details.

The parameters of the detection algorithm are tuned to maximise completeness and purity using N-body SDSS mock galaxy catalogues (Wechsler, 2006). The algorithm is applied to SDSS DR5 targeted galaxies, which are identified as spectroscopic galaxies at least 7.5 arcminutes from the survey edges, with a redshift $z > 0.03$ and an r band magnitude brighter than 17.7. A fixed spatial aperture of $1\,h^{-1}$ Mpc at the redshift of the target galaxy is calculated and placed on the target galaxy. Subsequently, the number of other galaxies residing within the aperture, and a 4D colour ellipse $[\sigma_{u-g}, \sigma_{g-r}, \sigma_{r-i}, \sigma_{i-z}]$ given by $[0.6, 0.48, 0.4, 0.4]$ produce a "number count". This process is repeated on 100 randomly selected galaxies with spectra taken under similar seeing conditions and with similar galactic extinction, which produces a distribution of number counts.

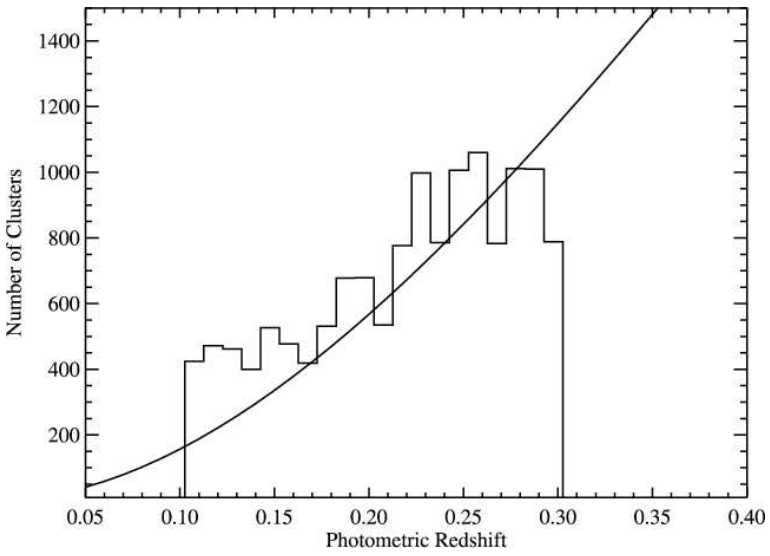

Figure 2.11: *This figure shows the number of clusters as a function of redshift for the maxBCG cluster catalog. The solid line shows the expectation for a volume-limited sample with a density of* 2.3×10^{-5} *clusters* h^3 *Mpc*$^{-3}$ *in a flat* $\Omega_m = 0.3, h = 0.7$ Λ*CDM cosmology.* Credit: Koester et al. (2007a).

The number count distribution can be used to calculate the probability of a galaxy lying within an overdensity of similar coloured galaxies. The process is repeated for each targeted galaxy, and the probabilities ranked. Above a threshold probability, all galaxies reside in high density regions of galaxies with similar colours. These are the C4 galaxies. The surface density of each group of C4 galaxies is measured, and a corresponding cluster center identified from the peak of the surface density.

The cluster algorithm was tested on the above simulation and found to be 99% pure for luminosities $> 3 \times 10^{11}\, L_\odot$ and 100% complete for the most massive clusters. Completeness is a function of mass and drops to 90% for masses $M_{200} \sim 2 \times 10^{14}\, M_\odot$. Figure 10 of Miller et al. (2005) show the completeness and purity as a function of r band luminosity and halo mass (and replicated here as Figure 2.12). We show the redshift histogram of the SDSS DR5 C4 cluster catalogue in Figure 2.13 and an Aitoff projection of the C4 clusters in Figure 2.14.

The final C4 cluster catalogue contains the RA and DEC of the cluster centres, the velocity dispersions and the summed r band luminosities.

2.1.9 The SDSS quasar catalogue

We use the quasar catalogue of Richards et al. (2008), which is the largest public quasar catalogue and consists of $1,172,157$ quasar candidates, of which no fewer than $850,000$ are expected to be bona fide quasars. The photometric catalogue is drawn from SDSS DR6 (Adelman-McCarthy et al., 2008), and covers $8,417$ square degrees to $i = 21.3$. The quasar identification algorithm

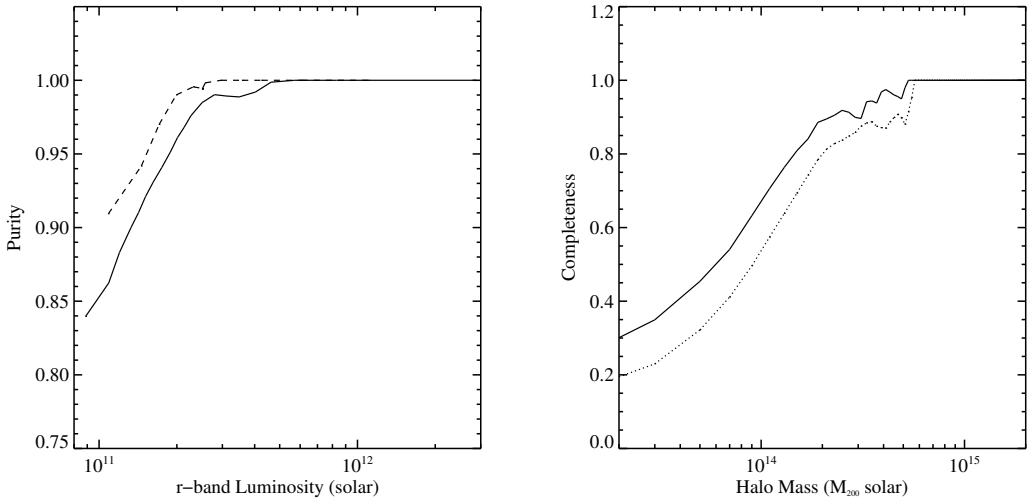

Figure 2.12: *The final measured purity and completeness of our C4 catalog using the mock SDSS catalog. The solid line is measured before the fiber collision algorithm is applied. The dotted line shows the effect (of) missing galaxies due to fiber collisions.* Credit: Miller et al. (2005).

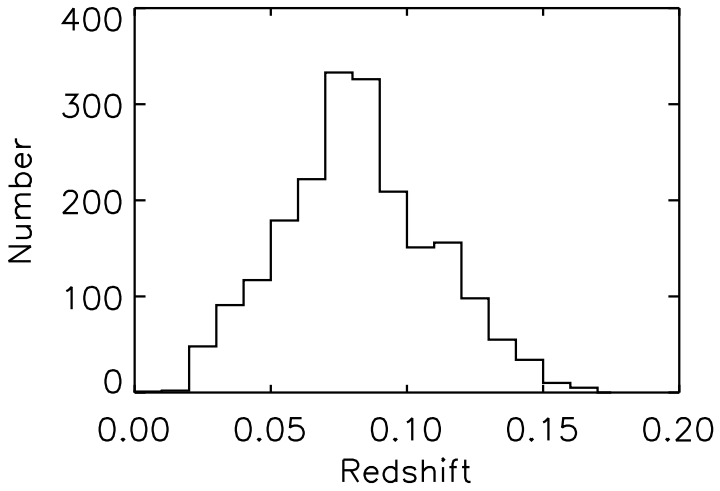

Figure 2.13: The redshift histogram of the SDSS DR5 C4 clusters.

uses a Bayesian classification algorithm to distinguish quasars from stars. The algorithm uses training sets of known quasars and stars, to classify quasar candidates and is trained on $75,382$ hand picked quasars, consisting of SDSS DR5 quasars, high redshift quasars from AAOmega-UKIDSS-SDSS QSO Survey and SDSS-Spitzer quasars. The star training set has $426,908$ SDSS identified stars and are chosen from a 1% random sample of point sources after probable quasar candidates have been removed. Using the four primary SDSS colours $(u-g, g-r, r-i, i-z)$,

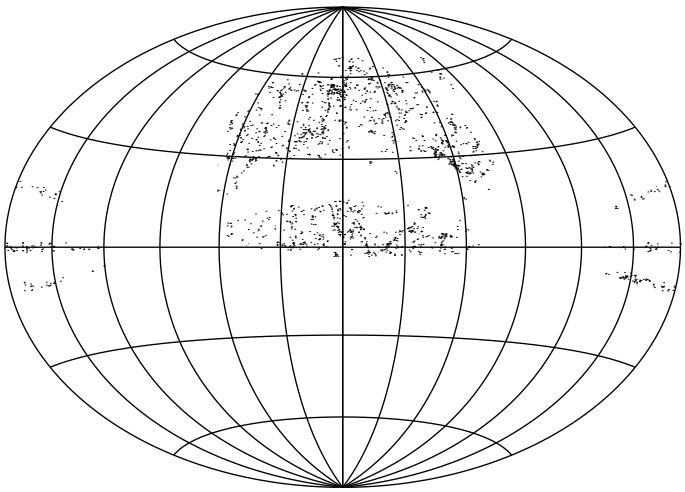

Figure 2.14: An Aitoff projection of the C4 cluster finding algorithm (Miller et al., 2005) applied to SDSS DR5 (Miller, private communication).

the algorithm assigns probabilities of candidates to be quasars (Richards et al., 2004). Overall the algorithm recovers quasars with $\sim 80\%$ purity and $\sim 70\%$ completeness with the most robust subsample being $> 95\%$ complete, and having $\sim 5\%$ stellar contamination.

Photometric redshifts are estimated following Weinstein et al. (2004) by minimising the colour difference of the quasar candidate from the median colours of true quasars as a function of redshift. The photometric redshifts span $0.08 < z \lesssim 6.3$, and for 83% of the sample, the redshifts are expected to be correct to within 0.3 at the 2σ level.

We have made purity cuts suggested in Table 4 of Richards et al. (2008) i.e. setting UVX=1 and $good \geq 0$, resulting in 96.4% star-galaxy separation efficiency. In future analysis we cross correlate the quasars with the MaxBCG and C4 clusters. To ensure there is no redshift overlap (which would cause a spurious signal), we apply further redshift cuts to the quasars of $z < 0.75$ ($z < 0.5$) when used with the MaxBCG (C4) clusters resulting in final data samples having $506,971$ $(531,856)$ quasars. An Aitoff projection of $100,000$ randomly selected quasars is shown in Figure 2.15.

2.2 X-ray data

This section introduces the X-ray identified cluster catalogues measured using the "Rönt -gensatellit" (hereafter ROSAT) and the "X-ray Multi-Mirror Mission - Newton" (hereafter XMM) satellites. We use three ROSAT X-ray identified cluster catalogues available in the literature. We then introduce the XMM Cluster Survey (of which the author is an active member, hereafter XCS)

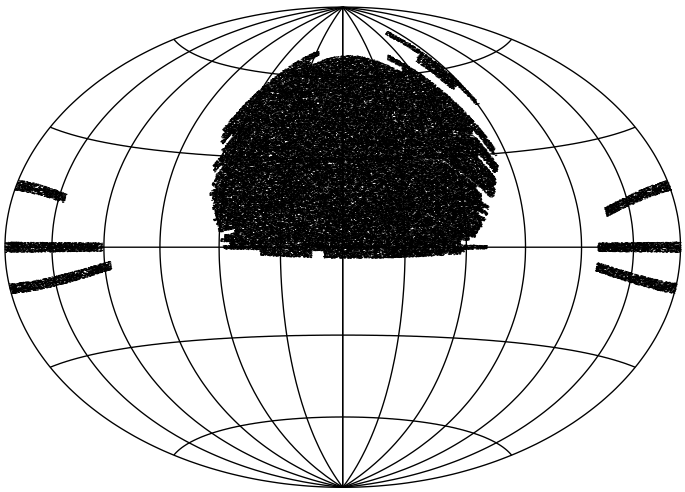

Figure 2.15: An Aitoff projection of $100,000$ randomly selected SDSS DR6 quasars from the catalogue of (Richards et al., 2008).

catalogue, and describe the methods developed to assign redshift estimates to the XCS clusters and measure purity. We finish with work by other members of the XCS to recompute luminosities and estimate temperatures for all the X-ray cluster catalogues.

2.2.1 ROSAT 400 square degree

Of the current publicly available X-ray identified cluster catalogues, the ROSAT 400 square degree deep (Burenin et al., 2006, hereafter R400d) is the most reliable. Below we briefly describe the cluster catalogue and refer to Burenin et al. (2006) for details.

The R400d is drawn from archival pointed observations of the ROSAT Position Sensitive Proportional Counter. The selected pointings were chosen to satisfy the following criteria: above a galactic latitude of $|b| > 25^{\circ}$, with an exposure time of > 1000 seconds, and a galactic hydrogen column of $N_H < 10^{21}\,\mathrm{cm}^{-2}$. Masks were placed around the Large and Small Magellanic Clouds and a minimum detection threshold of $3 \times 10^{-13}\,\mathrm{erg\,s}^{-1}\,\mathrm{cm}^{-2}$ was imposed. Photon maps were then made in the $0.5 - 2\,\mathrm{keV}$ band using public software (Snowden et al., 1997) and extended sources detected using the algorithm described in Vikhlinin et al. (1998). The extended sources were photometrically followed up on the Russian-Turkish 1.5 meter telescope in the North and the Danish 1.54 meter Southern telescope. Both telescopes provided photometry deep enough to detect a cluster out to a redshift ~ 1. Confirmed clusters have an excess in the number density of galaxies, or contains a single galaxy with typical properties of a BCG (known as a fossil group). This resulted in 266 confirmed clusters of which 115 had spectroscopic redshifts previously available from the literature. The remaining 89 clusters had dedicated spectroscopic follow

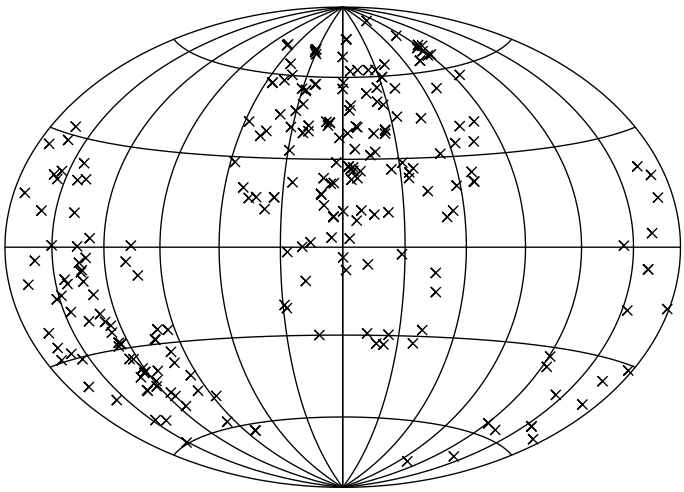

Figure 2.16: An Aitoff projection of the ROSAT 400 square degree deep (Burenin et al., 2006) X-ray identified clusters.

up performed using the KECK II, ESO 3.6 meter, NTT, Magellan, FLWO 1.5 meter, Nordic Optical Telescope and the Danish 1.54 meter telescopes.

The final catalogue comprises positions, redshifts, fluxes in the $0.5 - 2\,\mathrm{keV}$ band, and the total X-ray luminosity in the $0.5 - 2\,\mathrm{keV}$ band calculated for a flat ΛCDM cosmology with $\Omega_m = 0.3$, $H_0 = 71\,\mathrm{km\,s^{-1}\,Mpc^{-1}}$. An Aitoff projection of the R400d clusters is shown in Figure 2.16.

The X-ray luminosity for the R400d was determined by assuming a constant L-T relation and a simple β profile, using the luminosity function drawn from the low redshift ROSAT-ESO Flux Limited X-ray Galaxy Cluster Survey (Boehringer et al., 2004).

2.2.2 The ROSAT Brightest Cluster Sample

The ROSAT Brightest Cluster Sample (Ebeling et al., 1998, hereafter BCS) is an X-ray identified cluster catalogue found by cross correlating the ROSAT All Sky Survey with Abell and Zwicky clusters and the NASA/IPAC Extragalactic Database. Below we briefly introduce the BCS and refer the reader to Ebeling et al. (1998) for details.

Source positions were measured using the Standard Analysis Software System (Voges et al., 1992) to process data from the ROSAT All Sky Survey, using strips above a galactic latitude $|b| \leq 20^\circ$, with a count rate in the $0.11 - 2\,\mathrm{keV}$ band. The reduced source list was cross correlated with the Abell cluster catalogue in units of physical separation, calculated at the redshift of the cluster. Where redshifts had not been measured, the magnitude of the 10^{th} brightest cluster member was used as a proxy for redshift (Ebeling et al., 1996). Additionally, the Photon Event tables of the

selected fields were re-analysed using the Voroni Tessellation & Percolation procedure (Ebeling and Wiedenmann, 1993), which identifies arbitrary shaped extended sources and reliably measures their fluxes.

Optical counter parts to the X-ray extended sources were obtained from the Abell and Zwicky photographic plates and the digitised Palomar Observatory Sky Surveys using the SKYVIEW and STSCI WWW interfaces[9,10]. The catalogue contains 201 confirmed clusters with redshifts $z \leq 0.3$ and fluxes $\geq 4.4 \times 10^{-12}\,\mathrm{ergs}^{-1}\,\mathrm{cm}^{-2}$. The final catalogue includes the RA, DEC, redshift estimates, flux in the $0.11 - 2$keV band, and the X-ray luminosity created assuming a Einstein-de Sitter cosmology with $q_0 = 0.5$ and $H_0 = 50\mathrm{km\,s}^{-1}\,\mathrm{Mpc}^{-1}$. An Aitoff projection of the BCS catalogue is shown in Figure 2.17.

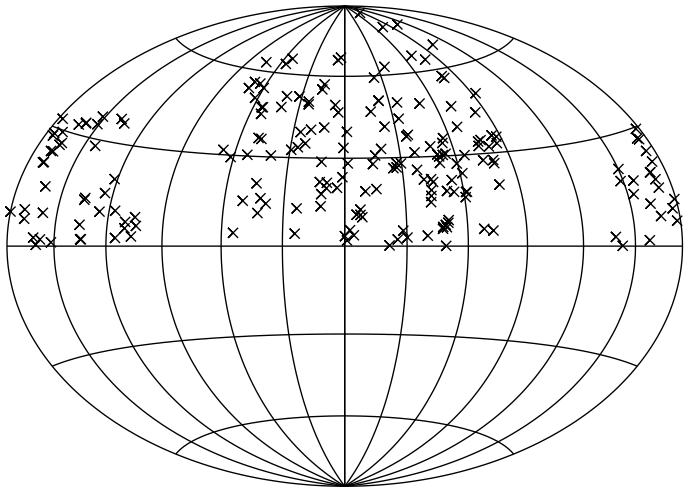

Figure 2.17: An Aitoff projection of the ROSAT Brightest Cluster Sample X-ray identified clusters (Ebeling et al., 1998).

2.2.3 The Extended Brightest Cluster sample

The ROSAT extended Brightest Cluster Sample (Ebeling et al., 2000, hereafter eBCS) is a low flux extension to Brightest Cluster Sample (see §2.2.2).

The flux range for the extended catalogue is $2.8 \leq f_X \leq 4.4 \times 10^{-12}\,\mathrm{erg\,s}^{-1}\,\mathrm{cm}^{-2}$ and includes 7 clusters above redshift 0.3. The final sample consists of 107 clusters, with properties determined as §2.2.2. An Aitoff projection of the eBCS catalogue is shown in Figure 2.18.

[9] http://skview.gsfc.nasa.gov/skyview.html
[10] http://archive.stsci.edu/dss

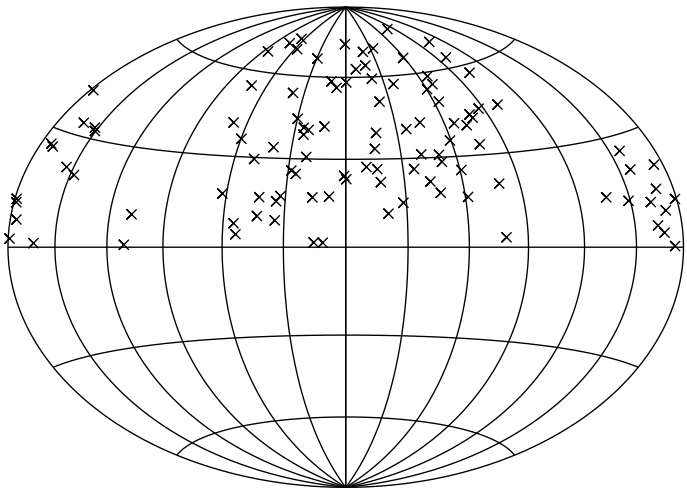

Figure 2.18: An Aitoff projection of the extended ROSAT Brightest Cluster Sample X-ray identified clusters (Ebeling et al., 2000).

2.2.4 The XMM Cluster Survey

The XMM Cluster Survey (Romer et al., 1999, hereafter XCS) is a serendipitous cluster survey using archival XMM-Newton photon maps from pointings of non clusters and is an order of magnitude more sensitive than ROSAT, with a minimum flux limit of $1 \times 10^{-14}\,\mathrm{erg\,s^{-1}\,cm^{-2}}$. The improved sensitivity will allow the XCS to be the largest X-ray cluster catalogue, detecting clusters out to redshifts > 1. The XMM Newton telescope is expected to operate until ~ 2013 returning an eventual total area of ~ 500 square degrees which can be used by the XCS.

Photon maps are created from XMM pointings centred on non-cluster objects (e.g high redshift active galactic nuclei), and because of the wide field of view of the XMM, we can serendipitously detect clusters in the photon map surrounding the pointing. The photon maps are then cleaned and masked for bright objects and bad pixels (Davidson et al. 2009 in prep), and an extended source catalogue is created by scanning the photon maps for extended photon overdensities (Davidson et al. 2009 in prep). The $0.5 - 2$keV band fluxes are calculated within an adaptive aperture determined by the pipeline (Lloyd-Davies et al. 2009 in prep) and the XCS DR1 extended source catalogue contains 1622 entries, which we plot using an Aitoff projection in Figure 2.19, and show a selection of the X-ray extended sources with corresponding optical images from the SDSS, in Figure 2.20.

Due to the potential high redshift of the XCS clusters, optical confirmation and redshift acquisition is only practical on large telescopes. For this purpose, the XCS has a dedicated photometric followup of the extended source catalogue using the NOAO 4 meter telescopes at Kitt Peak National Observatory in the north and at the Cerro Tololo Inter-American Observatory in the south.

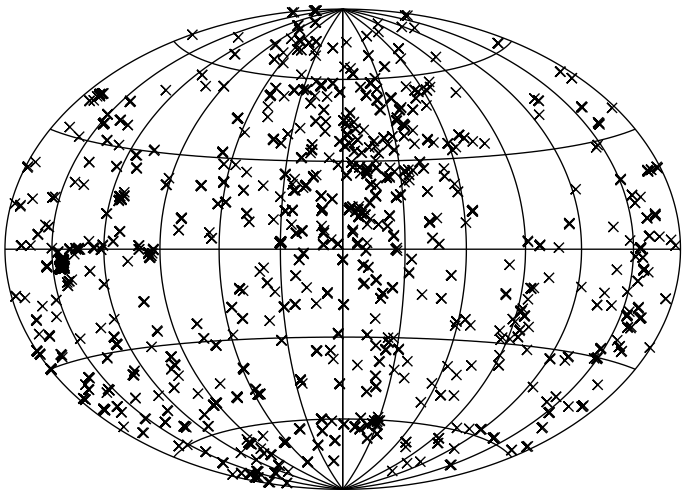

Figure 2.19: An Aitoff projection of the X-ray Cluster Survey extended source catalogue (Romer et al., 1999).

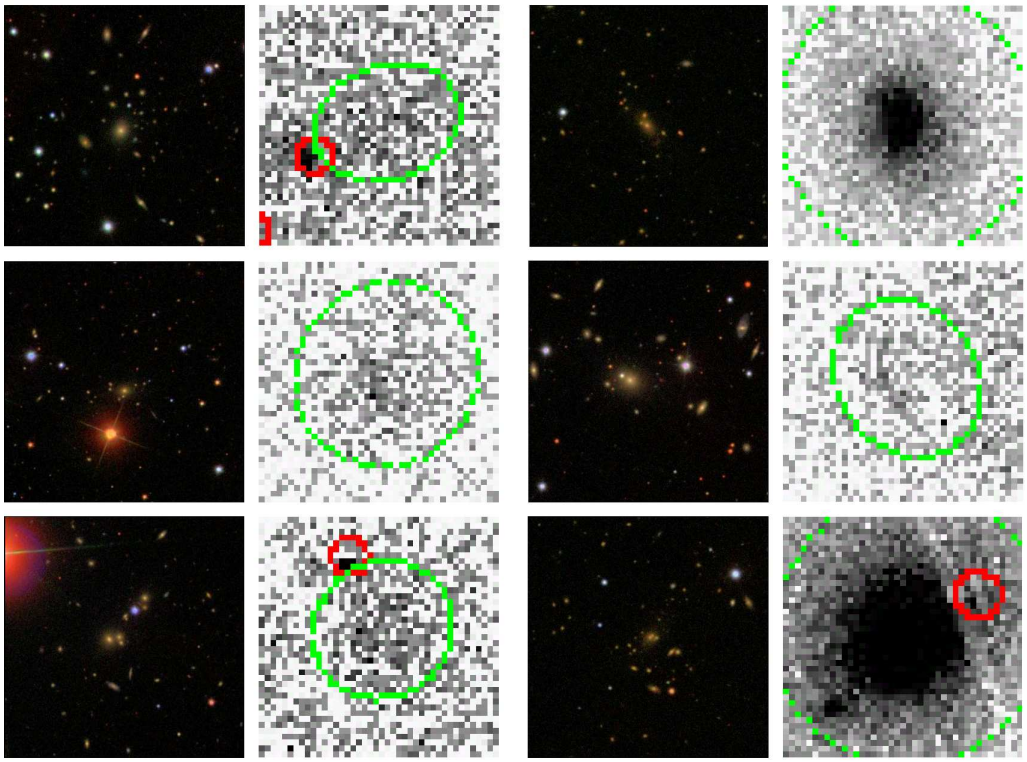

Figure 2.20: A selection of XCS extended sources (columns two and four) with corresponding SDSS optical images (columns one and three) centred at the coordinates of the extended source. The green ellipses on the X-ray images are extended sources and the red circles are point sources.

A pipeline has been developed to estimate photometric redshifts of the imaged galaxy overdensities (Mehrtens et al 2009 in prep) using the color-magnitude relation of red sequence galaxies (e.g, Hogg et al., 2004).

Each optical pointing of the ~ 2000 potential clusters requires a few kilo seconds in at least two photometric bands to obtain deep enough imaging to measure colours and magnitudes of cluster galaxies for the estimation of a redshift. For this reason we have developed an alternative method to optically confirm clusters and provide redshift estimates using the Sloan Digital Sky Survey. The methodology developed to achieve these aims and tests of the technique are described in the following sections.

Method overview

We begin with the empirical fact that early type galaxies are overwhelmingly found to populate the central regions of groups and clusters, as shown by Dressler (1980) using 55 clusters and $\sim 6,000$ galaxies and more recently using $> 100,000$ galaxies by Bamford et al. (2008), whose results are replicated here as Figure 2.21. Plotted are the fraction of early type galaxies f_{el}, as a function of local galaxy density Σ (the morphological classification of galaxies was performed using GalaxyZoo[11]), where galaxy clusters are represented by $\log_{10}\Sigma > 1$. We see the fraction of early type galaxies increases steadily with local galaxy density.

LRGs are early type galaxies, therefore by matching the LRGs catalogue of §2.1.6, with XCS extended sources, we can associate LRGs to X-ray clusters and assign the cluster a redshift using the LRG redshifts.

To decide at which radius an LRG can be associated to a cluster, we cross correlate them over a range of separations. We then test our redshift technique on the R400d X-ray identified cluster catalogue, which have known spectroscopic redshifts, and then apply the LRG redshift estimate technique to the XCS extended sources.

2.2.5 Associating LRGs to X-ray identified clusters

The centroid coordinates of the X-ray identified cluster are determined by the distribution of the Intra-Cluster Medium. This centroid can differ from the optically measured centroid which is ambiguous and may be assigned as the location of the BCG, or as the peak of the galaxy overdensity (if singular). Thus to assign LRGs to X-ray identified clusters we must first decide within which radii an LRG can be associated with an X-ray cluster. This can be achieved by cross correlating the X-ray clusters' centroids with LRG positions in physical radial co-ordinates at the redshift of the LRG. The cross correlation is then repeated using randomised X-ray co-ordinates and the ratio of the number of real to random matches at a particular separation is a measure of how likely a true match is to have occurred (i.e. the contamination).

[11] http://www.galaxyzoo.org

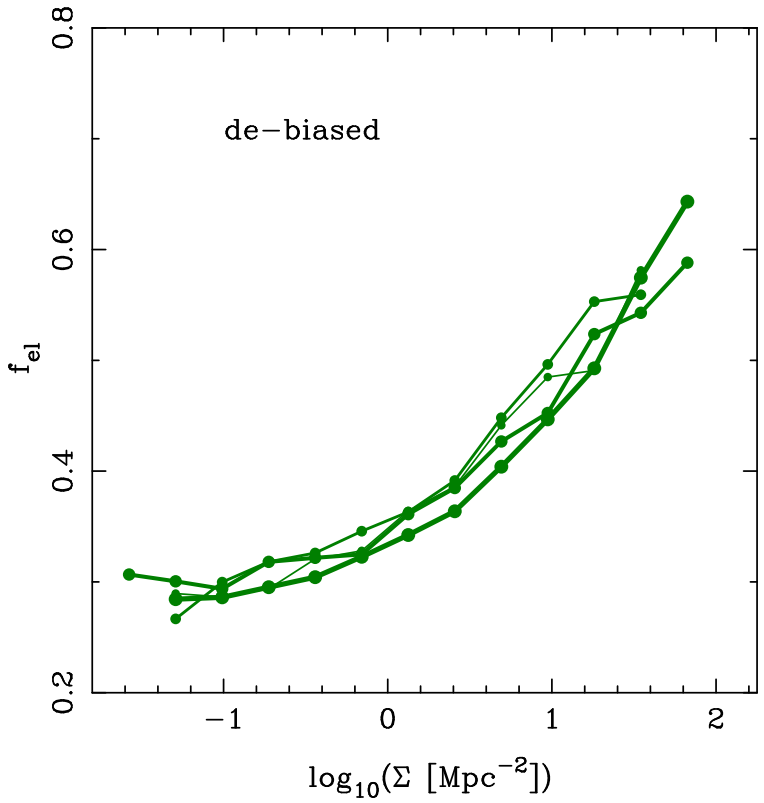

Figure 2.21: The fraction of early type (or elliptical) galaxies f_{el}, with increasing local galaxy density Σ. The morphological classifications of galaxies has been enabled through Galaxy Zoo. The fraction of early type galaxies increases with local density in each of the four redshift bins $z = [0.037, 0.051, 0.064, 0.078]$. Credit: Bamford et al. (2008).

We choose a large contiguous region well within the footprint of the SDSS to perform the matching, which reduces the effect of incompleteness at the survey edges. There are 66 R400d clusters in the contiguous region of the SDSS DR7 footprint bounded by RA$[135, 230]$, DEC$[5, 55]$. We set the random catalogue to be a factor of 100 larger than the subset of R400d clusters.

We perform the cluster centroid and LRG matching as a function of fixed physical radius r calculated at the redshift of the LRG. This entails calculating the angular diameter distance D_A using the redshift of each LRG which we do assuming flat $\Omega_m = 0.3, h = 0.7$ ΛCDM cosmology. For each real and random cluster the angular separation θ from each LRG to the centroid of the cluster is calculated. The angular separation and angular diameter distance are then converted to a physical radius using $r = \theta \, . \, D_A$.

Similar work was performed by Lin and Mohr (2004) and they found that 70% of Brightest Cluster Galaxies (bright LRGs) are found within 5% of the virial radius of X-ray selected clusters, which corresponds to 161kpc for Abell 2390 and 145 kpc for Abell 1689, see Table 2 of Lin and Mohr (2004). This work motivates our choice of matching radius ($175\,h^{-1}$ kpc) to be both

inclusive, and free from high levels of contamination. Figure 2.22 shows the ratio of the number of real to random matches as a function of increasing physical radial separation.

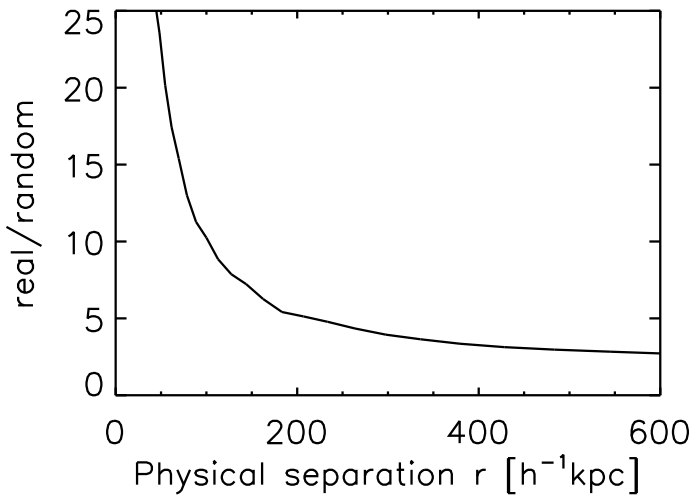

Figure 2.22: The R400d X-ray identified cluster centroid and SDSS LRG (from §2.1.6) cross correlation divided by the normalised random LRG cross correlation plotted as a function of physical angular separation r, calculated at the redshift of the LRG assuming flat $\Omega_m = 0.3, h = 0.7$ ΛCDM. The plot converges to 1 as expected at large radial separations.

The overdensity at low radii correspond to physical matches. The matching overdensity curve asymptotes to one on large scales. We note the ratio of real to false matches (i.e. the contamination) at $175\,h^{-1}$ kpc is 17.6%.

Having associated LRGs with clusters we continue in the following section by estimating the redshift of the cluster using the LRG redshifts. This will then be used to assign redshifts to the XCS clusters.

2.2.6 Initial redshift comparison

We compare the redshifts of the LRGs associated with the R400d clusters with the known redshifts from the R400d catalogue. In Figure 2.23(a) we show the redshifts of the LRGs with spectra plotted against the spectroscopic redshift of the R400d clusters. We see that the majority of the LRGs have similar redshifts to the clusters with a few outliers. We note that the number of outliers is 6%, which is below the 18% quoted previously. This is because the spectroscopic LRGs form a subset ($\sim 11\%$) of all the LRGs which were matched in §2.2.5. The redshift agreement of Figure 2.23(a) demonstrates the successful association of LRGs with clusters.

We plot the residuals of the LRG spectroscopic redshift against the cluster redshift divided by the

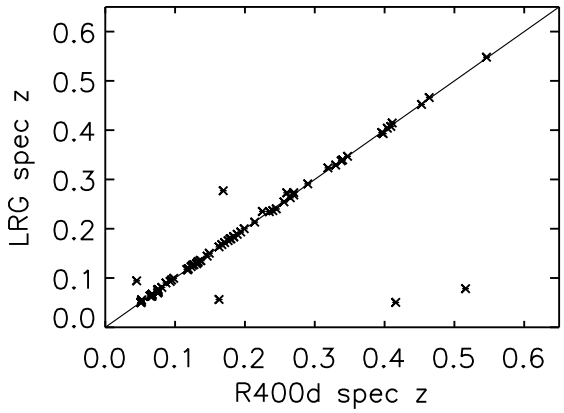

(a) Spectroscopic LRG redshifts plotted against the literature R400d cluster redshifts.

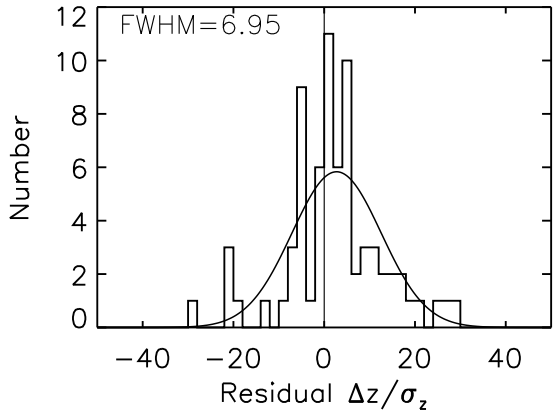

(b) The redshift residuals divided by the redshift errors.

Figure 2.23: Figure 2.23(a) shows the R400d spectroscopic cluster redshifts plotted against the spectroscopic redshifts of LRGs matched within 175kpc of the cluster centroids and Figure 2.23(a) shows the residuals divided by the spectroscopic redshift errors. This test demonstrates the ability to match LRGs to X-ray identified clusters, and use the LRG redshift as a proxy for cluster redshift. The line of equality is overplotted.

spectroscopic error in Figure 2.23(b). We fit a Gaussian and show the value of the Full Width at Half Maximum (hereafter FWHM). If the FWHM had the value 1 it would imply that the scatter is consistent with our error bars. The actual value is 6.95 which could be due to our comparison of LRG redshifts (not true cluster redshifts) with the literature cluster redshift, and a small amount of scatter in the LRG redshift caused by the velocity dispersions of the cluster is expected. If we

remove the outliers and only include -10 <residual< 10 in the fit, we do not find a large depreciation in the FWHM value (with a new value of 4.81). Although, if we assume that each cluster has a velocity dispersion of $600\,\mathrm{km\,s^{-1}}$ and convert this to a redshift error to add in quadrature to the LRG redshift error, we find the FWHM value is reduced to 1.03. This could be the reason for the initial discrepancy, and is a very approximate measurement of the average velocity dispersion of clusters.

We note that there is often more than one LRG associated with any one cluster as shown in Table 2.2, which lists the number of clusters which have multiple LRGs with photometric and spectroscopic redshifts. There is always at least 1 LRG with a photometric redshift for each cluster in the table because each LRG has a photometric redshift but only occasionally a spectroscopic redshift. We expect to see clusters with more than 1 LRG because clusters represent an overdensity of galaxies.

Number of LRGs per cluster	Number of clusters with associated LRGs of redshift type:	
	Spectroscopic	Photometric
0	27	0
1	52	42
2	7	28
3	3	13
4	1	5
5	0	0
6	0	2

Table 2.2: There is often more than one matched LRG per R400d cluster. This table shows the number of clusters with the corresponding number of matched LRGs with photometric redshifts, and the number of multiple matched LRGs per cluster with spectroscopic redshifts.

Only $\sim 11\%$ of SDSS LRGs have spectroscopic redshifts with the overwhelming majority having less reliable photometric redshifts, as shown by the increased number of data points in Figure 2.24(a), which compares the LRG photometric redshifts against the spectroscopic redshifts of the R400d clusters. We plot the residuals in Figure 2.24(b) which has a FWHM of 1.27. We do not expect the agreement of associating LRGs to clusters to have increased upon using photometric redshifts, but the much larger photometric errors do give less weight to each data point which reduces the FWHM. If we again assume a velocity dispersion of $600\,\mathrm{km}\,s^{-1}$ we find the FWHM is unchanged.

The degradation in agreement between the photometric redshifts (Figure 2.24) and the spectroscopic redshifts (Figure 2.23) is obvious. But, only a few of the associated LRGs have spectroscopic redshifts, the rest have photometric redshifts. By combining the redshifts of both the

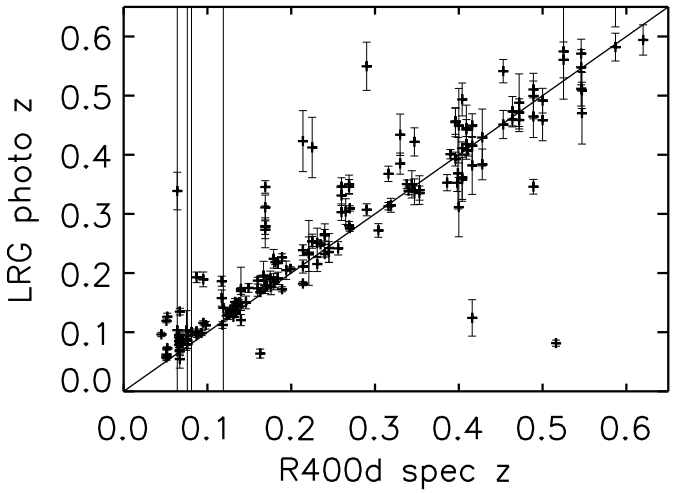

(a) Photometric LRG redshifts plotted against the literature R400d cluster redshifts.

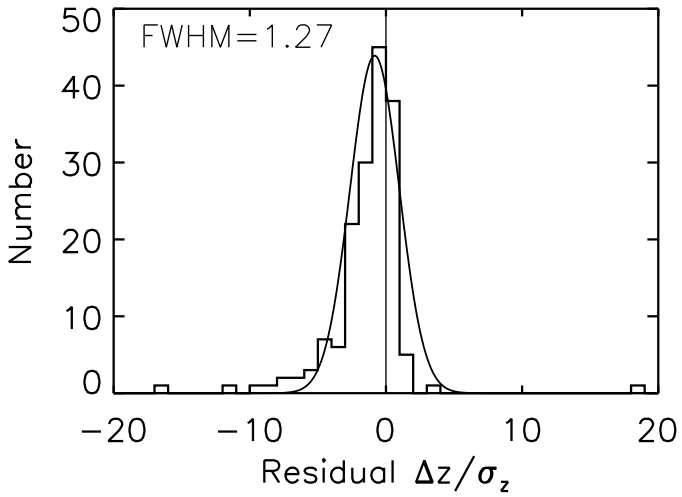

(b) The redshift residuals divided by the redshift errors.

Figure 2.24: Figure 2.24(a) shows the R400d spectroscopic cluster redshifts plotted against the photometric redshifts of LRGs matched to the cluster with the residuals divided by the redshift errors, plotted in Figure 2.24(b). The photometric errors are orders of magnitude larger than their spectroscopic counterparts. The line of equality is overplotted.

photometric and spectroscopic LRGs, we can include all possible redshift information when estimating cluster redshifts, as described in the next section.

2.2.7 Combining spectroscopic and photometric redshifts

We begin by modelling both the spectroscopic and photometric LRG redshifts as Gaussians with standard deviation σ corresponding to the redshift error, while the Gaussians tails are truncated to 0 beyond 3σ. Occasionally there may be ≥ 1 groups of LRGs with overlapping Gaussians along the line-of-sight of the cluster, and we plot an illustrative example of such a possible configuration in Figure 2.25. The lower redshift group in this illustrative example contains three LRGs, one of which has a very narrow Gaussian corresponding to a spectroscopic redshift, the other two having broader photometric redshift errors. The second group of two LRGs both have photometric redshifts. In this case we must decide which is the more likely group of LRGs to be inhabiting the cluster.

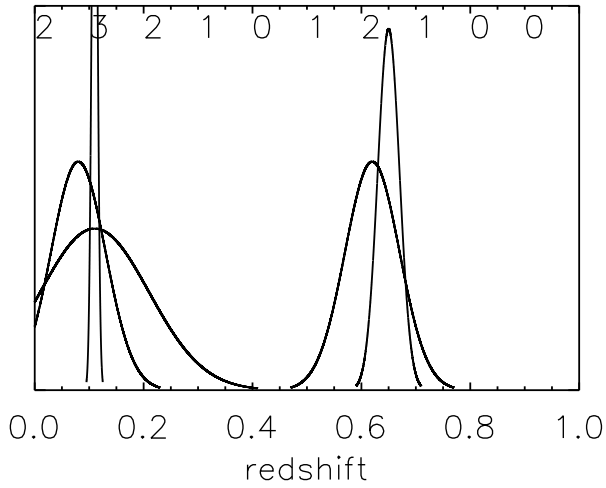

Figure 2.25: An illustrative example of the Gaussian modelled LRG redshifts along a particular line-of-sight. The width of the Gaussian is given by the photometric LRG redshift error if the spectroscopic redshift is unavailable and the Gaussian tails are truncated at 3σ. The numbers at the top of the plot show the number of overlapping Gaussians as a function of redshift.

We have developed a method to assign redshifts to a cluster under the circumstances of Figure 2.25 which will be described here and tested below.

The cluster assignment method (hereafter MLRG), scans the line-of-sight redshift space in intervals of 0.05, and segments of width 0.1. The number of Gaussians within each segment is recorded, as shown in our example by the numbers in top of Figure 2.25. A "primary" and "secondary" redshift are assigned according to the following criteria:

- If only one LRG is found along the line-of-sight then its redshift and error are assigned to the cluster.
- If one distinct group of LRGs is found, the weighted mean and weighted error is associated with the cluster.

- If more than one distinct clump of LRGs are found, a primary redshift is associated with the group with the highest number of LRGs, and a secondary redshift is determined from the group with a lower number of LRGs.
- If more than one distinct clump of LRGs are found, both containing the same number of LRGs, the primary redshift is that which has the smallest weighted error and the secondary redshift the next largest weighted error.
- In the unlikely event that more than one distinct clump of LRGs are found, both containing the same number of LRGs and having the same weighted error, the primary redshift is that which has the smallest weighted redshift, and the secondary redshift the larger weighted redshift.

We propose this method because we assume the X-ray emitting cluster to be that of the largest overdensity of line-of-sight LRGs, and the weighted error favours any spectroscopic redshifts. The final step in the decision tree is taken because the measured X-ray cluster luminosity function shows that low redshift lower luminous X-ray clusters are more common than high redshift X-ray bright clusters (Nichol et al., 2000). Measuring and retaining a secondary redshift enables potentially interesting, high redshift X-ray luminous clusters to be identified.

The final redshift estimate (MLRG z) using the combined photometric and spectroscopic LRG redshifts is plotted against the R400d spectroscopic cluster redshift in Figure 2.26(a), with residuals divided by the redshift errors plotted in Figure 2.26(b). We quantify the distribution in the next section.

2.2.8 Quantifying the redshift estimate technique

To quantify the results of assigning redshifts to X-ray identified clusters using the SDSS LRG sample created in §2.1.6, we measure the standard deviation σ of the measured redshifts from the line of equality, and the difference between the literature and measured redshifts, the systematic bias b given by

$$\begin{aligned} \sigma &= \frac{\sqrt{\sum \left(z_{cluster_i} - z_{MLRG_i}\right)^2}}{n}, \\ b &= \frac{\sum \left(z_{cluster_i} - z_{MLRG_i}\right)}{n}, \end{aligned} \tag{2.6}$$

where n is the number of clusters having literature redshifts $z_{cluster}$ and estimated redshifts z_{MLRG}. We find the values $\sigma, b = [0.006, 3 \times 10^{-5}]$ which shows that the method is unbiased. If we examine the average of the modulus of the bias, we find 0.020. This is largely dominated by the three outliers seen in Figure 2.26(a) which could be due to spurious matches, or to a break down in the redshift assignment technique. If we remove these three outliers we find the bias reduces to 0.0001, which is well within the re-derived 1σ standard deviation of 0.002.

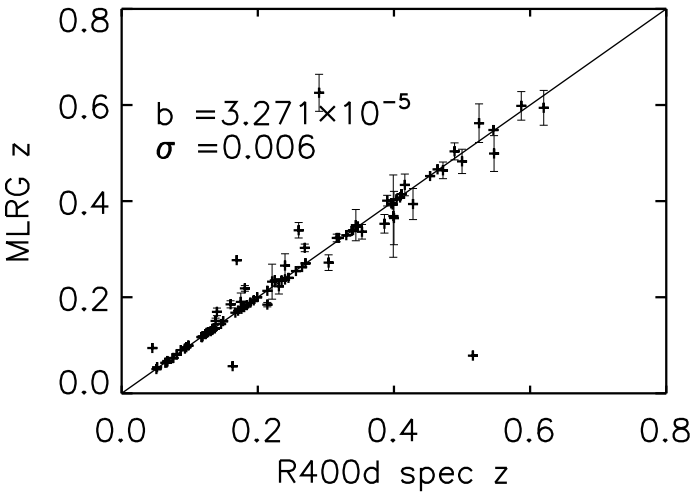

(a) The redshifts from the LRG redshift assignment method plotted against the R400d catalogue spectroscopic redshifts.

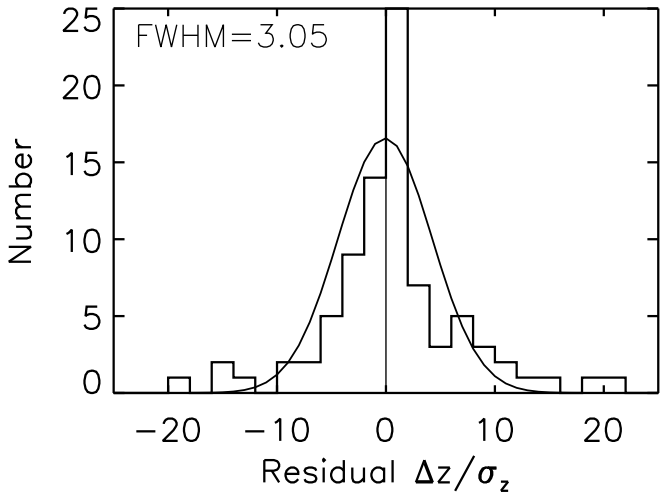

(b) The redshift residuals divided by the redshift errors.

Figure 2.26: Comparing the LRG redshift estimate technique MLRGz, with the R400d cluster catalogue with predetermined spectroscopic redshifts, Figure2.26(a). We show the line of equality, and the difference between the literature and measured redshifts, the bias b, and the standard deviation σ, described in §2.2.8. In Figure2.26(b) we plot the residuals divided by the redshift errors found using MLRG.

In Figure 2.26(b), we show the residuals of the MLRG redshift and the R400d catalogue redshift. We see that the FWHM value of 3.05 is between the spectroscopic value 6.95, and the photometric value 1.27, which is expected because we are combining both samples. The FWHM only reduces to 3.02 if we remove the three outliers, but if we again assume that each cluster has a velocity dispersion of $600\,\mathrm{km}\,s^{-1}$ and convert this to a redshift error and add in quadrature to the LRG redshift error, we find the FWHM value is reduced to 0.85.

It is possible that the primary and secondary redshift decision tree of MLRG, has failed to choose the correct primary redshift. Figure 2.27 shows the redshifts of clusters with both primary *and* secondary redshifts plotted against the R400d cluster redshifts.

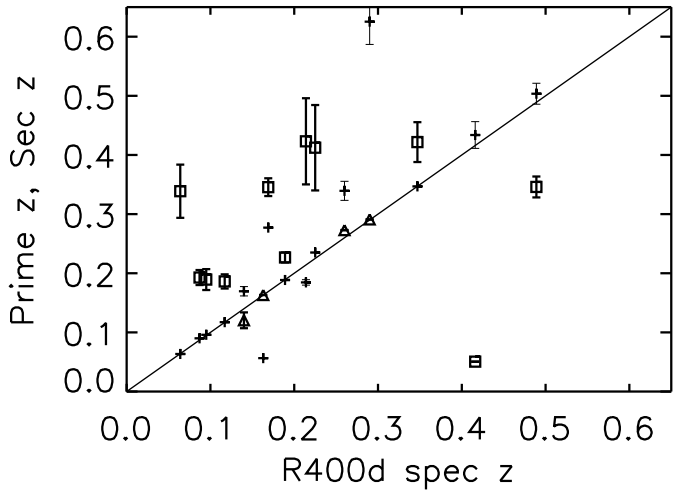

Figure 2.27: Primary and secondary redshift estimates plotted against literature redshifts for the R400d X-ray cluster catalogue. Secondary redshift closer (further) to the catalogue redshift than the primary redshifts are marked as triangles (squares). In $4/15$ cases the secondary redshift is closer to the catalogue redshift, therefore this process fails in $4/92$ cases.

On four (out of fifteen) occasions the secondary estimate is a better fit to the literature redshift and these cases have been highlighted on Figure 2.27 by triangles. In total, we note that this redshift process fails in 4 out of 92 cases. We discuss these cases below in order of increasing redshift.

- The first case corresponds to a configuration of three LRGs along the line-of-sight with photometric redshifts. The higher redshift group contains two LRGs and therefore makes the primary redshift. This cluster has coordinates RA,DEC $[184.452, 22.921]$.

- Along this line-of-sight there are two LRGs which both have spectroscopic redshifts. The lower LRG redshift error is marginally lower, 0.00017 compared to the improved secondary redshift with an error 0.00018. This cluster has coordinates RA,DEC $[35.867, -8.870]$.

- This cluster has one LRG with a spectroscopic redshift forming the secondary redshift and a group of two LRGs with higher photometric redshifts creating the primary redshift. This cluster has coordinates RA,DEC $[124.977, 56.577]$.

- This cluster has two LRGs at a high redshift with photometric errors, and a low redshift group with one spectroscopic LRG. This cluster has coordinates RA,DEC $[214.630, 25.179]$.

The results of applying MLRG to the remaining cluster catalogues (with less trustworthy redshifts, see §2.2.2 and §2.2.3) are shown in Figure 2.28 for the BCS, and Figure 2.29 for the eBCS. The scatter expected in these relationships is greater than the R400d catalogue due to the lack of spectroscopic redshifts, and can be seen by the FWHM values in the residual plots of Figures 2.28(b) and 2.29(b), which are both ~ 6. This value is twice as large as with the R400d clusters (3.05) and can be attributed to the less accurate literature redshift measurements, and to the lack of quoted literature cluster redshift errors. For example, if we again assume a velocity dispersion of $600\,\mathrm{km\,s^{-1}}$ we find the FWHM for both distributions is still high (~ 3) and so conclude that this effect is not purely a cluster redshift error problem but something more systematic. In order to reduce the FWHM to ~ 1 we need to add a velocity dispersion of $15,000\,\mathrm{km\,s^{-1}}$!

We have tested the redshift assignment method MLRG, and shown we can reproduce literature redshifts. We now apply MLRG to the XCS extended source catalogue and assign redshifts to those sources which have LRGs matches.

2.3 XCS cluster redshifts

Using LRGs from the SDSS and the MLRG method developed in §2.2.7 we can assign redshifts to the XCS extended sources which are without redshift measurements. There are 610 XCS extended sources within the SDSS DR7 footprint of which 202 have at least 1 LRG within 175kpc (calculated at the redshift of the LRG) of the X-ray centroid. The primary and secondary redshift histograms are shown in Figure 2.30.

The XCS extended sources for which redshifts estimates have been assigned from LRGs are, by definition, near an overdensity of LRGs and are therefore probably bona fide clusters (remembering that there is 18% expected contamination). The 67% of XCS extended sources within the SDSS footprint for which there are no LRG counterparts demonstrates the low level of purity of the XCS pipeline. To understand the level of purity I created an XCS extended source classification website called "Cluster Zoo"[12], using SDSS imaging. The construction of the classification website and the purity results are described in the following section.

[12] http://dsg.port.ac.uk/∼hoyleb/cluster_zoo/

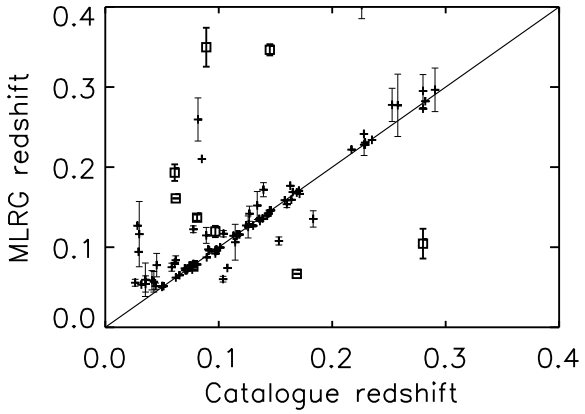

(a) The BCS catalogue redshifts plotted against the redshifts estimates using MLRG.

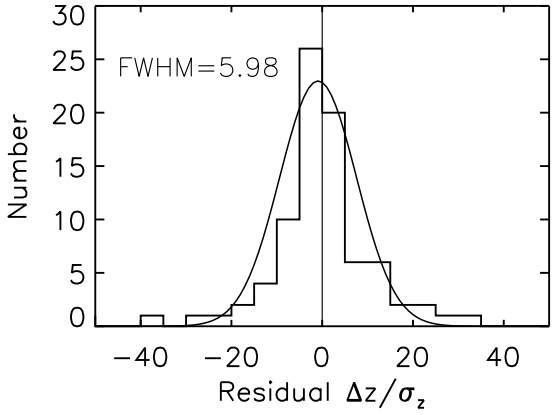

(b) The residuals divided by the redshift errors of the catalogue redshifts and MLRG redshifts

Figure 2.28: The top figure shows the redshift estimates using SDSS LRGs and MLRG (see §2.2.8) plotted against the literature redshifts for the BCS X-ray identified cluster catalogue. The primary (secondary) redshifts are plotted as crosses (squares) and overplotted is the line of equality. In the bottom figure we plot the redshift residuals divided by the redshift error determined by MLRG.

Cluster Zoo

Cluster Zoo has been loosely based on Galaxy Zoo[13] which is a web based classification interface linked to a database back end. Galaxy Zoo was designed to enable members of the public to classify SDSS galaxies into early and late types. Cluster Zoo extends this formalism but is designed

[13] www.galaxyzoo.org

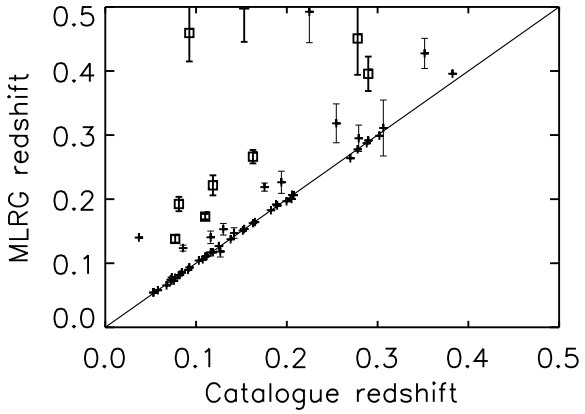

(a) The eBCS catalogue redshifts plotted against the redshifts estimates using MLRG.

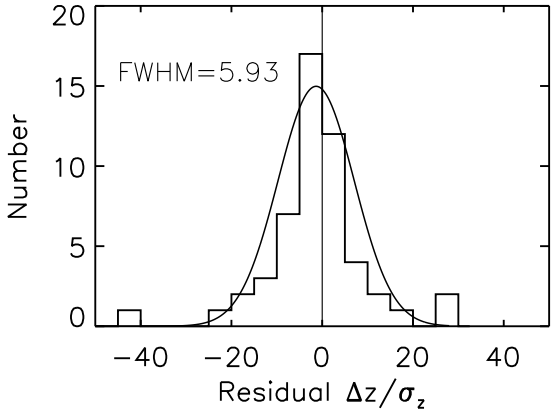

(b) The residuals divided by the redshift errors of the catalogue redshifts and MLRG redshifts

Figure 2.29: In the top figure we show the redshift estimates using SDSS LRGs and MLRG (see§2.2.8) plotted against the literature redshifts for the eBCS X-ray identified cluster catalogue. The primary (secondary) redshifts are plotted as crosses (squares) and overplotted is the line of equality. In Figures 2.29(b) we plot the redshift residuals divided by the redshift error determined by MLRG.

for research scientists, particularly members of the XCS collaboration.

Once logged into Cluster Zoo and authenticated, the user is presented with X-ray and optical images of an extended source at magnifications $3' \times 3', 6' \times 6'$ and $12' \times 12'$. The X-ray images are the reduced photon maps used in the XCS extended source identification pipeline. The optical images are dynamically pulled from the SDSS DR5 Navigate server centred at the RA,

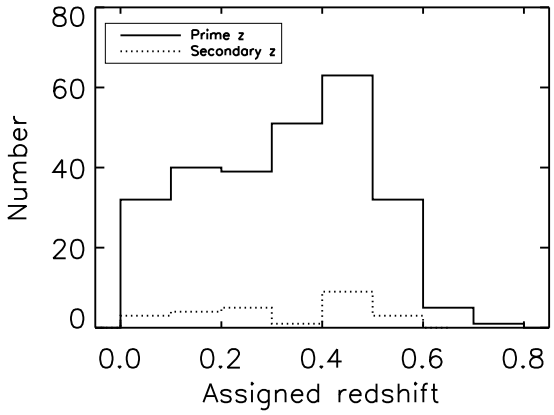

Figure 2.30: The redshift histogram of XCS extended sources assigned from SDSS LRGs using the method developed in §2.2.8. Primary (secondary) redshifts are shown by the continuous (dotted) line.

DEC of the extended source. An option allows the user to change between images of the pure X-ray photon maps, and the photon maps with overplotted ellipses corresponding to the pipelines identification of an extended source. The user also has the ability to view the plain and inverted SDSS images, and the SDSS optical image with overplotted X-ray contours. A screen shot of the website showing a cluster with X-ray contours overlaying the optical image is shown in Figure 2.31.

On the next page of the website, the user can view the masks of the XCS and SDSS which enable the user to understand problems with either images. After examining the images and masks, the user is asked to classify the extended source into various classifications whose definitions are described below.

- Gold Cluster/Group : A clear overdensity of galaxies is present and an X-ray extended source is clearly present and centred near the galaxy overdensity.
- Silver Cluster/Group: An overdensity of galaxies is present. An extended source is also present but not necessarily centred on the galaxies.
- Bronze Cluster/Group: An overdensity of galaxies is present. There is a questionable X-ray extended source which has, for example, a weak or messy signal or point source contamination.
- High-z Candidate: There is no overdensity of galaxies present. Although the X-ray extended source is present and of reasonable quality.
- Not a cluster/group: There is no overdensity of galaxies present. There is a questionable X-ray extended source.

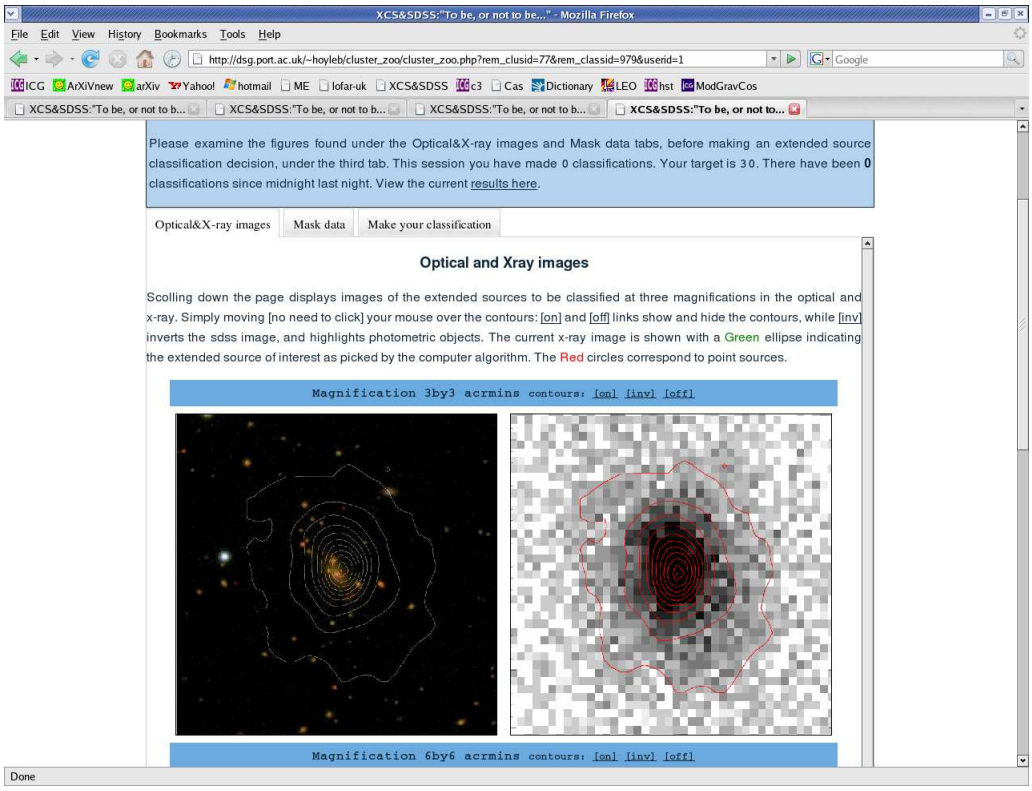

Figure 2.31: A screen shot of Cluster Zoo. A website designed to classify XCS extended sources. Images are display at various magnifications, with the ability to toggle X-ray isocontours on and off. By identifying an optical counter part to an X-ray extended source we can confirm a cluster. Likewise, well defined extended sources without an optical counterpart, will have a higher redshift than the SDSS imaging and can be targeted for high redshift followup.

- Cannot Classify: There is missing/bad SDSS or X-ray data possibly because of bright stars, masked regions or being near the edge of a field.
- Unsure: If you cannot use any of the above categories.
- The user may also leave a comment about the extended source.

The results are read by the HTML forms and sent via PHP to a MySQL database and stored in a classification table. Simultaneously, a counter for the classified extended source is incremented. The next extended source to be classified is drawn at random from the remaining extended sources with the lowest number of previous classifications. The method of determining the next extended source was chosen because we wanted a similar number of classifications for each extended source, and we could not guarantee that the XCS members would each classify all of the 610 objects in our list. This ensured that each of the extended sources are classified within ± 1 of every other in the list.

A total of $5,575$ classifications were made by 48 XCS users, resulting in 525 extended sources begin classified 9 times, and the remaining 85 extended sources being classified 10 times.

We examine the distribution of classifications (not clusters) by grouping the classifications into classification types. Additionally we group the classification types into two categories, "Clusters" which include Gold, Silver, Bronze and High redshift Candidates, and "non Clusters" which include the remaining categories. We do not examine the differing classifications for any one cluster, because although the classification criteria were designed to be quantitative, different people classified the same object into different categories (occasionally the same user would repeat classify the same cluster into two different categories), resulting in a more qualitative framework. We leave the analysis of these classifications to future work (see §6.2).

We can examine the percentage of classifications in each category as a function of extended source properties and examine how this can be used as a proxy for purity. Table 2.3 shows the percentage of classifications in each category and in the grouped categories as a function of soft counts, which are the number of X-ray photons in the energy band $0.5 - 2$keV.

Classification	The percentage of classified extended sources with soft counts		
	> 0	> 200	> 500
Gold Cluster	18	41	54
Silver Cluster	8	11	10
Bronze Cluster	13	12	9
High z Candidate	16	13	8
Not a Cluster	34	16	12
Cannot Classify	6	5	6
Unsure	4	3	2
Total			
Clusters	56	76	80
Non clusters	44	24	20

Table 2.3: The percentage of XCS extended sources classifications as grouped into categories using Cluster Zoo. The classifications are listed as a function of soft counts, which is the number of photons in the $0.5 - 2$keV band.

Table 2.3 demonstrates that the number of XCS extended sources to be classified as clusters (i.e. the purity) is relatively low if we include all extended sources (at 56%). This is because the XCS cluster finding pipeline was designed to be maximally inclusive and as such we expect to have contamination. As the number of Soft Counts increase the percentage of extended sources to be classified as clusters increases. Examining only extended sources with soft counts greater than 500 photons results in 80% of classifications identifying clusters, with 54% indicated as Gold

Cluster, the most reliable category.

Cluster Zoo has enabled the purity of the XCS extended source catalogue to be tested and confirmed Soft Counts is a proxy for purity. Additionally, data sets can be, and have been, drawn from the Cluster Zoo classifications corresponding to the properties of interest, for example a sample of potential high redshift clusters candidates have been identified and are in the process of being followed up (Standford et al 2009 in prep).

The XCS extended sources with redshifts (which are thought to be bona fide clusters) can now have X-ray luminosities and temperatures estimated using the X-ray fluxes and cluster redshifts assigned from §2.3. The next section introduces the pipeline to convert X-ray fluxes to X-ray luminosities, and to estimate temperatures for the XCS and the other X-ray cluster catalogues.

2.3.1 Uniform reprocessing of X-ray fluxes

Combining the different X-ray cluster catalogues (R400d, BCS, eBCS, XCS), is only possible if fluxes and luminosities are re-computed in identical energy bands, for a particular cosmology, and with the same pipeline. The approach developed by members of the XCS to re-derive X-ray properties for these X-ray cluster catalogues is briefly described below. We refer to Lloyd-Davies et al (2009, in preparation) for details. My role in this work is to provide redshift estimates for the XCS clusters for the conversion of flux to luminosity and temperature. We use the luminosities and temperatures in later sections.

Naively, one could convert the X-ray luminosity L_X between different cosmologies, e.g. cosmology 1 (denoted by$'$) and cosmology 2 (denoted by $''$), using the ratio of luminosity distances, D_L and the definition of flux f_X, i.e.

$$f_X \equiv \frac{L'_X}{4\pi D'^2_L} = \frac{L''_X}{4\pi D''^2_L} , \tag{2.7}$$

$$L''_X = L'_X \frac{D''^2_L}{D'^2_L} . \tag{2.8}$$

However, this fails to correctly account for the quoted catalogue fluxes being in different energy bands ($0.11 - 2.2$ keV for the ROSAT catalogues and $0.5 - 2$ keV for the XCS). Also, bolometric fluxes are required if luminosities are to be converted into temperatures, which are then required for the computation of masses. Cosmology also plays an intricate role in the measurement of X-ray fluxes, and the conversion to X-ray luminosities, and each X-ray cluster catalogue has been analysed according to its own cosmology (see §2.2.1-§2.2.4).

To correctly account for these differences, the original photon maps have been reanalysed for each of the cluster catalogues. We briefly describe this analysis below and refer to the flowchart 2.34.

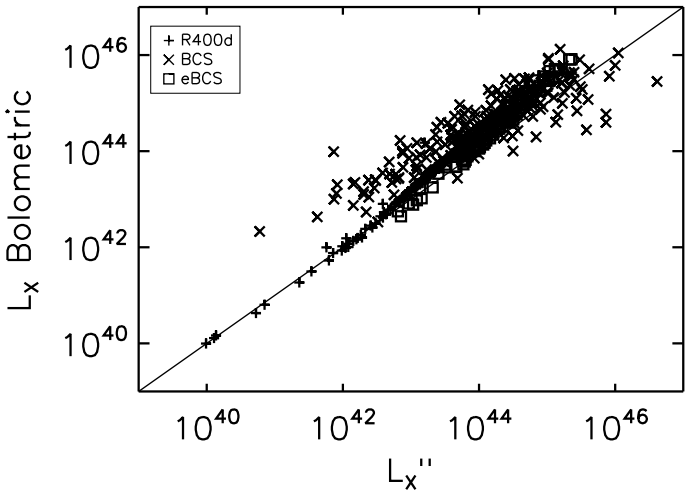

Figure 2.32: The differences in X-ray luminosity between the naively converted X-ray luminosities L''_X (see Equation 2.7), and the reanalysed bolometric luminosities, which use the photon maps for each catalogue, see §2.3.1.

Initially, an aperture is placed over the extended source, whose size is cosmology dependent via D_A and the cluster redshift. A random cluster temperature is then chosen to produce a spectral profile, which determines the corrected count rate from measured counts in the band of the X-ray detector, to an estimated bolometric count. The bolometric count rates are converted to a bolometric flux, through a redshift dependent K correction, and then to a bolometric luminosity, which is cosmology dependent in D_L. By assuming an X-ray luminosity - temperature relation (hereafter $L-T$), a new temperature estimate is obtained. The new temperature produces a new temperature profile, corrected count rates, fluxes, luminosities and finally an updated temperature. This iterative process is repeated until the temperature and luminosity have converged. By modifying the $L-T$ relation an estimate of the error on the temperature and luminosity is found.

The difference between the naive conversion of luminosities L''_X and the method described above is shown in Figure 2.32, and Figure 2.33. We see that there is an offset in the residuals which is to be expected because we are comparing luminosities in a fixed band to bolometric luminosities, which by definition, span the entire energy range. Some residuals are greater than zero which demonstrates how inaccurate the naive conversion of luminosities between cosmologies is, as we would not expect a converted luminosity in a band to be greater than the bolometric luminosity.

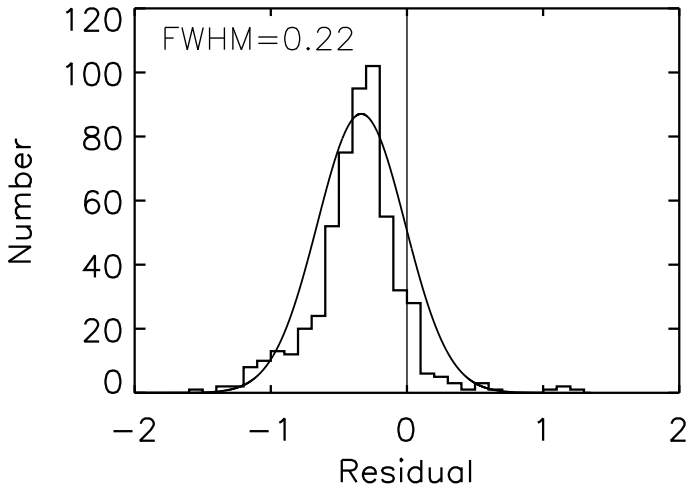

Figure 2.33: The residuals of the naive cosmology converted luminosities, and the full re-derived bolometric luminosities using the original photon maps, see §2.3.1.

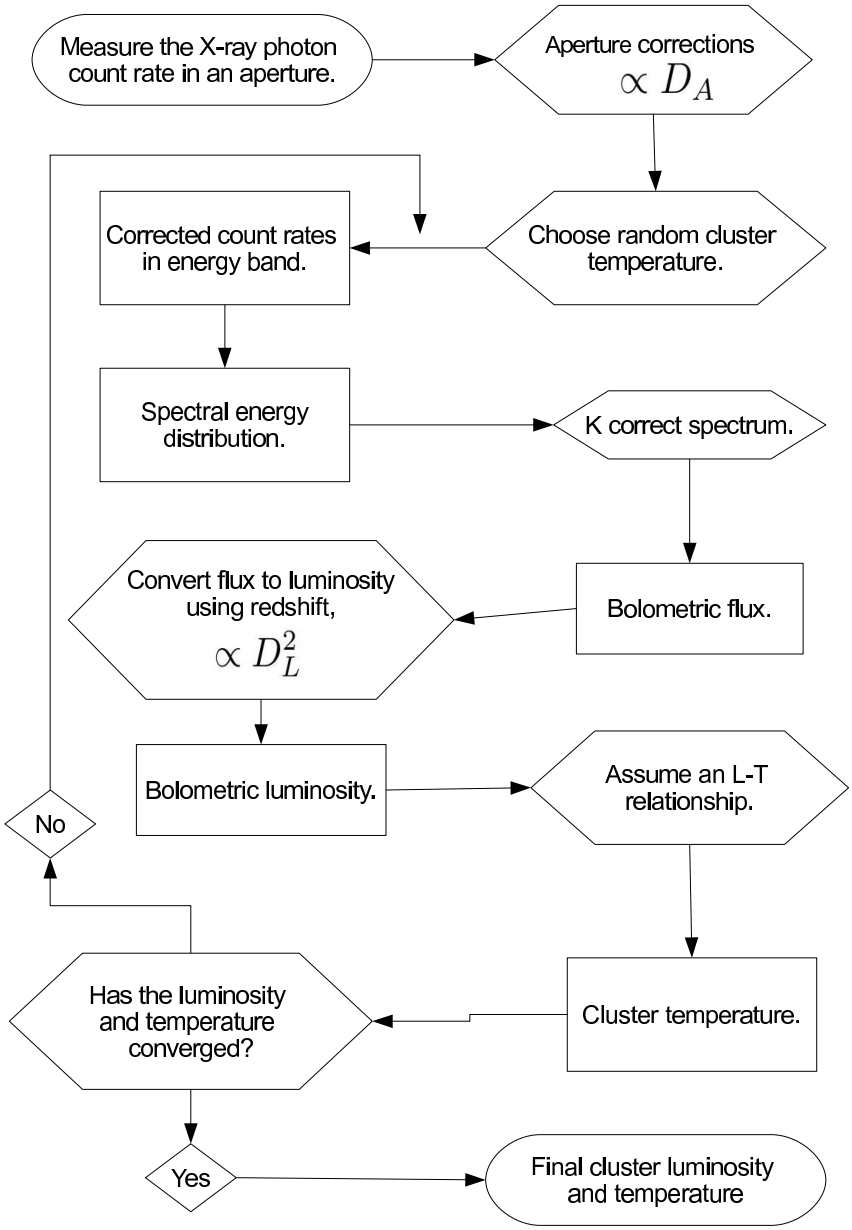

Figure 2.34: A flowchart detailing the conversion of X-ray count rates in an energy band to a final cluster temperature and luminosity. The role of cosmology is highlighted in the angular diameter distance D_A and the luminosity distance D_L.

2.4 Summary

In this chapter we have introduced the data catalogues used in the remaining chapters of this thesis. We have assimilated a massive LRG sample and used it to assign redshifts to X-ray identified clusters. We have measured the purity of the XCS cluster catalogue and have uniformly reprocessed the X-ray cluster catalogues obtaining luminosities and temperature estimates.

Table 2.4 presents the total number of X-ray and optical datasets. We only show the number of X-ray selected clusters which have at least 1 LRG within 175kpc of their centroid because the presence of an LRG will be critical in later sections (see §3.2.3). There are almost two orders of magnitude more optically identified clusters than X-ray clusters, but before they can be used for cosmology their masses must be determined.

In §3 we convert the X-ray cluster temperatures to masses and obtain optical properties for the X-ray clusters using SDSS data. We examine X-ray derived mass scaling relations with optical properties of the X-ray selected clusters and find that the total cluster optical luminosity scales with mass. In §4 we compare the optical mass estimates with those derived from weak lensing (§5), and then derive cosmological constraints.

Dataset	Wavelength	Acronym	Section reference	Size	Redshift range
Cluster	X-ray	R400d	§2.2.1	90	$0.003 < z < 0.888$
Cluster	X-ray	BCS	§2.2.2	92	$0.003 < z < 0.374$
Cluster	X-ray	eBCS	§2.2.3	53	$0.023 < z < 0.418$
Cluster	X-ray	XCS	§2.2.4	202	$0.051 < z < 0.765$
Cluster	Optical	MaxBCG	§2.1.7	$13,305$	$0.102 < z < 0.299$
Cluster	Optical	C4	§2.1.8	$2,037$	$0.007 < z < 0.165$
LRG	Optical		§2.1.6	$2,060,124$	$0.050 < z < 0.999$
Quasar	Optical		§2.1.9	$531,856$	$0.505 < z < 5.745$

Table 2.4: The different data sets introduced throughout this chapter. We show the type of data set, the wavelength of the electromagnetic spectrum that the catalogues are detected in, the catalogue acronym used throughout this and subsequent chapters, the section where we introduce the catalogue, the size of the data sets used in this thesis after cuts have been applied, and the redshift range of the data sets.

Chapter 3

X-ray derived cluster masses

To use clusters for cosmology one needs large numbers of clusters over a broad redshift range with well measured masses. The number of homogeneously selected optical clusters is two orders of magnitude higher than the number of homogeneously identified X-ray clusters. This is because optical surveys can be performed on the ground, where large detectors can be built and maintained relatively cheaply. X-ray instrumentation must be placed on a satellite, and therefore has a maximum size, much larger initial cost, and are expensive to maintain.

It would be advantageous to use optically selected cluster catalogues for cosmology because of their much larger size, but they lack easily obtainable, reliable mass estimates. X-ray identified clusters are lower in number, but have a cluster mass measurement derivable from the temperature of the intracluster medium. This chapter aims to find X-ray selected clusters with an optical counterpart in the SDSS, and perform comparisons of X-ray and optical properties. We identify an optical property, the total cluster optical luminosity, which scales with mass, allowing mass estimates to be applied to all optical clusters.

By using the optical luminosity to assign masses to the volume limited $13,000$ MaxBCG and $2,000$ C4 clusters we are able to build the cluster mass function and compare it to the theoretical mass function (in §4), thereby testing cosmological parameters to high precision and models of gravity using clusters of galaxies.

The chapter begins by introducing the physics of X-ray clusters and continues by identifying the optical counterparts of X-ray selected clusters. The optical properties of these clusters are then calculated and errors estimated. We compare X-ray and optical properties and measure how optical properties, in particular the total cluster optical luminosity, scales with cluster mass. We examine the robustness of the mass scaling relationship under the relaxation of the X-ray temperature to mass conversion assumptions, and show them to be robust. We finish by presenting the cluster mass estimates for the MaxBCG and C4 optical cluster catalogues.

3.1 X-ray cluster physics

This section introduces the mechanism responsible for galaxy cluster X-ray emission and describes the theoretical and observed temperature-to-mass conversion. We then derive other cluster properties from the mass.

3.1.1 Introduction

X-ray cluster are distinctly recognisable on the X-ray sky because the typical physical size of galaxy clusters produce a spatially extended source. The extent of this source is typically hundreds of kiloparsecs to a few megaparsecs and no other virialised objects are as extended; therefore the presence of extended X-ray emission is a direct indication of a cluster of galaxies.

X-rays are produced in the Intracluster Medium (hereafter ICM) which is a diffuse ionised intergalactic gas with a temperature of $\sim 10^7$ K and emits X-rays at the keV scale. The mechanism responsible for the emission of X-rays is Bremsstrahlung radiation (Sarazin, 1986), which occurs as electrons change direction in the proximity of ions. In order to conserve energy and momentum, high energy X-ray photons are thus emitted. The ICM is gravitationally bound to the cluster and is sensitive to the combined gravitational potential of the baryonic and non-baryonic matter.

3.1.2 X-ray temperature and mass

The theoretical relationship between cluster mass and the temperature of the ICM is found by equating the gas density ρ and pressure p, to the total gravitational potential g to obtain

$$\frac{1}{\rho}\frac{\mathrm{d}p}{\mathrm{d}r} = -g \, . \tag{3.1}$$

Under the assumption of an isothermal ideal gas, then $pV = N_A k_B T$ (with Avogadro's number N_A and the Boltzmann constant k_B). The temperature T of the ICM can be related to the cluster mass M by (e.g. Arnaud and Evrard, 1999)

$$M\big(<r\big) = -\frac{kT(r)r}{G\mu M_H}\left(\frac{\mathrm{d}\ln\rho}{\mathrm{d}\ln r} + \frac{\mathrm{d}\ln T}{\mathrm{d}\ln r}\right) \, , \tag{3.2}$$

where μ, M_H are the mean molecular weight of the gas, and the mass of hydrogen respectively. Assuming a β density profile for the ICM (Cavaliere and Fusco-Femiano, 1978) of the form

$$\rho(r) = \rho_0(1 + (r/r_c)^2)^{-3\beta/2} \, , \tag{3.3}$$

where the density ρ is a function of radius r, and ρ_0, r_c are fitted quantities. Substituting Equation 3.3 into Equation 3.2 we get a relationship $M(<r) \propto T^{1.5}$.

This theoretical description is expected to be more complicated in reality, for example, the density profile of the ICM has been shown to differ from a β profile (e.g. Rasia et al., 2006), and

the temperature of the ICM can be boosted through mergers (e.g. Okabe and Umetsu, 2007), and from the output of active galactic nuclei (e.g. Gitti et al., 2007); all of these effects will modify the observed mass-temperature relation.

With these restrictions in mind however, the observed mass - temperature relationship has been shown to be stable. Vikhlinin et al. (2006) examined 13 low redshift clusters using CHANDRA[1] (a high resolution X-ray satellite) and obtained a mass - temperature relationship of the form $M_{500} \propto T^{1.5-1.6}$, where M_{500} is the radius within which the average density is $500\,\bar{\rho}_m$. Additionally, Dai et al. (2006) stacked the ROSAT All Sky Survey X-ray emission of 2MASS[2] identified optical clusters into 5 richness bins. They observe a mass - temperature correlation within an aperture M_{200}, at which the average density enclosed is $200\,\bar{\rho}_m$ given by

$$M_{200} = 10^{13.56\pm0.05} T^{1.59\pm0.17} h^{-1} M_{\odot} \; . \tag{3.4}$$

We use this mass-temperature conversion when estimating masses for the X-ray selected clusters. In the next section we derive other properties such as radius and redshift error from the mass, which will be useful in later sections.

3.1.3 Cluster properties derived from mass

The literature X-ray cluster catalogues (R400d, BCS, eBCS) fail to provide errors on their cluster redshifts. We thus assign redshift errors to all of the X-ray clusters, by converting the cluster mass into a velocity dispersion estimate. The velocity dispersion is the spread in the measured redshifts of different cluster members, and is due to the galactic motion projected along the line-of-sight. We stress that neither the velocity dispersion, nor the galaxy redshifts have been measured. If they had, we could have used the galaxy velocity dispersion as a proxy for mass in much the same way as we use the ICM, because they both feel the same gravitational potential well. Instead, we predict a velocity dispersion from a cluster mass and use it to estimate a cluster redshift error.

The velocity dispersion σ_v of the member galaxies in a relaxed system is calculated using the virial theorem which is applicable to systems which are stable and bound over long epochs. The virial theorem states $U + 2T = 0$, where U and T are the potential and kinetic energies respectively. Applying this to galaxy cluster results in the velocity dispersion as a function of mass M given by

$$\sigma_v^2 \;\; = \;\; \frac{GM}{2r} \; , \tag{3.5}$$

where G is Newton's gravitational constant and r is the radius. We convert the velocity dispersion into a cluster redshift error Δz using the relativistic redshift equation of $1+z = \sqrt{(1+v/c)/(1-v/c)}$

[1] http://chandra.harvard.edu/

[2] http://www.ipac.caltech.edu/2mass/

giving

$$\Delta z \;=\; \left(\sqrt{\frac{1+v'/c}{1-v'/c}}-1\right)-z\;, \tag{3.6}$$

where v' is the recession velocity due to the original redshift z, plus the velocity dispersion. Additionally, the cluster radius R_{200} at which the averaged mass enclosed is $200\,\bar{\rho}_m$ is given in terms of cluster mass by

$$R_{200} \;=\; \left(\frac{2\,G\,M}{\left(1+z\right)^3 H_0^2\,\Omega_m\,200}\right)^{1/3}\;. \tag{3.7}$$

The cluster radius can be converted into an angle subtended on the sky θ at the observer, using the angular diameter distance D_A of the cluster, and is given by

$$\theta \;=\; \frac{R}{D_A}\,. \tag{3.8}$$

Typically, the cluster radius is quoted as R_Δ within which the average mass enclosed M_Δ is Δ times the background density. The number of galaxies found within this radius is quoted as Ng_Δ. A standard choice of $\Delta = 200$ is adopted in the literature, and close to the critical value of $\Delta = 178$ for spherical collapse in an Einstein de Sitter cosmology.

In §3.1.3 and §3.1.2, we introduced and derived X-ray properties of clusters. In §3.2 we derive the optical properties of the X-ray cluster, for those clusters that we have associated LRGs (see §2.2.5).

3.2 Optical properties of X-ray clusters

In this section, we describe the matching of X-ray selected clusters with optical counterparts within the SDSS footprint. We describe the procedure of determining cluster membership and measure optical luminosities and the number of member galaxies.

3.2.1 Matching X-ray and optical clusters

In §2.2.5, we described the process of matching X-ray identified clusters with Luminous Red Galaxies. We use the matches found in §2.2.5 as the basis for the following work. Our sample consists of 437 X-ray identified clusters which fall within the SDSS footprint and can be assigned at least one LRG counterpart (see Table 2.4). The total number of X-ray clusters from each catalogue is shown in Table 3.1, with the total number of line-of-sight galaxies, and member galaxies, found following the methodology described below.

	R400d	BCS	eBCS	XCS
Number of Clusters	90	92	53	202
All galaxies	27329	116195	47683	20292
Cluster members	1184	2417	1424	360

Table 3.1: The total number of X-ray clusters from each catalogue within the SDSS footprint. We also show the total number of galaxies retrieved from CasJobs, along the line-of-sight and within cluster dependent apertures for each X-ray cluster catalogue. Also shown are the final number of cluster members after redshift and colour cuts.

3.2.2 Cluster membership

We upload the coordinates of the X-ray clusters with LRG counterparts into the SDSS Casjobs[3] and retrieve all main sample galaxies along the line-of-sight within an aperture which is cluster dependent and calculated using Equation 3.8. The galaxies are processed according to the flags described in §2.1.4 and the total numbers of galaxies per X-ray cluster retrieved along the line-of-sight with clean photometry are shown in Table 3.1.

We download redshifts and the extinction corrected model magnitudes g, r, i, z for each main sample galaxy. Where the spectroscopic redshifts are unavailable the photometric redshifts are used as the galaxy redshift (Csabai et al., 2003).

We determine cluster membership by making redshift and colour cuts to remove interloping galaxies which would spuriously increase both the summed cluster optical luminosity, and the number of cluster members, using the following criteria:

- We retain only galaxies which fall within 3σ of the error on the cluster redshift, calculated using Equation 3.6.
- The brightest r band LRG (found in §2.2.5) which still resides within each cluster after the above redshift cuts, is promoted to the status of Brightest Cluster Galaxy (hereafter BCG) for further colour cut analysis.
- Any main sample galaxies brighter in the r band than the BCG are removed as suspected interlopers.
- Finally, we remove galaxies which are not within 3σ of the $g - r$ colour of the BCG.

These steps ensure only early type galaxies are retained as cluster members, the brightest of which (the BCG) is drawn from our set of LRGs. The total number of final member galaxies per X-ray catalogue is shown in Table 3.1.

We note in Table 3.1 that the largest X-ray catalogue, the XCS has the fewest total number of

[3] http://casjobs.sdss.org/casjobs/default.aspx

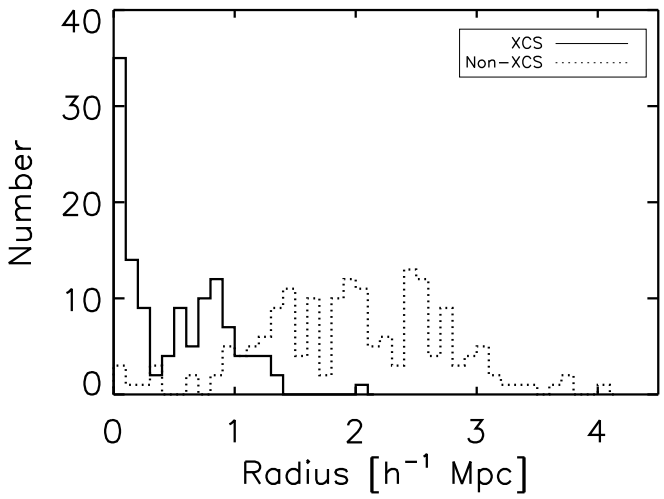

Figure 3.1: A histogram showing the number of X-ray clusters in our sample against radius. The XCS is unique because it is made using XMM data which probes an order of magnitude lower fluxes than the other ROSAT X-ray cluster catalogues. The increase in sensitivity allows smaller mass (radius) systems to be detected.

member galaxies. This can be understood in terms of the flux sensitivity of XMM which is $1-2$ orders of magnitude more sensitive than the ROSAT satellite. At a particular redshift, the lower flux systems are the less massive systems and have smaller radii and apertures (see §3.1.3). In Figure 3.1, we plot the radius histogram for the XCS and the combined histogram for the other X-ray cluster catalogues. The histograms show that the XCS are biased towards detecting smaller systems which have less member galaxies.

In the next section we measure the total optical luminosity of the X-ray selected clusters using their member galaxies and determine the luminosity error.

3.2.3 Optical luminosity

In this section, we describe the measurement of total cluster optical luminosity and the number of galaxy members and describe the assignment of errors to these quantities.

Measuring the cluster optical luminosity

The colour cuts applied to the main sample galaxies ensure that all member galaxies have colours consistent with early-type galaxies at the redshift of the cluster. We apply the extinction and K corrections to the galaxy magnitudes and convert to the AB system following §2.1.2. The absolute magnitudes in the r and i bands of member galaxies are converted to luminosities using

$$L_{jband} = 100^{1/5(M_{sun_j} - M_{gal_j})} L_{\odot} \ , \tag{3.9}$$

where $M_{sun_j}, L_\odot$ are the absolute magnitude of the Sun in "band j" and the total solar luminosity respectively. For the SDSS bands $M_{sun}[u, g, r, i, z] = [6.38, 5.12, 4.64, 4.53, 4.51]$ (Blanton et al., 2003).

The luminosities across the r and i bands for each member galaxy are added, resulting in what we define here to be a "total galaxy luminosity". Finally, the total galaxy luminosity for the cluster members are summed to obtain what we define here to be a "total cluster optical luminosity" L_{opt}^{TOT}. The number of member galaxies in each cluster is stored as N_g. In §3.2.4 we introduce the luminosity cuts we make to allow the comparison of clusters at different redshifts and then assign errors to these measured optical quantities in §3.2.5.

3.2.4 Completeness

The SDSS is an apparent magnitude limited survey, which means that at higher redshifts the intrinsic brightness of the faintest observable objects increases. To compare the optical luminosities of clusters at differing redshifts, a cut in absolute magnitude must be made to allow the equal sampling of the magnitude distributions. We choose to have a complete sample over the redshift range up to the most distance of the MaxBCG clusters ($z = 0.3$). In Figure 3.2 we show the absolute magnitude in the R and I bands of the cluster galaxies which satisfy the member selection criteria of §3.2.3. We show the modification in the distribution for cluster galaxies within the redshift ranges $0.1 < z < 0.15$ and $0.25 < z < 0.3$, and we can see that above -19 the high redshift galaxies fail to probe the same magnitude range as the low redshift galaxies. Removing the fainter galaxies at lower redshifts allows an unbiased comparison of cluster luminosities up to a redshift 0.3.

We note that the number of clusters in our sample is unchanged after applying the absolute magnitude cuts. This means that each cluster has at least 1 galaxy brighter than -19 in the R, I bands, which is to be expected as each cluster contains by definition at least 1 LRG.

3.2.5 Error on optical luminosity

The error on the total optical luminosity for each cluster is calculated by 1000 Gaussian Random Samples (hereafter GRS) of the galaxy and cluster properties. A GRS chooses a new variable X' from a Gaussian distribution centred at X with a standard deviation ΔX, where X is the property of interest and ΔX is its 1σ error.

Each realisation of the GRS modifies the cluster and galaxy redshifts, and the galaxy magnitudes m_i. This is the only reasonable way to measure a luminosity error because simply adding the error derived from the galaxy magnitudes would produce a very small luminosity error and would fail to account for the possibility that an early type galaxy, which should be included in the cluster, has just been missed because of the colour and redshift cuts.

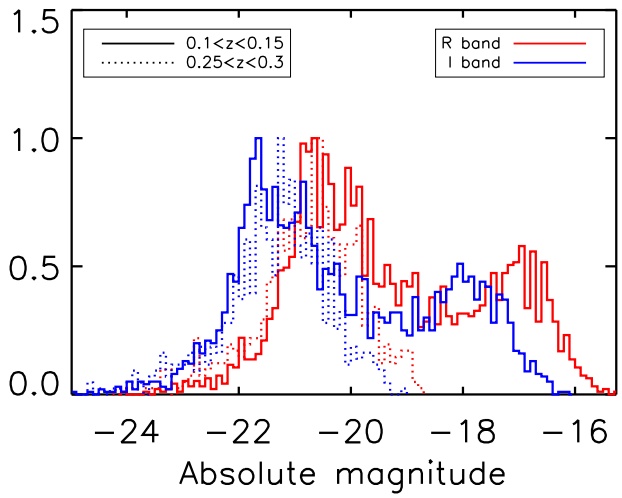

Figure 3.2: Histograms of the absolute magnitude of the member galaxies of all X-ray selected clusters. The red (blue) colours show the R (I) band absolute magnitude. The solid (dotted) lines show the distributions for clusters at redshifts $0.1 < z < 0.15$ ($0.25 < z < 0.3$).

More specifically, we sample from flux error Δf_x and not magnitude error Δm, because flux errors result from the error on the photon number count, which is Gaussian in the large number limit, and magnitude errors are less well behaved with $m + \Delta m$ being much larger than $m - \Delta m$. We convert the magnitude error to a flux error using the propagation of error formulae applied to Pogson's equation ($m = -2.5 \log_{10} f_x - 48.6$) resulting with

$$\Delta f_x = \frac{\ln(10)}{2.5} f_x \Delta m \ . \tag{3.10}$$

We use Pogson's equation instead of the SDSS arcsine conversion (see Equation 2.1) because the difference between the two is smaller than 1%, for objects fainter than the apparent magnitudes g, r, i of $[22.60, 22.29, 21.85]$. Any cluster galaxies which are fainter than these apparent magnitudes are all later removed by the cuts on absolute magnitude (outlined above).

Each realisation assigns a new redshift to the cluster and new redshifts and magnitudes to the galaxies. A new BCG is identified as the brightest R band LRG (using the sampled magnitudes) which still falls within the redshift range of the cluster (using the new sampled cluster and LRG redshifts) and these new cluster redshifts, galaxy redshifts and colours determine cluster membership as in §3.2.3.

If the redshift error on the cluster, or on the LRGs, is large, all of the LRGs can be scattered out of the cluster. These realisation by definition produce no BCG and so no colour cuts can be applied to the BCG. In these cases no optical luminosity or member galaxy number is computed.

The distributions of the total luminosities and number of galaxy members for each cluster are ranked to produced a median and the percentiles are used to calculate the 1σ $[17\% - 83\%]$ and 2σ $[2.5\% - 97.5\%]$ errors. We present a selection of the resulting GRS distributions for three of the R400d clusters indicated by the black lines on Figure 3.3, and three XCS clusters in Figure 3.4. The left panels show the distributions of total cluster optical luminosity, and the right panels show the distributions in number of member galaxies. We present the identifier (RA and DEC, or name) of the selected clusters and the number of GRS realisation which contain a BCG allowing for the measurement of optical properties below the figures.

To understand the shape of these error distributions, we repeat the above analysis but only sampling from one property, while keeping the others fixed. Figure 3.3 and 3.4 also show how the sampled distributions of the number of galaxies and the total optical luminosity change if sampling occurs from just the cluster redshifts (red lines), galaxy redshifts (orange lines) or galaxy colours (blue lines). Each histogram has been scaled to have the same height as the black line. These plots show the origin of the structure in the error distribution and the large error tails. For example, in Figure 3.3(a), the long tail and spread of the fully sampled luminosity distribution (black lines) is similar to the luminosity distribution when we just sample from the galaxy redshifts (yellow line) while keeping the redshift of the cluster and the galaxy colours unchanged. This trend is similar in the N_{gal} distribution Figure 3.3(b) for the same cluster, and we note that the fully sampled distributions have been created from 808 of the 1000 GRS. The 192 cases which were dismissed from the fully sampled error distribution, occurred because all the LRGs (identified in §2.2.7) had been scattered out of the redshift range of the cluster either by the sampling from the redshift of the cluster, or by sampling of the LRG redshifts.

In Figures 3.3(c), 3.3(d) we see that the error distribution made by sampling from all properties, closely matches the error distribution of sampling just from the magnitudes of the galaxies, while keeping the redshifts of the galaxies and cluster unchanged. We note a larger proportion of GRS realisations retain an LRG and are able to produce measurable properties. This cluster has a redshift and error of $0.064, 0.002$, and has a spectroscopic LRG with redshift and error $0.063, 0.0002$, which means that the GRS of the LRG and cluster redshifts will remain almost unchanged. The LRG is therefore likely to fall within the 3σ redshift range of the cluster, allowing it to be promoted to BCG, and the optical properties of the cluster to be derived from it. This accounts for the large number of usable GRS.

In Figure 3.3(e), 3.3(f) we see a multi modal distribution when sampling from all properties (black lines), which is a superposition of sampling from the redshifts (yellow and red lines) and sampling from the galaxy colours (blue lines). The two highest peaks are due to the presence of two photometric LRGs associated with the cluster with redshifts $0.582, 0.663$, and errors $0.024, 0.047$, with the cluster having a redshift and error of $0.587, 0.006$. If the cluster position is sampled, generally the lower redshift LRG is identified as the BCG, but occasionally the cluster redshift moves to scatter out the lower redshift LRG and thus allows the higher redshift LRG to be promoted to

the status of BCG. The low number of usable GRS show that occasionally, sampling from the redshifts, scatter all of the LRGs out of the cluster. If only the magnitudes are sampled, we notice that the cluster is almost equally likely to contain two or three galaxies. The additional inclusion of another galaxy will boost the optical luminosity, as seen in the optical luminosity distribution plot (blue line).

We conclude that failing to sample from any of the three properties; galaxy redshift, galaxy colour, or cluster redshift, would not fully represent the final error distribution on the total cluster optical luminosity and the number of galaxies within the cluster. We additionally note that for some small groups, there are only a few (or one) galaxy members in each cluster, as shown in Figure 3.4. When this occurs, the realisations from the GRS produce a much smaller distributions of luminosities (see Figures 3.4(a), 3.4(b), 3.4(e), 3.4(f)) and therefore produces a smaller associated optical error. The total sampled distributions (black lines) are in these cases well described by the sampled galaxy redshifts (yellow lines) and colours (blue lines), with little effect from sampling from the cluster redshift. The optical luminosity errors for these clusters span ~ 0.04 in log space, compared to more populated clusters (see Figure 3.3(a)) which span a much larger range (~ 1.2). We use these optical luminosity errors as they are, because no alternative presents itself. For the N_{gal} distributions which all have the same value (e.g. 1 galaxy) we use the Poisson error.

We have measured the optical luminosity and the number of galaxies from each X-ray identified cluster. In the next section the optical properties are compared with the X-ray luminosity and X-ray derived mass (see §3.1.2), to quantify how optical cluster properties scale with mass.

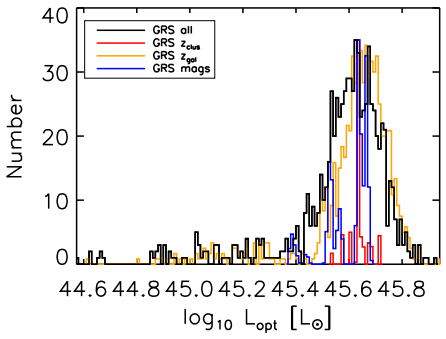

(a) RA,DEC 150.53°, 68.98°

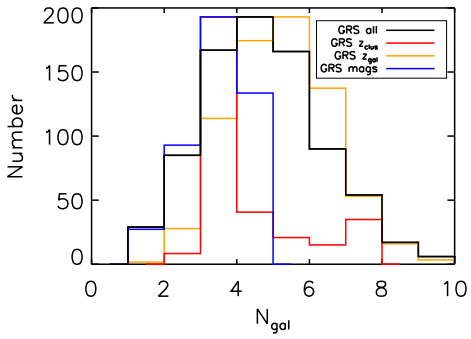

(b) GRS:808

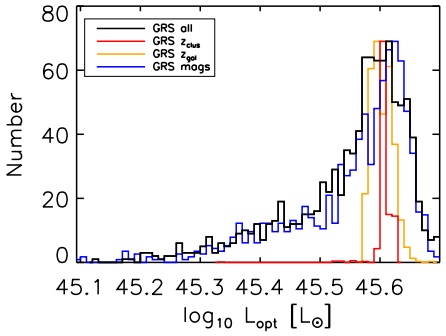

(c) RA,DEC 122.60°, 42.27°

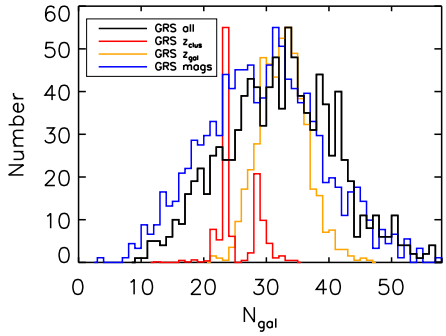

(d) GRS:999

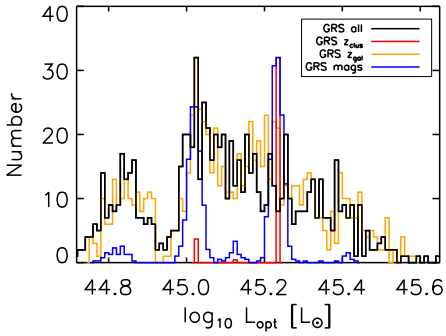

(e) RA,DEC 149.01°, 41.12°

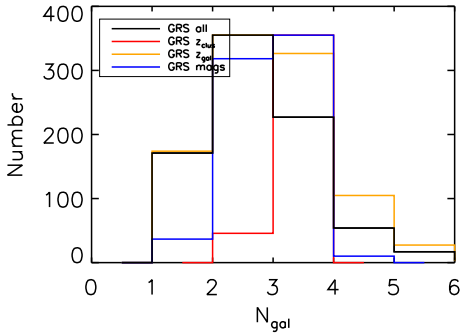

(f) GRS:827

Figure 3.3: Histogram pairs for 3 R400d clusters showing the total cluster luminosity L_{opt} (left plots) and the number of member galaxies N_{gal} (right plots) found after 1000 realisations of Gaussian Random Sampling from the cluster and galaxy redshifts, and the galaxy colours. The left hand plots show the RA, DEC of the cluster and the right hand plots show the number of GRS realisations which retained a BCG, which is needed to obtain optically measured properties.

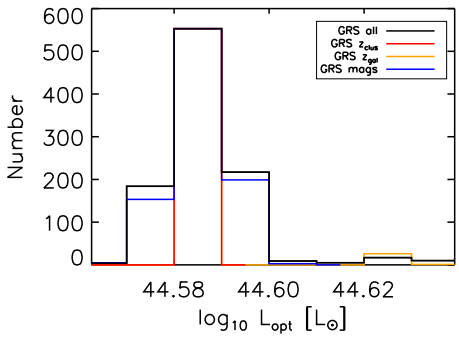

(a) XMMXCS J091938.8+371614.1

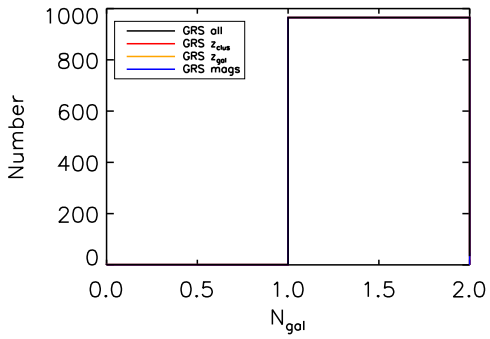

(b) GRS:999

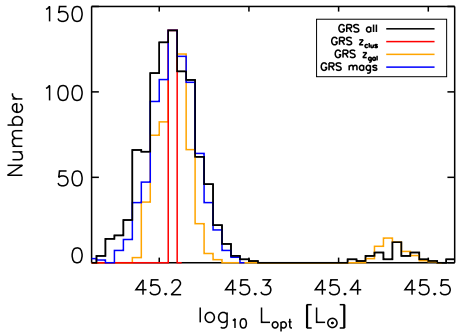

(c) XMMXCS J105909.8+244454.9

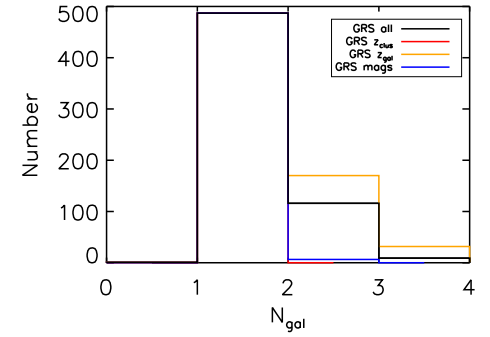

(d) GRS:975

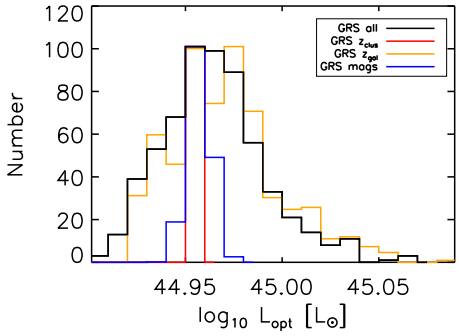

(e) XMMXCS J104422.4+213024.7

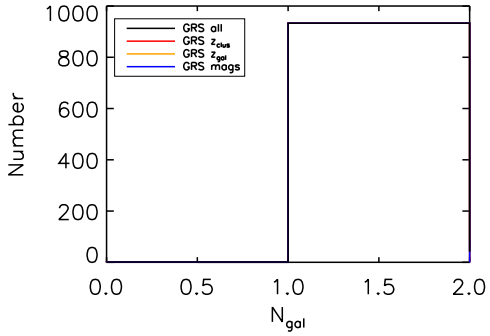

(f) GRS:612

Figure 3.4: Histogram pairs for 3 XCS clusters showing the total cluster luminosity L_{opt} (left plots) and the number of member galaxies N_{gal} (right plots) found after 1000 realisations of Gaussian Random Sampling (GRS) from the cluster and galaxy redshifts, and the galaxy colours. The left hand plots show the cluster name and the right hand plots show the number of GRS realisations which retained a BCG, which is needed to obtain optically measured properties.

3.3 Optical and X-ray scaling relations

This section compares the optical and X-ray properties of clusters and measures how optical properties scale with mass. We introduce optical-X-ray relationships from the literature and we find that optical luminosity traces X-ray luminosity and X-ray derived mass. We show the robustness of the scaling relationships if we under/over estimate the cluster temperatures.

3.3.1 Previous scaling relationships

The relatively low numbers of X-ray selected clusters with photometry has meant that clusters have had to be selected from heterogeneous samples. Miller et al. (1999) compiled 126 X-ray selected clusters from the literature and completed (where unavailable) measurements of optical luminosities. They found a simple scaling between the optical and X-ray luminosity of

$$\log_{10} L_X = \log_{10} L_{opt}^{\alpha}\ h^{-2}\ \mathrm{erg\,s^{-1}}\ , \tag{3.11}$$

where α varies between X-ray samples from 0.90 ± 0.17 to 1.18 ± 0.08.

The ROSAT All Sky X-ray Survey has enabled many optical selected clusters with poor individual X-ray measurements to be stacked to increase the X-ray signal-to-noise. Dai et al. (2006) stacked $4,333$ 2MASS optically selected clusters in richness and redshift bins and measured the X-ray luminosity and temperature for the combined stacked clusters. They find the number of galaxies within an overdensity of 200 times that of the background $\overline{Ng}_{200}$, to be related to the stacked X-ray luminosity $\overline{L}_X$, and mass $\overline{M}_{200}$ by

$$\overline{L}_X = 10^{42.48\pm0.07}\ \overline{N}g_{200}^{1.56\pm0.11}\ h^{-2}\ \mathrm{erg\,s^{-1}}\ , \tag{3.12}$$

$$\overline{M}_{200} = 10^{13.58\pm0.06}\ \overline{N}g_{200}^{0.56\pm0.10}\ h^{-1}\ M_{\odot}\ . \tag{3.13}$$

More recently, Rykoff et al. (2007) has stacked $\sim 17,000$ optical MaxBCG clusters in richness bins and measure the stacked X-ray luminosity $\overline{L}_X$ in the $0.1 - 2.4\,\mathrm{keV}$ ROSAT band to have the following relationship with the stacked number of galaxies $\overline{N}g_{200}$,

$$\overline{L}_X = 10^{43.55\pm0.03}\ \overline{N}g_{200}^{1.82\pm0.05}h^{-2}\ \mathrm{erg\,s^{-1}}\ . \tag{3.14}$$

The normalisations of the two relationships (Equation 3.12 and 3.14) differ at the 8.9σ level (and could highlight large systematic errors). The slope between these relations agree at the 2σ level.

In the next section we compare our measured relationships between L_{opt}, N_g and L_X for *individual* clusters with the above relations which are found by *stacking* clusters. By stacking clusters previous works have increased signal to noise, reducing the statistical errors, but may have large systematic errors, especially if the stacked objects are not similar. By examining the relationship from individual clusters we will have larger statistical errors, but will not be effected by the same systematic effects.

3.3.2 Measured $Ngal$ and luminosity

In this section, we quantify the relationship between the number of galaxies Ng_{200} within an aperture R_{200} (calculated from the X-ray derived mass, see §3.1.3) against the X-ray luminosities and X-ray derived cluster mass M_{200}.

In Figure 3.5 we plot Ng_{200} against the bolometric X-ray luminosity and the total cluster optical luminosity. We have developed a novel line fitting routine, described in §B.1, to fit data with asymmetric error bars, thus providing the lines of best fit between the number of galaxies within the cluster Ng_{200} and the X-ray mass and luminosity, given by

$$L_X = 10^{42.2^{+0.39}_{-0.40}} \, Ng_{200}^{1.57\pm0.65} \, h^{-2} \, \mathrm{erg\,s^{-1}} \, , \quad (3.15)$$

$$M_{200} = 10^{13.25\pm0.42} \, Ng_{200}^{1.00^{+0.85}_{-0.46}} \, h^{-1} \, M_\odot \, . \quad (3.16)$$

Comparing Equation 3.15 with the relation of Rykoff et al. (2007) (Equation 3.14), we find that the values of the normalisations agree at 3.2σ. The errors measured here are larger than those of both Rykoff et al. (2007), and Dai et al. (2006), which we can attribute to the low number (a few hundred) of clusters for which we have individual measurements, compared with the stacking of many thousands of clusters. Although previous works are in disagreement with each other (compare Equations 3.12 and 3.14) which could be due to large systematic uncertainties. If their systematic errors were of the similar size to our statistical errors, the disagreement between us would then be reduced to the 1.7σ level.

We find agreement within the $1\,\sigma$ errors between the slope of the relationships, which is encouraging because of differences in measuring the number of galaxies and X-ray luminosities, between the literature and this work (see §3.2.3, §2.3.1). For example, the MaxBCG impose a cut on the minimum number of galaxies a cluster must have to be included in the catalogue $Ng \geqslant 10$, compared to our criteria $Ng \geqslant 1$. This improves the constraining power of the slope for lower Ng systems, which we find to also appear to follow the expected relationship. Additionally, we have estimated bolometric X-ray luminosities, which we have shown (in Figure 2.32) to be brighter than X-ray luminosities in a band.

Comparing the normalisations of Equation 3.16, with Equation 3.13, shows agreement at the 1σ level. The slopes of the two relationships are different (1.00 and 0.56), but again agree within the 1σ error of Equation 3.16. The MaxBCG catalogue used by Rykoff et al. (2007) places a minimum threshold on the absolute magnitude of galaxies before they can be included as cluster members, which is $M_r < -16$ in the SDSS r band. This is lower than the minimum threshold imposed here $M_r < -19$ (see §3.2.4), and therefore for the same mass systems we expect Rykoff et al. (2007) to find more galaxies, shifting the points on the x-axis right. For a fixed normalisation, this would decrease the expected slope, which would increase agreement between us. Furthermore, assumptions about the data errors and the line fitting routine can change the

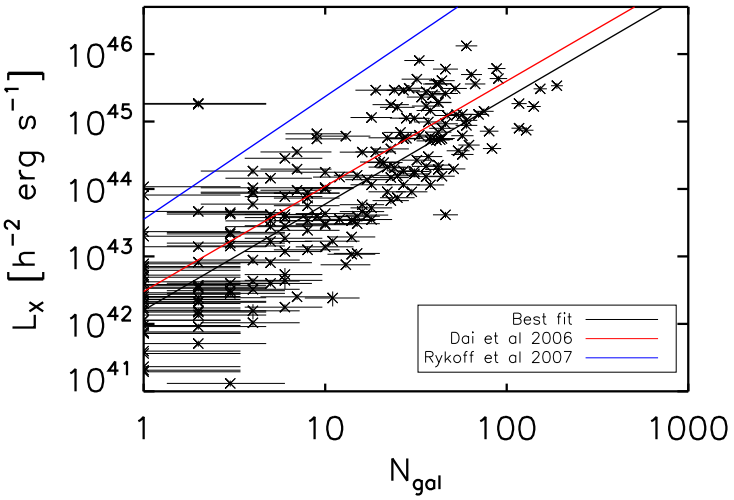

(a) The number of optically identified cluster member galaxies against the bolometric X-ray luminosity.

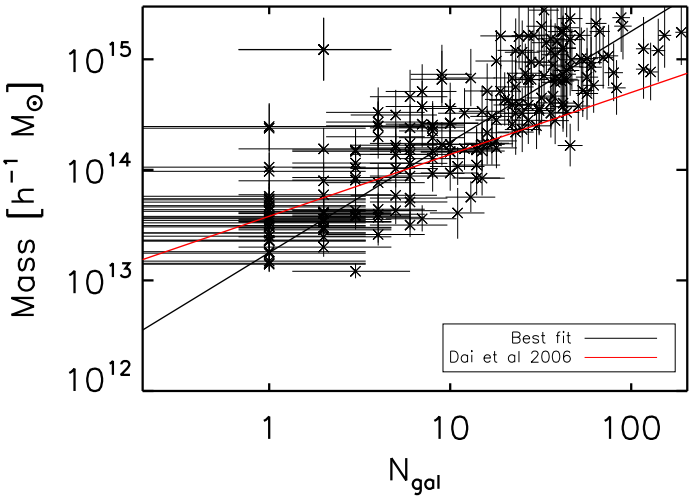

(b) The number of optically identified cluster member galaxies against the X-ray derived cluster mass, see §3.1.2.

Figure 3.5: The relationship between the number of cluster galaxies within R_{200} against the bolometric X-ray luminosity and the cluster mass. Errors on Ng_{200} are from Gaussian Random Sampling from the positions and colours of the cluster and galaxies (see §3.2.5). X-ray luminosity errors are calculate according to §2.3.1 (but are barely visible on these axis scales) and cluster mass errors are from the temperature errors and Equation 3.4.

resulting correlation (e.g. see §B.1). Although, with these restrictions in mind, the agreement is encouraging as these tests have shown that our results are similar to the literature.

3.3.3 Optical luminosity and X-ray properties

In Figure 3.6, we present the correlation between optical and X-ray luminosity, with optical luminosity and X-ray derived cluster mass (see §3.1.2) shown in Figure 3.7.

The lines of best fit found using §B.1 are given by

$$L_X \propto L_{opt}^{2.27\pm0.51}\ h^{-2}\ \mathrm{erg\,s^{-1}}\ , \tag{3.17}$$

$$L_{opt} = 10^{34.84\pm0.18}\ M_{200}^{0.73^{+0.30}_{-0.27}} h^{-2}\ \mathrm{erg\,s^{-1}}\ . \tag{3.18}$$

Comparing Equations 3.17 and 3.11, we find a larger slope, which disagrees with Miller et al. (1999) at the 3σ level. This is not expected to be due to the difference between their use of X-ray luminosities in a band, to the bolometric luminosities used here; this difference has been shown to be small. We must conclude that the differences come from the optical measurements, which are homogeneous using SDSS data here (see §3.2.3), and heterogeneous in Miller et al. (1999). Additionally, we K + evolution correct the magnitudes to $z = 0.3$ (see §2.1.2), whereas Miller et al. (1999), correct to $z = 0$ using older (and inferior) models.

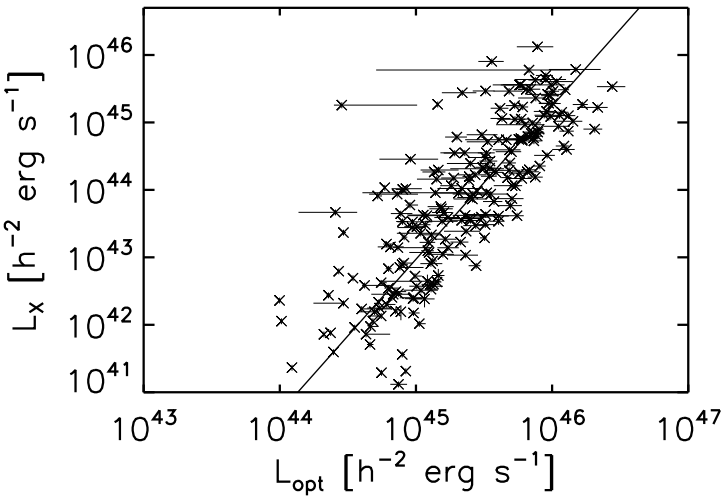

Figure 3.6: The total summed r, i band cluster optical luminosity L_{opt}, against the bolometric X-ray luminosity L_X. The faintest X-ray clusters are found to contain few galaxies. The optical error estimation in these cases produces relatively small errors.

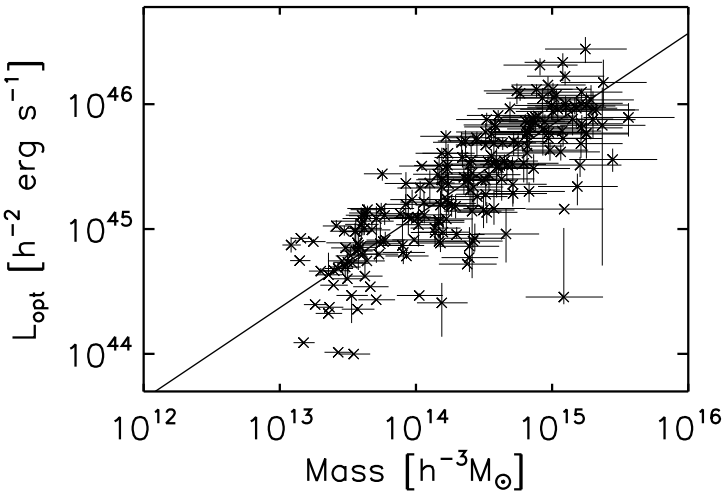

Figure 3.7: The summed r, i band optical luminosity plotted against X-ray derived cluster halo mass using a temperature to mass prescription from Dai et al. (2006), see §3.1.2.

3.3.4 The effect of poorly estimating the cluster temperature

The optical properties of the X-ray identified clusters are derived from the galaxy members which in turn is related to the cluster temperature through the conversion of mass to the velocity dispersion (and redshift error), and then to the cluster radius (see §3.1.3). If the cluster temperature were poorly estimated, then the resulting derived cluster properties and optical measurements will also be misrepresented.

To examine the effect of poorly estimated cluster temperatures on the resulting optical - mass scaling relationships (Equations 3.15 and 3.18), we repeat the entire analysis of this chapter, using a maximum and minimum cluster mass derived from the errors on the cluster temperature (see 2.3.1) and the errors on the mass - temperature relation, Equation 3.4. For a particular cluster, the maximum mass M^{max} is derived from a new cluster temperature, which is the cluster's temperature plus the 1σ temperature error, and converted to mass using Equation 3.4 with the coefficients set to include their upper 1σ errors. A corresponding minimum mass estimate M^{min} is calculated similarly, but with the temperature and conversion coefficients values set to themselves minus their 1σ errors.

Both M^{min} and M^{max} for each cluster are converted to cluster redshift errors and radii (see §3.1.3), and galaxies along the line-of-sight are retrieved, and checks for cluster membership performed (see §3.2.2). Errors on the optical properties are calculated for both the mass estimates as before (see 3.2.5).

We have used the temperature and temperature errors to obtain the minimum and maximum mass

estimates, which means we cannot use the original mass errors on the data points. Instead, we assume a 10% error in the masses (including the original mass estimate) when performing the lines of best fit, to allow direct comparisions between the final relationships. We choose to impose this level of error because the typical temperature error is of this order, and this error weights both high and low mass systems equally when determining the line of best fit. Figure 3.8 shows the X-ray mass-optical luminosity relationship for the minimum, original, and maximum mass measurements.

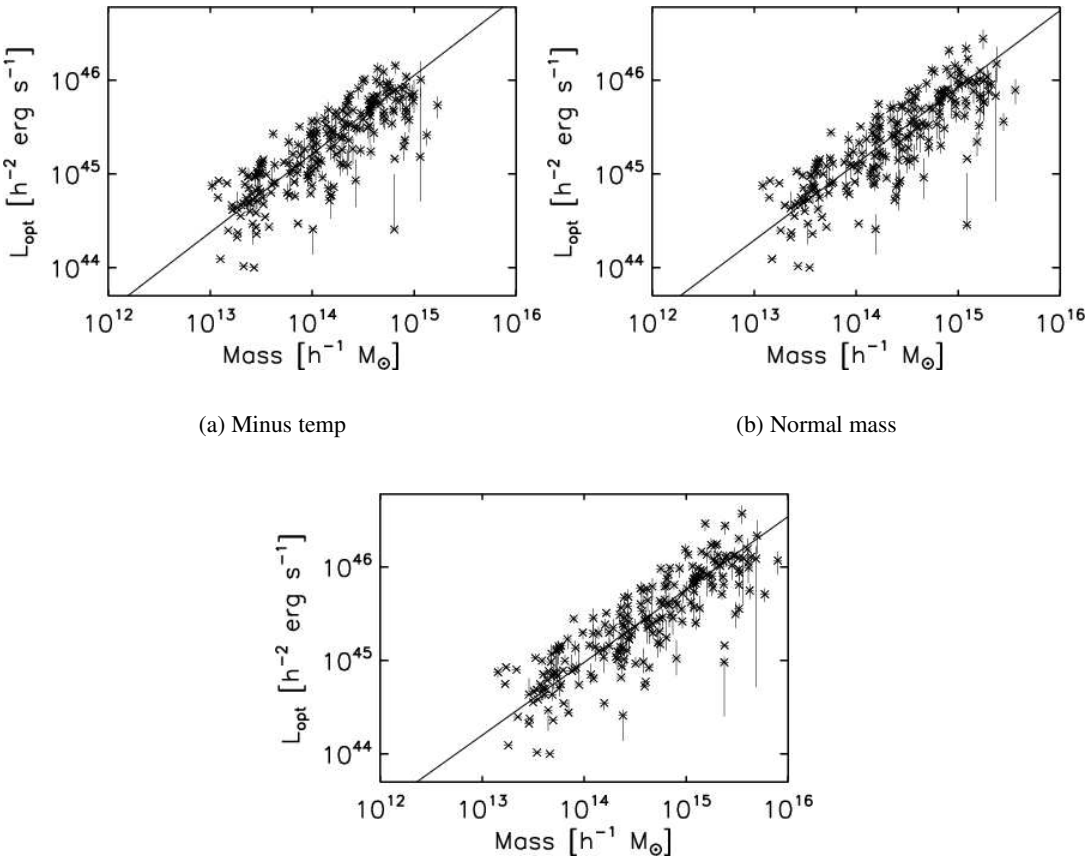

(a) Minus temp

(b) Normal mass

(c) Plus mass

Figure 3.8: The optical luminosity mass scaling relationship under the relaxation of the temperature to mass conversion assumptions. The normalisation changes from $10^{33.5} - 10^{34.1}$ and the slope from $0.84 - 0.73$.

Comparing Figures 3.8(a) and 3.8(b), we see the entire distribution of points is shifted to lower masses, which is to be expected as we have assigned lower masses to the clusters. We also see a change in the distribution for the most optically bright systems, with fewer (from 17 to 6) being above 10^{46} erg s^{-1}. This is caused by a lower radius and aperture returning fewer galaxies along the line-of-sight, and a smaller cluster redshift error, which places more stringent constraints on

cluster membership, and therefore lowers the number of galaxies that form the total optical luminosity. For the less optically luminous systems, there is no change in optical cluster luminosity because these systems only contained single galaxies, which lie within even the most stringent radial, and redshift error cuts. Comparing Figures 3.8(c) and 3.8(b), we see the expected shift in mass towards the more massive clusters, and the number of optically bright clusters above $10^{46}\,\mathrm{erg\,s^{-1}}$, has increased from 17 to 31, which can again be attributed to the increase in the number of cluster members.

We derive the best fitting lines (using §B.1) for the minimum, original and maximum mass assignments, given by

$$L_{opt}^{min} = 10^{33.49\pm0.18}\ M_{200}^{min\ 0.84^{+0.29}_{-0.23}} h^{-2}\ \mathrm{erg\,s^{-1}}\ , \tag{3.19}$$

$$L_{opt} = 10^{33.67\pm0.14}\ M_{200}^{0.81^{+0.26}_{-0.26}} h^{-2}\ \mathrm{erg\,s^{-1}}\ , \tag{3.20}$$

$$L_{opt}^{max} = 10^{34.06\pm0.16}\ M_{200}^{max\ 0.73^{+0.19}_{-0.19}} h^{-2}\ \mathrm{erg\,s^{-1}}\ . \tag{3.21}$$

The change in the slope between cases is well within the 1σ errors of Equation 3.20. The normalisation varies by only 1.6σ between the minimum and maximum cases.

The change in the relationship between optical and X-ray luminosity is shown below,

$$L_{opt}^{min} = 10^{26.86\pm0.14}\ L_{X}^{min\ 0.42^{+0.11}_{-0.11}} h^{-2}\ \mathrm{erg\,s^{-1}}\ , \tag{3.22}$$

$$L_{opt} = 10^{28.92\pm0.19}\ L_{X}^{0.37^{+0.16}_{-0.16}} h^{-2}\ \mathrm{erg\,s^{-1}}\ , \tag{3.23}$$

$$L_{opt}^{max} = 10^{25.09\pm0.14}\ L_{X}^{max\ 0.46^{+0.12}_{-0.12}} h^{-2}\ \mathrm{erg\,s^{-1}}\ . \tag{3.24}$$

We see that the difference between the relationships is again within the 1σ errors on the slope, but by 6.3σ on the normalisation, which is probably due to the scale at which the clusters are located. For example, a small change in the slope (of data points located between 10^{44} to 10^{46}) will result in a large change in the intercept. The relatively close agreement we have found shows how stable this relationship is.

We expect the slopes and normalisations of Equations 3.19 -3.24 to be similar because as we shift the clusters to make them more (less) massive, the number of galaxies which produce the optical luminosity increases (reduces). This has the effect of translating the data points up and to the left (or down and to the left) as we see in Figure 3.8. Although, the good agreement between the scaling relations, and that they lie within the 1σ errors, means the true scaling relations (Equations 3.18, 3.17) can be used with confidence.

We have shown that the optical luminosity scales with X-ray derived mass within the redshift

range $z < 0.3$, and is stable under the incorrect estimation of the cluster temperature. In §3.4, we assign mass estimates to the MaxBCG and C4 clusters of galaxies.

3.4 Optically derived cluster masses

In §3.3.3, we found that optical luminosity scales with mass. We wish to apply these optical based mass estimates to the MaxBCG and C4 clusters, using their catalogue optical luminosity. Before this can be achieved we must quantify the relationship between the catalogues' luminosities and luminosities calculated in §3.2.3. In this section, we match the clusters, compare the luminosities and present the final mass histograms.

3.4.1 Comparing catalogue luminosities

To compare the luminosities between the optical catalogue clusters and the X-ray clusters with measured optical properties (as §3.2.3), we match clusters in position and redshift space under the following conditions: the optical catalogue cluster centroid must fall within $1\,h^{-1}$ Mpc of the X-ray cluster centroid calculated at the redshift of the optical cluster, and be within $\Delta z < 0.01$ of each others redshifts. We choose a $1\,h^{-1}$ Mpc matching radius because we are correlating clusters not galaxies whose centroids have different definitions (see §2.2.5). For the MaxBCG (C4) cluster catalogues there are 67 (57) matched clusters under these conditions.

In Figure 3.9, we plot the the total cluster luminosity from §3.2.3 as L_{opt}, against the summed r, i band luminosity from the BCG and member galaxies for each MaxBCG cluster as L_{MaxBCG}, and against the optical luminosity from the C4 catalogue as L_{C4} in Figure 3.10.

We do not expect there to be exact agreement between the quoted catalogue luminosities and the luminosities measured from §3.2.3 in Figures 3.10 and 3.9, because of the differences in measuring the number of galaxies and the conversion from apparent magnitudes to luminosity.

The relationship between the MaxBCG optical luminosities and ours is shown in Equation 3.25,

$$L_{opt} \quad = \quad 10^{-7.52\pm0.17} L_{MaxBCG}^{1.16\pm0.41}\,, \tag{3.25}$$

and for the C4 catalogue, this relationship has the form of Equation 3.26,

$$L_{opt} \quad = \quad 10^{-14.74\pm0.24} L_{C4}^{1.31\pm0.49}\,. \tag{3.26}$$

Using the above relations and the measured optical luminosity to mass relationship (Equation 3.18), we present the cluster mass histograms in the next section.

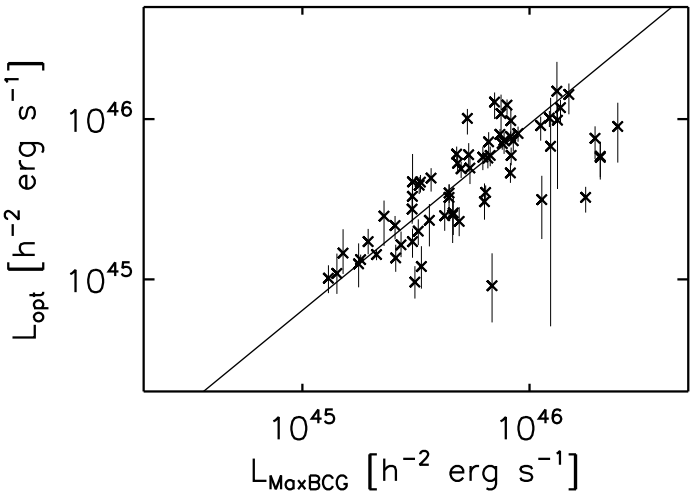

Figure 3.9: The total optical cluster luminosity for the union of the MaxBCG clusters and the X-ray clusters from §3.2.3.

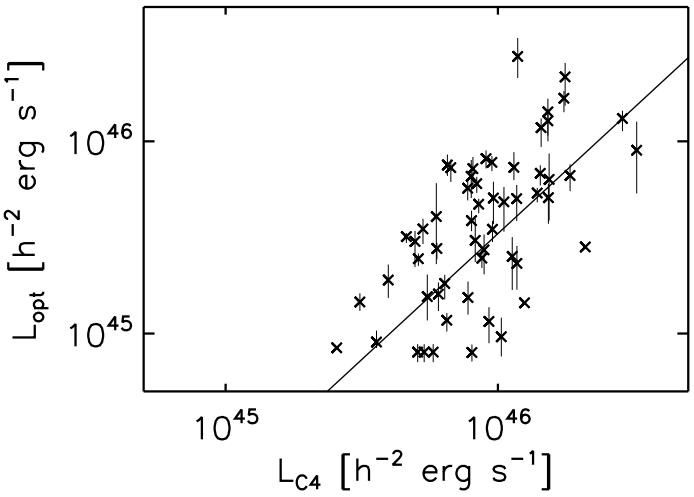

Figure 3.10: The total optical cluster luminosity for the union of the C4 clusters and the X-ray clusters from §3.2.3.

3.4.2 Cluster masses

Using the optical luminosity conversions of §3.4.1, with the measured optical luminosity-mass relation (Equation 3.18) we present the following cluster mass number density histograms for the MaxBCG clusters (solid lines) and the C4 clusters (dotted lines) in Figure 3.11. We assume a flat $\Omega_m = 0.3, h = 0.7$ ΛCDM cosmology for the calculation of volumes.

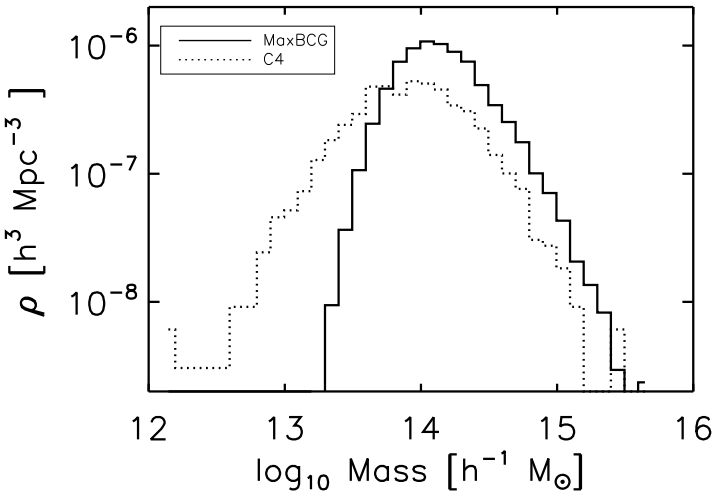

Figure 3.11: The MaxBCG (solid line) and C4 (dotted line) number density histograms for cluster mass, derived from the optical luminosity of the catalogues (see §3.4.1) and the measured optical luminosity mass relationship, Equation 3.18.

The MaxBCG solid line of Figure 3.11 is very encouraging because we expect to have detected clusters with masses above $\sim 5 \times 10^{13} M_\odot$ based on simulations (see Figure 2.10) and the solid line shows that all of the MaxBCG clusters are above $10^{13} M_\odot$. The maximum MaxBCG cluster mass is $2.99 \times 10^{15} M_\odot$ which is in good agreement with what is expected for massive clusters, see §1.2. The dotted line represents the C4 clusters and shows a slightly larger distribution of masses. We do not expect cluster or group masses to fall much below $\sim 10^{12} M_\odot$, and the lowest mass C4 cluster is $1.77 \times 10^{12} M_\odot$, which is reasonable. Both distributions have the same modal values $\sim 10^{13.5-14.2} M_\odot$, which shows self consistency across the different optical cluster catalogues. For both volume limited surveys, we expect to find approximately equal number densities of clusters as a function of mass, but we see a deficit of a factor of ~ 2, for the C4 clusters above $\sim 10^{13.5}$, and surplus of a factor of a few, below $\sim 10^{13.5}$. They are in general agreement which is encouraging, and the difference could be caused by an incorrect C4 optical luminosity - mass conversion, which could tighten the dispersion in mass, and make the less massive systems more massive. This may increase the number density of more massive clusters, while reducing the number density of less massive clusters, increasing the agreement between the two cluster catalogues. This discrepancy leads us to use the C4 mass with caution in our subsequent research. Finally, the lack of outliers outside of the expected typical cluster mass ranges, demonstrate the robustness of using the total optical luminosity as a proxy for cluster mass.

We have demonstrated that the optical luminosity of the MaxBCG and C4 clusters can be used as a proxy for mass. We use these mass estimates to reconstruct the mass function and constrain gravity in §4. In the next section we compare the mass estimates obtained above with those for individual clusters and groups of clusters from weak gravitation lensing analysis.

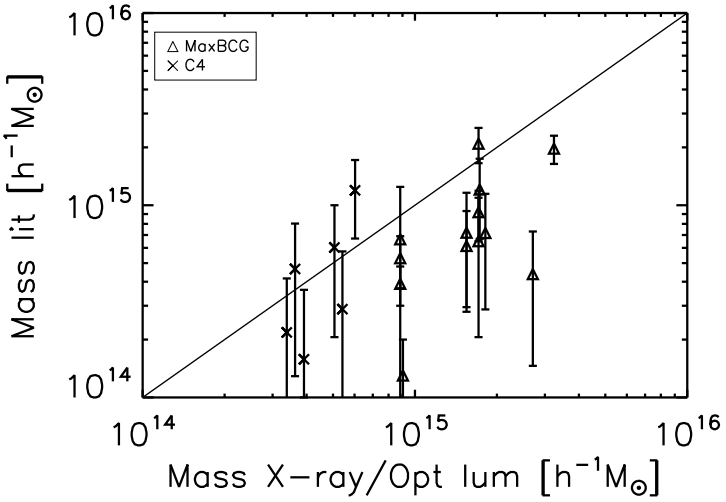

Figure 3.12: Comparing weak lensing cluster masses from the literature with the masses assigned to the MaxBCG (triangles) and C4 (crosses) clusters in §3.4.2. Overplotted is the line of equality.

3.4.3 Literature cluster masses

We compare the cluster masses determined above with those from the literature using two methods. First we preform a comparison with individual clusters which have a weak lensing mass measured in the literature, and then we perform a comparison with a statistical weak lensing mass approach using the MaxBCG clusters.

Individual clusters

We use the list of clusters with individual weak gravitational lensing compiled by Dahle (2007) and obtain cluster centroid coordinates from the NASA/IPAC Extragalactic Database[4]. We follow the advice of Dahle (2007) and use only clusters with recent (> 2004) analysis (which are performed in concordance cosmology) due to the difficulty of comparing cluster mass estimates calculated in different cosmological models. We note that the direct comparisons of weak lensing cluster masses estimates is fraught with complications due to the heterogeneous modelling of the cluster mass profile and the background galaxy redshift distribution and the width, depth and telescope used to obtain the photometry.

In Figure 3.12 we show those MaxBCG and C4 clusters which have masses measured in the literature against the masses determined in this chapter, and list the clusters and their references in Table 3.2.

Concentrating on the C4 clusters (crosses) in Figure 3.12, we see that the masses estimates agree

[4]http://nedwww.ipac.caltech.edu/

Catalogue & ID	Name	RA	DEC	Reference
MaxBCG 2263	Abell 1682	196.70	46.549	Dahle
MaxBCG 12612	Abell 1689	197.87	−1.338	Bardeau et al. (2007)
MaxBCG 3882	Abell 1914	216.51	37.825	Dahle
MaxBCG 3882	Abell 1914	216.51	37.825	**?**
MaxBCG 4809	Abell 2034	227.55	33.527	**?**
MaxBCG 2241	Abell 2219	250.08	46.687	Dahle
MaxBCG 2241	Abell 2219	250.08	46.687	Hoekstra (2007)
MaxBCG 2241	Abell 2219	250.08	46.687	Bardeau et al. (2007)
MaxBCG 1406	Abell 773	139.49	51.706	Dahle
MaxBCG 3628	Abell 963	154.29	39.016	Dahle
MaxBCG 3628	Abell 963	154.29	39.016	Hoekstra (2007)
MaxBCG 3628	Abell 963	154.29	39.016	Bardeau et al. (2007)
MaxBCG 8558	MS1231+15	188.46	15.426	Hoekstra (2007)
C4 1	Abell 2142	239.56	27.224	**?**
C4 107	Abell 1767	204.03	59.206	Kubo et al. (2009)
C4 29	Abell 2048	228.80	4.3862	Kubo et al. (2009)
C4 30	Abell 2199	247.15	39.551	Kubo et al. (2009)
C4 45	Abell 2244	255.67	34.060	Kubo et al. (2009)
C4 70	C41003	184.42	3.6558	Kubo et al. (2009)
C4 147	RXJ1720.1+2638	260.03	26.634	Dahle

Table 3.2: A compilation of MaxBCG and C4 clusters with weak lensing mass measurements from the literature. We present the cluster catalogue and ID, the cluster name and coordinates and reference the paper where the mass measurement is documented.

within the errors. The MaxBCG clusters (triangles) are biased low in $5/8$ cases, which could be due to weak lensing modelling assumptions, as seen by the spread of estimates for clusters Abell 1914, Abell 2219 and Abell 963 shown by the triangles with identical X-ray masses in Figure 3.12.

Stacking clusters

We compare the MaxBCG mass estimates obtained above (c.f. Equation 3.25 and 3.18) with those of Rozo et al. (2009), who group clusters by the number of member galaxies N_{200}, and examine the stacked weak lensing shear of background galaxies to obtain cluster mass M_{200} given by

$$\langle \ln N_{200} | M \rangle = A + \alpha(\ln M - \ln M_{pivot}). \tag{3.27}$$

with best fit values $A, \alpha, M_{pivot} = [2.34 \pm 0.10, 0.757 \pm 0.066, 1.09 \times 10^{14}]$. We rearrange Equation 3.27 to obtain $M = M(N_{200})$ and compare with the X-ray mass estimates in Figure 3.13.

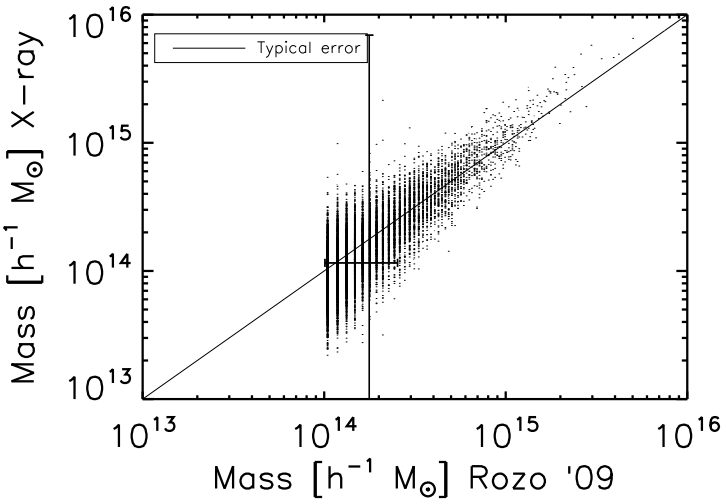

Figure 3.13: Comparing the mass estimates of the MaxBCG clusters using the X-ray derived mass and a statistical weak lensing mass from Rozo et al. (2009). The line of equality and typical error are overplotted.

The discreet steps along the Rozo mass axis are caused by the mass being a function of the number of member galaxies which are integer. The typical error in each direction is shown on the figure. We see that the weak lensing mass estimate derived from the X-ray is in good agreement at intermediate mass, but is biased high for the most massive systems compared to Rozo et al. (2009). The X-ray errors are an order of magnitude larger than those measured by Rozo et al. (2009) which are partially due to the conversions between optical luminosities and optical luminosity and mass. Additionally Rozo has stacked many clusters (e.g. 5167 for the N_{200} bin $11 - 14$) to obtain these mass errors, whereas we have applied a mass and error to each cluster.

3.5 Summary

In this chapter we have assembled a sample of 296 X-ray clusters with optical counter parts. This is the largest comparison of X-ray and optical properties for individual clusters to date. We make some assumptions while converting X-ray luminosity and X-ray temperature to cluster mass. We show that the total cluster optical luminosity scales with cluster mass and quantify the relationship. We explore the temperature-mass conversion and show the final mass - optical luminosity relation does not change dramatically.

We find an empirical relationship between optical luminosity L_{opt}, and X-ray derived cluster mass M_{200}, to have the form,

$$L_{opt} \quad = \quad 10^{34.84\pm0.18}\ M_{200}^{0.73^{+0.30}_{-0.27}}\ . \tag{3.28}$$

We note that the errors on the mass exponent are $\sim 40\%$ which are broad, but are not used in future analysis, because we employ a more general error based on the number clusters at each redshift (see §4.4.2). We then use this optical luminosity - mass scaling relation to assign masses to the massive MaxBCG and C4 optical cluster catalogues. The optical cluster catalogues contain orders of magnitude more clusters than X-ray catalogues, and have well understood completeness and purity and are well suited to be used as probes of cosmology.

To perform cosmology with clusters of galaxies, one needs large datasets with well understood mass estimates. We have built a dataset of $\sim 13,000$ MaxBCG clusters, and $\sim 2,000$ C4 clusters, spanning a redshift range $0.05 < z < 0.3$ to which we have applied mass estimates allowing the reconstruction of the mass function to probe cosmology (see §4). In §5 we recalculate the masses of the optical cluster catalogues using weak lensing, a technique which is independent of the X-ray analysis, and we compare the mass estimates of both approaches in §4.

Chapter 4

Cosmological constraints

The abundances of galaxy clusters as a function of mass and redshift is called the "Cluster Mass Function" (hereafter CMF) and varies with cosmology through changes of the linear growth of structure and the density contrast required for a structure to collapse gravitationally.

We introduce the CMF in §4.1 and review literature which compares the theoretical CMF (assuming General Relativity) with that as measured by simulations. We continue the literature review with a more general theoretical CMF and simulations performed to measure its parameters. We then introduce a modified theory of gravity model and describe the modifications to the CMF within this class of models. In §4.2 we formally derive the mass function and demonstrate its dependence on cosmological parameters. We then briefly compare the mass estimates from §3 and §5 and show them to be consistent, and convert the MaxBCG and C4 cluster mass measurements from §3 into CMFs. We proceed in §4.4 by constraining the normalisation of the power spectrum σ_8, the matter content of the Universe Ω_m, the equation of state of dark energy w_0, and a branch of modified gravity models which interpolate between ΛCDM and the 5d "Dvali-Gabadadze-Porrati" (hereafter DGP) brane world model.

We find the measured CMF is most sensitive to σ_8 and Ω_m and obtain independent, competitive constraints on these parameters. However we find less constraining power on the other parameters examined (e.g the equation of state of dark energy), unless we assume strong priors.

4.1 Introduction

Clusters are formed when the large and small scale density fluctuations δ reach some critical threshold density δ_C and then collapse to form a cluster. The threshold density can be thought of as a barrier, which if the peaks of the density field pass, gravitational collapse will occur and a cluster halo will form. The combination of the large and small scale fluctuations are represented pictorially in Figure 4.1, with the critical collapse threshold shown by a dotted line.

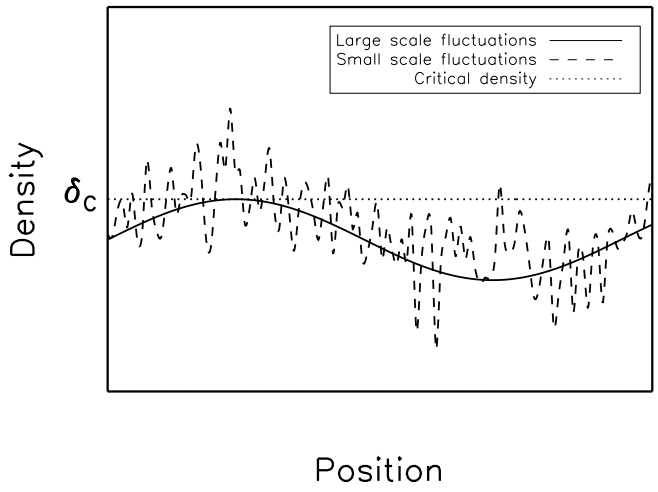

Figure 4.1: A pictorial representation of the large (solid line) and small (dashed line) density fluctuations combining to cross the critical threshold barrier (dotted line). Once the density fluctuations cross the barrier they would then collapse to form dark matter halos. An excess of collapsing structures will occur around a large scale overdensity. Occasionally a small scale overdensity is large enough to cross the barrier even if located in a large scale underdensity.

The small scale density fluctuations, combined with large scale density fluctuations, produce clustering of density peaks crossing the barrier as seen in Figure 4.1, which then collapse to form dark matter halos. As these density fields evolve with time, increasing numbers of density peaks will cross the barrier and collapse, producing a cluster abundance function that changes with redshift. The background evolution of the density field, and the evolution of the threshold collapse density, determines which peaks collapse. For any particular peak, or point in the density field, the path towards the barrier can be viewed as a random walk through the density field, which has a set of possible paths that will allow the point to cross the barrier and collapse to form a halo.

Assuming the initial density fields are Gaussian, the theoretical properties of the CMF were first described by Press and Schechter (1974) who assumed that objects collapsed spherically, to produce spherical dark matter halos. To test the accuracy of the theoretical CMF, N-body simulations are performed and the CMF measured (e.g. Lacey and Cole, 1994).

Simulating the CMF

In simulations, cluster halos are identified as overdensities of dark matter particles, with their masses given by the combined dark matter particle mass. There are many algorithms to locate clusters in simulations; two common varieties are the Friends of Friends (Davis et al., 1985, hereafter FoF) and the Spherical Overdensity (Lacey and Cole, 1994, hereafter SO) algorithms. The FoF routine builds groups of dark matter particles by identifying all pairs separated within a distance b of another group member. The resulting web of pairs describe an isodensity contour, with

a density proportional to the separation scale b. Cluster halos are identified as groups of dark matter particles within an isodensity contour above a threshold density. Alternatively, the SO routine begins at the site of largest particle overdensity and places a sphere around the particles and calculates the average particle density within the sphere. The radius is increased until the average particle density corresponds to a critical density, at which point the sphere corresponds to the identification of a cluster halo. The process is then repeated at the next highest region of overdensity. Once all the cluster halos have been found, and their masses measured, a CMF is obtained.

Lacey and Cole (1994) tested the CMF of Press and Schechter (1974) using an early N-Body simulation with 128^3 dark matter particles, in a Einstein-de Sitter cosmology using the SO cluster finder. We show their simulated CMFs f in Figure 4.2 (solid lines) plotted as a function of mass M with the Press and Schechter (1974) prediction overplotted (dashed line).

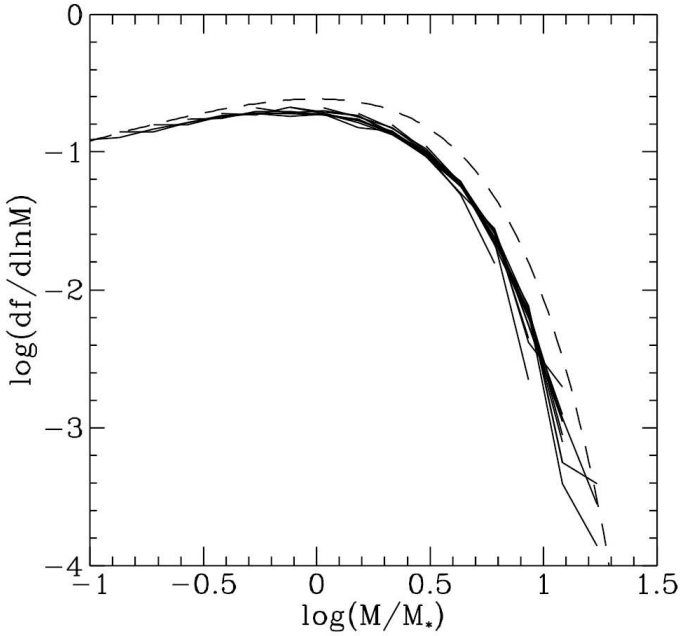

Figure 4.2: The solid lines represent the measured CMF f as a function of mass M for different halo formation times in an early simulation, assuming an Einstein-de Sitter cosmology (Lacey and Cole, 1994). M_* is a characteristic scale given by $\sigma_M(M_*, z) = \delta_C$ whose value here is $\sim 8 \times 10^{13} M_\odot$. The dashed line shows the theoretical spherical collapse prediction of Press and Schechter (1974). Credit: Lacey and Cole (1994).

Figure 4.2 shows the over prediction of cluster halos (dashed line) by a few factors for masses above $\sim 10^{13} M_\odot$ using the spherical collapse model of Press and Schechter (1974).

The generalised CMF

Sheth et al. (2001) extended the spherical collapse formalism to allow structures to collapse along one or two axes before the third. This tri-axial collapse produces ellipsoidal shaped dark matter halos and modifies the collapse density, which is equivalent to a scale dependent barrier. The ellipsoidal collapse formalism has been shown to be a better fit to simulated random walks (Sheth et al., 2001; Sheth and Tormen, 2002), and in Figure 4.3 we reproduce the results of Sheth and Tormen (2002), which shows the improved agreement for the ellipsoidal collapse (solid lines) and the corresponding prediction for the spherical collapse model (dotted lines).

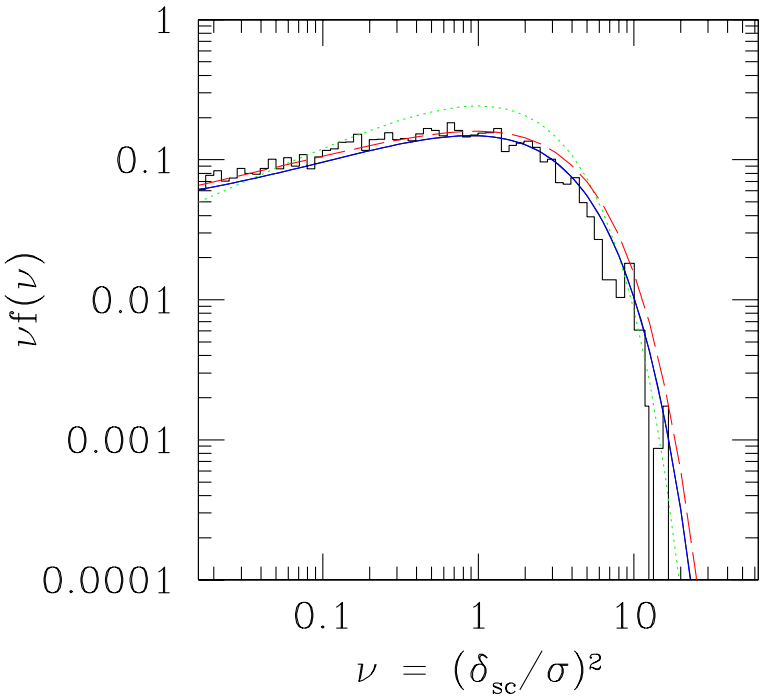

Figure 4.3: The mass function $f(\nu)$ (multiplied by ν) as a function of ν for simulated random walks. The dotted line is the prediction for spherical collapse, the solid line is the analytic approximation to the ellipsoidal collapse (see Equation 4.19), and the dashed line is the fit to the data. Credit: Sheth and Tormen (2002).

Additionally, Jenkins et al. (2001) performed N-body simulations with 10^9 particles in a volume of 27 h^{-3} Gpc^3 assuming an Einstein-de Sitter cosmology and found the ellipsoidal collapse CMF to be a better approximation to the simulated CMF than the spherical collapse model. Figure 4.4 reproduces their results and shows the simulated data (short dashed line), the spherical

collapse CMF (long dashed line), the ellipsoidal collapse CMF (dotted line), and a fit to the simulation (solid line).

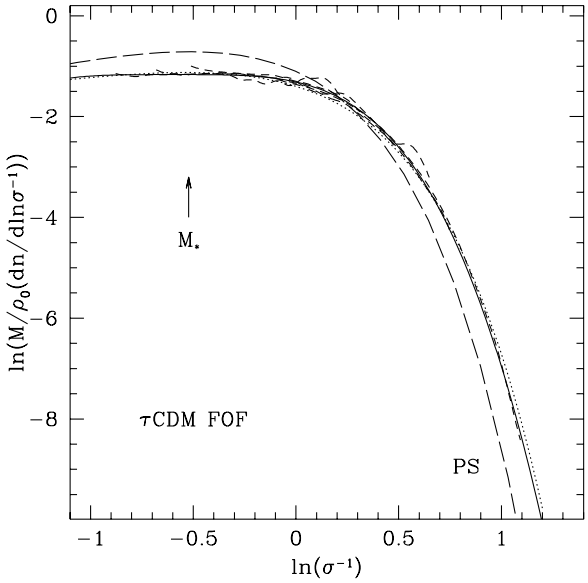

Figure 4.4: A replication of Figure 3 of Jenkins et al. (2001), showing the measured CMF using a simulation with 10^9 particles (short dashes lines), assuming an Einstein-de Sitter cosmology (τCDM). Over plotted is the CMF prediction for spherical collapse (long dashes), ellipsoidal collapse (dotted line) and a fit to the simulation (solid line). Credit: Jenkins et al. (2001).

Tinker et al. (2008) compared the CMF from a suite of 18 N-body simulations (ranging in size from 512^3 to 1024^3 particles in a box of side 100 to $800\,h^{-1}$ Mpc) to the CMF of Sheth and Tormen (2002) and the simulation fit of Jenkins et al. (2001). Figure 4.5 reproduces their results (with their f given by Equation 4.19 and σ is the smoothed variance of the density field, see Equation 4.16) and shows the simulated data points (coloured points) and the CMF from Sheth and Tormen (2002) (red dashed line) to be within 5% for the most massive systems $\log(1/\sigma) < -0.2$ and within 10% until the low mass systems $\log(1/\sigma) > 0.35$.

The previous theoretical analysis and simulations have been performed with the framework of General Relativity. In the next section we introduce a modified theory of gravity which reproduces Einstein's gravity on small scales but provides a mechanism for a Λ free accelerated expansion of the Universe on large scales. We then describe work by Schaefer and Koyama (2008) to compute the CMF within this particular modified gravity theory.

4.1.1 The cluster mass function within modified gravity

There are a very large number of possible modifications to General Relativity, of which one is the "Dvali-Gabadadze-Porrati" model (Dvali et al., 2000, hereafter DGP) which is well studied

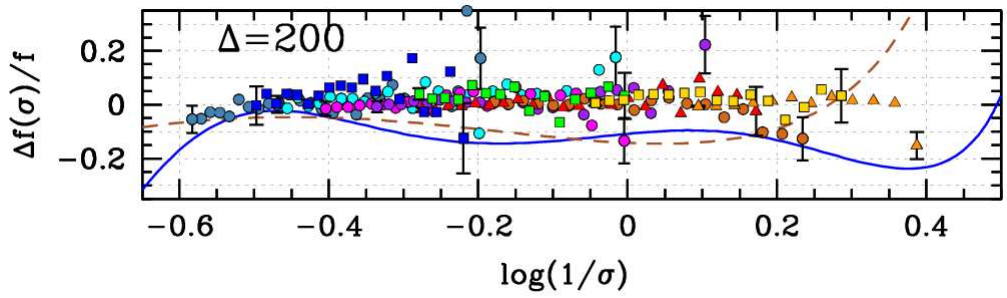

Figure 4.5: A replication of Figure 7 of Tinker et al. (2008) showing the CMF as a function of scale from a suite of simulations (coloured points). The red dashed line is the CMF of Sheth and Tormen (2002) and the blue solid line that of Jenkins et al. (2001). Credit: Tinker et al. (2008).

and physically motivated (see below, and e.g. Koyama, 2008). We only address this particular modified gravity theory because it is the only example for which the CMF has been calculated (Schaefer and Koyama, 2008).

An introduction to DGP

In this section we give a brief introduction to the 5 dimensional DGP gravity model (Dvali et al., 2000), but a detailed analysis is outside the scope of this thesis, see e.g. Lue et al. (2004b); Koyama (2008).

The DGP model was proposed to explain the accelerated expansion of the observable Universe without the need for dark energy, by introducing new physics. This is motivated because the value of Λ is $\sim 10^{120}$ orders of magnitude smaller than expected from particle physics. DGP is inspired by string theory, and suggests the Universe is a 4-d "brane", embedded in a higher 5-d "bulk". All standard model physics is constrained to the brane apart from gravity which "leaks" off into the bulk at large distances, thereby reducing the force of gravity and allowing the expansion of the Universe on the 4-d brane to accelerate.

This additional new physics manifests as a modified Hubble function, in terms of a cross over scale r_c, which marks the transition between the force of gravity being described by a 4-d theory and being described by a 5-d theory, and has the form

$$\frac{H(z)}{r_c} = H(z)^2 - \frac{8\pi G_4}{3}\rho_m \,, \tag{4.1}$$

with matter density ρ_m, and the value of the gravitational constant on the brane G_4. The Hubble function can be rewritten in terms of a quantity α which interpolates between pure DGP (with $\alpha = 1$) and ΛCDM (with $\alpha = 0$) and given by (Dvali and Turner, 2003)

$$H'^2(a) = \left(1 - \Omega_m\right) H'^{\alpha}(z) + \frac{\Omega_m}{a^3} \,, \tag{4.2}$$

where $H'(z) = H(z)/H_0$. Equation 4.2 can be re-written as Equation 4.1 when $\alpha = 1$, and $r_c = 1.0/H_0(1-\Omega_m)$. This parameterisation of the Hubble function is not unique but introduced because while neither pure DGP or ΛCDM may be the correct description of gravity, the interpolation allows us to qualitatively describe any deviation from these models.

DGP has been tested experimentally with supernovae data (of Riess et al., 2004; Astier et al., 2006) by Song et al. (2007) who rule out a simple flat DGP model at $\sim 3\sigma$, but are less constraining of more complicated curved DGP models. Subsequently, Thomas et al. (2008) combine weak lensing measurements from the Canada France Hawaii Telescope Legacy Survey (Fu et al., 2008) with the Baryon Acoustic Oscillations (Percival et al., 2007) and supernovae data (Astier et al., 2006) to rule out $\alpha = 1$ at the 2σ level.

The mass function within DGP

The theoretical predictions for spherical collapse in Einstein gravity have been extended to a suite of modified gravity models by Schaefer and Koyama (2008) who solved the spherical collapse equations for modifications to General Relativity. They use the α parameterisation (see Equation 4.2) which interpolates between ΛCDM ($\alpha = 0$) and DGP ($\alpha = 1$), and they find a modification of a factor of a few between the different models for massive clusters. Figure 4.6 is a replication of their results, and shows the ratio $Q(M, z)$ of the mass function in modified gravity to ΛCDM, as a function of mass, at redshifts $z = 0.3$ (thin lines), and $z = 0.7$ (thick lines), in the spherical collapse regime. The solid lines in both cases correspond to DGP, with decreasing $\Delta\alpha = 0.2$ intervals shown by the decreasing amplitude dotted lines.

Figure 4.6 shows that if the masses of clusters can be measured accurately, and a large, complete cluster dataset identified, then clusters of galaxies could distinguish between ΛCDM and DGP within this spherical collapse framework.

The DGP model is young in comparison to General Relativity and is only now beginning to be explored to the same level of detail as ΛCDM. The theoretical ellipsoidal collapse formalism has not been derived in DGP or interpolated models and simulations are only now becoming available (Khoury and Wyman, 2009; Schmidt, 2009) and have yet to be compared with the CMF of Schaefer and Koyama (2008). In light of these deficiencies, we restrict the subsequent analysis to testing the CMF in the spherical collapse regime, when interpolating between ΛCDM and DGP.

Summary

This section has shown that the ellipsoidal collapse CMF of Sheth and Tormen (2002) is a good (within 5%) fit to the CMF of simulations performed within the framework of standard Einstein gravity. We have also shown how this has been developed to include spherical collapse models within DGP but which have yet to be compared to simulations.

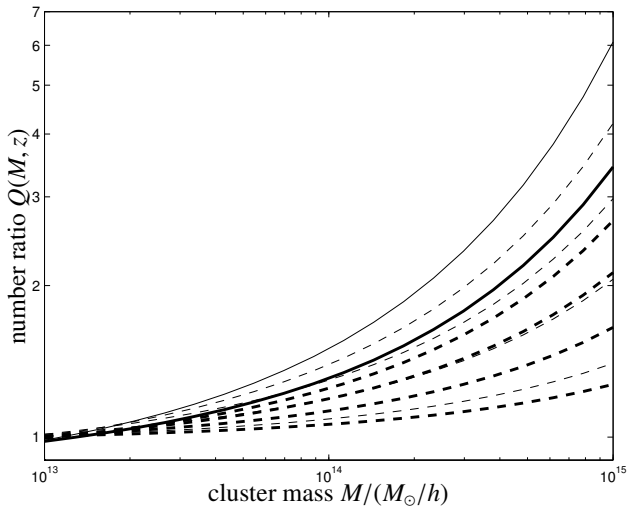

Figure 4.6: A replication of Figure 6 of Schaefer and Koyama (2008) showing the ratio $Q(M, z)$ of the mass function in modified gravity to ΛCDM as a function of mass, at redshifts $z = 0.3$ (thin lines) and $z = 0.7$ (thick lines) in the spherical collapse regime. The solid lines in both cases correspond to DGP, with decreasing $\Delta\alpha = 0.2$ intervals towards ΛCDM shown by the decreasing amplitude dotted lines. Credit: Schaefer and Koyama (2008).

In the next section we introduce and derive the theoretical CMF and discuss the components which are cosmology dependent. We then present the sensitivity of the mass function to cosmological parameters and continue by comparing the mass functions measured from §3 and §5, and use them to constrain cosmological models.

4.2 The mass function

In this section we provide a brief theoretical description of the derivation of the CMF, and discuss the components of the mass function which are cosmology dependent. We refer to Press and Schechter (1974); Bond et al. (1991); Sheth et al. (2001); Bond and Myers (1996), and Schaefer and Koyama (2008) for details. We then continue by describing the modification to the mass function in the spherical and ellipsoidal collapse regimes and show how the mass function predictions change with cosmological parameters.

4.2.1 Derivation of the mass function

We begin the derivation of the mass function by assuming a Gaussian density field (with variance after smoothing on some scale M given by σ_M) whose distribution P for a density fluctuation δ_M is given by

$$P(\delta_M)\,\mathrm{d}\delta_M = \frac{1}{\sqrt{2\pi\sigma_M^2}} \exp\left(-\frac{\delta_M}{2\sigma_M}\right)\mathrm{d}\delta_M \ , \tag{4.3}$$

and the probability that at some point the density field is greater than the critical density δ_C is given by

$$P_{>\delta_C}(M) = \int_{\delta_C}^{\infty} P(\delta_M)\,\mathrm{d}\delta_M \;= 1 - \int_0^{\delta_C} P(\delta_M)\,\mathrm{d}\delta_M, \tag{4.4}$$

$$= (1/2)\left(1 - \mathrm{erf}\big(\nu(M,z)/\sqrt{2}\big)\right)\;, \tag{4.5}$$

where the final line has been written in terms of the error function $\mathrm{erf}(x)$, which has the property

$$\frac{\mathrm{d}}{\mathrm{d}\,x}\mathrm{erf}(x) = \frac{2}{\sqrt{\pi}}\,\exp\big(-x^2\big)\;, \tag{4.6}$$

and ν is given by

$$\nu\big(M,z\big) = \frac{\delta_c(z)}{D_+(z)\sigma_M}\;, \tag{4.7}$$

where $\delta_c(z)$ is the collapse overdensity as a function of redshift, and D_+ the growth function are explained in more detail below.

The mass function $n(M)$ is then defined as the comoving number density of halos of mass M

$$n\big(M\big) \;=\; \frac{\bar{\rho}}{M}\left|\frac{\mathrm{d}}{\mathrm{d}M}P_{>\delta_C}(M)\right|\;, \tag{4.8}$$

$$=\; \sqrt{\frac{2}{\pi}}\;\frac{\bar{\rho}}{M^2}\left|\frac{\mathrm{d}}{\mathrm{d}\ln M}\ln\sigma_M\right|\;\nu\;\exp -\nu^2/2\;. \tag{4.9}$$

The dependence of the mass function on cosmology is through the parameter $\nu\big(M,z\big)$, and in the following sections we describe the components of Equation 4.7 in more detail.

4.2.2 The critical collapse density

The value of the critical collapse density δ_C is redshift independent with a value of 1.686 in an Einstein-de Sitter model (Press and Schechter, 1974), but has a more complicated redshift dependence in ΛCDM and modified gravity models, and we use the fitting function provided by Schaefer and Koyama (2008) for the spherical collapse regime (i.e. $\delta_C \to \delta_{sc}$),

$$\delta_{sc}(z) = a - b\;exp\big(-cz\big)\;, \tag{4.10}$$

where a, b, c are constants with values given in Table 4.1 (which is a replication of Table 1 of Schaefer and Koyama, 2008) and are dependent on cosmological models through changing α.

The corresponding ellipsoidal collapse $\delta_{ec}(z)$ is related to the spherical collapse overdensity

	a	b	c
$\alpha = 0$	1.6823	0.0129	1.5648
$\alpha = 0.2$	1.6820	0.0314	1.0912
$\alpha = 0.4$	1.6806	0.0582	0.9994
$\alpha = 0.6$	1.6774	0.0942	0.9369
$\alpha = 0.8$	1.6710	0.1397	0.8722
$\alpha = 1$	1.6585	0.1945	0.8020

Table 4.1: The parameters of the critical collapse density Equation 4.10 in the spherical collapse formalism for models which interpolate between ΛCDM ($\alpha = 0$) and DGP ($\alpha = 1$). Credit: Schaefer and Koyama (2008).

$\delta_{sc}(z)$ by Sheth et al. (2001),

$$\delta_{ec}(\sigma, z) \quad = \quad \delta_{sc}(z) \left(1 + \beta \left[\frac{\sigma^2}{\delta_{sc}^2(z)}\right]^{\gamma}\right) \ , \tag{4.11}$$

where the constants β, γ have values $0.47, 0.615$, and have been found from simulations assuming an Einstein-de Sitter cosmology, and change little ($< 10\%$) for cosmologies within General Relativity (Jenkins et al., 2001). We reiterate that the ellipsoidal collapse formalism has yet to be developed for DGP and will restrict our modified gravity analysis to the spherical collapse regime.

We have discussed the critical collapse density in the spherical and ellipsoidal collapse regime, in the next section we describe another component of Equation 4.7, the growth of structure.

4.2.3 The growth of structure

The growth of structure D_+ describes how density perturbations evolve and is found by solving the evolution equations (see §1.1.4) which can be written in terms of the scale factor a as,

$$\frac{\mathrm{d}^2}{\mathrm{d}a^2} D_+ + \frac{1}{a}\left[3 + \frac{\mathrm{d}}{\mathrm{d}\ln a}\ln H(a)\right]\frac{\mathrm{d}}{\mathrm{d}a} D_+ = \frac{3}{2a^2} G(a)\Omega_m(a) D_+(a) \ , \tag{4.12}$$

where $G(a)$ is given by (Lue et al., 2004a),

$$G(a) = \frac{2a^4}{3\Omega_m}\left[3H(a)\frac{\mathrm{d}}{\mathrm{d}a}H + a\left(\frac{\mathrm{d}}{\mathrm{d}a}H\right)^2 + aH(a)\frac{\mathrm{d}^2}{\mathrm{d}a^2}H\right] \ , \tag{4.13}$$

in ΛCDM, $G(a) = 1$, but is different in modified gravity. We interpolate between ΛCDM and DGP using α and rewrite the Hubble function as Equation 4.2. For standard ΛCDM, the Hubble function is written as,

$$H^2(a) = H_0^2\left(\frac{\Omega_m}{a^3} + \Omega_\Lambda a^{-3(1+w_0)}\right) \ , \tag{4.14}$$

where we have allowed the value of the equation of state of dark energy w_0, to be constant, but not necessarily -1.

We solve the above growth equations numerically using Maple[1], for three sets of cosmological models;

- Flat $h = 0.7,\ w = -1,\ \Lambda$CDM with $\Omega_m = [0.1, 0.2, .., 1.0]$ and $\sigma_8 = [0.1, 0.2, .., 2.0]$. We additionally examine $\Omega_m = [0.25, 0.35]$ for greater accuracy when interpolating around the currently accepted value $\Omega_m = 0.26$ (e.g. Dunkley et al., 2009).
- Flat $h = 0.7,\ \Omega_m = 0.26,\ \Lambda$CDM with constant $w_0 = [-0.1, -0.2, .., -2.0]$ and $\sigma_8 = [0.1, 0.2, .., 2.0]$.
- Flat $h = 0.7,\ \Omega_m = 0.26\ w = -1$ with $\alpha = [0, 0.1, .., 1]$ and $\sigma_8 = [0.1, 0.2, .., 2.0]$.

We perform the numerical calculation across the small interval ranges to allow for the smooth interpolation of the growth of structure for any value (of these three branches of cosmology), as required by the analysis in §4.5. These sets of parameters are by no means exhaustive, but a fuller analysis is beyond the time frame of this thesis (see §4.5 and §6.5).

In the next section we introduce the final component of Equation 4.7, the variance of the smoothed density field σ_M.

4.2.4 The variance of the density field

The smoothed variance of the density field is normalised by σ_8, which is a specified value (e.g. $\sigma_8 = 0.8$ Dunkley et al., 2009) of the smoothed variance on scales of $8\ h^{-1}$Mpc. Typically a smoothing top hat filter $W(x, M)$ in real space is chosen, which in Fourier space is given by

$$W^*\big(k; R\big) = \frac{3}{k^3R^3}\ \big(\sin(kR) - kR\cos(kR)\big)\ , \tag{4.15}$$

and converts the variance at a specified mass M to the variance at a length scale R using $M = 4/3\pi R^3\Omega_m\rho_c$ resulting in

$$\sigma^2(R) = 4\pi\ \int_0^\infty \mathrm{d}k\ \frac{k^2}{(2\pi)^3}\ \big|W^*\big(k; R\big)\big|\ P(k)\ . \tag{4.16}$$

We use the linear power spectrum $P(k) = k^{n_S}T(k)^2$ with spectral index $n_S = 1$ and the transfer function $T(k)$ from Bardeen et al. (1986)

$$T(q) = \frac{\ln(1 + 2.34q)}{2.34q}\left(1 + 3.89q + (16.1q)^2 + (5.46q)^3 + (6.71q)^4\right)^{-\frac{1}{4}}\ , \tag{4.17}$$

where $q \equiv k/\Gamma\ h^{-1}$Mpc, and $\Gamma = \Omega_m\ h\ \exp\big(-\Omega_B(1 + \sqrt{2h}/\Omega_m)\big)$ (Sugiyama, 1995).

[1] http://www.maplesoft.com/

The power spectrum and σ_M are calculated at $z = 0$ and redshifted using the growth function D_+ to conserve their present day values.

In the next section we describe the modification to the mass function in the spherical and ellipsoidal collapse regime.

4.2.5 The mass function within spherical and ellipsoidal collapse

We can re-write the mass function (Equation 4.9) as a function of $F(\nu)$,

$$n(M) = \frac{2\bar{\rho}}{M^2} \left| \frac{\mathrm{d}}{\mathrm{d}\ \ln M} \ln \sigma(M) \right| \times F(\nu) \ , \tag{4.18}$$

where $F(\nu)$ is a function which changes if collapse occurs spherically (in spherically symmetric shells) or elliptically (along one or two axis before the third). Sheth et al. (2001) performed random walk simulations (see §4.1) and found a functional form for $F(\nu)$ given by

$$F(\nu) = 2A \left(1 + \frac{1}{\nu^{2q}}\right) \left(\frac{\nu^2}{2\pi}\right)^{1/2} \exp\left(-\frac{\nu^2}{2}\right) \ , \tag{4.19}$$

with parameters A, q having values $[0.3222, 0.3]$ for ellipsoidal collapse, and $[1/2, 0]$ for spherical collapse. We note that in the case of spherical collapse we recover Equation 4.9. To obtain predictions for the mass function in these spherical and ellipsoidal collapse regimes, we use the corresponding function form of $F(\nu)$ (Equation 4.19), and the value for critical collapse δ_C (Equation 4.10 or 4.11).

4.2.6 Cluster collapse summary

In this section we have written down the equations for obtaining the cluster mass function within General Relativity (in particular for ΛCDM with a constant equation of state of dark energy) and within DGP. This comprehensive review enables us to calculate the theoretical CMF for a host of cosmological models which we can then compare with the measured mass function (see §4.4.2) and constrain cosmological parameters.

In the next section we present predictions for how the CMF varies with cosmological parameters $\sigma_8, \Omega_m, w_0, \alpha$ and cluster halo mass, in both the spherical and ellipsoidal collapse regimes (where applicable). .

4.3 Sensitivity to cosmology

In Figures 4.7 and 4.8 we show how the mass function $n(M, z)$ for clusters of mass $M = 10^{14}\ h^{-1}\ M_\odot$ changes with redshift, while varying one parameter in a fiducial flat ΛCDM cosmology with parameters $h = 0.7, \sigma_8 = 0.8, \Omega_m = 0.3, w_0 = -1$. We only show predictions for $z < 0.3$ which corresponds to the redshift range of MaxBCG and C4 clusters (see §2.1.7 and

§2.1.8). On each figure we plot the fiducial cosmology as a solid line, and show the predictions for spherical collapse in blue, and ellipsoidal collapse in red.

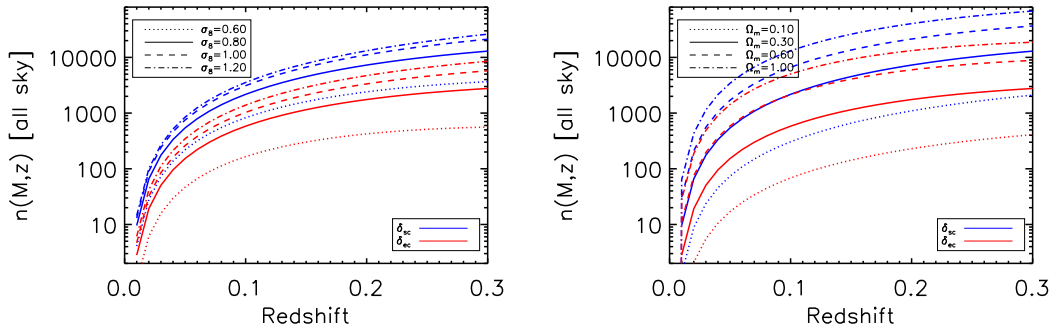

(a) Vary σ_8

(b) Vary Ω_m

Figure 4.7: The theoretical CMF for clusters of mass $M = 10^{14}\ h^{-1}\ M_\odot$ as a function of redshift, assuming a flat ΛCDM cosmology with parameters $h = 0.7, \sigma_8 = 0.8, \Omega_m = 0.3, w_0 = -1$. Figure 4.7(a) shows the effect of varying σ_8, with the effect of varying Ω_m seen in Figure 4.7(b). The blue lines show the predictions for spherical collapse δ_{sc}, and the red lines show the predictions for ellipsoidal collapse δ_{ec}. The solid lines show the fiducial cosmology.

Figure 4.7(a) shows the CMF predictions for different values of σ_8 (the normalisation of the variance of the matter power spectrum, smoothed on a scale of $8\,h^{-1}$ Mpc). We see that all the spherical collapse models (blue lines) have a larger amplitude than the ellipsoidal collapse models (red lines), e.g for the lines $\sigma_8 = 0.6$ ($\sigma_8 = 1.0$) they differ by a factor of 4.5 (2.8) at $z = 0.01$ to 2.8 (3.7) at $z = 0.3$. This is to be expected from previous work (see Figure 4.2) which informs us that the spherical collapse CMF predicts more clusters at all redshifts than the ellipsoidal collapse CMF. We also note that changing σ_8 from 0.6 to 1.0 changes the predicted CMF by a factor of 3.2 (5.1) at $z = 0.01$ to 5.9 (10.4) at $z = 0.30$ within spherical (ellipsoidal) collapse. The potential of using the CMF to constrain σ_8 is clear; relatively small changes in σ_8 produce (at $z = 0.3$) an order of magnitude difference between models.

By comparison, in Figure 4.7(b) we show the effect on the CMF by varying the matter content of the Universe Ω_m, while retaining spatially flat ΛCDM. The difference between the spherical collapse and ellipsoidal collapse for the model with $\Omega_m = 0.6$ (1.0) is 2.2 (2.7) at $z = 0.01$ and 3.7 (4.2) at $z = 0.3$, and the difference between $\Omega_m = 0.6$ and $\Omega_m = 1.0$ models is 2.1 (2.5) at $z = 0.01$ and 1.8 (2.0) at $z = 0.30$ within spherical (ellipsoidal) collapse. These figures show that the CMF is sensitive to changes in σ_8 and $\sim 1/3$ less sensitive to changes in Ω_m.

Additionally we can probe the effect on the CMF by changing the equation of state of dark energy w_0, to a different valued constant in Figure 4.8(a), and modifying the force of gravity, using

the parameter α which interpolates between ΛCDM and DGP in Figure 4.8(b). In both plots we show the difference between the varied CMF and the fiducial CMF to highlight the differences between the models. We only plot the spherical collapse predictions in Figure 4.8(b) because the ellipsoidal dynamics have not been determined (see §4.2.2).

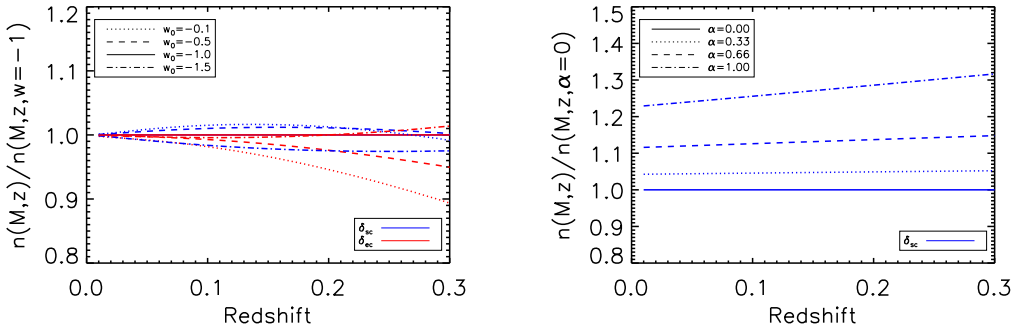

(a) Vary w_0

(b) Vary α

Figure 4.8: The CMF with varied parameters divided by the fiducial CMF (calculated for clusters of mass $M = 10^{14}\ h^{-1}\ M_\odot$ assuming a flat ΛCDM cosmology with parameters $h = 0.7, \sigma_8 = 0.8, \Omega_m = 0.3, w_0 = -1$) as a function of redshift. Figure 4.8(a) shows the effect on the mass function by changing the equation of state of dark energy w_0 to a different valued constant. Figure 4.7 shows the effect of varying the theory of gravity through a parameter α, where $\alpha = 0$ describes ΛCDM, and $\alpha = 1$ describes DGP. The blue lines show the predictions for spherical collapse δ_{sc} and the red lines show the predictions for ellipsoidal collapse δ_{ec}. The solid lines show the fiducial cosmology.

Figure 4.8(a) shows the change in the CMF as w_0 varies. We see that at low redshift the curves converge for all models, and they differ by less than 3% within the spherical collapse regime and 5% for the ellipsoidal collapse in all but the most extreme case of $w_0 = -0.1$ and then the difference is 10% only at $z = 0.3$.

Figure 4.8(b) compares the difference between changing the model of gravity and the fiducial model, which we see to be almost constant as a function of redshift (changing by only 9% in the pure DGP case from $0.01 < z < 0.30$) and presents itself as a $\sim 10\%$ offset depending on the value of α. If the difference between the theoretical CMF from ΛCDM and DGP were larger (for example $> 100\%$) it would have already been measured. The actual value is $\sim 10\%$ which means that it may just be detectable with our dataset. If the signal was a lot lower (for example $< 1\%$) it would probably still be undetectable.

Figure 4.8 shows that the constraining power of the CMF for varying w_0 is a much smaller ($< 5\%$) effect than the constraining power of σ_8 and Ω_m and is probably too small to be constrained here.

Although, if we assume values for all other parameters (from other probes e.g Cosmic Microwave Background radiation, see 1.1.6) we can attempt to place constraints on α.

Until now we have only presented the CMF at a fixed mass ($M = 10^{14}\ h^{-1}\ M_{\odot}$) but by measuring the masses of clusters, we can constrain the CMF for a range of different masses. In Figure 4.9 we show the expected change in the mass function for different mass systems, while keeping to the fiducial cosmology. This shows us that we expect to find orders of magnitude (e.g. ~ 500 to ~ 3500) more $10^{14} M_{\odot}$ than $10^{15} M_{\odot}$ clusters (depending on redshift and collapse regime).

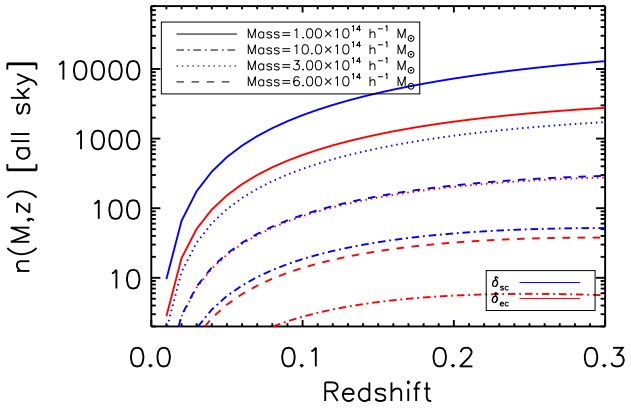

Figure 4.9: The CMF as a function of redshift for clusters with a range of masses in a flat ΛCDM cosmology with parameters $h = 0.7, \sigma_8 = 0.8, \Omega_m = 0.3, w_0 = -1$. The blue lines show the predictions for spherical collapse δ_{sc} and the red lines show the predictions for ellipsoidal collapse δ_{ec}.

4.3.1 Previous constraints

Homogeneous measurements of the CMF has only been possible recently with sensitive pointed X-ray surveys, deep but small area ground based imaging (from the Canada France Hawaii Telescope, hereafter CFHT) or relatively shallow but large area imaging and spectroscopy (from the SDSS).

Gladders et al. (2006) identify 956 clusters in redshift range $0.35 < z < 0.95$ using a red sequence cluster finder (Gladders and Yee, 2000) applied to 72.07 square degrees of CFHT data. They use the richness within $500\ h^{-1}$ kpc as a mass proxy (Yee and Ellingson, 2003) and after marginalising over mass-richness fitting parameters, constrain $\sigma_8 = 0.67^{+0.18}_{-0.13}$ and $\Omega_m = 0.31^{+0.11}_{-0.10}$ assuming flat ΛCDM ($w_0 = -1$) cosmology.

Vikhlinin et al. (2009) followed up 37 high redshift $z > 0.55$ X-ray clusters selected from the

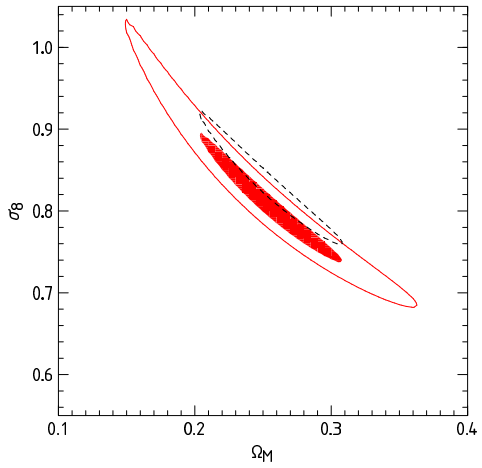

Figure 4.10: A replication of Figure 3 of Vikhlinin et al. (2009) showing the $\sigma_8 - \Omega_m$ confidence contours of the (combined low and high redshift) mass functions. The dotted line corresponds to the effect on the cosmological parameters of changing the mass-observable relationship by 9%. Credit: Vikhlinin et al. (2009).

R400d catalogue, see §2.2.1, with CHANDRA[2] to obtaining accurate temperature measurements. Additionally they included 49 low redshift ($z < 0.25$) clusters selected from the ROSAT All Sky Survey with measured temperatures. They use the X-ray temperature measured in an annulus $(0.15 - 1)R_{500}$, as a mass proxy. Assuming a flat ΛCDM with a constant equation of state of dark energy w_0, they constrain the combination $\sigma_8(\Omega_m/0.25)^{0.41} = 0.832 \pm 0.033$ and $w_0 = -1.14 \pm 0.21$ using clusters alone, and break the $\sigma_8 - \Omega_m$ degeneracy using constraints from the Cosmic Microwave Background (Dunkley et al., 2009), Supernovae (Astier et al., 2006) and Baryon Acoustic Oscillations (Percival et al., 2007), and find $\sigma_8 = 0.786 \pm 0.011, \Omega_m = 0.268 \pm 0.016$, and $w_0 = -0.991 \pm 0.045$. Figure 4.10 is a replication of their results showing the $\sigma_8 - \Omega_m$ confidence contours of the combined low and high redshift mass functions. The dotted line of Figure 4.10 corresponds to the effect on the cosmological parameters of changing the mass-observable relationship by 9%.

Rozo et al. (2009) used the stacked weak lensing shear maps of SDSS galaxies (see Sheldon et al., 2007) around the MaxBCG clusters, and employed the number of cluster galaxies as a proxy for mass (see Johnston et al., 2007), to fit the mass function for cosmological parameters assuming a flat ΛCDM. After marginalising over fitting parameters they constrain $\sigma_8(\Omega_m/0.25)^{0.41} = 0.832 \pm 0.033$ which reduce to $\sigma_8 = 0.807 \pm 0.020$ and $\Omega_m = 0.265 \pm 0.016$ when combined with constraints from the Cosmic Microwave Background (Dunkley et al., 2009). Figure 4.11 is a replication of their results, showing the one and two σ confidence contours in the $\sigma_8 - \Omega_m$ plane, assuming a flat ΛCDM cosmology with $w_0 = -1$, additionally shown are the confidence contours from the CMB (Dunkley et al., 2009) and the combined confidence contours.

[2] http://chandra.harvard.edu/

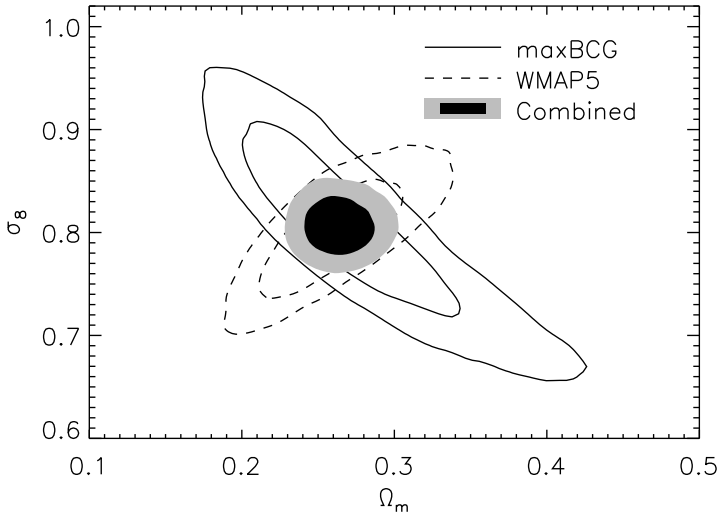

Figure 4.11: A replication of Figure 5 of Rozo et al. (2009) showing the one and two σ confidence contours in the $\sigma_8 - \Omega_m$ plane, assuming a flat ΛCDM cosmology with $w_0 = -1$. Additionally shown are the confidence contours of WMAP (Dunkley et al., 2009) and the combined contours. Credit: Rozo et al. (2009).

The above results show that clusters of galaxies can be used to place independent, constraints on cosmological parameters when compared to other probes of cosmology, e.g using supernovae (with $\Omega_m = 0.31 \pm 0.21$, e.g. Astier et al., 2006), or using the Cosmic Microwave Background radiation (with $\sigma_8 = 0.796 \pm 0.036$, e.g. Dunkley et al., 2009), see Table 1.2.

The effect on the obtained cosmological parameters Ω_m and σ_8 through changing the mass-observable relationship (e.g by 9%) has been shown to be small ($\sim 1\%$), see Figure 4.10.

All previous analysis has been undertaken within the framework of General Relativity, and in particular ΛCDM. There are currently no cosmological constraints on modified theories of gravity using clusters of galaxies.

This thesis has shown that the optical luminosity of optically selected clusters scales with the dark matter halo mass derived from the X-ray temperature. In the next section, we convert the measured cluster masses to cluster mass functions, applying completeness, purity and survey area corrections. We then fit for the cosmological parameters σ_8, Ω_m, w_0 and α.

4.4 The measured cluster mass function

In this section we show that the mass limits of the MaxBCG and C4 clusters from §3 and §5 are consistent, and convert them to usable mass functions by incorporating completeness and survey area corrections.

4.4.1 Comparing cluster mass estimates.

Due to the inability to obtain cluster mass estimates for any one cluster or subgroup of clusters using the weak lensing magnification bias from §5, a direct comparison with the cluster mass estimates from §3 cannot be performed. However, we can show that the range of mass estimates from both techniques are consistent.

The 68% cluster mass limits using the weak lensing magnification bias are in the range $[0.8-3.4]$ $\times 10^{15}\ h^{-1}\ M_{\odot}$ (from Table 5.7), which we can compare with the upper masses as assigned from the total optical luminosity (see Figure 3.11) which are $10^{15.5}\ h^{-1}\ M_{\odot} \simeq 3.16 \times 10^{15}\ h^{-1}\ M_{\odot}$. We see that the upper mass limits are in good agreement, and are also in agreement with expected cluster mass limits (see §1.2). We conclude that even though we cannot measure the mass of any one cluster using the magnification bias, the upper limits for the stacked sample are in agreement with the masses from §3, and all the mass estimates are within the expected range of masses for galaxy clusters.

In §6.4 we discuss how the constraints from the magnification bias could be improved with increased data samples, but in the remainder of this chapter we use the mass estimates from §3 to build a mass function and probe cosmological parameters.

4.4.2 Cluster masses to mass function

To compare the measured clusters masses with the theoretical mass functions, we must first correct for incompleteness and purity, which corrects for clusters which have not been detected by the cluster finding algorithms and false detections. Additionally we must correct for the surveyed region covering only part of the sky.

To correct for incompleteness we use Figures 2.10 and 2.12 which measure completeness as a function of mass using N-body simulations applied to the MaxBCG (see 2.1.7) and C4 (see 2.1.8) cluster finding algorithms, and approximate the curves by two lines between $8 \times 10^{13} \rightarrow 10^{15}$ for the MaxBCG catalogue and three lines between $2 \times 10^{13} \rightarrow 5.5 \times 10^{14}$ for the C4 catalogue. Above these masses, the cluster catalogues are believed to be complete. We cannot probe cosmology using masses below the minimum mass ranges shown in Figures 2.10 and 2.12 because of the lack of completeness corrections. The lines approximating the completeness corrections, and the applicable mass ranges are shown in Table 4.2.

The MaxBCG cluster catalogue is $95-100\%$ pure (see §2.1.7) and the purity of the C4 catalogue is $> 90\%$ (see §2.1.8) which is a factor of 8 smaller than the correction due to completeness. We therefore do not correct for purity in the analysis which follows.

Additionally, we account for the partial sky coverage of each of the SDSS data releases. The

Completeness correction approximation lines.		
MaxBCG clusters		
Mass range M_{200} $[h^{-1}\ M_{\odot}]$	Slope $\times 10^{-14}$	Intercept
$1 \times 10^{14} \rightarrow 2 \times 10^{14}$	-0.222	1.555
$2 \times 10^{14} \rightarrow 1 \times 10^{15}$	-0.014	1.138
C4 clusters		
Mass range M_{200} $[h^{-1}\ M_{\odot}]$	Slope $\times 10^{-14}$	Intercept
$2 \times 10^{13} \rightarrow 1 \times 10^{14}$	-0.655	2.559
$1 \times 10^{14} \rightarrow 2 \times 10^{14}$	-0.074	1.399
$2 \times 10^{14} \rightarrow 5.5 \times 10^{14}$	-3.869	5.774

Table 4.2: The completeness corrections applied to the MaxBCG and C4 CMFs. We show the range at which the correction is applied, and the slope and intercept of the line approximating the completion correction curves of Figures 2.10 and 2.12.

MaxBCG use $7,500$ square degrees (Koester et al., 2007a) or $\sim 18\%$ of the sky, and the C4 catalogue using the whole of the SDSS DR5 spectroscopic coverage ($5,740$ square degrees) which corresponds to $\sim 14\%$ of the sky.

Figure 4.12 shows the uncorrected numbers of clusters as a function of mass as derived from the total optical luminosity (solid lines), the number of clusters after the completeness corrections are applied (dotted lines), and the number of clusters after both completeness and survey corrections have been applied (dashed lines). The MaxBCG clusters are shown in red, and the C4 clusters in blue. We only show (and use in subsequent analysis) the number of clusters at the mass ranges for which we can apply completion corrections, because below these mass ranges, we do not know the levels of completeness. Additionally, we mark the horizontal line Number$= 50$ which corresponds to the minimum number of clusters in each mass bin, that will be used for cosmological modelling and is described in more detail below.

The completeness corrections shown in Figure 4.12 increase the number of clusters at lower mass, which modifies the slopes of the MaxBCG number density curve slightly, but more drastically for the C4 curve. The modification improves the agreement between the slopes of the two cluster catalogues. The translation of the number densities once the survey corrections are also applied is expected, because of the scale dependent multiplication of the curves by ~ 5.

Before we compare the completeness and survey area corrected CMF curves with the theoretical CMFs, we impose an additional cut on the upper mass of the CMFs, as shown by the intersection of the horizontal line on Figure 4.12 with the corrected mass curves. We do this because of the gap in the mass curve for the C4 clusters (at 15.3 and 15.4 on the mass axis) where there are zero

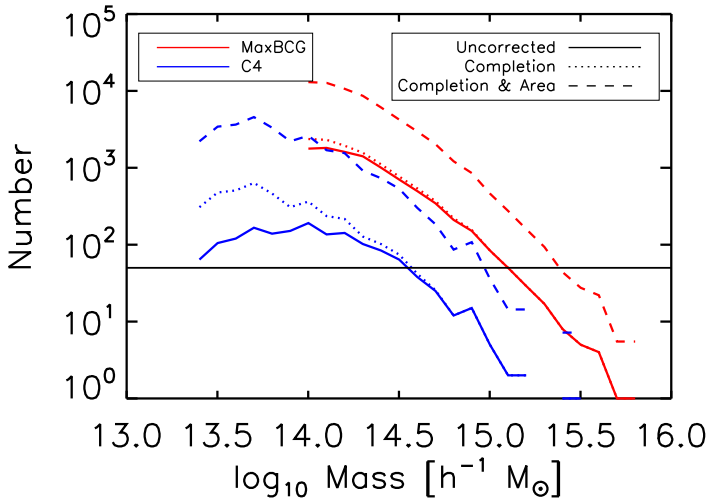

Figure 4.12: The total number of MaxBCG (red) and C4 (blue) clusters as a function of mass. We plot the uncorrected number of clusters (solid lines), the number of clusters after the completeness corrections are applied (dotted lines), and the number of clusters after both the completeness and survey area corrections have been applied (dashed lines).

clusters. After making completeness and survey area corrections (blue dashed line) we would expect to find > 10 clusters (within this mass range) if the mass curve was smooth (which it appears to be at lower mass) but we find none. This cut makes the mass curve more trustworthy. We choose to only use a corrected CMF if there are at least 50 clusters per mass interval which corresponds to a minimum limit of ~ 10 real clusters per mass bin. We impose this cut because for 10 detected clusters the Poisson error is moderate, but at much lower values (e.g 1) we would expect 0 clusters occasionally (which is well within the Poisson error). This cut reduces the maximum mass of the CMFs used to $2 \times 10^{15}\ h^{-1}\ M_\odot$ for the MaxBCG clusters and $8 \times 10^{14}\ h^{-1}\ M_\odot$ for the C4 clusters.

We have constructed the CMF for each mass branch and decided the range of masses which will be used for subsequent analysis. We now describe the error on each mass branch of the CMF. If we are conservative and examine the full 1σ error of the X-ray derived cluster masses, using the upper and lower 1σ errors on the X-ray to mass conversion (Equation 3.4), and the 1σ error on the optical luminosity to mass conversion (Equation 3.18) *and* the 1σ error on the measured optical luminosity to catalogue optical luminosity conversion (Equation 3.26), we find the resulting mass range to be approximately an order of magnitude larger than the measured mass (i.e. in the range 10^{14} to $10^{15}\,h^{-1}\ M_\odot$). These large mass errors allow clusters to have negative mass, and are therefore unrealistic and are not used in the following cosmological analysis.

We therefore decided to assign errors to each mass branch of the CMF by calculating the total number of clusters at each redshift slice examined (e.g between $0.10 < z < 0.11$ there are

5010 clusters in the MaxBCG) and then use the Poisson error on this number, as the error on each redshift slice of each mass branch of the CMF. This means that each CMF will have the same magnitude error at each redshift. The magnitude of the error is conservative because it allows any cluster at that redshift to have any mass (as allowed by the X-ray mass error distribution).

Figure 4.13 shows the final corrected cluster mass functions, for a range of masses using the MaxBCG (red) and C4 (blue) summed optical luminosity as a mass proxy (see §3) with errors given by the Poisson error on the total number of clusters at each redshift.

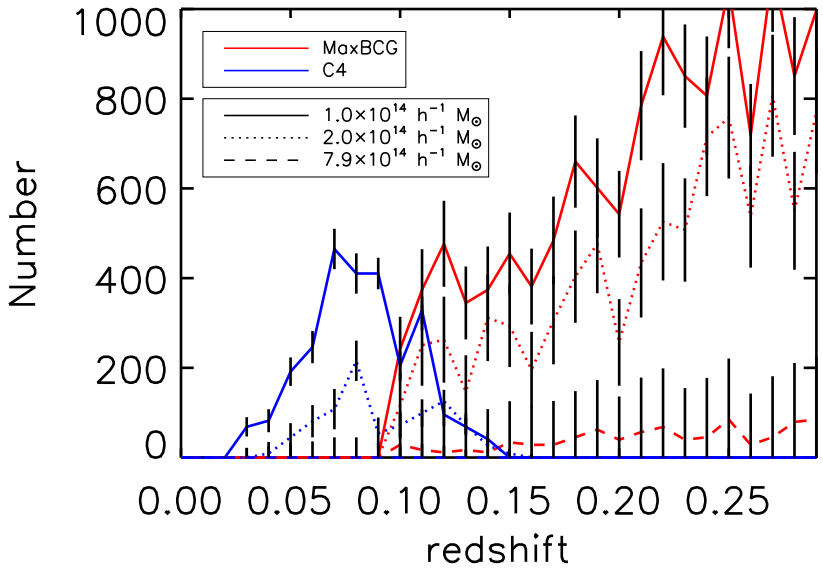

Figure 4.13: The final corrected cluster mass functions, for a range of masses using the MaxBCG (red) and C4 (blue) summed optical luminosity as a mass proxy (see §3) with errors given by the Poisson error on the total number of clusters at each redshift.

Examining the amplitudes and gradients of the three mass curves of Figure 4.13 shows excellent general agreement between the low redshift C4 catalogue and the higher redshift MaxBCG catalogue. There is a distinct drop in the C4 catalogue after a redshift of $z = 0.1$ which is caused by the reduced completeness of the SDSS above $z = 0.11$.

In the next section we fit the completeness and survey area corrected MaxBCG and C4 CMFs for a range of cosmological models.

4.5 Fitting cosmological parameters

We perform a restricted grid based minimum χ^2 analysis (see §5.4.1) fitting the measured mass functions to the theoretical CMF to find the best fitting flat cosmological parameter combina-

tions σ_8 & Ω_m assuming $w_0 = -1$, σ_8 & w_0 assuming $\Omega_m = 0.26$, and σ_8 & α assuming $\Omega_m = 0.26, w_0 = -1$. Additionally we examine the effect of the mass function on the probed cosmological parameters between the spherical and ellipsoidal collapse predictions.

We restrict our analysis to a grid based approach on these parameters because each cosmology requires the solution of the theoretical CMF equations, which is currently performed on a case by case basis in Maple[3]. To perform a more advanced parameter space minimisation technique, for example Markov Chain Monte Carlo (e.g. Andrieu and Thoms, 2008, hereafter MCMC), we would need to automate the solution of the CMF equations for the required parameters. This is beyond the time frame of this thesis, but would allow us to explore a fuller, more varied set of parameters, for example the combinations Ω_m & w_0 & σ_8 & α & H_0. We present our analysis in two formats; by marginalising over any free parameters (e.g. marginalise over σ_8 in the σ_8 & Ω_m analysis to obtain a constraint on Ω_m), or by assuming a fixed value on free parameters (e.g. set $\sigma_8 = 0.8$ in the σ_8 & Ω_m analysis to obtain a constraint on Ω_m). We keep $h = 0.7$ throughout the analysis. This approach is not exhaustive and does not examine the errors on fixed parameters (e.g. H_0= $70 \pm 1.3\,\mathrm{km\,s^{-1}}$ Mpc, as measured by Dunkley et al., 2009), which we discuss in more detail in §6.5.

4.5.1 Constraints on σ_8 & Ω_m

Figure 4.14 show the 2d likelihood contours for the cosmological parameters σ_8 & Ω_m in the spherical (left figures) and ellipsoidal (right figures) collapse regimes, with constraints using the MaxBCG (C4) catalogue on the top (bottom) row. The 1 and 2 σ errors are shown by black and green, with the white region showing the range of parameter space probed.

Figures 4.14(b) shows the constraints on the mass function are within concordance cosmology $\sigma_8 \sim 0.8$ and $\Omega_m \sim 0.3$ with a large part of the σ_8 parameter space being ruled out at more than 2σ. In comparison, all probed values of Ω_m are allowed at the 2σ level, which demonstrates the weaker constraining power of the CMF to this parameter (see §4.3).

The spherical collapse constraints are systematically lower than those from ellipsoidal collapse mass functions which allows us to ask the question; which collapse mechanism is more probable given the parameter values of the concordance cosmological model (e.g. $\Omega_m = 0.26, \sigma_8 = 0.80$, as measured by Dunkley et al., 2009)? We see that for the MaxBCG (C4) dataset the ellipsoidal collapse model is within 2σ (15σ) of $\Omega_m = 0.3, \sigma_8 = 0.8$ whereas the spherical collapse model is 11σ (18σ) away from the fiducial cosmology. For both datasets the predictions built on the assumption that clusters can be formed into elliptical structures are preferred (by 9σ for the MaxBCG sample and 3σ for the C4 sample).

This is in good agreement with Evans and Bridle (2008) who measured the shape of cluster halo

[3] www.maplesoft.com

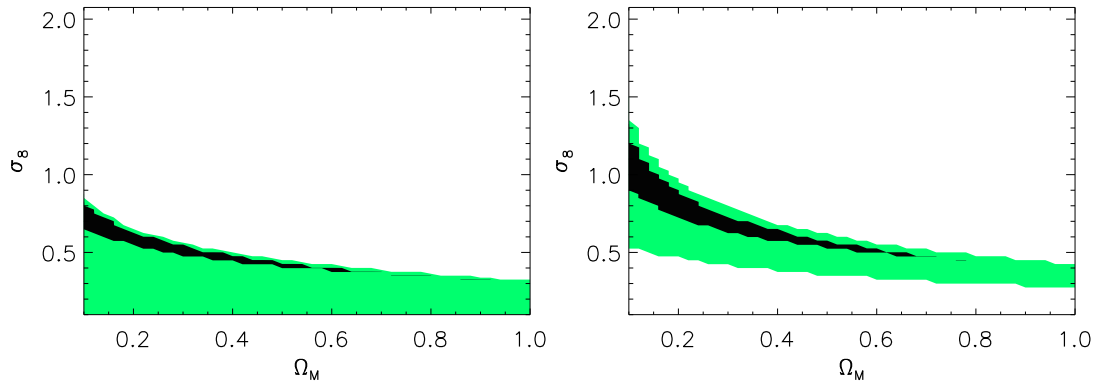

(a) MaxBCG SC

(b) MaxBCG EC

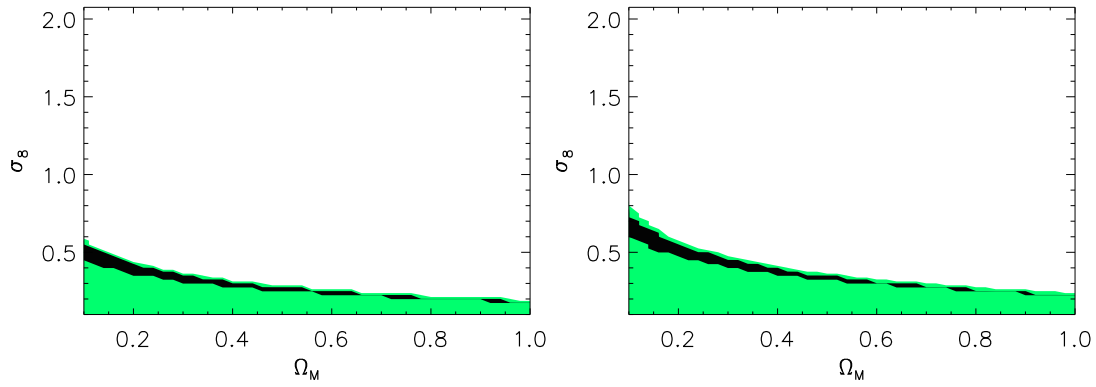

(c) C4 SC

(d) C4 EC

Figure 4.14: The 2d σ_8 & Ω_m likelihood surfaces for the MaxBCG (top) and C4 (bottom), assuming a flat ΛCDM with $h = 0.7, w_0 = -1$. The left (right) figures show the constraints in the spherical (ellipsoidal) collapse regime. The 1 and 2σ contours are shown by black and green, with the white region showing the range of parameter space probed

profiles using weak lensing shear maps around isolated MaxBCG clusters. They find the halo shape to be inconsistent with a spherical mass profile at the 99.6% level.

Returning to Figure 4.14, we note that the C4 confidence contours are lower than the MaxBCG contours. This could be due to the poorly constrained mass-optical luminosity scaling relationship for the C4 clusters (Equation 3.18) that relies on the conversion between the C4 optical luminosity (from the catalogue) to the measured luminosities (see §3.2.3) as given by Equation 3.26, which is less well constrained than the MaxBCG catalogue luminosity to measured luminosity conversion equations.

For succinctness we restrict the subsequent presentation of our analysis to the ellipsoidal collapse regime, but present the results within both collapse frameworks in Table 4.5.

In Figure 4.15 we show the 1d normalised Probability Distribution Functions (hereafter PDF) for σ_8 and Ω_m, after marginalising over free parameters (e.g. to obtain a constraint on Ω_m we marginalise over σ_8) for the MaxBCG (top figures) and C4 (bottom figures) samples in the ellipsoidal collapse regime.

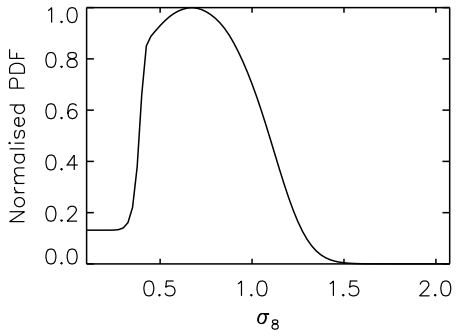

(a) MaxBCG EC

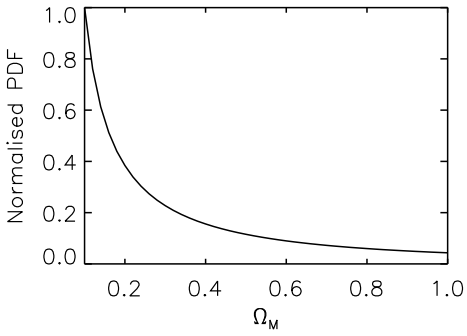

(b) MaxBCG EC

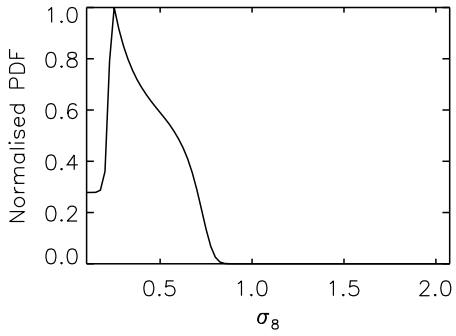

(c) C4 EC

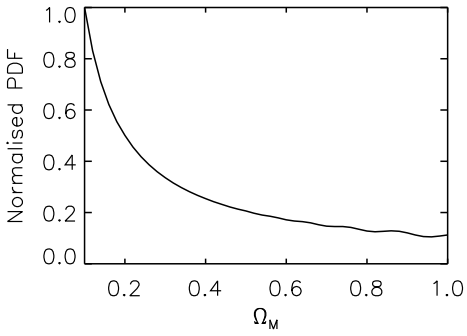

(d) C4 EC

Figure 4.15: The 1d likelihood distributions for σ_8 and Ω_m after marginalising over the other parameter, and assuming $h = 0.7,\ w_0 = -1$. The top (bottom) figures show the constraints from the MaxBCG (C4) clusters within the ellipsoidal collapse (EC) regime.

We calculate the 1 and 2 σ errors (corresponding to an area enclosed by 66% and 97.5% of the normalised PDF) for the case where we marginalise over the free parameter (σ_8 or Ω_m), and the case when we assume a fixed value for the free parameter ($\sigma_8 = 0.8$ or $\Omega_m = 0.26$) and present the resulting parameter values in Table 4.5.

Examining Table 4.5 we see that the best fitting values of Ω_m after marginalising over σ_8 are peaked at the boundary of the explored parameter space, thus we are only able to place a 68%

Measured values				
	MaxBCG dataset		C4 dataset	
Parameter (constraints)	68% of PDF	98.5% of PDF	68% of PDF	98.5% of PDF
Ω_m $(w_0 = -1)$	$0.10^{+0.28}_{-0.00*}$	$0.10^{+0.74}_{-0.00*}$	$0.10^{+0.38}_{-0.00*}$	$0.10^{+0.80}_{-0.00*}$
Ω_m $(w_0 = -1, \sigma_8 = 0.8)$	0.20 ± 0.04	$0.20^{+0.06}_{-0.08}$	$-$	$-$
σ_8 $(w_0 = -1)$	0.67 ± 0.25	$0.67^{+0.57}_{-0.40}$	$0.25^{+0.30}_{-0.02}$	$0.25^{+0.45}_{-0.12}$
σ_8 $(w_0 = -1, \Omega_m = 0.26)$	0.73 ± 0.05	$0.73^{+0.13}_{-0.25}$	$0.48^{+0.03}_{-0.05}$	$0.48^{+0.03}_{-0.38}$
Previous results				
Parameter (constraints)	Reference	1σ		
Ω_m $(w_0 = -1)$	Gladders et al. (2006)	$0.31^{+0.11}_{-0.10}$		
Ω_m (CMB + BAO + SNe)	Vikhlinin et al. (2009)	0.268 ± 0.016		
Ω_m $(w_0 = -1$ + CMB)	Rozo et al. (2009)	0.265 ± 0.016		
σ_8 $(w_0 = -1)$	Gladders et al. (2006)	$0.67^{+0.18}_{-0.13}$		
σ_8 (CMB + BAO + SNe)	Vikhlinin et al. (2009)	0.786 ± 0.011		
σ_8 $(w_0 = -1$ + CMB)	Rozo et al. (2009)	0.807 ± 0.020		

Table 4.3: The ranges of parameter values within 68% and 98.5% confidence after other parameters have been marginalised over, or fixed to their values shown. The * values indicates the error contours fail to converge within the parameter space explored and the $-$ values cannot be measured.

upper estimate on $\Omega_m < 0.38$ (< 0.48) for the MaxBCG (C4) clusters. This is in agreement with Gladders et al. (2006) at the 1σ level, but does show that without a prior attached to σ_8 our values are not competitive. If we assume $\sigma_8 = 0.8$ (e.g. from Dunkley et al., 2009) the best fitting value for the MaxBCG sample becomes more consistent with previous studies having a value of $\Omega_m = 0.20 \pm 0.04$, which is just (1.2σ) outside of the values measured by Vikhlinin et al. (2009) and Rozo et al. (2009). The shape of the C4 likelihood function does not allow the measurement of Ω_m with fixed $\sigma_8 = 0.8$ because the PDF consists on one non zero value which is at the boundary of the parameter space $\Omega_m = 0.1$.

Turning our attention to the constraints on σ_8 after marginalising over Ω_m we see that the best value is peaked within the explored parameter space, and the 1σ value for the MaxBCG sample of $0.67^{+0.25}_{-0.25}$ is consistent with Gladders et al. (2006) having an identical peak but $\sim 60\%$ larger errors. The C4 constraint on σ_8 is just consistent with Gladders et al. (2006) at the 1σ level. If we place a prior of $\Omega_m = 0.26$ (from Dunkley et al., 2009) we find good agreement between MaxBCG and Vikhlinin et al. (2009) and agreement just outside the 1σ level with Rozo et al. (2009). The constraints from C4 on σ_8 at fixed Ω_m are much less consistent (at 3.1σ) with the results from the MaxBCG and previous studies.

We conclude that the constraints from MaxBCG are in good agreement with the constraints from previous studies especially when a prior has been placed on the free parameter. The C4 constraints are in disagreement with both the MaxBCG and previous work, and we consider this to be due

to the large uncertainty in applying mass estimates to the C4 clusters (see §3.4). In the analysis which follows we further restrict the presentation of our results to those from MaxBCG dataset, but show all results in Table 4.5.

4.5.2 Constraints on w_0 & α

We continue with the constraints on the parameters w_0 (in the ellipsoidal collapse regime) and α (in the spherical collapse regime) from the MaxBCG analysis holding the parameter $\Omega_m = 0.26$ and marginalising over σ_8 as shown in Figure 4.16.

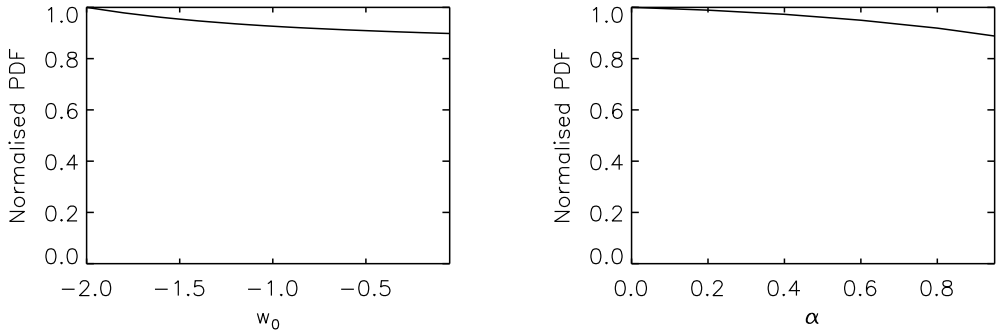

(a) MaxBCG EC

(b) MaxBCG SC

Figure 4.16: The 1d normalised probability distributions functions for w_0 and α after marginalising over free parameters using the MaxBCG dataset. We highlight the ellipsoidal collapse (EC) and spherical collapse (SC) regimes beneath the figures.

Examining Figure 4.16 we see that the constraining power of the MaxBCG CMF on w_0 and α is minimal, showing no sign of a well defined peak or of the likelihood contour converging within the explored parameter space. The reason for this is apparent from the differences between the theoretical CMFs for varying parameters (see Figure 4.7, 4.8) which differ by an order of magnitude between σ_8 models but $\lesssim 5\%$ between different values of w_0 and $\lesssim 20\%$ for different values of α.

If we continue by placing then prior $\sigma_8 = 0.8$ on the likelihood surface we find that the values still fail to converge, because the entire parameter space is still allowed at the 68% level. This means that we cannot place constraints on w_0 in the ellipsoidal collapse regime using the MaxBCG dataset, or on α in the spherical collapse regime.

Modified gravity collapse ansatz

We have shown that if we assume priors of $\Omega_m = 0.26$ and $\sigma_8 = 0.8$, the ellipsoidal collapse framework is preferred to the spherical collapse framework by the measured MaxBCG CMF. We

have also shown that we are unable to place constraints on the parameter α within the spherical collapse framework for MaxBCG. We therefore make the following ansatz: let us assume that the mapping between the dynamics of spherical cluster collapse and ellipsoidal cluster collapse is the same in the modified gravity models examined here as it is in ΛCDM.

We justify this ansatz by recalling that DGP is a modification to General Relativity on very large scales (of order the horizon $\sim 10^4\,h^{-1}$Mpc) and clusters form on much smaller scales ($\sim 10\,h^{-1}$Mpc) and so we propose that the effect on the dynamics of the cluster collapsing mechanism to be fairly small. Let us assume that the modification to the collapse mechanism is encompassed in the spherical collapse formalism, allowing us to use the same mapping between the collapse regimes as before. We note that the original ellipsoidal collapse prescription was formed on simulations in an $\Omega_m = 1.0$ Einstein-de Sitter cosmology and yet the more recent simulation assuming ΛCDM are still well described by the same prescription (to within $< 10\%$, see Jenkins et al., 2001). Our ansatz is that this mapping will not change in the branches of modified gravity explored here.

This ansatz allows us to examine the likelihood surface of α using the MaxBCG dataset and the prior $\Omega_m = 0.26$ by marginalising over σ_8 or by placing the additional prior $\sigma_8 = 0.8$, and we present the results in Table 4.4.

Measured value		
	MaxBCG dataset with ellipsoidal collapse ansatz	
Parameter (constraints)	68% of PDF	98.5% of PDF
α ($\Omega_m = 0.26$)	< 0.60	< 0.90
α ($\Omega_m = 0.26, \sigma_8 = 0.8$)	< 0.30	< 0.65
Previous results		
Parameter (constraints)	Reference	1σ
α (BAO + SNe)	Thomas et al. (2008)	< 0.58

Table 4.4: The ranges of parameter values within the 68% and 98.5% confidence regions after other parameters have been marginalised over, or fixed to their values shown.

Examining Table 4.4 shows that if our ansatz is correct, we can place competitive constraints on α which are in excellent agreement with Thomas et al. (2008) without the need to know the value of σ_8. If we assume the prior $\sigma_8 = 0.8$ we find that we can rule out pure $\alpha = 1$ DGP at the 3σ level. This is in good agreement with Song et al. (2007) who also rule out pure DGP at the 3σ level.

We summarise our main results in §4.6 and present the full table of results in §4.5.3 .

4.5.3 Table of results

In this section we present all the results from both the MaxBCG cluster catalogue and the C4 catalogue within both the ellipsoidal and spherical collapse framework in Table 4.5.

Marginalised Probability distributions					
		MaxBCG dataset		C4 dataset	
Parameter (constraint)	Collapse	68% of PDF	98.5% of PDF	68% of PDF	98.5% of PDF
$\Omega_m\ (w_0 = -1)$	SC	$0.10^{+0.30}_{-0.00*}$	$0.10^{+0.76}_{-0.00*}$	$0.10^{+0.40}_{-0.00*}$	$0.10^{+0.82}_{-0.00*}$
$\Omega_m\ (w_0 = -1, \sigma_8 = 0.8)$	SC	$0.10^{+0.00}_{-0.00*}$	$0.10^{+0.02}_{-0.00}$	-	-
$\sigma_8\ (w_0 = -1)$	SC	$0.57^{+0.10}_{-0.25}$	$0.57^{+0.22}_{-0.47*}$	$0.20^{+0.22}_{-0.02}$	$0.20^{+0.30}_{-0.10*}$
$\sigma_8\ (w_0 = -1, \Omega_m = 0.26)$	SC	$0.55^{+0.02}_{-0.02}$	$0.55^{+0.05}_{-0.45*}$	$0.37^{+0.00}_{-0.05}$	$0.37^{+0.00}_{-0.27*}$
$w_0\ (\Omega_m = 0.26)$	SC	$-2.0^{+1.30}_{-0.00*}$	$-2.0^{+1.85}_{-0.00*}$	-	-
$w_0\ (\Omega_m = 0.26, \sigma_8 = 0.8)$	SC	-	-	-	-
$\alpha\ (\Omega_m = 0.26)$	SC	-	-	-	-
$\alpha\ (\Omega_m = 0.26, \sigma_8 = 0.8)$	SC	-	-	-	-
$\Omega_m\ (w_0 = -1)$	EC	$0.10^{+0.28}_{-0.00*}$	$0.10^{+0.74}_{-0.00*}$	$0.10^{+0.38}_{-0.00*}$	$0.10^{+0.80}_{-0.00*}$
$\Omega_m\ (w_0 = -1, \sigma_8 = 0.8)$	EC	$0.20^{+0.04}_{-0.04}$	$0.20^{+0.06}_{-0.08}$	-	-
$\sigma_8\ (w_0 = -1)$	EC	$0.67^{+0.25}_{-0.25}$	$0.67^{+0.57}_{-0.40}$	$0.25^{+0.30}_{-0.02}$	$0.25^{+0.45}_{-0.12}$
$\sigma_8\ (w_0 = -1, \Omega_m = 0.26)$	EC	$0.73^{+0.05}_{-0.05}$	$0.73^{+0.12}_{-0.25}$	$0.47^{+0.02}_{-0.05}$	$0.47^{+0.02}_{-0.37*}$
$w_0\ (\Omega_m = 0.26)$	EC	$-2.0^{+1.30}_{-0.00}$	$-2.0^{+1.85}_{-0.00}$	-	-
$w_0\ (\Omega_m = 0.26, \sigma_8 = 0.8)$	EC	-	-	-	-
$\alpha^{\#}\ (\Omega_m = 0.26)$	EC	$0.00^{+0.60}_{-0.00}$	$0.00^{+0.90}_{-0.00}$	-	-
$\alpha^{\#}\ (\Omega_m = 0.26, \sigma_8 = 0.8)$	EC	$0.00^{+0.30}_{-0.00}$	$0.00^{+0.65}_{-0.00}$	-	-

Table 4.5: The ranges of parameters within 1 and 2 σ after other parameters have been marginalised over or held fixed. The SC (EC) corresponds to the spherical (ellipsoidal) collapse framework. The * values indicates the error contours fail to converge within the parameter space explored and the - means the parameter was unable to be measured. The $^\#$ indicates the use of an ellipsoidal collapse ansatz (see §4.5.2).

4.6 Summary

In this chapter we have introduced and derived the theoretical cluster mass function (hereafter CMF) and shown that the Sheth et al. (2001) (hereafter elliptical) prescription for cluster collapse, which is an extension of the Press and Schechter (1974) (hereafter spherical) formalism is good at modelling the CMF from N-body simulations to within $\sim 5\%$ (Tinker et al., 2008), and have shown how the CMF varies with cosmological parameters σ_8, Ω_m, w_0 within ΛCDM and for models which interpolate between ΛCDM and DGP using a quantity α.

We then compared the cluster mass estimates for the MaxBCG and C4 clusters from two independent techniques; using the total optical luminosity as a mass proxy (see §3) and using the weak lensing magnification bias (see §5), and showed that while we could not compare the masses of any one cluster, or group of clusters, the upper mass estimates are in good agreement.

We continued by converting the cluster masses from §3 to a mass function and corrected for completeness and survey area, and performed a χ^2 analysis, fitting to the cosmological parameters outlined above.

We presented our results in two formats; by marginalising over free parameters, and by assuming a fixed prior on parameters (such as that from Dunkley et al., 2009, using the Cosmic Microwave Background radiation), for each cluster dataset and each of the two collapse (ellipsoidal and spherical) mechanisms.

We find that the measured CMF of the MaxBCG produces consistent and competitive constraints on the parameters σ_8 and Ω_m if the ellipsoidal collapse formalism is adopted. We also find that the CMF from the C4 cluster catalogue is inconsistent with all current observations, and conclude this is due to the poorly constrained catalogue optical luminosity to measured optical luminosity conversion, which results in poorly estimated cluster masses, see §6.3 for further discussion.

We find that we are unable to constrain α if we remain within the spherical collapse framework, but working under the ansatz that the mapping between ellipsoidal and spherical collapse changes little between ΛCDM and the modified gravity models described here, we find excellent results; ruling out the pure DGP model examined here at 3σ, in good agreement with previous studies (Thomas et al., 2008; Song et al., 2007).

We summarise our most interesting constraints in Table 4.6.

Marginalised Probability distributions		
	MaxBCG cluster mass function	
Parameter (Constraints)	68% of PDF	98.5% of PDF
Ω_m $(w_0 = -1, \sigma_8 = 0.8)$	0.20 ± 0.04	$0.20^{+0.06}_{-0.08}$
σ_8 $(w_0 = -1, \Omega_m = 0.26)$	$0.73^{+0.05}_{-0.05}$	$0.73^{+0.13}_{-0.25}$
α $(w_0 = -1, \Omega_m = 0.26, \sigma_8 = 0.8$ + EC)	< 0.30	< 0.65

Table 4.6: The 68% and 98.5% confidence values for each parameter with the shown prior constraints.

Chapter 5

Magnification bias

This chapter introduces gravitational lensing and emphasises weak gravitational lensing, and using the magnification bias to measure bias around optically selected clusters of galaxies. This is desirable because the value of the cluster - dark matter bias is a function of mass, which will potentially allow us to measure the mass of the optical cluster catalogues independently of the X-ray (which relies on complicated gas-astrophysics to derive a mass estimate). Weak lensing measures the total matter content of a system, irrespective of its dynamical state (which can strongly effect the temperature of the X-ray emitting gas, e.g. Okabe and Umetsu, 2007).

We begin by deriving and computing the theoretical predictions for the shape and amplitude of the magnification bias given our data sets and then describe the experimental methods to perform the measurement. We find that the measured signal is Poisson dominated and as such are unable to measure the mass of any cluster, or subgroup of clusters.

We continue by developing the formalism to convert a future measurement of bias to a cluster halo mass, using the "peak background split" formalism. We show that for our Poisson dominated upper estimate of bias, the upper limit on the stacked cluster masses are within the expected range.

5.1 Introduction

Gravitational lensing is a firm prediction of General Relativity and was first observed during the solar eclipse of 1919 by Arthur Eddington, and in 1979 on galactic scales by Walsh et al. (1979). Gravitational lensing is most prominent when the source and lens are aligned along the line-of-sight and the effects can be most vividly seen in the central regions of massive galaxy clusters, where the gravitational potential is large. In Figure 5.1 we show the distortion of background images due to the cluster of galaxies, Abell 2218.

We introduce the terminology for a simple lens system with the aid of Figure 5.2 and follow the derivations of Bartelmann and Schneider (2001). Light leaves source S, located a distance D_S

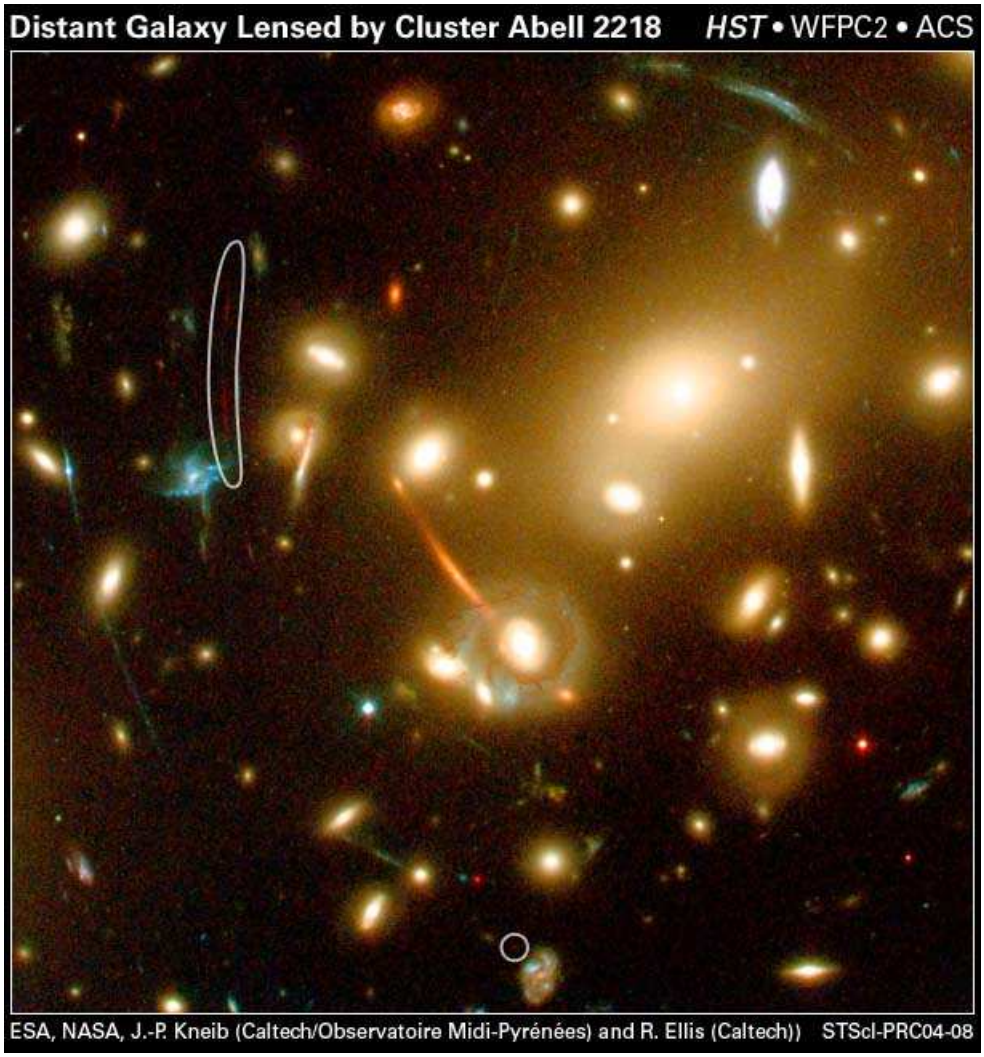

Figure 5.1: Gravitational lensing of background galaxies caused by the massive cluster of galaxies Abell 2218. The source galaxies are distorted, magnified and multiply imaged depending on the spatial configuration of the sources and lens, and the density profile of the lens. Credit: the European Space Agency and NASA.

from the observer O and is bent by a lens of mass M located a distance D_L from the observer; here all distance measures are angular diameter distances. The angular displacement of the source along the line-of-sight is θ_S and the line of closest approach of the source light ray and the lens is called the impact parameter ξ; this corresponds to an angular separation at the observer of θ_I. In the small angle approximation the deflection angle α, is related to the derivative of the lensing potential Ψ perpendicular to the line of sight, given by

$$\alpha = \frac{D_S}{D_{LS}} \nabla_\theta \Psi \ , \tag{5.1}$$

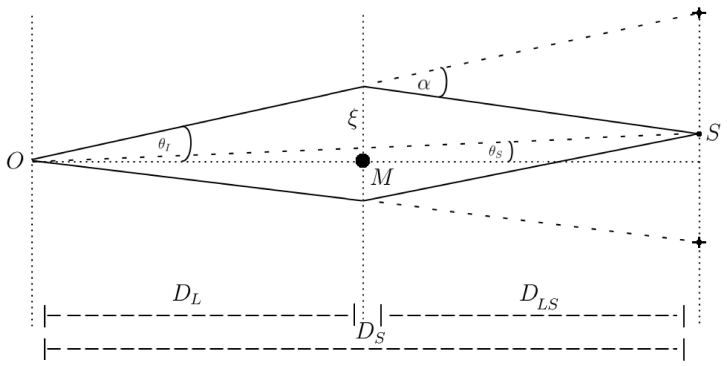

Figure 5.2: A weak lensing schematic of a simple lens, S located D_S from the observer O, with a lens of mass M a distance D_L from observer. The observed angular displacement of the source from the physical line of sight displacement is denoted by α. D_S, D_L, D_{LS} are angular diameter distances.

where the derivative $\nabla_\theta = \left(\frac{\partial}{\partial\theta_1}, \frac{\partial}{\partial\theta_2}\right)$ occurs in the plane of the sky, and the lensing potential Ψ is the line-of-sight integral of the gravitational potential Φ and given by

$$\Psi \;=\; \frac{2D_{LS}}{c^2 D_L D_S}\int \Phi \,\mathrm{d}D \;. \tag{5.2}$$

Here the integral is performed over the comoving distance. Similarly, the surface density Σ is the integrated density along the line-of-sight and is given by,

$$\Sigma \;=\; \int \rho \mathrm{d}D \;. \tag{5.3}$$

The critical surface density Σ_c, marks the transition from the strong lensing regime to the weak lensing regime (described in §5.1.2) and has the form

$$\Sigma_c \;=\; \frac{c^2}{4\pi G}\frac{D_S}{D_{LS}D_L} \;. \tag{5.4}$$

The convergence κ is the ratio of the surface density to the critical surface density, given by

$$\kappa \;=\; \frac{\Sigma}{\Sigma_c} \;. \tag{5.5}$$

The usefulness of the convergence is described in the next section and calculated for a simple lens profile. The convergence can be rewritten as the second derivative of Ψ,

$$\kappa \;=\; \frac{1}{2}\left(\partial_1^2 + \partial_2^2\right)\Psi \;, \tag{5.6}$$

and other second order derivatives of Ψ, known as shear γ, can be taken,

$$\gamma_1 = \frac{1}{2}\big(\partial_1^2 - \partial_2^2\big)\Psi \ , \tag{5.7}$$

$$\gamma_2 = \partial_{1,2}\Psi \ . \tag{5.8}$$

5.1.1 The convergence

The magnitude of the convergence (κ) indicates whether we are in the strong ($\kappa \gtrsim 1$) or weak ($\kappa \lesssim 0.1$) lensing regime. For a simple matter profile, known as the Singular Isothermal Sphere (hereafter SIS), describing a spherical mass at uniform temperature with density ρ (which is proportional to the square of the velocity dispersion σ_v^2) given by $\rho = \sigma_v^2/(2\pi G\xi^2)$, the convergence is

$$\kappa\big(\xi\big) = \frac{M\big(<\xi\big)}{4\,\xi^2\,\Sigma_c} = \frac{M\big(<\xi\big)}{4\,\theta_I^2\,D_L^2\,\Sigma_c} \ . \tag{5.9}$$

where $M(<\xi)$ is the mass within radius ξ. The SIS can explain the flatness of observed spiral galaxy rotation curves out to large radii and assumes the galaxy is embedded in a dark matter halo with a constant velocity dispersion.

In Figure 5.3 we plot κ as a function of angle for three different mass $[0.1, 1, 10] \times 10^{14}\,h^{-1}\,\mathrm{M}_\odot$ SIS systems, and see that κ is below 0.1 for all but the most massive systems on scales larger than $\sim$ 1 arcminute. In the next section we briefly describe the differences between the strong and weak lensing regimes.

5.1.2 Strong and weak gravitational lensing

The magnitude of the convergence indicates the transition from strong to weak gravitational lensing regimes. Depending on the observer-lens-source configuration, strong lensing can produce multiple images of a single source galaxy, or under increasing alignment an "Einstein ring". As the misalignment increases, or κ reduces, the sources are no longer multiple imaged but just become distorted. The shape of the gravitational potential can be reconstructed using the distorted or multiple images. In the strong lensing regime only a few source galaxies are needed to reconstruct this gravitational potential. Examples of strong lensing distorting background source images can be seen within the inner regions of the cluster of galaxies in Figure 5.1.

In the weak lensing regime, images are no longer dramatically altered. To infer the lensing potential from the shapes or luminosities of galaxies the signal must be measured statistically by combining many objects. For example, in cosmic shear studies, which reconstructs a density profile from the distorted shapes of galaxies, the number N of stacked galaxies must be large, to ensure the signal-to-noise is greater than $\sigma_\gamma/\sqrt{N}$, where $\sigma_\gamma = 0.3$ describes the intrinsic distribution of galaxy shapes.

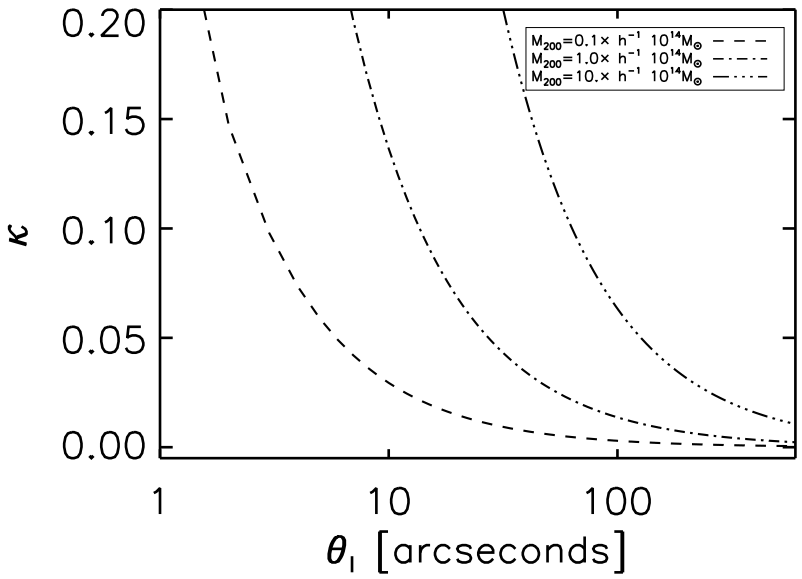

Figure 5.3: The convergence κ, as function of separation angle θ_I for a SIS of three different masses. $k \lesssim 0.1$ corresponds to the weak lensing regime.

The distortion and magnification of the source galaxies is introduced in the next section.

Magnification, shear and convergence

Gravitational lensing conserves surface brightness as the images are distorted. The magnification μ is defined as the ratio of the lensed θ_I and unlensed θ_S solid angles, and can be expressed in terms of the Jacobian matrix $\mathcal{A}$ where

$$\begin{aligned} \mathcal{A}(\vec{\theta}) &= \frac{\partial \vec{\theta}_S}{\partial \vec{\theta}_I}, & (5.10)\\ &= \left(\delta_{ij} - \frac{\partial^2 \psi(\vec{\theta})}{\partial\theta_i \partial\theta_j}\right), & (5.11)\\ &= \begin{pmatrix} 1-\kappa-\gamma_1 & -\gamma_2 \\ -\gamma_2 & 1-\kappa+\gamma_1 \end{pmatrix}, \end{aligned}$$

where $\gamma_{1,2}$ were defined in Equation 5.7 and 5.8. The magnification μ (the ratio of lensed to unlensed solid angles) is given by

$$\begin{aligned} \mu &= \frac{1}{\det \mathcal{A}}, & (5.12)\\ &= \frac{1}{\left(1-\kappa\right)^2 - |\gamma|^2}, & (5.13) \end{aligned}$$

where $\gamma = \gamma_1 + \mathrm{i}\gamma_2$. In the weak lensing regime κ and γ are small and the magnification can be approximated by,

$$\mu \approx 1 + 2\,\kappa\,, \tag{5.14}$$

$$\approx 1 + \delta\mu\,, \tag{5.15}$$

where $\delta\mu = 2\,\kappa$ is small compared to 1. This relationship will be used further in §5.2.4.

The convergence describes the enlargement of the solid angle and the shear γ_1, γ_2, describe the distortion of the image. Figure 5.4 demonstrates these effects on a circular source object.

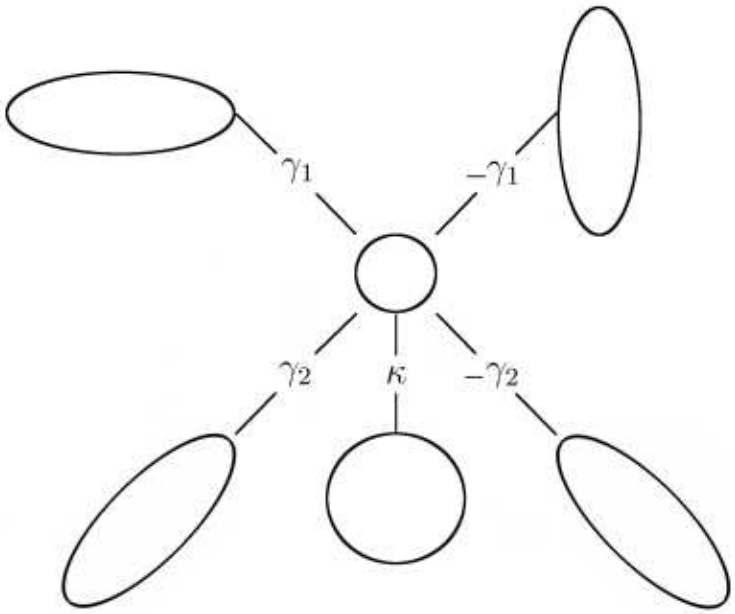

Figure 5.4: The effect of shear γ_1, γ_2 and convergence κ on a circular source shown by the central circle. The convergence enlarges the image but maintains its shape, whereas the shear distorts the image.

To first order, the final image distortion is a superposition of κ and γ. In the remainder of this chapter we concentrate on determining the gravitational potential of low redshift clusters through the measurement of the magnification of high redshift quasars which are detected as point sources. The magnification of point sources increases their measured fluxes (as surface brightness is conserved), allowing quasars which would have had a flux below the flux limit of the survey to be detected, thereby increasing the number density of observable quasars. Reconstructing the gravitational potential from the change in number density of point sources, is called the magnification bias, and is described in detail in the next section.

5.2 The magnification bias

In this section, we introduce and derive the magnification bias and provide equations suitable to its measurement by cross correlating high redshift quasar sources with low redshift cluster lenses. We discuss previous results from the literature which have been largely discrepant with theoretical models until the completion of the SDSS.

5.2.1 Introduction

The magnification bias is a measure of the change in the number density of lensed objects compared with the unlensed number density and is measured statistically, through the cross correlation of sources with lenses. The effect can be measured for any background sources and foreground lenses (provided a quantity $(\alpha - 1)$ is not zero, see below), and we choose to use high redshift quasars as the sources and low redshift clusters as lenses, because of the availability of large robust quasar and cluster catalogues (see §2.1.9, §2.1.7, §2.1.8), and additionally, to ensure no redshift overlap between the sources and lenses. A physical association between sources and lenses would cause spurious correlations which could even change the sign of the measured weak lensing signal. The magnification bias is measured statistically because the effect is small and only relatively low number densities of quasars and clusters are available. We continue with a derivation of the expected modification to the unlensed number density in the weak lensing regime.

The number density of the unlensed quasar distribution $\langle n_{\rm Q} \rangle$ is modelled by a power law in flux f given by,

$$\langle n_{\rm Q} \rangle \;\; = \;\; a_0 f^{-s(f)} \; , \tag{5.16}$$

where a_0 is a normalisation constant and $s(f)$ is a function of flux. Gravitational lensing causes two effects on the lensed number density $n_{\rm Q}$. The solid angle of the sky is stretched, reducing the number density $n_{\rm Q} \rightarrow \frac{\langle n_{\rm Q} \rangle}{\mu}$; simultaneously all fluxes are magnified $f \rightarrow \frac{f}{\mu}$, which increases the number density of detectable quasars. Combining these effects leads to an overall modification of the number density given by,

$$n_{\rm Q} {\rm d}f \;\; = \;\; \mu^{\alpha(f)-1} \langle n_{\rm Q} \rangle \, {\rm d}f \; , \tag{5.17}$$

where $\alpha(f) - 1$ is a function of flux (or magnitude m), and is measured from the source distribution using

$$\alpha(m) - 1 \;\; = \;\; 2.5 \frac{\rm d}{{\rm d}m} \Big(\log_{10} \langle n_{\rm Q}(m) \rangle \Big) - 1 \; . \tag{5.18}$$

When $\alpha(m) - 1$ is large and positive, the number density (c.f Equation 5.17) is enhanced. As $\alpha(m) - 1 \rightarrow 0$ the measured number density equals the unlensed number density. This occurs when the two competing effects, the stretching of the sky and the flux magnification cancel out. As $\alpha(m) - 1$ goes negative, we expect a deficit in the lensed number density, compared to the

unlensed number density. In Figure 5.5, we plot the number density of high redshift quasars as a function of the SDSS apparent magnitudes $[u, g, r, i, z]$, and show the corresponding values of $\alpha(m) - 1$, which were found by differentiating a spline fit curve to the quasar number densities in each band (and using Equation 5.18) and will be useful in later sections. We reiterate that the change in the sign of the expected signal is very specific to weak lensing, as it is difficult to imagine a systematic effect which could cause such magnitude dependent correlations.

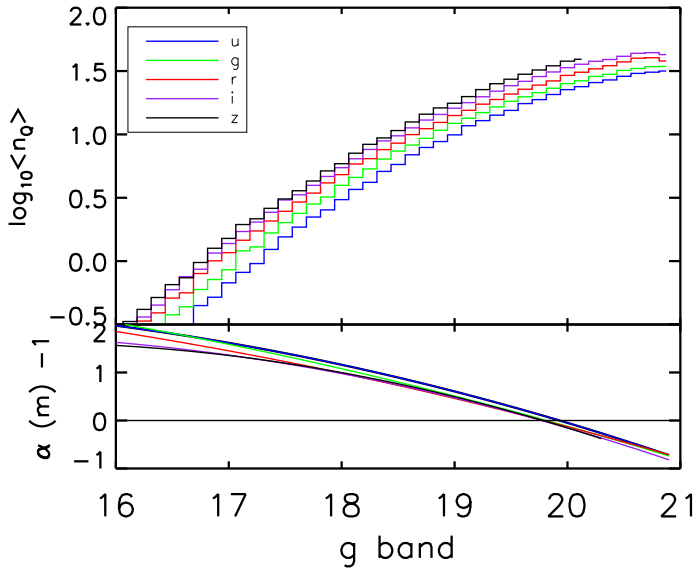

Figure 5.5: The top plot shows the number density of SDSS DR6 quasars as a function of the SDSS apparent magnitudes $[u, g, r, i, z]$. The lower plot shows the value of $\alpha(m) - 1$ which indicates how the measured lensed number density differs from the unlensed number density as a function of magnitude. When $\alpha(m) - 1$ is positive, lensing produces an excess of quasars above the unlensed number density, and a deficit when $\alpha(m) - 1$ is negative.

5.2.2 Previous work

Before the completion of the SDSS, various groups attempted to measure the magnification bias of distance quasars around foreground galaxies with relatively small number statistics has led to discrepant results.

Croom and Shanks (1999a) used the cross correlation estimator $\omega_{qg}(\theta)$ to measure the modification in the number density of foreground $b_J < 23$ galaxies drawn from five AAT plates around 150 high redshift optically selected quasars from the Durham/AAT UVX survey (Boyle et al., 1986) and X-ray selected quasars from ROSAT. They measure an anti-correlation on all scales which is in disagreement with their models which assume a flat Einstein-de Sitter cosmology, and their result is replicated here as Figure 5.6.

Norman and Impey (1999) cross correlate 32 radio loud high redshift ($z = 0.9$ to 2.0) quasars

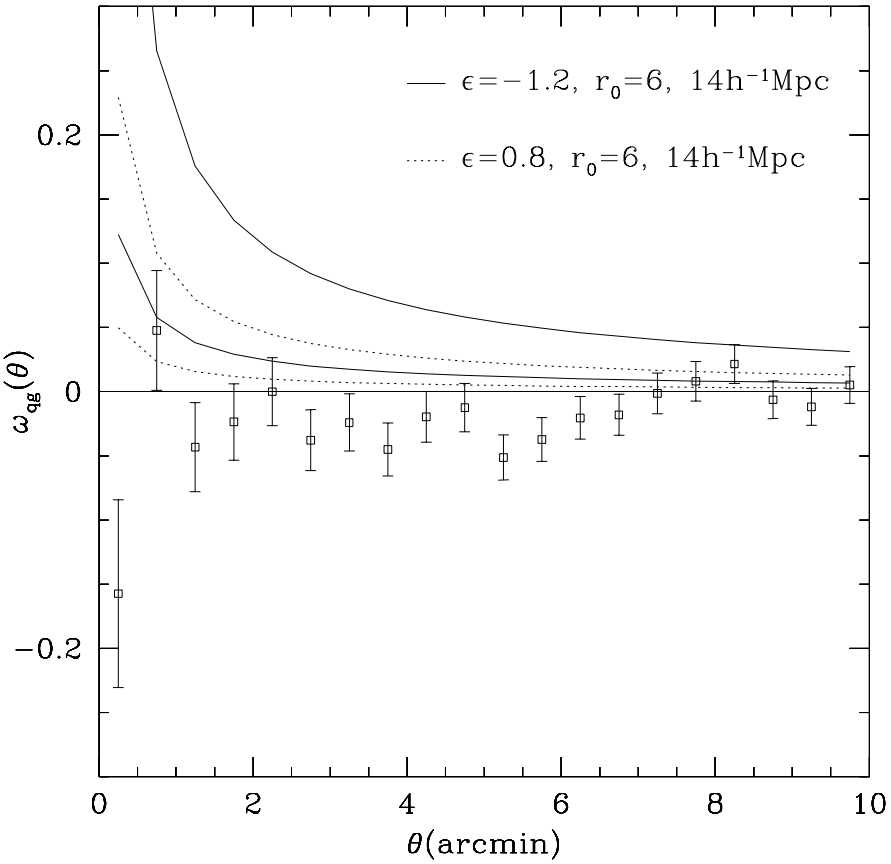

Figure 5.6: A reproduction of Figure 8 of Croom and Shanks (1999a) showing the measured anti-correlation ω_{qg} between low redshift galaxies and 150 high redshift quasars as a function of angular separation θ. Overplotted are models which assume a flat Einstein-de Sitter cosmology and co-moving clustering evolution (solid line) or linear theory clustering evolution (dotted lines). Credit: Croom and Shanks (1999a).

selected from the 1Jy catalogue of Kuehr et al. (1981) with $\sim 5 \times 10^4$ low redshift ($z = 0.2$ to 0.3) galaxies. Figure 5.7 is a reproduction of their results, showing a noisy measurement in moderate agreement with the expected signal from Dolag and Bartelmann (1997).

Furthermore, Croom and Shanks (1999b) measured the cross correlation of AAT quasars (Boyle et al., 1986) with low redshift groups and clusters. They fit SIS models to the galaxy clusters and require velocity dispersions a few factors larger than previously measured (Ratcliffe et al., 1998) to obtain consistent results. Figure 5.8 is a reproduction of the Croom and Shanks (1999b) result, and shows the measured cross correlation ω_{CQ} as a function of separation angle θ with model predictions for a SIS.

The first high significance detection of the magnification bias was performed by Scranton et al. (2005a) who cross correlated $200,000$ high redshift SDSS DR5 quasars with $13,000,000$ low

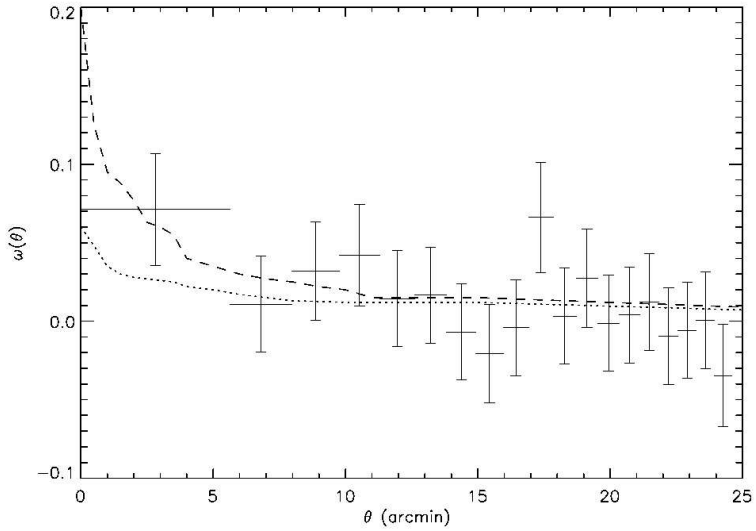

Figure 5.7: A reproduction of Figure 12 of Norman and Impey (1999) showing the noisy cross correlation $\omega(\theta)$ between low redshift galaxies and 32 high redshift quasars as a function of angular separation θ. Overplotted are models from Dolag and Bartelmann (1997) for a flat $h = 1.0$ Einstein-de Sitter cosmology (dashed lines) and a flat $\Omega_m = 0.3, h = 1.0$ ΛCDM cosmology (dotted lines). Credit: Norman and Impey (1999).

redshift SDSS DR5 main sample galaxies. They showed the theoretical models of Bartelmann (1995) were well fit by the measured signal. Figure 5.9 reproduces the Scranton et al. (2005a) result, and shows the magnification bias in each SDSS photometric band in excellent agreement with flat $\Omega_m = 0.29, h = 0.72$ ΛCDM model.

This work was extended by Menard et al. (2009) using $85,000$ high redshift $z > 1$ quasars and low redshift main sample galaxies drawn from SDSS DR3 (Abazajian et al., 2005) to constrain the effect of reddening by intergalactic dust.

We complement and extend these previous SDSS works by measuring the magnification bias around $\sim 15,000$ low redshift galaxy clusters of $\sim 500,000$ high redshift quasars; we then fit the measured signal for cosmology and bias. In the next sections, we derive the expected signal and perform the measurement.

5.2.3 Theoretical derivation

The magnification bias measures the modification of the number density of source quasars, which is measured by cross correlating the lenses (here clusters) and the sources (here quasars). The angular cross-correlation function $\xi_{\rm CQ}(\phi)$ between quasars Q, and clusters C, can be written as,

$$\xi_{\rm CQ}(\theta) \;=\; \left\langle \frac{\Big(n_{\rm C}(\vec{\theta}+\vec{\phi}) - \langle n_{\rm C}\rangle\Big)}{\langle n_{\rm C}\rangle} \frac{\Big(n_{\rm Q}(\vec{\theta}) - \langle n_{\rm Q}\rangle\Big)}{\langle n_{\rm Q}\rangle} \right\rangle , \tag{5.19}$$

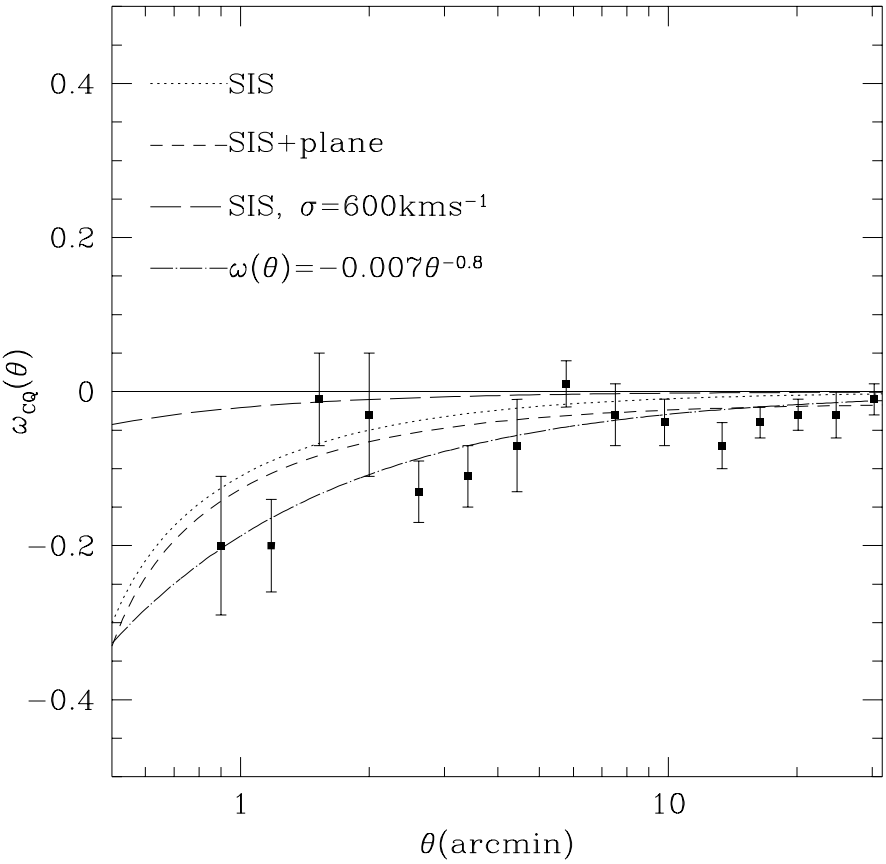

Figure 5.8: A reproduction of Figure 2 from Croom and Shanks (1999b) showing the cross correlation $\omega_{CQ}(\theta)$ between high redshift quasars and low redshift groups and clusters as as function of separation θ. Overplotted are predictions for the magnification of a singular isothermal sphere. The velocity dispersion required to fit this model is a few factors larger than the measured value for groups and clusters. Credit: Croom and Shanks (1999b).

where $\langle n_{\rm Q,C} \rangle$ are the mean number densities of quasars and clusters averaged over the sample. Assuming isotropy, $\xi_{\rm QG}(\theta)$ does not depend on the direction of the lag angle $\vec{\phi}$, and although not written explicitly $\xi_{\rm CQ}(\theta)$ is a function of quasar magnitude m through $n_{\rm Q}(m)$.

Substituting the quasar part of Equation 5.19 with Equation 5.17 and expanding the magnification under the assumption of weak lensing $\mu^{\alpha(m)-1} \approx 1 + (\alpha(m) - 1)\delta\mu$, we obtain

$$\frac{n_{\rm Q}(m, \vec{\theta}) - \langle n_{\rm Q}(m) \rangle}{\langle n_{\rm Q}(m) \rangle} \quad = \quad (\alpha(m) - 1)\, \delta\mu(\vec{\theta})\ . \tag{5.20}$$

The cluster-dark matter bias b, described in detail in §5.5, is the ratio of the overdensity of the luminous matter (here clusters, C) to the dark matter (here DM) by $\delta\rho_C/\rho_C = b\ \delta\rho_{DM}/\rho_{DM}$. When substituted into the cluster part of Equation 5.19, and written in terms of the line-of-sight

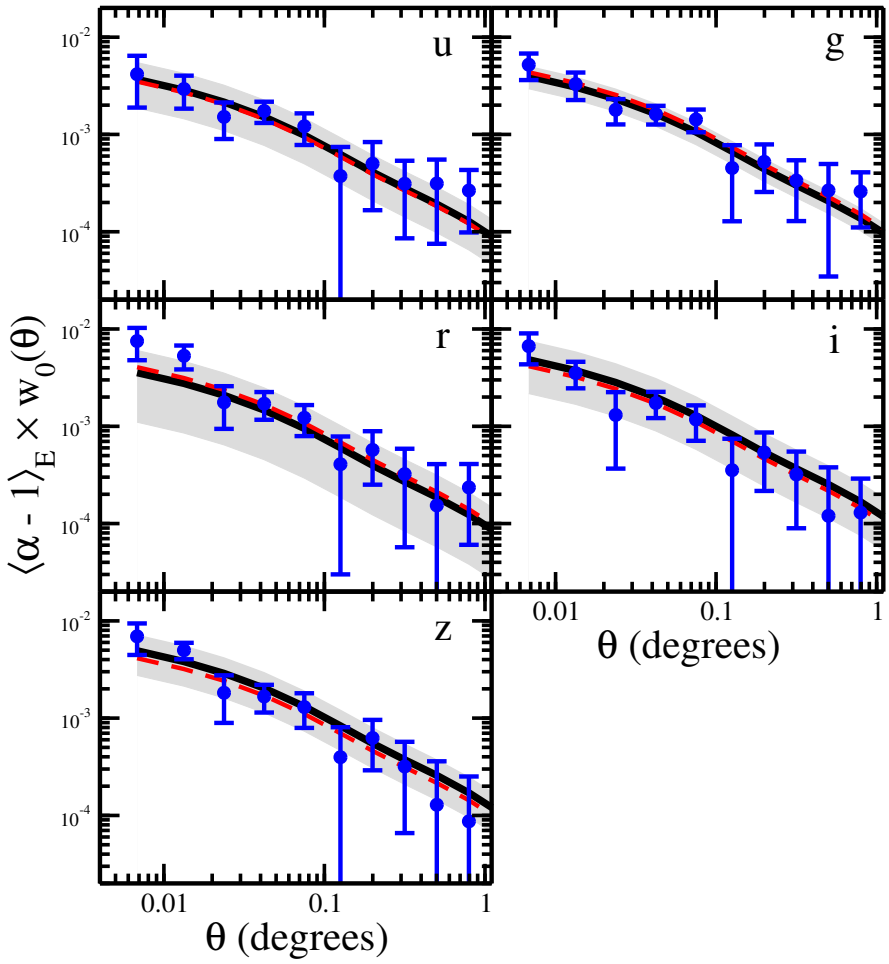

Figure 5.9: A reproduction of Figure 8 from Scranton et al. (2005a) showing the cross correlation $\omega_0(\theta)$ weighted by $\langle \alpha - 1 \rangle$ which allows the stacking of the signal across the entire band. Overplotted are predictions for a flat $\Omega_m = 0.29, h = 0.72$ ΛCDM cosmology. Credit: Scranton et al. (2005a).

integrated density field $\bar{\delta}(\vec{\theta})$ (see e.g. Equation 5.32), we obtain,

$$\frac{n_{\rm C}(\vec{\theta}) - \langle n_{\rm C} \rangle}{\langle n_{\rm C} \rangle} = b\,\bar{\delta}(\vec{\theta})\,. \tag{5.21}$$

Substituting Equations 5.20 and 5.21 into Equation 5.19 yields the theoretically expected modification to the cross correlation of,

$$\xi_{\rm CQ}(m,\theta) = \big\langle (\alpha(m) - 1)\;\delta\mu\;b\;\bar{\delta}(\vec{\theta}) \big\rangle, \tag{5.22}$$

$$= b\,\big\langle (\alpha(m) - 1) \big\rangle\;\xi_{\mu\bar{\delta}}(\vec{\theta})\,, \tag{5.23}$$

where the average is performed spatially. In the final step, we have re-written the $\left\langle \delta\mu \; \bar{\delta}(\vec{\theta}) \right\rangle$ correlation as the magnification-density cross correlation $\xi_{\mu\bar{\delta}}$, which is a weak function of magnitude, and we address this in §5.2.8. For now, we ignore the magnitude dependence and continue by describing $\xi_{\mu\bar{\delta}}$ in more detail in the next section.

5.2.4 The matter magnification cross correlation $\xi_{\mu\delta}(\theta)$

We follow Bartelmann and Schneider (2001), in deriving the cross correlation between the line-of-sight integrated density field and the magnification.

First we recall that $\delta\mu = 2\,\kappa$ (Equation 5.14) and that κ is related to the lensing potential Ψ (by Equation 5.6) which is itself related to the gravitational potential Φ (by Equation 5.2) and can be written as

$$\kappa_{eff}(\theta, w) \;=\; \frac{1}{c^2}\int_0^w \mathrm{d}w' \, \frac{f_K(w-w')}{f_K(w)} f_K(w') \frac{\partial^2}{\partial x_i \partial x_i}\Phi[f_K(w)\theta, w] \;, \tag{5.24}$$

where the subscript $_{eff}$ describes the effective potential along the line-of-sight due to the potential $\Phi[f_K(w)\theta, w]$, and the co-moving distance kernel $f_K(w)$ is given for different values of curvature K by,

$$f_K(w) \;=\; \begin{cases} K^{-1/2}\sin(K^{1/2}w) & (K>0) \\ w & (K=0) \\ (-K)^{-1/2}\sinh\left((-K)^{1/2}w\right) & (K<0) \end{cases} \;. \tag{5.25}$$

In the work that follows, we assume flat models where $f_K(w) = w$ (w is the co-moving distance). We can then use the Poisson equation (relating the second derivative of the potential to the matter density δ) written in terms of the Hubble Constant as,

$$\nabla^2\Phi \;=\; \frac{3\,H_0^2\,\Omega_m}{2\,a}\delta \;, \tag{5.26}$$

and by inserting this into Equation 5.24 yields

$$\kappa_{eff}(\theta, w) \;=\; \frac{3\,H_0^2\,\Omega_m}{2\,c^2}\int_0^w \mathrm{d}w' \, \frac{f_K(w-w')}{f_K(w)} f_K(w') \frac{\delta[f_K(w)\,\theta, w]}{a} \;. \tag{5.27}$$

If the sources (here, quasars) $G_{\rm Q}(w)$ are spread across a range of co-moving distances, the effective potential must be averaged (over co-moving distance), i.e.

$$< \kappa_{eff}(\theta) > \;=\; \int_0^{w_{\rm H}} \mathrm{d}w \, G_Q(w)\, \kappa_{eff}(\theta, w) \;, \tag{5.28}$$

where the integration limit goes to horizon scales $w_{\rm H}$, and $G_{\rm Q}(w)$ is normalised to have unit area. This can then be rewritten as

$$< \kappa_{eff}(\theta) > \;=\; \frac{3\,H_0^2\,\Omega_m}{2\,c^2}\int_0^w {\rm d}w'\,W_{\rm Q}(w)\,f_K(w)\frac{\delta[f_K(w)\theta,w]}{a}\;. \tag{5.29}$$

where

$$W_{\rm Q}(w) \;\equiv\; \int_w^{w_{\rm H}} {\rm d}w'\,G_{\rm Q}(w')\,\frac{f_K(w'-w)}{f_K(w')}\;. \tag{5.30}$$

Now we can recall that $\delta\mu = 2\,\kappa$ and perform the cross correlation with δ, which corresponds to the cluster lenses (which have a distribution $G_{\rm C}(w)$) to produce

$$\begin{aligned}\big\langle\delta\mu\,\delta\big\rangle(\theta) \;&=\; \frac{3\,H_0^2\,\Omega_m}{c^2}\int{\rm d}w'\int{\rm d}w\,W_{\rm Q}(w)\,f_K(w)\,G_{\rm C}(w') \\ &\times\; \frac{\big\langle\delta[f_K(w)\theta,w]\delta[f_K(w')\theta,w']\big\rangle}{a}\;.\end{aligned} \tag{5.31}$$

Next we rewrite $\big\langle\delta\mu\,\delta\big\rangle$ as $\xi_{\mu\delta}$ and the $\big\langle\delta\delta\big\rangle$ cross correlation as the matter power spectrum P_δ, and use Limbers equation which projects a 3d distribution onto a 2d surface resulting in

$$\begin{aligned}\xi_{\mu\delta}(\theta) \;&=\; \frac{3H_0^2\Omega_m}{c^2}\int_0^{w_{\rm H}}{\rm d}w'\,f_K(w')\,W_{\rm Q}(w')\,G_{\rm C}(w')\,a^{-1}(w') \\ &\times\; \int_0^\infty\frac{k{\rm d}k}{2\pi}\,P_\delta(k,w')\,J_0\big(f_K(w')k\theta\big)\;,\end{aligned} \tag{5.32}$$

where J_0 is the Bessel function of the 1^{st} kind and a is the scale factor. We see that Equation 5.32 is a function of magnitude through the function $W_{\rm Q}(w)$ and discuss this dependence in §5.2.8. We continue in §5.2.5, §5.2.6, and §5.2.7 with a description of technical details to evaluate Equation 5.32.

5.2.5 The matter power spectrum

The matter power spectrum describes the clustering strength as a function of scale. We calculate the nonlinear matter power spectrum using Code for Anisotropies in the Microwave Background (Lewis and Bridle, 2002, hereafter CAMB)[1] and the HALOFIT (Smith et al., 2003) routine. We modify the standard input parameters by increasing the maximum value of k to 1000, well within the nonlinear regime, and choose this maximum k value for Bessel function sampling reasons described below. For future computational ease, we set the higher k-space sampling feature in the parameter input file,

```
transfer_interp_matterpower = T,
```

which increases the density of the matter power spectrum samplings by a factor of $\sim$ 6 in k. In Figure 5.10 we plot the nonlinear power spectra from two flat cosmologies (solid lines are

[1] http://camb.info/

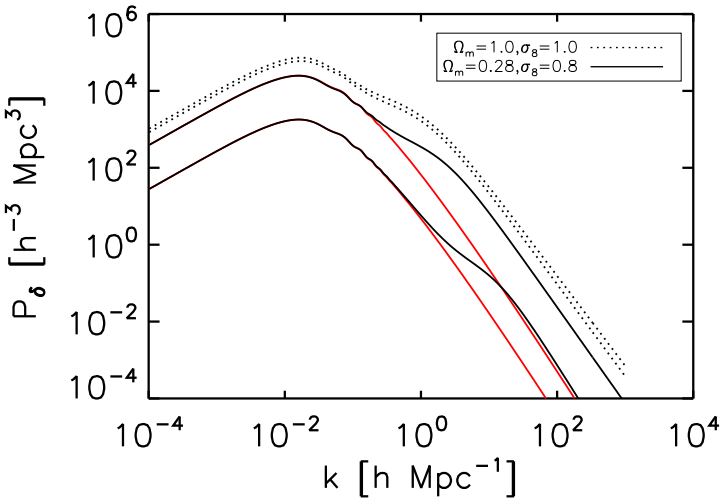

Figure 5.10: The non linear matter power spectra P_δ against wave number k for flat $\Omega_m = 0.28, h = 0.7, \sigma_8 = 0.80$ ΛCDM (solid lines) and flat $h = 0.7, \sigma_8 = 1.0$ Einstein-de Sitter (dotted lines) cosmologies. We plot the power spectra at redshifts $z = 0$ (top curves) and $z = 4$ (lower curves), and in red we show the linear power spectra for the ΛCDM model.

$\Omega_m = 0.28, h = 0.7, \sigma_8 = 0.80$ ΛCDM, dotted lines are $h = 0.7, \sigma_8 = 1.0$, Einstein-de Sitter), at redshifts $z = 0, 4$ and show how the linear and non linear power spectrum differ for the ΛCDM model. We plot different values of σ_8 to reduce the number of overlapping lines on the plot. These different cosmologies evolve differently, but are difficult to compare qualitatively due to the redshift dependence of comoving distances (and time). In fact, in the ΛCDM model, structures collapse slower than in the Einstein-de Sitter model. The ΛCDM nonlinear power spectrum is enhanced compared to the linear power spectrum (red lines) on small scales due to non linear gravitational effects such as clustering of galaxies.

5.2.6 Integrating Bessel functions

The evaluation of Equation 5.32 is complicated by the presence of the Bessel function whose argument is a multiple of a co-moving distance of the order of 10^3, a k value of size $1 - 1000$ and an angle of order ~ 0.1 radians. For these argument values the Bessel function becomes rapidly oscillatory as a function of k, which to correctly integrate, must be finely sampled. We sample from the Bessel function at each co-moving distance w, by interpolating $P_\delta(k, w)$ in k, 10^7 times at regular intervals in real and logarithmic space. Failure to sample finely the k integrand of 5.32 produces features in the integrand function which at best fails to be smooth, and at worst misses entire oscillations. The effect of sparsely sampling the Bessel function is shown in Figure 5.11 for an increasing number of sample interpolations N_{interp}, with the resulting differences of integrating over k for each curve shown in the lower legend. We see that failing to interpolate the curve correctly can change the value of the integration by ~ 3 orders of magnitude, and can even

change the sign of the result.

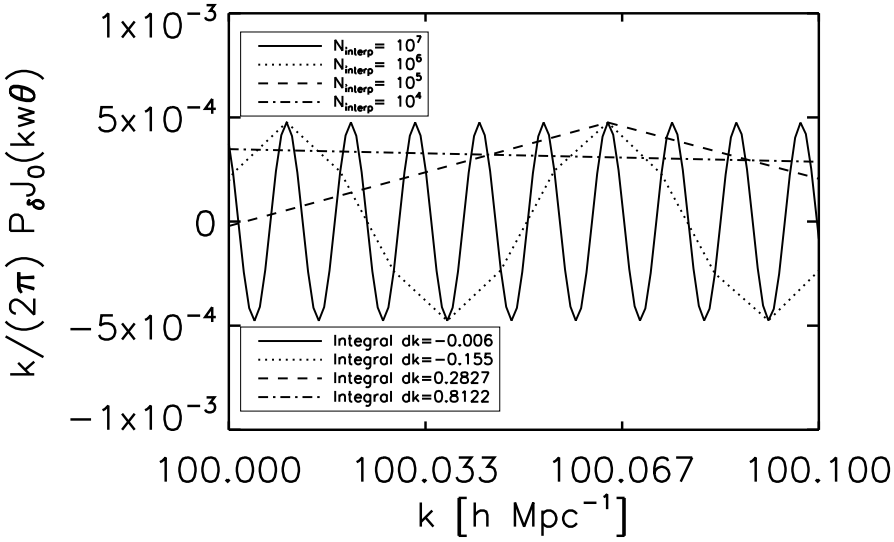

Figure 5.11: To compute Equation 5.32 at large angles and co-moving distances the Bessel function within the k integrand needs to be finely interpolated. We plot the k integrand as a function of the number of interpolation samples N_{interp}. We also show the value of the k integral.

Our choice of interpolating the Bessel function 10^7 times, correctly reproduce the smooth function seen in Figure 5.11. Additional complications in the integration arise because we cannot perform the k integral from 0 to ∞. CAMB outputs a user defined maximum value of k, which leads to an additional source of error. For a fixed maximum value of k, the value of the argument of the Bessel function changes with angle and co-moving distance, which changes the value of the integrand at maximum k. This affects the integral because it is being stopped at different amplitudes. To overcome this, we decide to integrate the k integrand up to the final crossing of the x-axis from below, shown pictorially in Figure 5.12. For this configuration, the power spectrum has been interpolated at $z = 4.0$; we find a difference in the two integrals of 0.005%, which is small, but this integration is performed at each redshift (see Equation 5.32) and could amount to corrections at the $\sim 1\%$ level.

In the next section we describe the technique used to decrease the time taken to calculate $\xi_{\mu\delta}$ for each cosmology listed in Table 5.1, and then explore the magnitude dependence of $\xi_{\mu\delta}$.

5.2.7 Parallelising the computation of $\xi_{\mu\delta}$

We automate the pipeline that calls CAMB, and calculates the matter power spectrum over a range of redshifts, for the set of cosmologies shown in Table 5.1. The pipeline continues by calculating

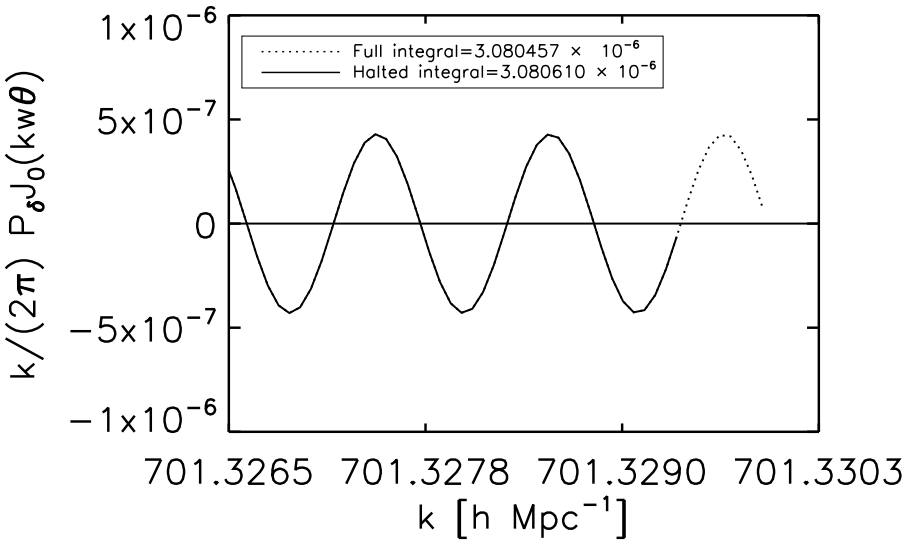

Figure 5.12: The integration is halted at the last crossing of the x-axis from below shown by the solid line. The dotted line is the curve before the truncation. The difference in the full integration to the halted integration is shown in the legend.

the normalised co-moving distributions of the sources and lenses and finally determines the expected cross correlation $\xi_{\mu\delta}(\theta)$ of Equation 5.32.

The computation time of each cosmology is around 10 minutes on a machine with two quad-core 2.8GHz Xeons processors with 16GB of RAM. We sample over 2000 cosmologies to smoothly probe the 2d space Ω_m and σ_8. To speed up this process, we wrote the pipeline to allow a form of parallelisation within IDL. This was accomplished by setting up CAMB in several directories and running IDL from those directories. The list of desired cosmological parameters were placed in a parameter file in the directory above the CAMB installations. Each IDL thread read a line from the parameters file and re-wrote the CAMB parameter input file to reflect the desired parameters. This line of parameters was then removed from the cosmology parameters file, and written to a completed parameters file. IDL then called CAMB to obtain a matter power spectrum with these parameters, and then calculated the cross correlation (Equation 5.32).

This enabled the multiple running of IDL and CAMB from many directories and reduced the linear computation time from ~ 2.5 weeks to ~ 5 days.

The range of cosmologies shown in Table 5.1, were chosen to be evenly spread around concordance cosmology $\Omega_m \sim 0.3$ $\sigma_8 \sim 0.9$, while still exploring parameter space in fine enough grids to obtain good constraints. In the next section, we explore the magnitude dependence of $\xi_{\mu\delta}$.

CAMB cosmologies	
Variable & Range	Increment
$0.1 \leq \Omega_m \leq 0.68$	0.02
$0.1 \leq \sigma_8 \leq 2.0$	0.005

Table 5.1: The 2-D range of CAMB computed cosmologies for which the HALOFIT nonlinear matter power spectra at a range of redshifts is calculated, and the theoretical magnification bias signal for both the MaxBCG and C4 clusters is determined.

5.2.8 The magnitude dependence of $\xi_{\mu\delta}$

In Equation 5.32, we see that the value of the cross correlation depends on the redshift distributions of clusters and quasars which are a function of mass or optical luminosity (for the clusters) and magnitude (for the quasars) through the normalised comoving distance distribution. In this section, we demonstrate how the expected cross correlation changes as a function of magnitude, due to the change in the redshift distribution of quasars of differing magnitudes.

We choose to examine the change in Equation 5.32, due to the differing redshift distributions of g band SDSS quasars at three magnitude (m) ranges, $16 < m < 16.2$, $18 < m < 18.2$ and $20 < m < 20.2$. Figure 5.13 shows the ratio (as a function of co-moving distance) of W_Q calculated for each magnitude range (see Equation 5.30) to W_Q calculated for the faintest magnitude range ($20 < m < 20.2$). The discrete steps are caused by our course redshift steps (converted to comoving coordinates). We see that W_Q is similar across all magnitude ranges at low comoving distances, which is because the integral is carried out from $w = 0$ to $w = w_{\rm H}$ and the distribution G_Q is normalised, so we expect the ratio of the integrals to be close to 1. Comparing the ratios in the range $1000 - 5000h^{-1}$ Mpc shows that the fainter distribution has more power on intermediate scales, but less power on large scales.

We determine the ratios of the full cross correlation signal $\xi_{\mu\delta}$ as a function of angular separation θ, for differing redshift distributions of g band quasars using the magnitudes ranges $16 < m < 16.2$ and $18 < m < 18.2$, divided by $\xi_{\mu\delta}$ calculated in the magnitude range $20 < m < 20.2$. We note there is a constant (with respect to angle) $\sim 1.7\%$ ratio difference between the magnitude ranges $18 - 18.2$ and $20 - 20.2$, and a constant $\sim 10.3\%$ ratio difference for the $16 - 16.2$ and $20 - 20.2$ quasars.

In §5.3.2, we stack the cross correlation signal across magnitude ranges for each band, which we perform by weighting the signal by the number of quasars at each magnitude range. This means we give a low weighting to the brightest quasars, as there are two orders of magnitude less of them (see Figure 5.5), and a higher weighting to the fainter quasars. We therefore can neglect the difference in $\xi_{\mu\delta}$ as a function of magnitude because we have found the difference between the fainter quasars to be small. Additionally, in §5.2.7 and §5.2.6, we discussed computational

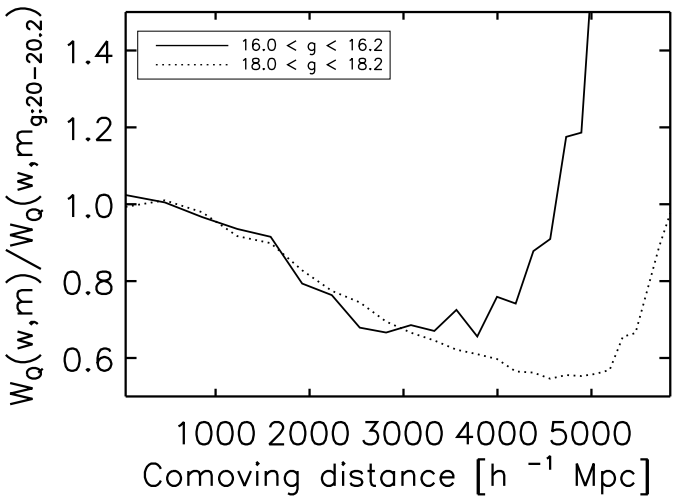

Figure 5.13: The W_Q function (see Equation 5.30) evaluated for different three different g band magnitude slices; $16 < m < 16.2$, $18 < m < 18.2$ and $20 < m < 20.2$. We plot the value of W_Q as a function of comoving distance, calculated in a flat $\Omega_m = 0.3, h = 0.7$ ΛCDM cosmology, divided by the value of W_Q calculated in the faintest magnitude slice.

difficulties in calculating Equation 5.32, which is performed for a list of cosmologies (see Table 5.1) and takes $\sim$ 10 minutes, using the full quasar and cluster sample for each cosmology. If we had to repeat this calculation for each magnitude range, for each band, and for each cluster redshift distribution, the time taken to calculate the prediction for one cosmology could run to days.

In the previous sections we have introduced the matter power spectrum necessary for the computation of Equation 5.32, and continued by discussing technical difficulties in the computation of $\xi_{\mu\delta}$, and shown it to have little dependence on magnitude, for the purposes considered here. In the next section we present the effect of cosmology on $\xi_{\mu\delta}$.

5.2.9 Theoretical results

We have calculated the expected cross correlation $\xi_{\mu\delta}$ for cosmologies given by Table 5.1 and our distributions of clusters and quasars. The dependence of the cross correlation for varying σ_8 and Ω_m in flat $h = 0.7$ ΛCDM for the MaxBCG clusters (see §2.1.7), and quasars (see §2.1.9), is shown in Figure 5.14 with the parameter values chosen for illustration.

We see from Figure 5.14 that the amplitude of the expected curve is a function of σ_8, which can be seen by the order of magnitude difference between the $\sigma_8 = 0.2$ and $\sigma_8 = 1.0$ models. The effect of changing Ω_m from 0.12 to 0.44 changes not only the amplitude of the signal, but also the shape of the curve, especially at large separations. The magnification bias ξ_{CQ} (Equation 5.23) contains

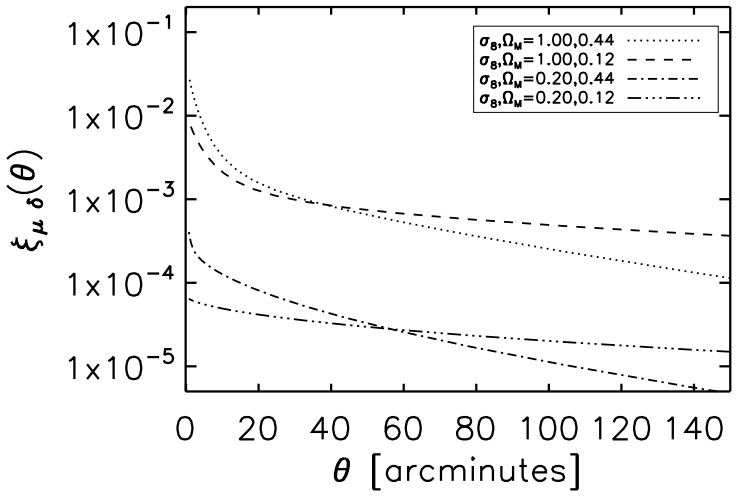

Figure 5.14: The theoretical cross correlation $\xi_{\mu\delta}(\theta)$ calculated for the low redshift MaxBCG cluster lenses and high redshift SDSS DR6 quasar sources with median redshifts $[0.23, 1.68]$. We show a range of Ω_m, σ_8 values within a flat $h = 0.7,\ \Lambda$CDM cosmology.

the $\xi_{\mu\delta}$ cross correlation term and a multiplicative bias factor b, which, using Figure 5.14, we see will lead to a strong degeneracy between σ_8 and b.

We have computed the theoretical curves of the magnification bias. In the next section we describe the experimental methodology developed to measure the signal for both the C4 and MaxBCG cluster catalogues.

5.3 Experimental methods

In this section we describe the measurement of the magnification bias. We document the creation of random catalogues and tests of the pipelines. We stack our results to increase signal-to-noise, fit for cosmology, and measure bias. In section §5.5 we convert the measured bias to a cluster mass.

To motivate the following discussion on random catalogues, we reproduce the cross correlation equation (Equation 5.19) in terms of clusters C and quasars Q,

$$\xi_{\rm CQ}(\theta) \;=\; \left\langle \frac{\Big(n_{\rm C}(\vec{\theta}+\vec{\phi}) - \langle n_{\rm C}\rangle\Big)}{\langle n_{\rm C}\rangle} \frac{\Big(n_{\rm Q}(\vec{\theta}) - \langle n_{\rm Q}\rangle\Big)}{\langle n_{\rm Q}\rangle} \right\rangle . \tag{5.33}$$

We expand Equation 5.33 in terms of the individual cross correlations between the clusters and quasars (n_C, n_Q), and the random clusters and quasars (n_{R_C}, n_{R_Q}) as,

$$\xi_{CG}(m,\theta) = \frac{\langle n_C n_Q(m)\rangle(\theta) - \langle n_{R_C} n_Q(m)\rangle(\theta) - \langle n_C n_{R_Q}(m)\rangle(\theta) + \langle n_{R_C} n_{R_Q}(m)\rangle(\theta)}{\langle n_{R_C} n_{R_Q}(m)\rangle(\theta)} . \quad (5.34)$$

We note that to compute Equation 5.34, each of the cross correlations must be normalised by their total number densities, to account for the potential differences in size of the data and random catalogues.

To perform the cross correlation (Equation 5.34) experimentally we need to build robust random catalogues. If the catalogues are not random (perhaps containing a positional bias) the measured cross correlation could suffer from an unwanted systematic offset. In the next section we discuss the creation of these random catalogues.

5.3.1 Random catalogues

To perform the cross correlation described by Equation 5.34, random catalogues with similar spatial and magnitude properties to the clusters and quasars are required. To create the random datasets we form masks by splitting the sky into equal area regions using the Hierarchical Equal Area isoLatitude Pixelization[2] (Gorski et al., 2005, hereafter HEALPix) routine.

Survey masks

We create the masks by identifying the exact area of the completed surveys applicable to each dataset. This entails downloading a large random selection of galaxies from the SDSS Casjobs[3] web server for each data release. We download between 15% and the total number of galaxies, depending on the size of the available catalogue, which corresponds to between $1,021,724$ objects for SDSS DR5 spectroscopic survey and $20,598,091$ objects for the SDSS DR6 photometric survey. We cannot directly use these randomly selected galaxies as there could exist a slight positional bias in the data which would lead to large scale offsets in the cross correlation. We circumvent this problem by applying a pixelisation mask to the randomly selected galaxies and retaining only pixels with $N_{gal} > 0$, and then create a random sample using the remaining pixelized regions. HEALPix pixelises the sky (or more formally a sphere) into a user defined number of equal area regions (but the pixel shapes differ widely). We set Nside $= 1024$ or, more specifically, the number of pixels required to cover the whole sky to $12,582,912$, which equates to ~ 11.8 square arcminutes per pixel. A random selection of the pixelised specroscopic DR5 mask is shown using an Aitoff projection in Figure 5.15.

Each pixel may contain multiple galaxies, therefore there are always $N_{pixels} \lesssim N_{galaxies}$, and the pixelized region corresponds to the footprint of the survey. Each HEALPix pixel has a unique number identifier which will be key in creating the random catalogues in the next section.

[2] http://healpix.jpl.nasa.gov
[3] http://casjobs.sdss.org/casjobs/

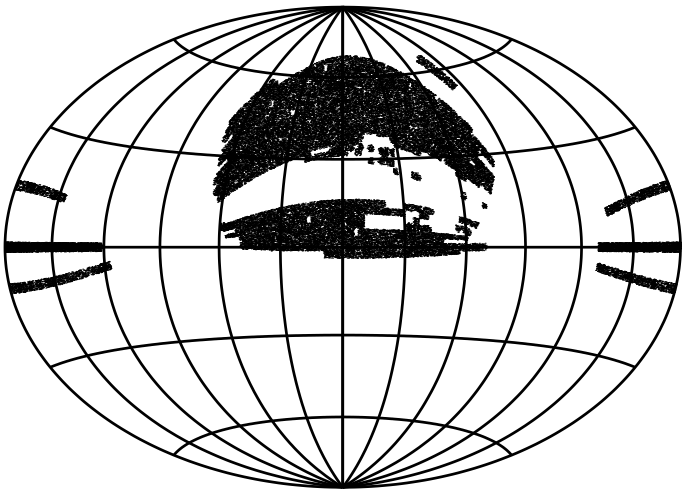

Figure 5.15: An Aitoff projection of the randomly selected mask pixels for the SDSS DR5 spectroscopic sample. Each pixel size corresponds to ~ 11.8 square arc minutes.

Random catalogues

The shape variation of the HEALPix pixels does not allow the easy random population of the pixelized mask. So to achieve this we first randomly populate a sphere and apply the HEALPix pixelization to these random points. We then retain the random points whose pixel number is also found in the mask. This process is repeated continuously until we have the desired number of random points, which for the random C4 cluster catalogue is 50 times the number of C4 clusters; the other random catalogues are 20 times greater than their counterparts.

To enable the random catalogues to directly mimic the data, we keep only the quasar and clusters found to be within the same mask as used to create the random catalogues. We retrieve 99.6% of the MaxBCG clusters and 99.1% of DR6 quasars, which could imply the quasars are not completely drawn from the main galaxy sample, or that we need more randomly selected main sample galaxies. As the percentage of lost quasars is so small (0.09%) we ignore this effect. We recover all of the spectroscopic C4 clusters. We additionally construct the random quasar catalogue to mimic the magnitude distribution of the real quasars. This is achieved by choosing a real quasar at random and mapping its magnitudes (in each band) to a random quasar. This process is repeated until all random quasars have magnitudes, and correctly models the real quasar magnitude distributions.

Any positional bias in the random catalogues will manifest as an offset in the cross correlation signal. In the next subsection we perform checks on the random catalogues to ensure they are spatially random.

The HEALPix pixel repeat rate		
Pixel repeated [times]	Measured %	Randomly expected %
1	56.263	56.269
2	32.272	32.395
3	9.399	9.227
4	1.783	1.811
5	0.248	0.264
6	0.031	0.031
7	0.003	0.003

Table 5.2: Testing the randomness of the random catalogues, for the distribution of pixel repeat rates expected when a pixel is drawn from $2,318,177$ pixels after $1,330,500$ draws and replacements. Column one is the pixel repeat rate, column two shows the actual pixel repeat rate for the random catalogue. The final column is the expected repeat rate for a random number distribution.

Tests of the random catalogues

To check the spatial randomness of the random catalogues, we use the HEALPix pixel numbers. We observe how many times each pixel has been populated and compare with the expected repeat rate; this calculation can be reformulated as: how many times would one expect a particular pixel to be chosen, when drawing and replacing M times from N pixels?

This is a problem described by a binomial distribution, which requires the calculation of factorials. The large number of random data points (e.g. $\sim 10^7$) used here, makes a calculation of the factorial and expected distribution impossible. We therefore use the IDL random number generator **ran2**[4], which uses a different routine from that used in the creation of the random catalogues (**randomu**[5]), to randomly select and replace M times from N pixels (or integers). We can compare the expected distribution of repeated pixels with the measured distribution of repeated pixels of the random catalogues, which should have the same repeat rate distributions.

For example, an incarnation of the random MaxBCG cluster catalogue has been drawn from $2,318,177$ unique mask pixels, of which $1,330,500$ draws and replacements are made. The results of the actual and expected distributions are shown in Table 5.2, which in the first column lists the number of times a pixel has been repeatedly chosen. The next column lists the percentage of mask pixels of the random catalogue which have been chosen that number of times, and in the final column, we show the expected percentage of pixel (or integer) repeat rates from a purely random number distribution.

[4]http://astro.uni-tuebingen.de/software/idl/aitlib/misc/ran2.html
[5]http://idlastro.gsfc.nasa.gov/idl_html_help/RANDOMU.html

The high level of agreement between the actual and expected pixel repeat rates in Table 5.2 shows that the distribution of multiply selected pixels is very close to that expected from a purely random number distribution. As each pixel corresponds to an equal area of the survey mask, we can conclude that the spatial distribution of the random catalogue is highly random, as required for the cross correlations. In §5.3.2 we introduce the cross correlation and the stacking procedure necessary to improve the signal-to-noise, before testing the cross correlation and data stacking pipelines in §5.3.3.

5.3.2 Stacking the cross correlation

The relatively low number densities of quasars in each magnitude bin, e.g, there are only $[23,\ 3951,\ 19604]$ quasars in the g band magnitude ranges of $[16.3-16.4,\ 18.8-18.9, 20.3-20.4]$, over the full $\sim\ 10,000$ square degrees of the SDSS, means we can can improve the signal-to-noise by stacking the data across magnitude ranges and bands. But, we cannot simply take an average across each magnitude range because the sign of the magnification bias measurement is expected to vary as a function of $\big(\alpha(m)-1\big)$. This expected change in the sign of the signal is a test of the detection of the magnification bias, as no contamination is expected to reproduce this sign change, and we test for this feature in §5.3.7. To combine the signal from each magnitude we multiply the measured signal by the value of $\big(\alpha(m)-1\big)$ at that magnitude, which turns the expected signal to positive definite, i.e.

$$\big(\alpha(m)-1\big)\,\xi_{CG}(m)\ \geqslant\ 0 \text{ for all } m\ . \tag{5.35}$$

Notice that multiplying $\xi_{CG}(m)$ by $\big(\alpha(m)-1\big)$, requires a *squared* factor of $\big(\alpha(m)-1\big)$ to appear on the right hand side of Equation 5.23.

The brighter magnitude number density (see Figure 5.5) is two orders of magnitude lower than the fainter number density, which implies we should weight higher the measured signal using the fainter quasars, because of the increase in the signal-to-noise. We therefore weight $\big(\alpha(m)-1\big)\xi_{CG}$ by the number of quasars in the magnitude range, which assigns a higher weighting to the signal as the signal-to-noise increases. This produces a weighted cross correlation per band i of,

$$\big\langle\alpha-1\big\rangle\xi_{CG_i}\ \ =\ \ \frac{\int \mathrm{d}m\ n_Q(m)\big(\alpha(m)-1\big)\ \xi_{CG_i}(m)}{\int \mathrm{d}m\ n_Q(m)}\ , \tag{5.36}$$

where the integral can run over the entire magnitude range of the band, or over parts of the full magnitude range. We can therefore split the signal into two regions, that where the signal is expected to be positive, and that where the signal is expected to be negative (see §5.3.7).

Furthermore, we stack the data across each band to produce a final weighted cross correlation $\langle\alpha-1\rangle\xi_{CQ}$ using,

$$\langle\alpha-1\rangle\xi_{CQ} \;=\; \sum_{i=1}^{5}\langle n_C n_Q\rangle_i\langle\alpha-1\rangle_i\xi_{CG_i}\Big/\sum_{i=1}^{5}\langle n_C n_Q\rangle_i\,. \tag{5.37}$$

For our test data, we use Poisson errors as the measurement error, but use the jackknife error (both described in §5.3.5) for the MaxBCG and C4 measurement, because Poisson errors typically underestimate large scale errors and covariances.

The random catalogues have been made and tested, and the magnification bias measurement and normalisation identified (see Equation 5.34). We proceed by testing the cross correlation pipelines, and the magnification bias stacking software using simulated data.

5.3.3 Tests of the software

In this section we test the cross correlation and magnification bias software by using artificial data created with known properties.

The cross correlation software

The cross correlation of independent random datasets is by definition zero. Following the random catalogue creation of §5.3.1, four random catalogues have been created to mimic the catalogues of "true" and "random" data. The "cluster" dataset has 10^4 objects and the "quasar" catalogue contains 10^6 entries with the "random" catalogues being an order of magnitude larger.

Figure 5.16 adds confidence to the validity of the cross correlation software and our random catalogue creation, by showing the convergence of the cross correlation to zero on large scales. Above a few arcminutes, this signal has converged to below 1%. The actual cross correlations are peformed with more than two orders of magnitude more random quasars $(904,238,020)$ than used here, which will lead to smaller errors. We use lower number densities for the "test" datasets in this section because of considerable time reduction ($\sim$week), when cross correlating these smaller datasets.

The magnification bias test data

To test the magnification bias software we create simulated data for each of the individual cross correlation components in Equation 5.34 to correctly mimic the expected signal. This is performed by assigning the three components with a random catalogue correlation (where no signal is expected, e.g. $\langle n_C n_{R_Q}\rangle, \langle n_{R_C} n_Q\rangle, \langle n_{R_C} n_{R_Q}\rangle$) the number of pairs expected from a purely random distribution. For the component which contains the signal ($\langle n_C n_Q\rangle$) we then insert an overdensity or deficit around the random background level to mimic the expected signal.

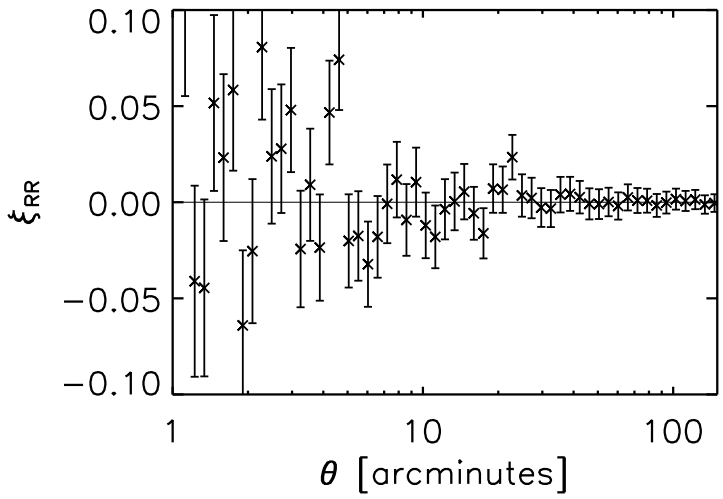

Figure 5.16: Testing the cross correlation code with random datasets.

To test the normalisation procedure, we create the uncorrelated random data sets to have similar number densities as the data used for the actual measurement by assigning the number of random pairs relative to the area of the the search annuli $\theta + \Delta\theta$ and to the number densities of the datasets. For each photometric band the final number of pairs at each magnitude for these random components are given by,

$$\langle n_{R_C} n_Q(m) \rangle = n_{R_C} n_Q(m) \pi \big((\theta + \Delta\theta)^2 - \theta^2 \big) \,, \tag{5.38}$$

$$\langle n_C n_{R_Q}(m) \rangle = n_C n_{R_Q}(m) \pi \big((\theta + \Delta\theta)^2 - \theta^2 \big) \,, \tag{5.39}$$

$$\langle n_{R_C} n_{R_Q}(m) \rangle = n_{R_C} n_{R_Q}(m) \pi \big((\theta + \Delta\theta)^2 - \theta^2 \big) \,. \tag{5.40}$$

For the SDSS DR6 quasar catalogue, the expected signal presents itself as an overdensity in bright quasars, and an under density in faint quasars, depending on the sign of $\big(\alpha(m) - 1\big)$, see Figure 5.5. We create $\langle n_C n_Q \rangle$ to reflect this property, by multiplying the randomly expected cross correlation by a function $Q(m)$ which encodes the magnitude dependence of the expected signal, such that,

$$\langle n_C n_Q \rangle = Q(m) \langle n_{R_C} n_{R_Q} \rangle \,, \tag{5.41}$$

where $Q(m)$ is found by equating the expected signal of Equation 5.23, to the measured signal of Equation 5.34,

$$\frac{\langle n_C n_Q \rangle}{\langle n_{R_C} n_{R_Q} \rangle} - 1 = b \big(\alpha(m) - 1 \big) \, \xi_{\mu\delta} \,, \tag{5.42}$$

and by substituting Equation 5.41 into Equation 5.42 we obtain

$$Q(m) \quad = \quad b\left(\alpha(m)-1\right)\xi_{\mu\delta}(\theta)+1\ , \tag{5.43}$$

and we set the value of bias to 3.4 (for motivation see §5.4.2). We choose to use the estimator $\xi_{\mu\delta}$ from the MaxBCG cluster dataset. Examining Equation 5.43 shows that the function $Q(m)$ has the correct statistics depending on the sign of $\left(\alpha(m)-1\right)$ e.g,

$$\left(\alpha(m)-1\right)\begin{cases} >0 & Q(m)\rightarrow \text{overdensity} \\ =0 & Q(m)\rightarrow \text{no change} \\ <0 & Q(m)\rightarrow \text{underdensity} \end{cases}.$$

This allows the test $\left\langle n_C n_Q(m)\right\rangle$ data component with the correct statistics to be computed,

$$\left\langle n_C n_Q(m)\right\rangle \quad = \quad n_C n_Q(m)\pi\left((\theta+\Delta\theta)^2-\theta^2\right)Q(m)\ . \tag{5.44}$$

Magnification bias software test

For the pipeline test, each photometric band is split into five magnitude ranges with each magnitude range containing approximately equal numbers of quasars. The values of $\left\langle\alpha(m)-1\right\rangle$ for each magnitude range, and the combined $\left\langle\alpha-1\right\rangle$, calculated using Equation 5.36, are shown in Table 5.3, and we see that $\left\langle\alpha(m)-1\right\rangle$ is large and positive for the brightest quasars, reducing in size for slightly fainter quasars and going negative for the faintest quasars. This trait is expected from Figure 5.5, which shows the quasar number densities, and corresponding values of $\left(\alpha(m)-1\right)$ at each magnitude.

	$\left\langle\alpha(m)-1\right\rangle$					
SDSS Band	Apparent magnitude					
	$16.0<19.5$	$19.5<20.1$	$20.1<20.5$	$20.5<20.8$	$20.8<20.9$	Total $\left\langle\alpha-1\right\rangle$
u	0.608	0.034	−0.308	−0.568	−0.723	0.460
g	0.529	−0.039	−0.360	−0.598	−0.738	0.460
r	0.488	−0.053	−0.355	−0.580	−0.711	0.440
i	0.494	−0.071	−0.406	−0.666	−0.820	0.486
	Apparent magnitude					Total $\left\langle\alpha-1\right\rangle$
	$16.0<19.1$	$19.1<19.6$	$19.6<19.9$	$19.9<20.2$	$20.2<20.3$	
z	0.701	0.237	−0.017	−0.232	−0.378	0.380

Table 5.3: The number weighted average values of $\left\langle\alpha(m)-1\right\rangle$ calculated from the quasar distribution for the MaxBCG cluster catalogue. We show the SDSS filter, the value for each magnitude range and the stacked value for each band. Each of the five magnitude bins contain roughly equal numbers of quasars. The SDSS z band has a lower magnitude limit due to the incompleteness at fainter magnitudes and therefore has a higher (less negative) apparent magnitude.

Each ξ_{CQ} measurement is stacked as described in §5.3.2, and the stacked value of $\langle \alpha - 1 \rangle$, averaged across each band has a final value of 0.447, and is inputted into Equation 5.23 to calculate the theoretical model. The final weighted signal $\langle \alpha - 1 \rangle \xi_{CQ}(\theta)$, as a function of separation angle θ, is shown in Figure 5.17 with the model overplotted.

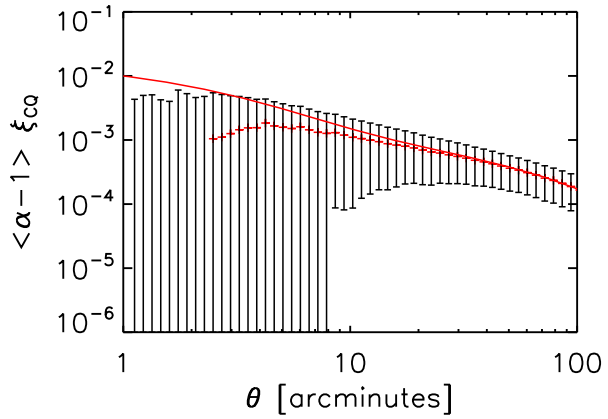

Figure 5.17: Testing the magnification bias pipeline with data created as §5.3.3. The data points with Poisson errors, are the stacked signal across each of the five bands and magnitude ranges, as described in §5.3.2 and Table 5.3. We overplot the expected model using the averaged final value of $\langle \alpha - 1 \rangle = 0.447$ and a bias of 3.4.

At large scales, the agreement is excellent but at smaller scales the measured and expected values diverge, but remain within the Poisson errors. As the scale reduces further still the disagreement between the signal measured from the simulated data and the expected signal grows. We found this effect to be an artifact of treating a discrete density field (the number of quasars is an integer) as continuous, because we cannot measure a fractional number of quasars. To check this hypothesis, we modified the simulated data to allow for the number of pairs to be a "real number" rather than an "integer number" and repeated the calculation. Figure 5.18 shows the effect on the agreement between the real number simulated data, and expected curve, with excellent agreement even at small scales. The effect of having integer numbers of data pairs is reduced as the number of pairs increases, as can be seen in the large scale agreement of Figure 5.17.

An alternative stacking technique is to multiply each quasar in the numerator of Equation 5.34 by the value of $(\alpha(m) - 1)$ at that point in magnitude space, which is equivalent to all the data being simultaneously stacked to produce one measurement per band, per angle. We average over the bands, and average over values of $\langle \alpha - 1 \rangle$, to produce the expected curve. Figures 5.19 show this stacking method for integer and real number pairs.

Figures 5.18 and 5.19 demonstrate that the magnification bias pipeline is working. In §5.3.4 we apply this pipeline to measure the magnification bias around the MaxBCG and C4 clusters.

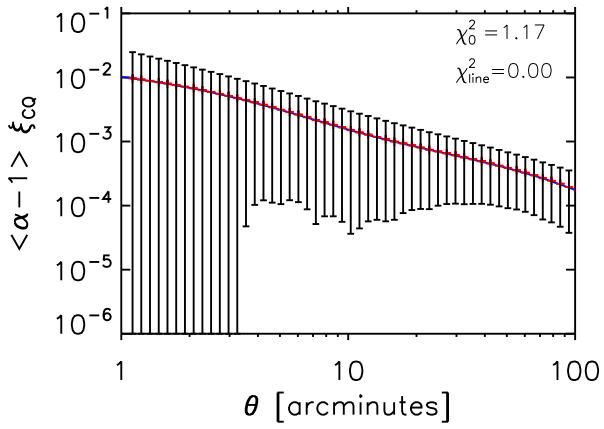

Figure 5.18: Testing the magnification bias pipeline with real number data pairs. The data points with Poisson errors (see §5.3.5), are the measured signal stacked across each of the five bands and magnitude ranges, as described in 5.3.2 and Table 5.3. The expected curve fits the data points.

5.3.4 Measuring the magnification bias

In this section we describe two approaches to estimate the errors on the measurement of the cross correlation, the jackknife error and the Poisson error. We compare the error estimates and then present the results of the magnification bias as measured for the MaxBCG and C4 cluster catalogues. We finish by splitting the stacked measurement into a positive and negative expected component, which would provide conclusive evidence of the weak lensing nature of the magnification bias.

5.3.5 Errors on the measurement of the magnification bias

We use two techniques to assign errors to the weighted correlation function, the Poisson error which is used when there is expected to be no covariance between data sets, and is due to counting statistics. The Poisson error has been used exclusively when creating the simulated data due to the lack of jackknife errors. The jackknife error is more accurate at describing covariances of cross correlation measurements on large scales. We describe both error estimates below and compare them for the magnification bias measurement around the MaxBCG clusters.

Poisson errors

Counting processes are modelled by Poisson statistics. Cross correlations are real pair number counts divided by random number counts. To calculate the Poisson error on the magnification

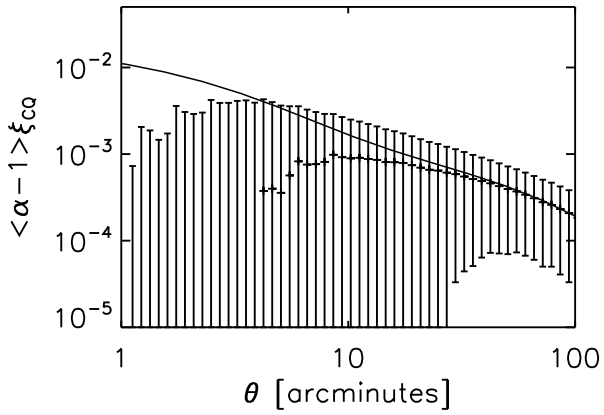

(a) Test data with integer number pairs

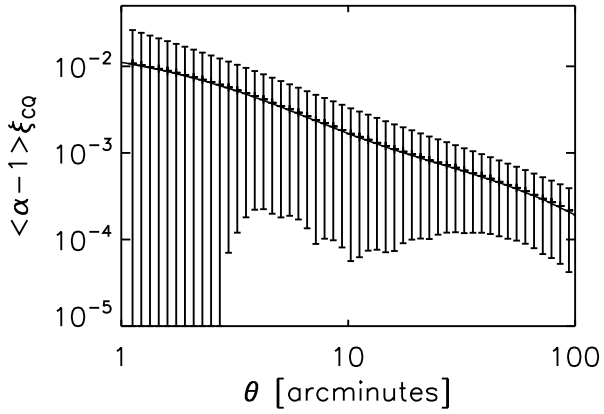

(b) Test data with real number pairs

Figure 5.19: The magnification bias ξ_{CQ} multiplied by the band averaged value of $< \alpha - 1 >$ as a function of increasing angular separation θ. We multiply each quasar in the numerator of Equation 5.34 by the value of $(\alpha(m) - 1)$ at that magnitude. Errors are Poisson. The departure from expected at small scales in 5.19(a) is due to the discreteness of the density fields.

bias measurement we use the propagation of error formula applied to Equation 5.34,

$$\Big(\Delta\xi(\theta)\Big)^2 = \big(\Delta\langle n_C n_Q\rangle \frac{\mathrm{d}\xi}{\mathrm{d}\langle n_C n_Q\rangle}\big)^2 + \big(\frac{\mathrm{d}\xi}{\mathrm{d}\langle n_{R_C} n_Q\rangle}\Delta\langle n_{R_C} n_Q\rangle\big)^2 + \big(\frac{\mathrm{d}\xi}{\mathrm{d}\langle n_C n_{R_Q}\rangle}\Delta\langle n_C n_{R_Q}\rangle\big)^2 + \big(\frac{\mathrm{d}\xi}{\mathrm{d}\langle n_{R_C} n_{R_Q}\rangle}\Delta\langle n_{R_C} n_{R_Q}\rangle\big)^2 , \quad (5.45)$$

and model the 1σ errors by $\Delta n = 1 + \sqrt{n+1}$ (Gehrels, 1986). Substituting into Equation 5.45 and rearranging, yields the Poisson error,

$$\Big(\Delta\xi(\theta)\Big)^2 = \frac{1}{\big\langle n_{R_C} n_{R_Q}\big\rangle^2}\Bigg(\Delta\big\langle n_C n_Q\big\rangle^2 + \Delta\big\langle n_{R_C} n_Q\big\rangle^2 + \Delta\big\langle n_C n_{R_Q}\big\rangle^2 + \frac{\Delta\big\langle n_{R_C} n_{R_Q}\big\rangle^2}{\big\langle n_{R_C} n_{R_Q}\big\rangle^2}\Big(\big\langle n_C n_Q\big\rangle - \big\langle n_{R_C} n_Q\big\rangle - \big\langle n_C n_{R_Q}\big\rangle\Big)^2\Bigg) . \quad (5.46)$$

We note that Equation 5.46 reduces to the standard correlation error in the limit of large random catalogues $\big(\Delta\xi\big)^2 = \big(1+\xi\big)/n_C n_Q$.

The Poisson error of the weighted measurement is found by reapplying the propagation of error formula to Equation 5.37 resulting in

$$\Big(\Delta\big(\big\langle\alpha-1\big\rangle\xi(\theta)\big)\Big)^2 = \big\langle\alpha-1\big\rangle^2\Big(\Delta\xi(\theta)\Big)^2 + \Big(\Delta\big\langle\alpha-1\big\rangle\Big)^2\xi(\theta)^2 , \quad (5.47)$$

where $\Delta\big\langle\alpha(m)-1\big\rangle$ is the Poisson error on the number of quasars in each magnitude bin.

Jackknife errors

Alternatively, jackknife re-samplings can be used to estimate the error of a statistic t, from a data sample. Here the statistic is the weighted cross correlation $\big\langle\alpha-1\big\rangle\xi_{CQ}$. The jackknife process splits the sample into N_{JK} roughly equal area regions. The i^{th} region is removed and $t_{N_{JK},i}$ calculated for the remaining $N_{JK}-1$ data sample. This region is replaced and the next region removed and t recalculated. This process is repeated N_{JK} times and an array of weighted cross correlations obtained.

The variance of t is given by

$$V(t) = \frac{N_{JK}-1}{N_{JK}}\sum_i \Big(t_{N_{JK},i} - \big\langle t_{N_{JK}}\big\rangle\Big)^2 , \quad (5.48)$$

where $\big\langle t_{N_{JK}}\big\rangle$ is the mean of the measurements $t_{N_{JK},i}$. The variance $V(t)$, should be used with caution, as it can be related to the size and shape of the removed regions, and we examine this effect by comparing the error from four jackknives, performed by splitting the survey area into $N_{JK} = [10, 30, 50, 100]$ approximately equal area subregions.

The jackknife covariance matrix cV describes the correlation between data points θ_i and θ_j and is given by

$$cV(\theta_1,\theta_2) = \frac{N_{JK}-1}{N_{JK}}\sum_{ij}\Big(t_{N_{JK},i}(\theta_1) - \big\langle t_{N_{JK}}(\theta_1)\big\rangle\Big)\Big(t_{N_{JK},j}(\theta_2) - \big\langle t_{N_{JK}}(\theta_2)\big\rangle\Big) , \quad (5.49)$$

We compare with the Poisson errors and jackknife errors in the next section.

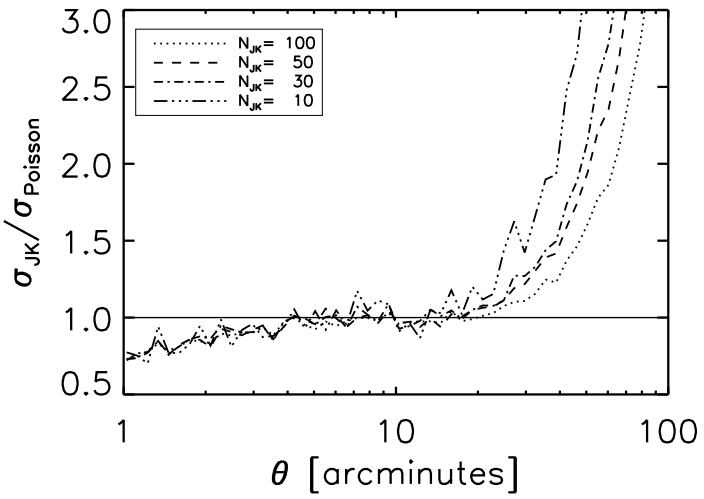

Figure 5.20: The ratio of jackknife error σ_{JK}, to Poisson error $\sigma_{Poisson}$ on the weighted magnification bias measurement for the MaxBCG cluster sample. The lines correspond to splitting the sky into N_{JK} equal area regions.

Error comparison

Figure 5.20 shows the ratio of the jackknife errors to Poisson error as a function of angular separation for the weighted magnification bias using the MaxBCG clusters and SDSS DR6 quasars.

The agreement at medium angular separation suggests the error in this regime can be approximated by Poisson. At higher angular separations the ratio increases, which is where covariances are expected, with the jackknives measure. At lower angles the jackknife errors are smaller than the Poisson errors, which means the numbers of pairs at these separations are very small. The fact that the jackknife errors and Poisson errors are almost always within a factor of two of each other, show that the datasets are Poisson dominated.

We examine the consistency between the different N_{JK} jackknife errors in Figure 5.21, which suggest that on small and intermediate scales the jackknifes are very similar, only diverging at high angular separations. We choose to use the $N_{JK} = 30$ error estimator in the remainder of this chapter, which remain within a factor of two of the other estimators across all scales.

5.3.6 Stacking the clusters

In this section, we present the results of measuring the magnification bias around the MaxBCG and C4 cluster catalogues. We follow the stacking techniques documented in §5.3.2 and §5.3.3, and calculate errors as in §5.3.5.

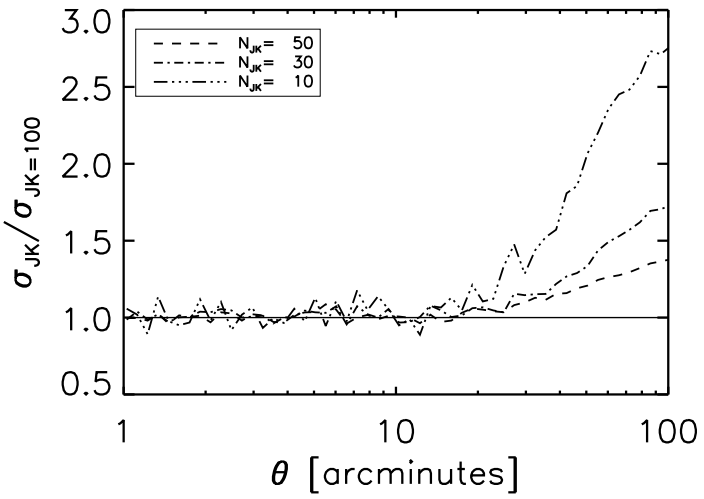

Figure 5.21: The ratio of jackknife error σ_{JK} at $N_{JK} = [10, 30, 50]$ with $N_{JK} = 100$, on the weighted magnification bias measurement for the MaxBCG cluster sample. The lines correspond to splitting the sky into N_{JK} equal area regions.

Figures 5.22 and 5.24 show the weighted cross correlation $\langle\alpha - 1\rangle\xi_{CQ}$ as a function of separation angle θ, when the measurements are performed in five magnitude ranges and then stacked across the bands. The red (blue) data points show the Poisson error (jackknife error). The slight angular offset between the different coloured data points is artificial, and allows the comparison of the different error estimates. Overplotted is the expected theoretical line assuming a flat $\sigma_8 = 0.9, \Omega_m = 0.3, h = 0.7$ ΛCDM cosmology, with bias set at 3.4 and the stacked averaged value of $\langle\alpha - 1\rangle = 0.447$ $(= 0.450)$ for MaxBCG (C4) clusters. Both figures show a fair amount of scatter around the line of best fit, with some data points and their 1σ falling below the axis of the plots (on these log plots the θ axis should be evenly populated). As shown in Figure 5.20, and in Figures 5.22 and 5.24, the Poisson error bars are similar in size to the jackknife error. This means that we are Poisson noise dominated, which implies that our data samples are not large enough to measure the magnification bias accurately. If we could increase the number of clusters, perhaps with future southern sky surveys, we could reduce the scatter and error on these data points, see §6.4. We have also investigated binning the data in different angular separations, without major improvement. We also show the covariance matrix for the MaxBCG dataset in Figure 5.23. We note that the off diagonal terms of the covariance matrix are small until $\gtrsim 60$ arcminutes, as expected from Figure 5.20.

Alternatively, we can combine the data into one magnitude bin by multiplying each quasar pair in the numerator of Equation 5.34 by the value of $\big(\alpha(m) - 1\big)$, at that magnitude. We then stack this signal across each band, and show the results in Figure 5.25, for the MaxBCG clusters, and Figure 5.26 for the C4 clusters. For clarity, we plot only Poisson errors for these data points, and overplotted is the theoretical expectation under the same cosmology and bias. Here the combined,

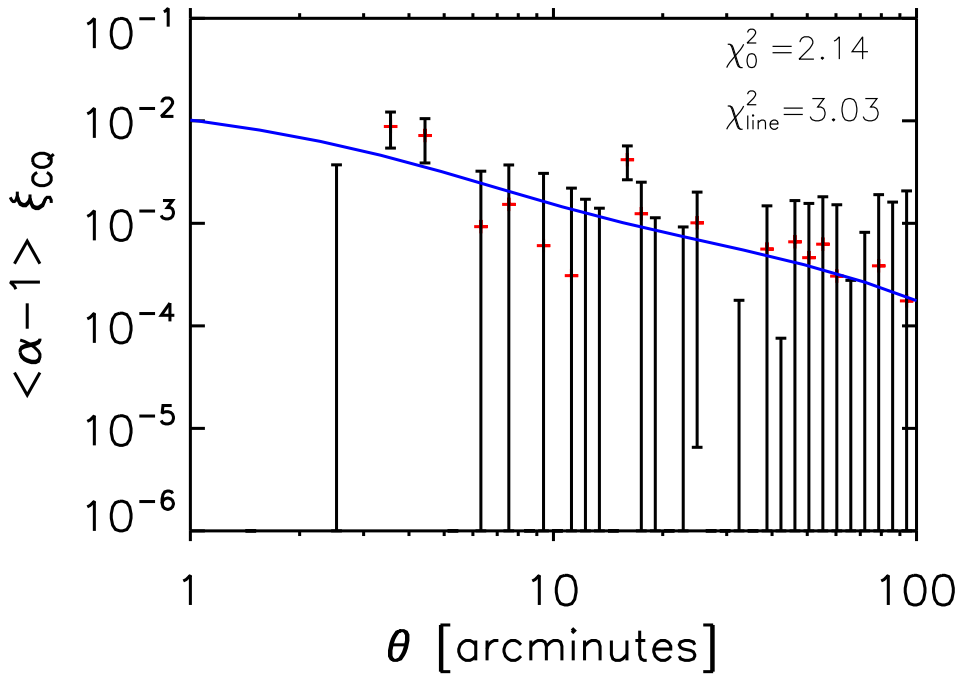

Figure 5.22: The weighted magnification bias $\langle\alpha-1\rangle\xi_{CQ}$ as a function of separation angle θ for the MaxBCG cluster sample. We plot the data points with the jackknife errors, and show the detection significance χ^2_0 and the reduced χ^2 for the expected theoretical line assuming a flat $\sigma_8 = 0.9, \Omega_m = 0.3, h = 0.7$ ΛCDM cosmology, with bias set at 3.4, and $\langle\alpha-1\rangle = 0.447$ as measured from the data.

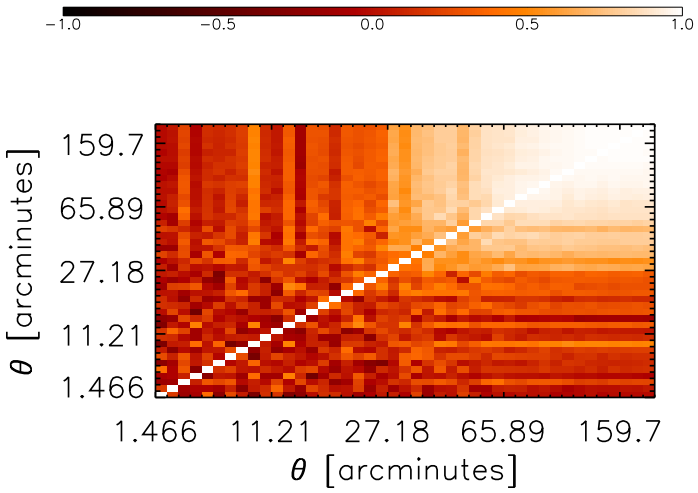

Figure 5.23: The covariance matrix for the weighted magnification bias $\langle\alpha-1\rangle\xi_{CQ}$ as a function of separation angle θ for the MaxBCG cluster sample.

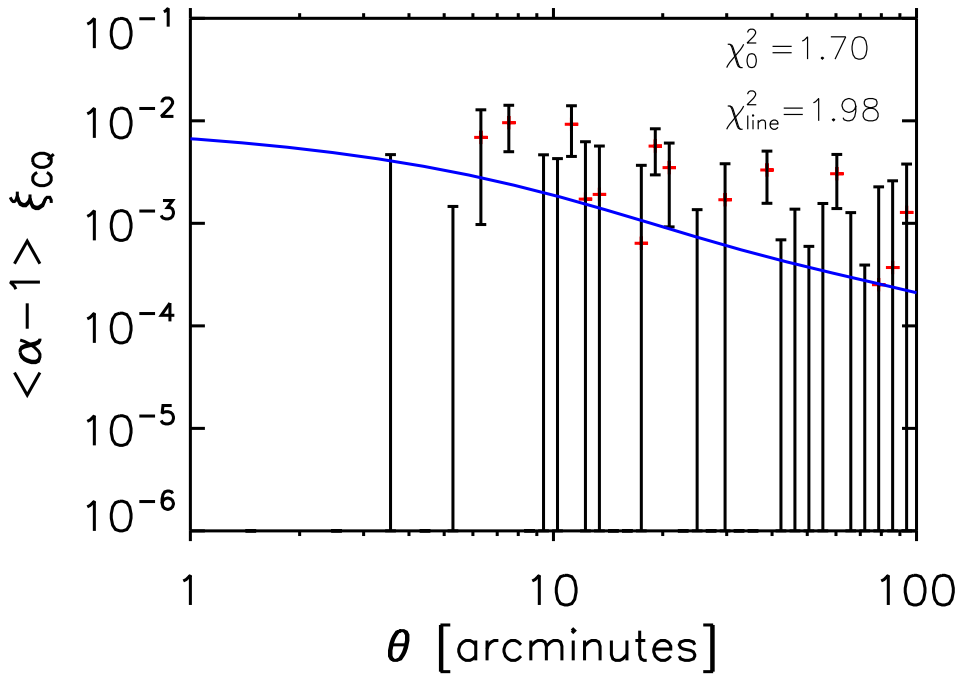

Figure 5.24: The weighted magnification bias $\langle\alpha - 1\rangle\xi_{CQ}$ as a function of separation angle θ for the C4 cluster sample. We plot the data points with the jackknife errors, and show the detection significance χ_0^2 and the reduced χ^2 for the expected theoretical line assuming a flat $\sigma_8 = 0.9, \Omega_m = 0.3, h = 0.7$ ΛCDM cosmology, with bias set at 3.4, and $\langle\alpha - 1\rangle = 0.450$ as measured from the data.

stacked value of $\langle\alpha - 1\rangle$ is 0.471 for both the MaxBCG and C4 cluster catalogues.

These figures show that the data points are again, only a moderate fit to the expected line with a fair amount of scatter (again, on these log plots the θ axis should be evenly populated). This alternative binning technique has failed to drastically improve the signal-to-noise, and we conclude this is again due to the relatively low number densities of clusters and quasars forcing the measurement to be Poisson dominated.

With these restrictions in mind, we can still continue by examining the unweighted signal in the regimes where we expect a positive, and a negative correlation. The detection of a change in the sign of the cross correlation is the conclusive evidence that weak gravitational lensing has occurred, as systematics errors are not expected to reproduce the magnitude dependent correlation sign.

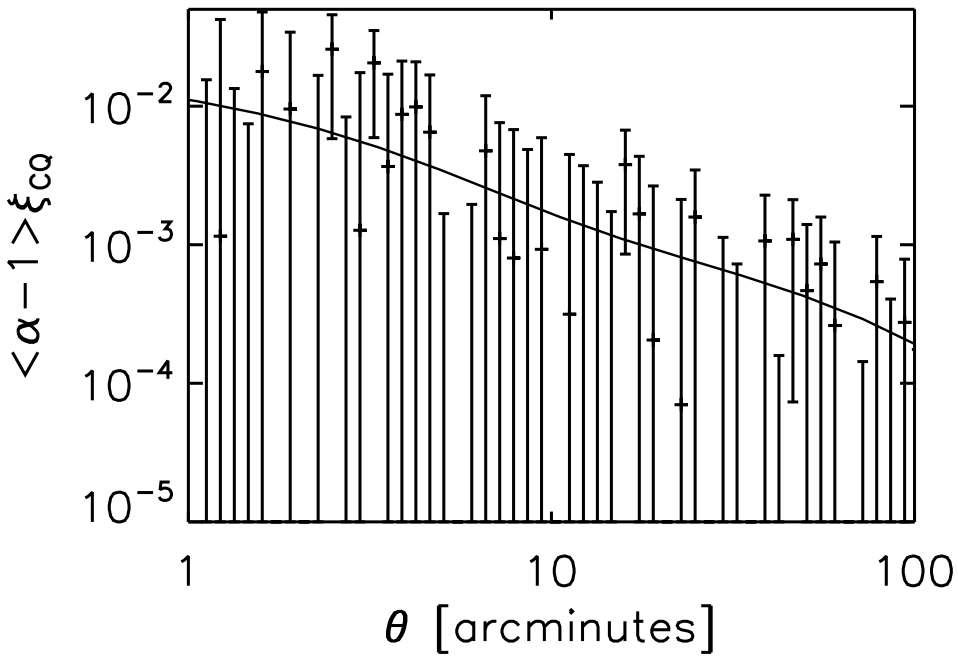

Figure 5.25: The cross correlation ξ_{CQ} with each quasar multiplied by the value of $\big(\alpha(m) - 1\big)$ at each magnitude, producing one measurement per band per angle, stacked across the bands for the MaxBCG clusters. We show Poisson errors, and overplot the theoretical expectation, assuming a flat $\sigma_8 = 0.9, \Omega_m = 0.3, h = 0.7$ ΛCDM cosmology, with bias set at 3.4, and the stacked value of $\big\langle \alpha - 1 \big\rangle = 0.471$ as measured by the data.

5.3.7 The expected sign change in the magnification bias

So far we have stacked the signal in each band, and stacked across the bands, to increase the signal-to-noise. We can however, split the data into two magnitude bins, those which are expected to produce a positive correlation, and those for which the correlation is expected to be negative. This is a direct test of the magnification bias, as no form of contamination is expected to reproduce this magnitude dependent feature. The transition between the positive and negative expected correlation occurs at the values $[19.9, 19.8, 19.8, 19.8, 19.8]$ in the photometric bands u, g, r, i, z, for our quasar dataset (see Figure 5.5). We stacked the positive signal for each band, and the negative signal for each band to increase the signal-to-noise. We expect the negative signal to have higher signal-to-noise because there are more fainter quasars (see Figure 5.5), and we have shown that we are Poisson dominated in §5.3.6. We present the ξ_{CQ} signal from Equation 5.23, without the $\big\langle \alpha - 1 \big\rangle$ weighting, which retains the expected signal sign change, for the test data in Figure 5.27, and actual data in Figures 5.28 and 5.29. Note, we still need to use an instance of $\big\langle \alpha - 1 \big\rangle$ for the theoretical curve as shown in Equation 5.23. Overplotted are the expected signals in a flat $\sigma_8 = 0.9, \Omega_m = 0.3, h = 0.7$ ΛCDM cosmology, with bias $= 3.4$, and $\big\langle \alpha - 1 \big\rangle = 0.605$ (-0.630) measured from the data for the positive (negative) branch.

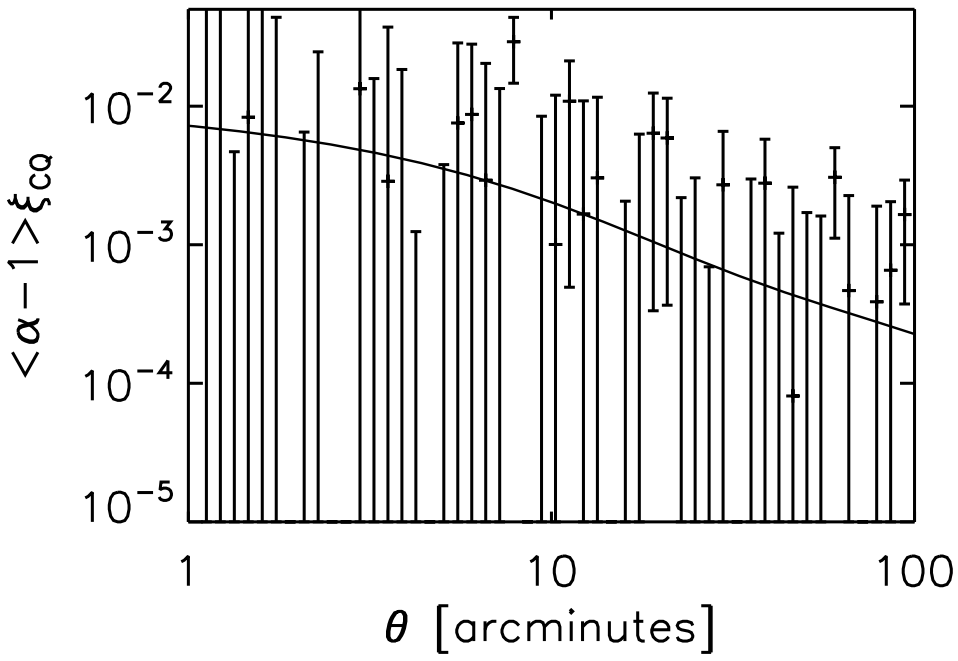

Figure 5.26: The cross correlation ξ_{CQ} with each quasar multiplied by the value of $\big(\alpha(m) - 1\big)$ at each magnitude, producing one measurement per band per angle, stacked across the bands for the C4 clusters. We show Poisson errors, and overplot the theoretical expectation assuming a flat $\sigma_8 = 0.9, \Omega_m = 0.3, h = 0.7$ ΛCDM cosmology, with bias set at 3.4, and the stacked value of $\big\langle \alpha - 1 \big\rangle = 0.471$ as measured by the data.

The simulated data shows excellent agreement with the theoretical curves on large scales. On smaller scales, Figure 5.27(a) shows a departure from theory, which is again due to the discrete nature of this data set. The increased number density of faint quasars compared to bright quasars, allows the data to agree with the expected negative correlation on smaller scales than the positive correlation. This discrepancy is removed once real number data pairs are allowed.

The real data, Figure **??** is somewhat noisier. We have already shown that our measurements are Poisson dominated with a high level of scatter, and so we expect to reduce the agreement between observation and theory when we split the signal into two. Accordingly, we could improve the signal-to-noise of this measurement by increasing the number of clusters and quasars, with additional surveys (see §6.4).

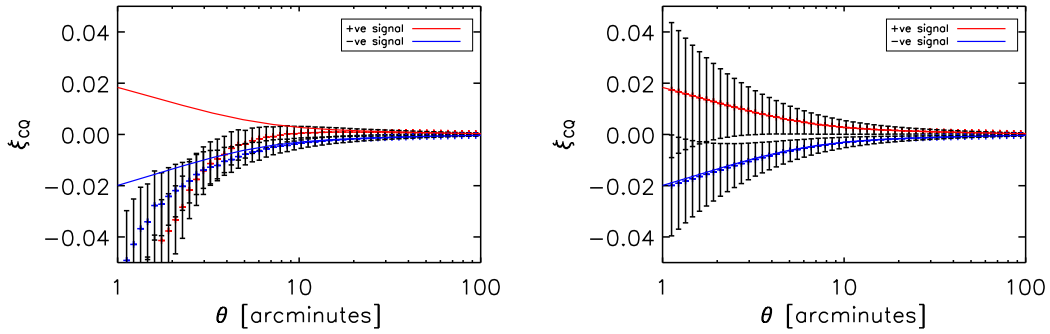

(a) Integer number pairs.

(b) Real number pairs.

Figure 5.27: The unweighted cross correlation ξ_{CQ} (Equation 5.23) as a function of angle, stacked in magnitude bins and averaged across bands, to produce a positive and negative signal. Overplotted is the expected signal in a flat $\sigma_8 = 0.9, \Omega_m = 0.3, h = 0.7$ ΛCDM cosmology, with bias $= 3.4$, and $\langle \alpha - 1 \rangle = 0.366$ (-0.397) measured from the data for the positive (negative) branch. The left plot show the simulated data points for integer number pairs of clusters and quasars, and the right plot shows real number pairs of (simulated) clusters and quasars. The detection significance χ^2_0 and the reduced χ^2 to the theoretical lines are shown on the plots.

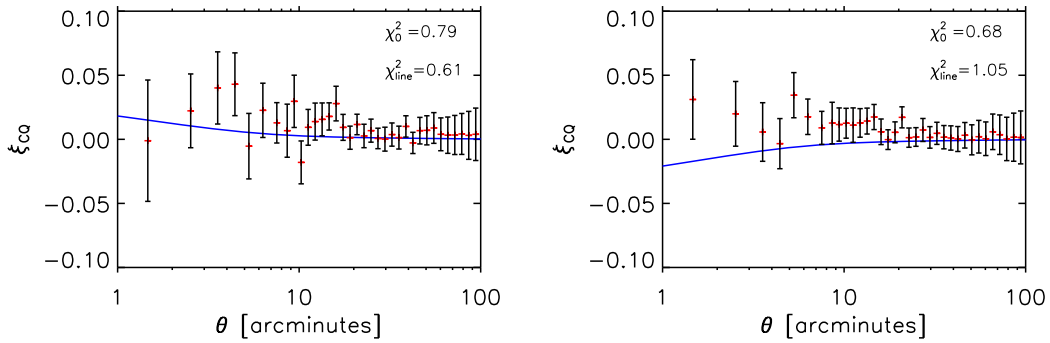

(a) The MaxBCG expected positive signal.

(b) The MaxBCG expected negativee signal.

Figure 5.28: The unweighted cross correlation ξ_{CQ} (Equation 5.23) as a function of angle, stacked in magnitude bins to produce a positive and negative signal. The left plot shows the signal for the expected positive signal using the MaxBCG clusters, and the right plot shows the expected negative signal. Overplotted are the expected signals assuming a flat $\sigma_8 = 0.9, \Omega_m = 0.3, h = 0.7$ ΛCDM cosmology, with bias set at 3.4, with a stacked value of $\langle \alpha - 1 \rangle = 0.366$ (-0.397) for the positive (negative) branch as measured by the data. The detection significance χ^2_0 and the reduced χ^2 to the theoretical lines are shown on the plots.

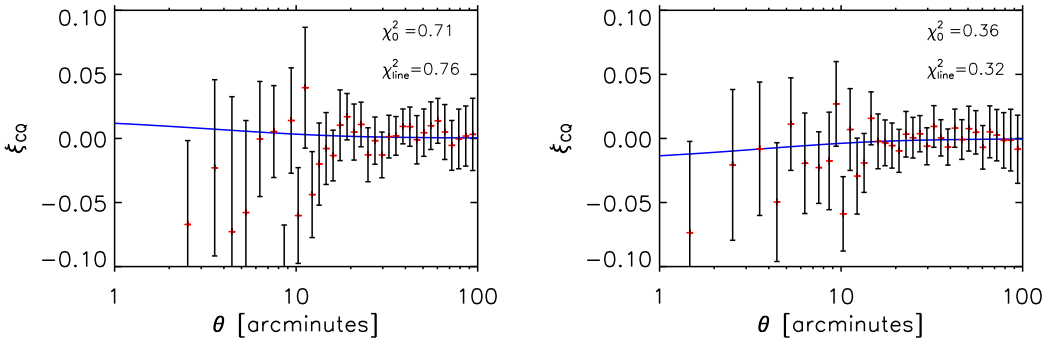

(a) The C4 expected positive signal.

(b) The C4 expected negative signal.

Figure 5.29: The unweighted cross correlation ξ_{CQ} (Equation 5.23) as a function of angle, stacked in magnitude bins to produce a positive and negative signal. The left plot shows the signal for the expected positive signal using the C4 clusters, and the right plot shows the expected negative signal. Overplotted are the expected signals assuming a flat $\sigma_8 = 0.9, \Omega_m = 0.3, h = 0.7$ ΛCDM cosmology, with bias set at 3.4, with a stacked value of $\langle \alpha - 1 \rangle = 0.366$ (-0.397) for the positive (negative) branch as measured by the data.

5.4 Fitting cosmology and measuring bias

In this section, we use the measurement of the magnification bias around the MaxBCG and C4 cluster to perform a χ^2 fit to the cosmological models (as listed in Table 5.1 and calculated in §5.2.7), and fit for σ_8, Ω_m, and bias. We then convert the measured value of bias into a upper bound on cluster mass, using theoretical models.

5.4.1 Constraining parameters

In this section we present the results of fitting the theoretical curves, see §5.2.9, to the measured magnification bias data. We first demonstrate the accuracy of our software using simulated data, and then present the significance contours after marginalising over other parameters.

We perform a minimum χ^2 analysis, summing over angular separations θ, comparing the weighted magnification bias measurement $\langle \alpha - 1 \rangle \xi_{CG}$ (with jackknife error σ), to the predictions for different theoretical models $M = M(\Omega_m, \sigma_8, b)$. The value of χ^2_{ijk} for each $\Omega_{m_i}, \sigma_{8_j}, b_k$ produces a likelihood surface and is given by,

$$\chi^2_{ijk} = \sum_{\theta} \left(\frac{\langle \alpha - 1 \rangle \xi_{CG}(\theta) - M_i(\theta, \Omega_{m_i}, \sigma_{8_j}, b_k)}{\sigma(\theta)} \right)^2, \tag{5.50}$$

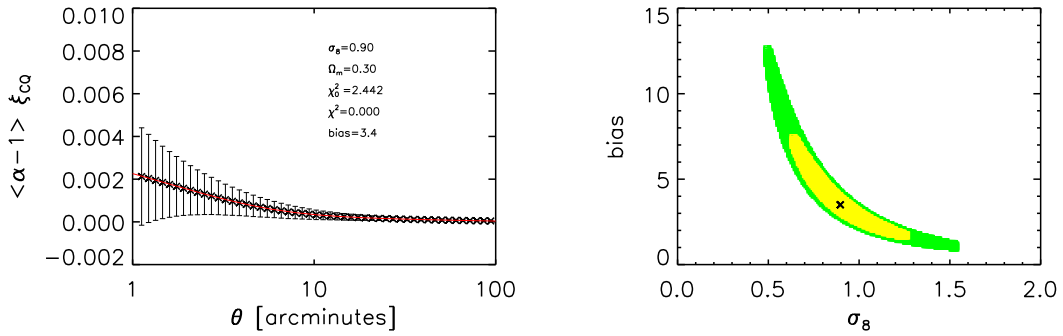

(a) Best fit parameters

(b) 2d contours

Figure 5.30: The results of a χ^2 likelihood scan to the simulated data, created in a $\sigma_8 = 0.9, \Omega - m = 0.3, h = 0.7$ ΛCDM with bias set to 3.4 (see §5.3.3). Figure 5.30(a) shows the test data points with the theoretical expectation for the best fitting cosmology overplotted. Additionally, we show the values of the best fitting model, the corresponding reduced χ^2 value of the best fit, and the reduced detection significance χ^2_0. These best fitting parameters are highlighted by a cross on the 2d slice through the likelihood surface, corresponding to $\Omega_m = 0.3$, shown in Figure 5.30(b), with the yellow (green) region representing 68% (98.5%) of the PDF.

and the significance of the detection, is given by,

$$\chi^2_0 = \sum_\theta \left(\frac{\langle \alpha - 1 \rangle \xi_{CG}(\theta)}{\sigma(\theta)} \right)^2, \tag{5.51}$$

and the reduced χ^2 is found by dividing their values by the number of degrees of freedom.

In Figure 5.30, we show the results of a χ^2 likelihood scan to the simulated data, created with cosmological parameters set to $\sigma_8 = 0.9, \Omega_m = 0.3, h = 0.7$ ΛCDM and a bias of 3.4, see §5.3.3. Figure 5.30(a) shows the simulated data points with the best fitting theoretical prediction, and overplotted are the reduced detection significance $\chi^2_0 = 2.44$ (there are 51 data points), the values of the model parameters, and the corresponding reduced $\chi^2 = 0.0002$. The small value of the χ^2 is due to the simulated data being created from the model, which is correctly recovered. The small value of the detection significance is due to the relatively large Poisson error bars, which further shows the need to increase the data sample. In Figure 5.30(b) a 2d slice through the likelihood surface, corresponding to $\Omega_m = 0.3$ is shown, with the yellow (green) contours representing 68% (98.5%) of the Probability Distribution Function (hereafter PDF), and the black cross shows the best fitting model.

We apply this pipeline to the MaxBCG and C4 magnification bias measurements, and show the

2d parameter error contours, after marginalising over the third parameter using,

$$\exp\left(-\chi^2_{ij}/2\right) = \int \mathrm{d}k \, \exp\left(-\chi^2_{ijk}/2\right) , \tag{5.52}$$

shown in Figures 5.31 and 5.32, with the marginalised parameter indicated beneath the plot.

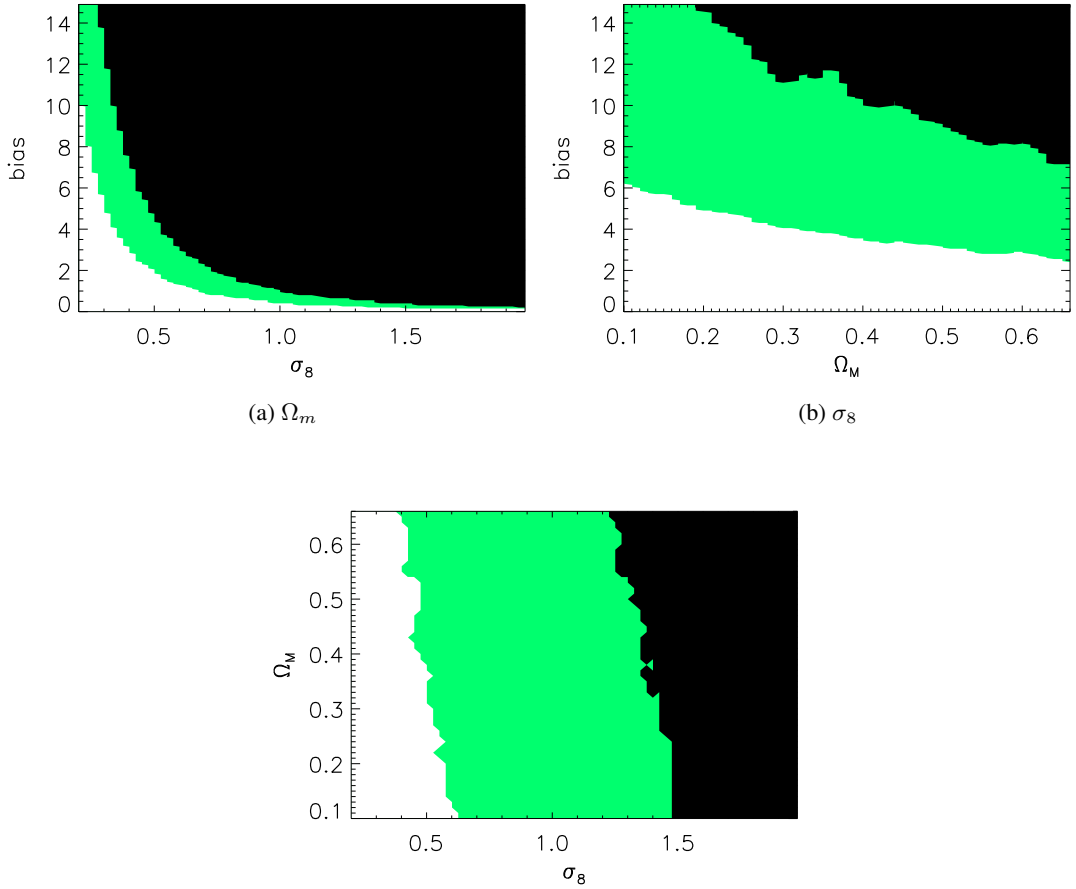

(a) Ω_m (b) σ_8

(c) bias

Figure 5.31: The probability surfaces found from fitting cosmological models to the MaxBCG magnification bias measurement. Figures 5.31(a)-5.31(c) show the 68% (white) and 98.5% (green) contours of the PDF after marginalising over the third parameter, as indicated below the each figure. The examined parameter space is shown by the black regions.

The quality of the data allows the null hypothesis (i.e. not a detection) to be a good fit to the magnification measurement; recalling that bias is a multiplicative factor in the theoretical prescription (Equation 5.23) therefore allows any value of Ω_m and σ_8 to produce a reasonable fit to the data for very low values of bias. Likewise if σ_8 is sufficiently small, all values of bias and Ω_m are allowed. Figure 5.31(a) shows the 2d bias-σ_8 likelihood surface, after marginalising over Ω_m, with concordance values $\sigma_8 \sim 0.8$, bias ~ 3.4, being just outside of the green 98.5% contours

of the PDF. The effect of the null hypothesis fitting the data, is apparent as the 98.5% contours asymptote on both axis. Figure 5.31(b) shows the weak constraining power of the combination of bias and Ω_m, the currently accepted value of bias and Ω_m are well within the 68% confidence region but even at high values ($\Omega_m = 0.68$) the 1σ contours have yet to converge. Marginalising over bias, Figure 5.31(c) shows that $\sigma_8 > 1.5$ is ruled out at the 98.5% level.

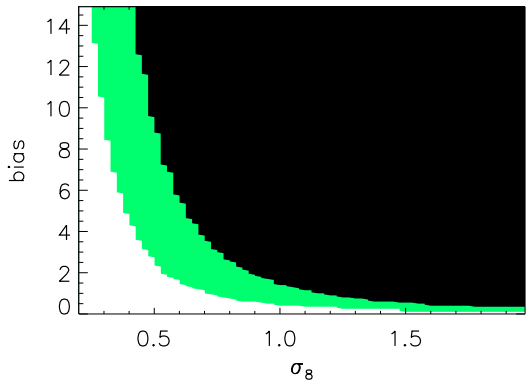

(a) Ω_m

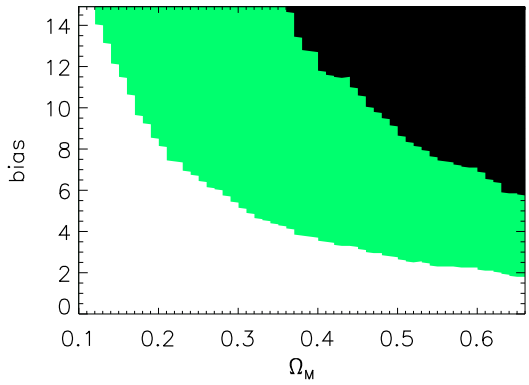

(b) σ_8

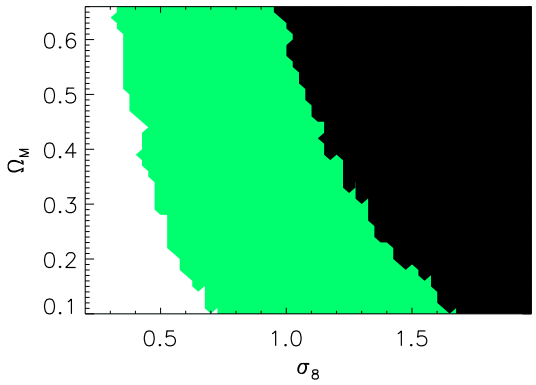

(c) bias

Figure 5.32: The probability surfaces found from fitting cosmological models to the C4 magnification bias measurement. Figures 5.32(a)-5.32(c), show the 68% (white) and 98.5% (green) contours of the PDF after marginalising over the third parameter, as indicated below each figure. The examined parameter space is shown by the black regions.

The C4 clusters have lower constraining power than the MaxBCG clusters, which is expected if the magnification bias signal is Poisson dominated, because of the lower number of C4 clusters. Although, the Figures 5.31 and 5.32 are consistent, which gives good confidence that the method is robust.

We continue by marginalising over two parameters, and presenting the probability distributions

for the remaining parameters in Figures 5.33 and 5.34.

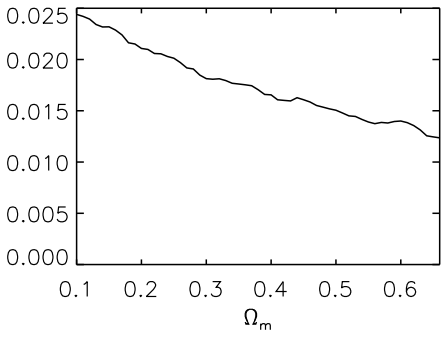

(a) σ_8, bias

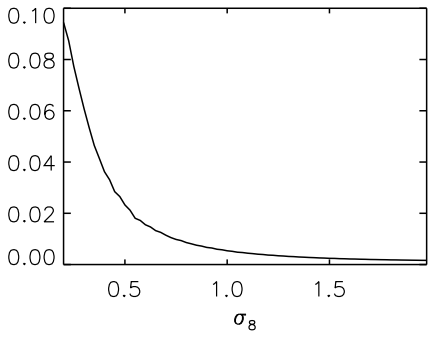

(b) Ω_m, bias

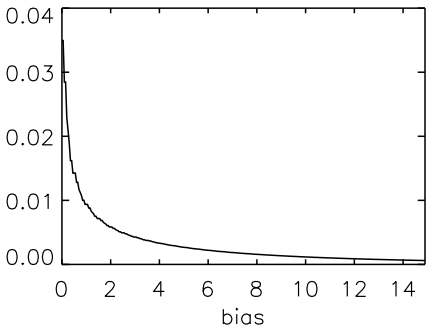

(c) σ_8, Ω_m

Figure 5.33: The 1d probability distributions found from fitting cosmological models to the MaxBCG magnification bias measurement, and marginalising over the other two parameters (shown below each figure).

The shape of the 1d probability distributions in Figures 5.33 and 5.34 are far from Gaussian, and is therefore meaningless to express an arithmetic mean of either the MaxBCG or C4 measurement of the parameters. We therefore quantify the spread of the probability distribution by measuring the area enclosed by 68% and 98.5%, and present these values in Table 5.4. We additionaly present the constraints on each parameter by setting other parameters to the WMAP 3 year best fitting values (e.g. examine bias if $\sigma_8 = 0.80$ and $\Omega_m = 0.26$ as measured by Dunkley et al., 2009) and note that this also fails to identify a peak in the probability distribution within the explored parameters space, although the upper limits are reduced to $\Omega_m < 0.24$, bias < 1.05, and $\sigma_8 < 0.50$. These value are below those measured by other probes (e.g. see Table 1.2) and conclude that this discrepancy is a result of the large scatter in the magnification bias measurement. Therefore in subsequent analysis we use the marginalised parameter limits. We convert the measured values

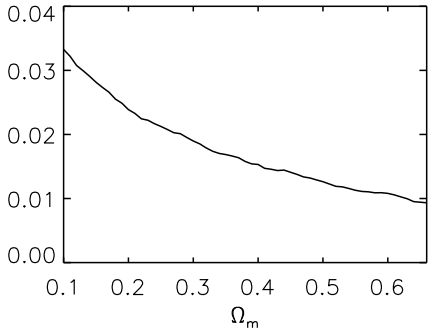

(a) σ_8, bias

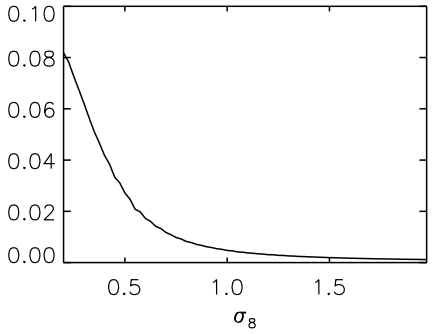

(b) Ω_m, bias

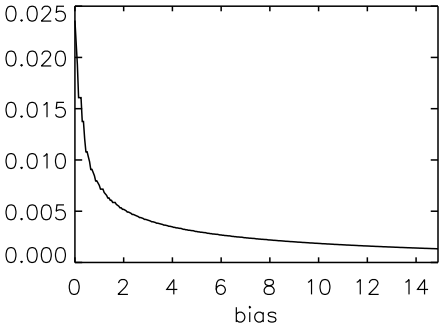

(c) σ_8, Ω_m

Figure 5.34: The 1d probability distributions found from fitting cosmological models to the C4 magnification bias measurement, and marginalising over the other two parameters (shown below each figure).

of bias to mass estimates in the next section. The upper limits of all the parameters agree consistently between the MaxBCG and C4 clusters. We note that the Ω_m upper limits are expected to be larger than those quoted in Table 5.4, because the probability distribution has failed to converge within the parameter space.

We began this chapter with the aim of using the magnification bias to measure the bias of clusters of galaxies, and have subsequently shown that the measurement is Poisson dominated, and the shapes of the 1d probability distributions produce only an upper estimate on the true value. If the measurement had produced more compelling constraints on bias, we could have split the clusters into sub groups, for example in bins of total cluster optical luminosity, and measured the bias for each sub group. Unfortunately, due to the Poisson dominated signal, this would lead to a more scattered measurement with larger errors, which would reduce constraints on bias, and therefore

Marginalised Probability distributions				
	MaxBCG		C4	
Parameter (constraints)	68% of PDF	98.5% of PDF	68% of PDF	98.5% of PDF
Ω_m	$0.10^\star - 0.40$	$0.10^\star - 0.60^\star$	$0.10^\star - 0.45$	$0.10^\star - 0.63^\star$
σ_8	$0.20 - 0.50$	$0.20 - 1.27$	$0.20 - 0.50$	$0.20 - 1.37$
bias	$0.00 - 4.00$	$0.00 - 11.6$	$0.00 - 6.25$	$0.00 - 13.20$
Ω_m (bias$= 3.4, \sigma_8 = 0.80$)	$0.10 - 0.24$	$0.10 - 0.31$	$0.10 - 0.22$	$0.10 - 0.35$
σ_8 (bias$= 3.4, \Omega_m = 0.26$)	$0.20 - 0.40$	$0.20 - 0.60$	$0.20 - 0.47$	$0.20 - 0.70$
bias ($\sigma_8 = 0.80, \Omega_m = 0.26$)	$0.00 - 1.05$	$0.00 - 2.15$	$0.00 - 1.50$	$0.00 - 3.55$

Table 5.4: The ranges of parameters within the shown confidence confidence regions, after other parameters have been marginalised over. The * indicate the error contours do not converge within the explored parameter space.

we only present an upper measurement of mass on the combined MaxBCG and C4 cluster catalogues, and show they are consistent with expected cluster masses.

In the §5.4.2, we introduce an alternative measurement of bias, using the MaxBCG cluster sample, and compare with our results. We then introduce the theoretical framework of bias, and calculate bias as a function of mass, which allows the placing of upper limits on the mass estimates of the MaxBCG and C4 clusters, using the results quoted in Table 5.4.

5.4.2 Comparison with alternative measurements of bias

The bias of the MaxBCG clusters has been measured by Huetsi (2007) who compared the autocorrelation of the MaxBCG clusters with the predicted dark matter power spectrum (in a flat ΛCDM cosmology with $\sigma_8 = 0.8, \Omega_m = 0.27, \sigma_8 = 0.85, h = 0.7$) modified to account for photometric redshifts, redshift space distortions, survey volume, and nonlinear effects. Figure 5.35 is a reproduction of their results, showing the 1σ error contours of the parameters bias b^2_{eff} and σ, which is the cluster redshift error converted to a position error. The solid lines show error ellipses from jackknife re-sampling, and the dotted lines correspond to model errors due to measuring the MaxBCG power spectrum (Feldman et al., 1994); the best fit values are shown by crosses. Table 2 of Huetsi (2007) presents the measured value of b^2, ranging from 11.3 ± 5.2 to 8.7 ± 2.5.

Comparing the square root of the bias^2 measurements of Huetsi (2007) (producing $3.36^{+0.70}_{-0.87}$ and $2.95^{+0.39}_{-0.46}$) with the 1σ marginalised upper measurements of bias from Table 5.4 for the MaxBCG clusters ($b < 4.0$) we find good agreement at the 1σ level. We cannot compare the agreement at the 2σ level because Huetsi (2007) present only the 1σ errors, similarly, the bias of the C4 clusters has not been previously measured, and so cannot be compared.

We have shown our measurement of bias for the MaxBCG clusters to be in agreement with previous studies, and continue in §5.5 to convert the measured upper limits of the bias to an upper mass estimate for the stacked clusters.

5.5 Cluster-halo bias

In this section we explore bias further and derive theoretical predictions for converting bias to cluster halo mass. We use the limit of the bias from §5.4.1 for the MaxBCG and C4 clusters to obtain cluster mass estimates in two regimes: where the shapes of the dark matter halos are assumed to be spherical, and where the halos are allowed to be ellipsoidal (see §4.2.5). We show that the upper bounds on the mass estimates are within expected values.

5.5.1 Introduction and derivation

Under the assumption of General Relativity, the observed matter content of the Universe has long been shown to be insufficient to gravitationally bind galaxies and clusters (Zwicky, 1933), with dark matter providing the additional, invisible mass. If initially the baryonic matter was spread throughout the Universe, it would naturally collapse in regions of high dark matter overdensity, with the most massive optical clusters forming in the highest density dark matter regions, and lower mass optical systems collapsing in less overdense regions. We do not necessarily expect

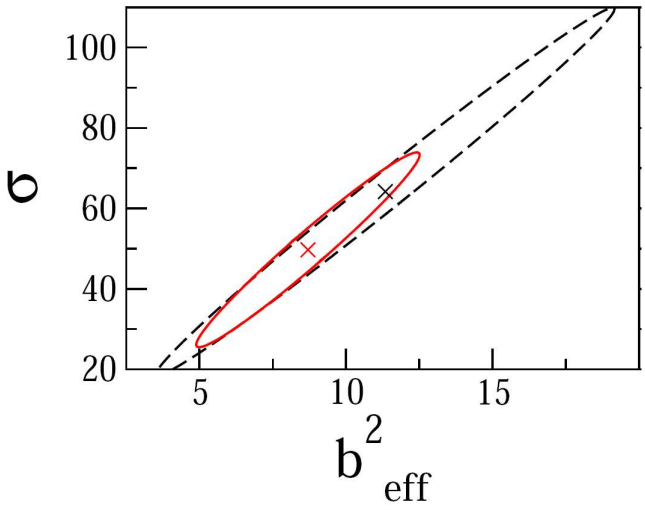

Figure 5.35: A reproduction of Figure 8 of Huetsi (2007) showing a power spectrum analysis of the MaxBCG clusters, with the measured bias b^2_{eff} against the redshift error (converted to a radial position error), $\sigma[h^{-1}\text{Mpc}]$. The ellipses correspond to the 1σ error contours, with the solid line corresponding to the error ellipse from jackknife re-samples of the survey area, and the dotted line correspond to errors from measuring the power spectrum (Feldman et al., 1994). Credit: Huetsi (2007).

the optical matter overdensity $\delta\rho_{Opt}$ to directly trace the dark matter overdensity $\delta\rho_{DM}$ equally on all scales, and therefore introduce bias $b(M)$ as,

$$\frac{\delta\rho_{Opt}}{\bar{\rho}_{Opt}} = b(M)\frac{\delta\rho_{DM}}{\bar{\rho}_{DM}} , \tag{5.53}$$

where $\bar{\rho}$ is the background density. Examining only the initial dark matter density field before gravitational in-fall, White et al. (1987) showed that there will be more optically visible collapsed structures at a given mass in an overdense region of the dark matter density field, compared to less dense dark matter regions. This can be understood in terms of the "peak background split" model, which describes how structures collapse when their matter overdensity reaches a critical value δ_C. If there are large δ_L and small δ_S scale fluctuations in the density field, and objects collapse once $\delta_L + \delta_S = \delta_C$, then lower δ_S structures can collapse in higher dense regions, producing an increase in the observed number density of collapse objects n, above the average number density n_0, such that

$$n \rightarrow n_0 + \frac{\mathrm{d}n}{\mathrm{d}\nu}\frac{\mathrm{d}\nu}{\mathrm{d}\delta_L}\delta_L , \tag{5.54}$$

where $\nu = \delta_C/\sigma_M$, and σ_M is the variance of the smoothed density field on scales M (Press and Schechter, 1974). In §4.2 we derive the mass function as a function of ν, under the assumption that collapse occurs in spherically symmetric shells δ_{sc}, or elliptically along one or two axis before the third δ_{ec}, which allows the evaluation of Equation 5.54 as

$$n = n_0\Big(1 + \delta_L\frac{\nu^2 - 1}{\sigma\nu}\Big) , \tag{5.55}$$

and using the definition of bias (Equation 5.53) we find

$$b_I(\nu) = \frac{\nu^2 - 1}{\sigma\nu} , \tag{5.56}$$

with the subscript I, reminding us we have only considered perturbations in the initial density field, which will evolve gravitationally through δ_L, linearly affecting the density of collapsed halos, producing

$$b(M) = 1 + \frac{\nu(M)^2 - 1}{\delta_C} . \tag{5.57}$$

Equation 5.57 shows explicitly the dependence of bias on halo mass M. In Figure 5.36 we plot the dependence of bias on mass, using the value of δ_C in both the regimes of spherical and ellipsoidal collapse (see §4.2.5). The dotted line show the theoretical prediction of Press and Schechter (1974), and a fit to N-Body simulations (dash dotted line, given by Equation 2 of Jing, 1999) both under the assumption of spherical collapse, and the dashed line shows the theoretical prediction under ellipsoidal collapse (Sheth et al., 2001), with the solid line (given by Equation 5 of Seljak and Warren, 2004), which is a fit to N-Body simulations.

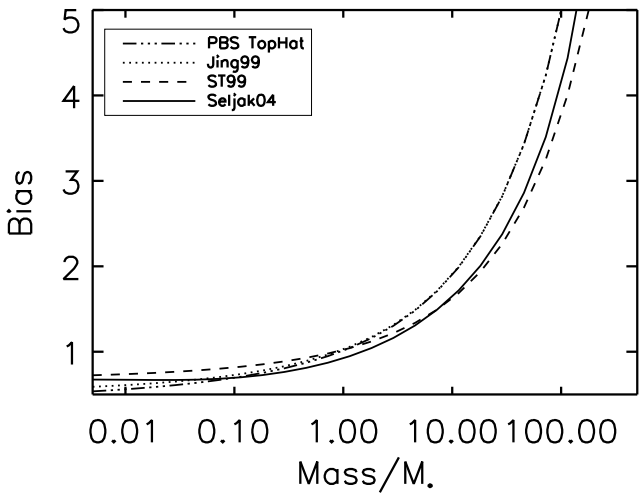

Figure 5.36: The theoretical predictions of bias as a function of mass expressed in terms of $M_\star = 8.73 \times 10^{12} h^{-1} M_\odot$, in the spherical (PBS TopHat) and ellipsoidal (ST99) collapse regime, and fitting formulae derived from N-body simulations (Jing99, Seljak04).

In the next section we use Figure 5.36 to convert the measurements of the one and two σ upper values of bias for the stacked MaxBCG and C4 clusters (see Table 5.4) to upper mass limits.

5.5.2 Mass from bias

Using the upper limits of bias from Table 5.5, and the mass to bias conversion shown in Figure 5.36, we convert the measured values of bias for the stacked MaxBCG and C4 clusters, and present the results in Table 5.5.

Upper mass limits for full sample $[\times 10^{15}\, h^{-1}\, M_\odot]$				
	MaxBCG		C4	
Prescription	68% of PDF	98.5% of PDF	68% of PDF	98.5% of PDF
PBS Top Hat	0.80	6.02	1.99	7.14
Jing99	0.86	6.02	1.99	7.14
ST99	1.58	10.10	3.47	11.86
Seljak04	1.29	5.88	2.56	6.57

Table 5.5: The upper mass limits from the confidence contours for the MaxBCG and C4 cluster, converted from a measurement of bias using four different theoretical prescriptions, see §5.5.1.

We expect the mass range of both the MaxBCG and C4 clusters to be $\sim 10^{13}$ to 10^{15} (see §1.2), and the 68% results shown in Table 5.5 are in good agreement with these values.

Although we have been unable to measure the mass of any one cluster, or subgroup of clusters using the magnification bias, we have shown that the upper mass limits for the stacked clusters are very reasonable, and consistent between the MaxBCG and C4 analysis. Additionally, we have shown that the measurement is currently Poisson dominated, so by increasing the number of cluster lenses, or more easily, the background sources, we could measure bias and cluster mass independently of the X-ray or other techniques.

5.6 Summary

In this chapter we have found limits on the MaxBCG and C4 clusters by converting a Poisson dominated weak lensing measurement of bias to a upper bound on the masses of the stacked clusters. We have discussed technical details and computed the theoretical magnification bias signal allowing the cosmological parameters σ_8, Ω_m and bias to vary, which has enabled the placing of independent constraints on these parameters, shown again in Table 5.6. We have shown that the upper limit for bias is in good agreement with measurements by other techniques, and consistent between both the stacked cluster datasets. We have also shown the signal is Poisson noise dominated, which could lead to more precise constraints on cluster masses, if the number densities of sources and lenses were to increase, see §6.4.

We are able to place upper mass limits on the cluster data sets, shown again in Table 5.7, which are in good agreement with typical cluster masses (see §1.2) but have been unable to measure the mass of any one cluster, or subgroup of clusters, which means the magnification bias is currently unable to be used to measure the cluster mass function. In §4, we use the cluster mass function measured in §3 to constrain cosmological parameters and models.

Marginalised Probability distributions				
	MaxBCG		C4	
Parameter	68% of PDF	98.5% of PDF	68% of PDF	98.5% of PDF
Ω_m	$0.10^\star - 0.40$	$0.10^\star - 0.61^\star$	$0.10^\star - 0.45$	$0.10^\star - 0.63^\star$
σ_8	$0.20 - 0.50$	$0.20 - 1.27$	$0.20 - 0.50$	$0.20 - 1.37$
bias	$0.00 - 4.00$	$0.00 - 11.6$	$0.00 - 6.25$	$0.00 - 13.20$

Table 5.6: The ranges of parameters within the shown confidence regions after other parameters have been marginalised over. The * indicates the error contours do not converge within the parameter space explored.

Upper mass measurements for full sample $[\times 10^{15} M_\odot]$				
	MaxBCG		C4	
Prescription	68% of PDF	98.5% of PDF	68% of PDF	98.5% of PDF
Spherical	~ 0.80	~ 6.02	~ 1.99	~ 7.14
Ellipsoidal	~ 1.58	~ 10.10	~ 3.47	~ 11.86

Table 5.7: The 68% and 98.5% upper mass limits for the MaxBCG and C4 cluster, converted from a measurement of bias using prescriptions assuming spherical and ellipsoidal shaped cluster halos.

Chapter 6

Conclusions and discussions

6.1 Introduction

I began in §1 by introducing the theoretical cosmological framework and describing how probes of cosmology have shaped the theory into the current cosmological model called ΛCDM. I showed that the constraining power of any one probe is generally small, but greatly improved by combining constraints from other cosmological probes.

I introduced clusters of galaxies as an alternative probe of cosmology, through a measurement of the cluster mass function (hereafter CMF) which is the abundance of clusters as a function of redshift and mass, and I showed briefly how the CMF changes with cosmological parameters. I then highlighted the benefits of using the CMF as an alternative probe of cosmology because it measures the growth of structure, as compared to more popular probes (Cosmic Microwave Background radiation, Supernovae, Baryon Acoustic Oscillations) which rely on measures of the geometry of the Universe.

6.2 Data catalogues

In §2 I introduced the optical and X-ray datasets used throughout the thesis, and developed a method to measure the redshifts of newly identified X-ray selected clusters discovered by the XMM Cluster Survey (hereafter XCS, of which I am a member), using existing optical imaging of luminous red galaxies. This has applications for the identification and redshift measurement of X-ray selected clusters using future imaging surveys (e.g. the Dark Energy Survey[1], hereafter DES, or the Large Synoptic Survey Telescope[2], hereafter LSST) and future X-ray observatories (e.g. the extended ROentgen Survey with an Imaging Telescope Array[3], hereafter eROSITA). I then described work to calculate the purity of the XCS cluster sample using imaging from the Sloan Digital Sky Survey (hereafter SDSS) and a classification website I created called Cluster

[1] http://www.darkenergysurvey.org/
[2] http://www.lsst.org/
[3] http://www.mpe.mpg.de/projects.html#erosita

Zoo[4].

I found that there was a high level of impurity (44%) of XCS clusters but identified a proxy for purity, the soft counts (the number of X-ray photons measured in the 0.5 to 2.0 keV band) which enabled me to increase purity to 80%. After the XCS collaboration had classified the extended sources, I presented the results by grouping the classifications, not the clusters, by category, because of the range of classifications for any one cluster (often including a spread of classifications for the same user on the same cluster). In order to group the clusters I would need to choose an arbituary threshold level of agreement between classifications, for example 70% of all classifications for any cluster must be the same category (e.g gold cluster, or not a cluster), or perhaps within the same grouped category (e.g cluster and non-cluster). I could also examine the effect of removing all of a users' classifications if they are found to disagree with the median classification too often. The XCS collaboration aim to make the XCS cluster catalogue public, and I will need to address these issues before release.

I then combined the XCS cluster catalogue with X-ray cluster catalogues from the literature and document work carried out by the XCS collaboration to uniformly re-compute the X-ray properties of all the cluster catalogues, which allows for them to be compiled into the largest X-ray cluster dataset available. Without my measurements of XCS cluster redshifts, this could not have been performed.

Even after the creation of this large X-ray cluster dataset, I showed that the optical cluster datasets are orders of magnitude more numerous, and are thus better suited to cosmological analysis.

6.3 Mass estimate: X-ray

I used the X-ray and optical datasets in §3 to identify X-ray identified clusters within the footprint of the SDSS and measured their optical properties; I also developed a method to estimate the errors on the measured optical properties. I then converted the X-ray temperature to a cluster mass, and quantified the relationship between mass and summed optical luminosity. I showed it to be stable under the effect of poorly estimating the temperature of the Intra-Cluster Medium or the temperature to mass conversion. I then identified the intersection of the X-ray clusters with measured optical properties, with those from the optical cluster catalogues, and compared the measured optical luminosity to the quoted optical luminosity, enabling us to estimate the mass of each cluster in the optical cluster catalogues. I finished the chapter by presenting the mass histograms for the optically selected cluster catalogues.

I noted a difference in the mass number densities of the C4 and MaxBCG clusters and attributed this to the poorly constrained relationship between the quoted C4 catalogue luminosities and the measured optical luminosities. This problem became more apparent when I tried to build a CMF

[4]http://dsg.port.ac.uk/hoyleb/cluster_zoo/index.php

and use it to constrain cosmological parameters, which resulted in us disregarding the dataset and concentrating on the MaxBCG clusters. To overcome these difficulties, I could use an alternative measurement of optical luminosity, for example by calculating R_{200} from the member galaxies, and then measuring the total optical luminosity as described in §3. This would replace the conversion formulae (c.f. Equation 3.26), bringing the comparison of the measured total optical luminosity closer to the X-ray derived cluster halo mass. I could also use the quoted R_{200} for the MaxBCG clusters and use this to recalculate the total optical luminosities, using the improved models of Maraston et al. (2008) which would replace the conversion formulae (c.f. Equation 3.25) which could reduce the scatter in the final optical luminosity to mass conversion and the corresponding errors.

Alternatively, the C4 clusters all have spectroscopic member redshifts and so I could measure a velocity dispersion for each cluster and convert that to a cluster mass. This would provide an X-ray independent method of measuring the cluster masses, which could be compared to those calculated in §3.

I have shown that the total cluster optical luminosity is a tracer of cluster halo mass. This result is important because it enables us to estimate the mass of any optically identified cluster and there are currently orders of magnitude more optical than X-ray identified clusters, and this ratio will only diverge in the future.

Allowing optically identified clusters to be assigned mass estimates has important implications for future optical surveys, for example DES or LSST in the south and the Panoramic Survey Telescope and Rapid Response System[5] in the north, which will perform deep imaging of the the sky, allowing clusters to be detected up to redshifts of $z \sim 1$.

Currently our total optical luminosity to X-ray mass relation is calibrated on $z < 0.3$ clusters and so before it could be used on high redshift clusters, it would first need to be calibrated and this thesis has laid the framework for this work to be undertaken. I have shown how X-ray clusters can be assigned redshifts, and how the measurement of optical and X-ray properties can be performed and their errors estimated.

The next generation of X-ray observatories (e.g. eROSITA) will be able to detect clusters and measure the temperature of the intracluster medium to greater accuracy, which when combined with future high redshift imaging surveys, will allow the mass to optical luminosity relationship to be measured to high statistical significance and possibly, allow its evolution with redshift to be examined.

[5] http://pan-starrs.ifa.hawaii.edu/public/

6.4 Mass estimate: magnification bias

In §5 I investigate an alternative method to measure the masses of the optically identified clusters using a technique from weak gravitational lensing called the magnification bias. After introducing the theoretical framework I described computational complications which arise when attempting to predict the theoretical signal. I continued by calculating the theoretical cross correlation signal for a broad range of cosmological parameters. I then measured the weak lensing signal around the clusters of galaxies and found it to be Poisson dominated, meaning I was unable to measure the cluster - dark matter bias of any one cluster, or subgroup of clusters. However we were able to place the constraints $0.10 < \Omega_m < 0.40$, $0.2 < \sigma_8 < 0.50$ and $0 <$bias< 4.0 assuming $w_0 = -1$, $h = 0.7$, ΛCDM and marginalising over free parameters (e.g. to obtain constraints on σ_8 I marginalised over Ω_m and bias). I found that holding free parameters fixed (e.g. to obtain constraints on σ_8 I assumed $\Omega_m = 0.26$ and bias$= 0.34$) reduced the upper limits; $\Omega_m < 0.24$, bias < 1.05, and $\sigma_8 < 0.50$ which (with the exception of Ω_m) are below the values measured by other probes (e.g. see Table 1.2) and conclude that this discrepancy is a result of the large scatter in the magnification bias measurement.

I presented a detailed analysis of the tests and checks I performed on simulated data to ensure the measurement could be trusted. I now described why I had been unsuccessful and suggest possible extensions to this work which could result in the detection of a strong signal.

I tried to measure the magnification bias around the MaxBCG (with $\sim 13,000$ clusters) and C4 (with $\sim 2,000$ clusters) datasets (as our lenses) using the SDSS quasar catalogue (with $\sim 500,000$ quasars, as our sources) and found that the signal was Poisson dominated. If I compare our number densities with those of Scranton et al. (2005a) (who detected the magnification bias signal at 8σ) I find they have 3 orders of magnitude more lenses (although generally the systems are less massive).

In order to use the magnification bias as a statistical measure of cluster mass in the future, I need to identify at least one order of magnitude more lenses or sources. This could in part be possible if I include radio detected quasars from the NVSS (Condon et al., 1998, adding ~ 1.8 million sources). I can additionally use any galaxies as sources, as long as they are distinct in redshift from the lenses, for example their are ~ 1 million SDSS LRGs (Collister et al., 2007) at a redshift $z > 0.4$. Although, before the high redshift LRGs were to be used, I would need to understand how their inherent clustering affects the expected signal. For the low redshift C4 clusters, the SDSS main sample galaxies could also be used, as long as their redshifts could be trusted to physically separate the sources and lenses.

Future surveys such as the DES or LSST will image a similar size region of the southern sky as the SDSS has in the northern sky, but to a deeper magnitude limit. The clusters and quasars found by DES like surveys will further increase the numbers of lenses and sources which may

enable a significant future measurement of bias around clusters using the magnification bias.

Even though the signal was Poisson dominated I was however able to place upper limit on the stacked measurement of bias. I then presented the derivation of cluster - dark matter halo bias, and showed the bias as a function of mass. I then converted the upper limit on the stacked measurement of bias to an upper limit on the stacked cluster masses.

An alternative technique to measure the cluster - dark matter halo bias around the MaxBCG and C4 clusters could be performed (e.g. by following Huetsi, 2007) by comparing the cluster auto-correlation to the dark matter power spectrum. This would allow us to place stronger constraints on cluster bias when used in conjunction with the weak lensing magnification bias measurement, and is work that is currently ongoing.

6.5 Cosmological constraints

I compared the cluster mass estimates from §3 and §5 in §4, and showed them to be consistent with each other and with the range of acceptable cluster masses.

I continued by converting the cluster mass estimates from §3 to a CMF and corrected for completeness. I noted that the error on the masses were very large and unphysical and opted to set the error on each mass branch of the CMF at each redshift, as the error on the number of clusters at that redshift. If I were to use the Poisson error on the number of clusters at each mass and redshift, I would not have accounted for the possibility that I may have miscalculated the mass of a large number of clusters, which should (or should not) have that mass. Using the Poisson error on the total number of clusters at each redshift allows for this spread of "true" cluster masses. I also decided to only use the cluster mass function if there were more than 50 clusters at that mass (combined across the redshift ranges of the catalogues). I justified this action because I could not trust the shape of the massive tail of the measured CMF. My choice of 50 completeness and area corrected clusters is arbitrary, but corresponds to ~ 10 detected clusters. I could have examined the effect on cosmological parameters of changing this arbitrary value, and this is a theme of ongoing research.

Subsequently, I computed the theoretically expected CMF for two different collapsing mechanisms, and for a range of cosmological parameters within ΛCDM, and for a class of modified gravity models. I showed how the theoretical CMF changes with a host of cosmological parameters. To my knowledge, this is the first time such a theoretical framework has been compiled together.

I then performed a grid based χ^2 minimisation procedure to fit to three sets of cosmological parameters. This involved solving the theoretical CMF equations which were performed in Maple[6]

[6] www.maplesoft.com

on a case by case basis. For a more accurate sampling of parameter space I would need to use a more advanced technique (e.g Markov chain Monte Carlo Andrieu and Thoms, 2008), coupled with an automated solution of the CMF equations to identify the parameters of interest and produce a theoretical CMF. This would also enable us to examine a fuller set of parameters and this is work that is currently ongoing.

If I assume concordant cosmological parameters (e.g. $\Omega_m = 0.26, \sigma_8 = 0.80$, as measured by Dunkley et al., 2009), I found the collapsing mechanism which produces ellipsoidal shaped clusters (Sheth et al., 2001) is preferred at 7σ to the spherical collapse mechanism (Press and Schechter, 1974). I also found the CMF as measured from the C4 dataset is untrustworthy and conclude this is due to the poorly constrained quoted catalogue luminosity to measured luminosity conversion (from §3.2). Continuing with the MaxBCG CMF and assuming ΛCDM with $w_0 = -1$ and $h = 0.7$, I find constraints on the parameter $\sigma_8 = 0.73 \pm 0.05$ and $\Omega_m = 0.20 \pm 0.04$ in agreement with other probes (e.g $\sigma_8 = 0.796 \pm 0.036$ and $\Omega_m = 0.258 \pm 0.030$ Dunkley et al., 2009, using the Cosmic Microwave Background Radiation). After the introduction and justification of an ansatz allowing the ellipsoidal CMF to probe a class of modified gravity models, I was able to rule out 5d DGP (Dvali et al., 2000) at 3σ, representing the first measurement of its kind using clusters.

In order to theoretically test our ansatz (which allowed me to assume the mapping between the spherical and ellipsoidal collapse regimes was the same in modified gravity models as in General Relativity); I have identified the starting point for this future work (Bond and Myers, 1996) and have discussed this problem with Dr. K. Koyama and Mr F. Silva both at the Institute of Cosmology and Gravitation, at the University of Portsmouth who are keen to pursue it. I also intend to computationally test this ansatz by running a cluster finder on recent simulations performed in DGP gravity (e.g. Khoury and Wyman, 2009; Schmidt, 2009) and will fit the simulated CMF for the parameters of the function $F(\nu)$ (c.f. Equation 4.19) allowing us to observe the change in its form between DGP and General Relativity. Running a suit of such simulations with different modified gravity parameters will allow a comparison of the simulated CMF to the measured CMF (e.g. from §4) and enable us to identify the best fitting parameters in these models of modified gravity.

6.6 Concluding remarks

Throughout this thesis, I have used the latest optical datasets drawn from SDSS; the MaxBCG cluster catalogue, and the C4 cluster catalogue, which have provided a large sample of clusters with well understood completeness and purity. I have applied mass estimates to these clusters from a re-computation of the X-ray properties of literature datasets, and from the latest XCS cluster catalogue, and have built a cluster mass function. I have used it to constrain cosmological parameters, models, and the cluster collapsing mechanism, and have found competitive cosmological constraints when combined with other probes of cosmology.

In the future, larger optical and X-ray datasets will become available allowing more clusters at higher redshifts to be detected and their masses using the techniques developed in this thesis to be estimated. Before this is achieved the following issues need to be resolved:

- The purity of X-ray cluster catalogues at ever decreasing flux limits.
- The scatter in the optical luminosity to X-ray derived mass relationship.
- A fairer approximation of the errors on the mass function.
- A more exhaustive scanning of parameter space.

This thesis has provided the theoretical framework and experimental methodology allowing clusters of galaxies to be used as current probes and future precision probes of cosmology.

Appendix A

General relativity

A.1 Derivations of the Friedmann equations

In this appendix, we give a full derivation of the Friedmann and acceleration equations (c.f Equations 1.5 and 1.6). We first present the Einstein Equation describing the distortion of space-time G in the presence of energy T, given by

$$G^{\mu}_{\nu} \; = \; R^{\mu}_{\nu} - \frac{1}{2}\delta^{\mu}_{\nu}R \; = \; 8\pi G T^{\mu}_{\nu} + \Lambda\delta^{\mu}_{\nu} \; , \tag{A.1}$$

where the metric δ^{μ}_{ν} in a Friedmann-Robertson-Walker universe is given by

$$\delta_{\mu\nu} \;\; = \;\; \begin{pmatrix} -1 & 0 \\ 0 & a^2\gamma_{ij} \end{pmatrix} \tag{A.2}$$

$$\gamma_{ij} \;\; = \;\; \begin{pmatrix} \frac{1}{1-K\chi^2} & 0 & 0 \\ 0 & \chi^2 & 0 \\ 0 & 0 & \chi^2\sin^2\theta \end{pmatrix} \tag{A.3}$$

and R is given by

$$R_{\mu\,\nu} \;\; = \;\; R^{\rho}_{\;\mu\,\rho\,\nu} \; , \tag{A.4}$$

$$R_{\mu\,\nu\,\rho\,\sigma} \;\; = \;\; \Gamma_{\mu\,\nu\,\sigma,\rho} - \Gamma_{\mu\,\nu\,\rho,\sigma} + \Gamma_{\mu\,\tau\,\rho}\Gamma^{\tau}_{\;\nu\,\sigma} - \Gamma_{\mu\,\tau\,\sigma}\Gamma^{\tau}_{\;\nu\,\rho} \; , \tag{A.5}$$

$$\Gamma_{\mu\,\nu\,\rho} \;\; = \;\; \frac{1}{2}\left(\delta_{\mu\,\nu,\rho} + \delta_{\mu\,\rho,\nu} - \delta_{\nu\,\rho,\,\rho}\right) \; . \tag{A.6}$$

and the space-space (i,j) and time-time $(0,0)$ components are given by

$$R_{ij} \;\; = \;\; \delta_{ij}\left(\frac{\ddot{a}}{a} + \frac{2\dot{a}^2}{a^2} + \frac{2K}{a^2}\right) \; , \tag{A.7}$$

$$R_{00} \;\; = \;\; -3\frac{\ddot{a}}{a} \; , \tag{A.8}$$

$$R \; = \; \delta^{\mu\nu}R_{\mu\nu} \;\; = \;\; \delta^{ij}R_{ij} + \delta^{00}R_{00} \; , \tag{A.9}$$

$$\;\; = \;\; 6\left(\frac{\ddot{a}}{a} + \frac{\dot{a}^2}{a^2} + \frac{K}{a^2}\right) \; . \tag{A.10}$$

The Friedmann and acceleration equations then come from the $G^0{}_0$ and $G^i{}_i$ components of Equation A.1,

$$G^0{}_0 = R^0{}_0 - \frac{1}{2}\delta^0{}_0 R = 8\pi G T^0{}_0 + \Lambda\delta^0{}_0 \,, \tag{A.11}$$

$$-3\frac{\ddot{a}}{a} - \frac{-6}{2}\left(\frac{\ddot{a}}{a} + \frac{\dot{a}^2}{a^2} + \frac{K}{a^2}\right) = +8\pi G\rho + \Lambda \,, \tag{A.12}$$

$$\left(\frac{\dot{a}}{a}\right)^2 = \frac{8\pi\rho}{3} + \frac{\Lambda}{3} - \frac{K}{a^2} \,, \tag{A.13}$$

$$G^1{}_1 = R^1{}_1 - \frac{1}{2}\delta^1{}_1 R = 8\pi G T^1{}_1 + \Lambda\delta^1{}_1 \,, \tag{A.14}$$

$$\left(\frac{\ddot{a}}{a} + \frac{2\dot{a}^2}{a^2} + \frac{2K}{a^2}\right) - \frac{6}{2}\left(\frac{\ddot{a}}{a} + \frac{\dot{a}^2}{a^2} + \frac{K}{a^2}\right) = -8\pi p + \Lambda \,, \tag{A.15}$$

$$\frac{\ddot{a}}{a} = -\frac{4\pi G}{3}(3p + \rho) + \frac{\Lambda}{3} \,. \tag{A.16}$$

Appendix B

Line fitting algorithm

B.1 Line fitting to data with asymmetric error bars

The measured errors for the optical and X-ray cluster properties (see §3) are asymmetric. There is no routine in IDL (or elsewhere) to analytically fitting data points with asymmetric error bars. In this appendix we document and test a technique to fit a line to data with asymmetric error bars which has been used throughout this thesis.

B.1.1 The algorithm

We model the error bars $x^{+\Delta x_1}_{-\Delta x_2}$, $y^{+\Delta y_1}_{-\Delta y_2}$ of the n points, as four distinct Gaussians of width $\Delta x_{i1}, \Delta x_{i2}$ and $\Delta y_{i1}, \Delta y_{i2}$, where $i = 0, 1, .., n$.

The algorithm begins by computing a bilinear regression line of best fit to the points disregarding any errors, given by $y = a_0 x + b_0$. The perpendicular distance from the line to the point x_i, y_i is then calculated. The distance is decomposed in the x and y directions. The y distance is divided by the error Δy_{i1} (Δy_{i2}) if the line is above (below) the point y_i to give the number of standard deviations the point is away from the line N_{y_i}. The x distance is likewise divided by the error Δx_{i1} (Δx_{i2}) if the line is right (left) of the point x_i which produces a corresponding N_{x_i}. A likelihood $\mathcal{L}_{x_i y_i a_0 b_0}$ for the point x_i, y_i is calculated by adding in quadrature N_{x_i} and N_{y_i}. The final likelihood $\mathcal{L}_{a_0 b_0}$, for the parameters a_0, b_0 is determined by multiplying the likelihoods at each of the points $[x_{i=1..n}, y_{j=1..n}]$, $\mathcal{L}_{a_0 b_0} = \prod_{ij} \mathcal{L}_{x_i y_i a_0 b_0}$.

We then begin a grid scan of parameter space around the initial fit values, $a_0 \pm \Delta a_0$, $b_0 \pm \Delta b_0$, where $\Delta a_0, \Delta b_0$ are chosen to be large. New parameters are then chosen from $a_0 \pm \Delta a_0$, $b_0 \pm \Delta b_0$ and the above process repeated. The measured likelihood for each of the scanned parameters a_j, b_k, $\mathcal{L}_{a_j b_k}$ produces a likelihood surface. The minimum of the likelihood surface produces new best fitting parameters a_1, b_1. The widths $\Delta a_1 = \Delta a_0/3, \Delta b_1 = \Delta b_0/3$ are reduced and the scanning process repeated to obtain a new likelihood surface which has the same evenly spaced number of points (i.e. a finer griding) as the previous iteration, which then produce new, best fitting parameter estimates a_2, b_2. This process is iterated until the $a_{n-1}/a_n, b_{n-1}/b_n$ both stabilise

to below 0.25%.

The full Likelihood surface is then used to find the $\pm 1\sigma$ and $\pm 2\sigma$ errors to the fit parameters a, b by identifying the minimum of the surface.

B.1.2 Testing the algorithm

We test the algorithm by comparing the returned parameters with publicly available IDL line fitting routines using simulated data, whose construction is described below. All of the IDL routines are able to deal with errors in one variable (1-d errors), and one routine ($\#5$), allows errors in both variables (2-d errors) but requires one variable to be dependent on another. No currently available routines allow for the fitting of data with asymmetric error bars.

The routines are described here:

- 1) LINFIT [1]. A line fitting function which minimises the chi-square error statistic.
- 2) ROBUST_LINEFIT[2]. An outlier-resistant two-variable linear regression.
- 3) ROBUST_LINEFIT with the BISECT keyword to find the bisecting fit.
- 4) MPFITFUN[3]. Robust non-linear least squares curve fitting.
- 5) FITEXY[4]. A line fitting routine which takes data with errors in both coordinates and performs a linear least-squares fit in one dimension.
- 6) ASYERR. The method described in §B.1.1. A chi-squared based adaptive scan of parameter space.

We simulate 5×10^3 data points randomly in the region $x = [0..100]$ using the line $y = 10.00x + 3.20 + R(x)$ where $R(x)$ is a uniformly distributed random number between 0 and $x/100$ in the small scatter cases, or between 0 and x in the large scatter cases. We run five tests on the routines of increasing complexity.

- No errors in either variable, with small intrinsic scatter.
- Random errors in the y variable, with small intrinsic scatter.
- Random errors in both x and y variables, with small intrinsic scatter.
- Random errors in both x and y variables, with large intrinsic scatter.
- Random asymmetric errors in both x and y variables, with small intrinsic scatter.

[1] http://star.pst.qub.ac.uk/idl/LINFIT.html
[2] http://idlastro.gsfc.nasa.gov/ftp/pro/robust/robust_linefit.pro
[3] http://www.physics.wisc.edu/∼craigm/idl/fitting.html
[4] http://idlastro.gsfc.nasa.gov/ftp/pro/math/fitexy.pro

Both the FITEXY and the ASYERR routine are able to fit data with errors in both directions but only ASYERR can fit to data with asymmetric errors. The results of the line fitting routines for each test case are shown in Table B.1.

Routine	No errs		1-d errs		2-d errs		2-d errs & large scatter		2-d asymmetric err	
	Slope	Intercept	Slope	Intercept	Slope	Intercept	Slope	Intercept	Slope	Intercept
1	10.00	3.21	10.00	3.25	–	–	–	–	–	–
2	10.01	3.21	10.01	3.21	–	–	–	–	–	–
3	10.01	3.21	10.01	3.21	–	–	–	–	–	–
4	10.01	3.21	10.00	3.25	–	–	–	–	–	–
5	10.01	3.21	10.00	3.05	10.00	3.31	10.91	−4.09	–	–
6	10.01	3.21	10.01	3.21	10.01	3.20	10.53	3.26	10.01	3.20

Table B.1: Testing the line fitting routine described in §B.1.1 against five publicly available IDL routines. The simulated data has a slope of 10.0 and an intercept of 3.20. Routine 5 FITEXY is the only other code which allows errors in both variables.

Table B.1 shows that in the case of no errors all of the routines converge to the same result. The intercept is not identical to the simulated data which can be explained by our addition of intrinsic scatter. The results of each routine remain robust if error bars are added in the y directions. If the intrinsic scatter remains small and errors are allowed in both the x, y variables we see the slope of FITEXY and ASYERR agree well. The intercepts are similar and within the 1σ errors of each other (FITEXY with error ± 0.36, ASYERR has error ± 1.27). The difference in the 1σ errors can be attributed to FITEXY requiring a dependent and independent variable and ASYERR assuming independent variables. As the intrinsic scatter of the simulated data increases, the slopes of the lines differ from each other and the intercepts are largely different. We note that ASYERR recovers the simulated line, but has large 1σ errors of [intercept,slope]=[± 5.27,± 0.13]. Only ASYERR is able to compute the line of best fit to data with asymmetric error bars, and recovers the inputted slope and intercept.

These results of the comparisons between line fitting routines show that the ASYERR routine is robust under these data conditions. We use this function when fitting all data.

Appendix C

Corrected modified gravity formalism

I have recently been made aware of an approximation made in Schaefer and Koyama (2008) when calculating the Hubble function at early times in their spherical collapse formalism. They used the ΛCDM instead of the full DGP Hubble function because many cosmologies differ little at early times, and resemble Einstein-de Sitter. Schaefer and Koyama (2008) assumed this approximation would be valid in their derivation within modified gravity.

The formalism without this approximation (using the full DGP Hubble function) was derived by Kobayashi and Tashiro (2009) who find the value of δ_c changes by $1-2\%$ between pure DGP and ΛCDM, and not the $\sim 30\%$ as described in Schaefer and Koyama (2008).

In Table C.1 we show updated values of δ_c in $\alpha = 1$ DGP (and for comparison, the values from Schaefer and Koyama, 2008) and note that the values scale similarly to those calculate for $\alpha = 0.4$ (see Figure 5 of Schaefer and Koyama, 2008).

Redshift	New δ_c for $\alpha = 1$	Old δ_c for $\alpha = 1$
0.00	1.648	1.464
0.10	1.649	1.478
0.21	1.650	1.492
0.30	1.652	1.505

Table C.1: Updated values of the critical collapse density δ_c in $\alpha = 1$ DGP. Credit: K. Koyama (private communication).

A fitting function (see Equation 4.10) has not been calculated for intermediate α models which we require in order to examine the effect of the updated δ_c on our analysis. To achieve this we map the parameter values a, b, c (see Equation 4.10) for the critical collapse density from the old $\alpha = 0.4$ curve to the new (denoted by $'$) $\alpha' = 1$, and we map the the parameter values for $\alpha = 0.2$ to $\alpha' = 0.5$. The equation for $\alpha = 0$ is unchanged in the mapping. This provides a fitting function

which allows us to interpolate the parameters a, b, c for intermediate values of α as before.

Proceeding as §4.3 we present in Figure C.1 the fractional change of the theoretical cluster mass function (hereafter CMF) in different α models to that of $\alpha = 0$ ΛCDM.

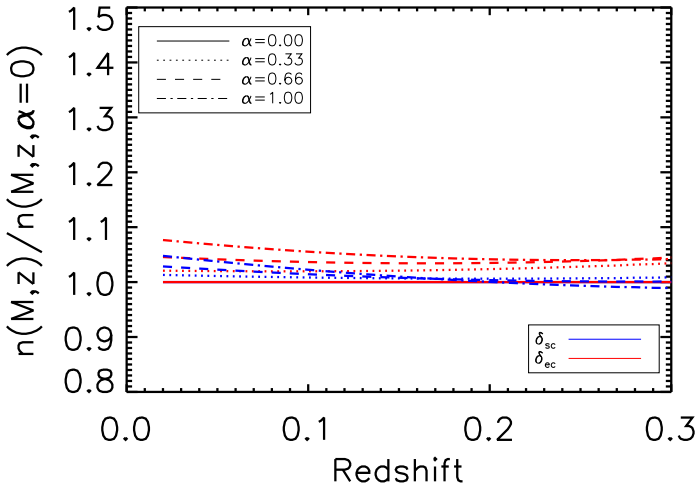

Figure C.1: The CMF with varied parameters divided by the fiducial CMF (calculated for clusters of mass $M = 10^{14}\ h^{-1}\ M_{\odot}$ assuming a flat ΛCDM cosmology with parameters $h = 0.7, \sigma_8 = 0.8, \Omega_m = 0.3, w_0 = -1$) as a function of redshift. We show the effect of varying the theory of gravity through a parameter α, where $\alpha = 0$ describes ΛCDM, and $\alpha = 1$ describes DGP. The blue (red) lines show the predictions for spherical (ellipsoidal) collapse δ_{sc} (δ_{ec}). The solid lines show the fiducial cosmology. This plot incorporates the correction to δ_c from Kobayashi and Tashiro (2009).

We see that the new theoretical predictions for the difference between ΛCDM and DGP is less than 5% (8%) for pure DGP at low redshift in the spherical (ellipsoidal) collpase regime, reducing to 1% (4%) at $z = 0.3$, which are much smaller than before and are now similar in magnitude to those for the equation of state of dark energy w (see Figure 4.8). This means that the former constraining power on α using the measured CMF will be much reduced.

We calculate the best fitting model using a χ^2 analysis as §4.5, and use the spherical to ellipsoidal mapping ansatz (see §4.5.2) to find that we are unable to place constraints on α by marginalising over σ_8 (because the PDF fails to converge over the full parameter space) in both the spherical and ellipsoidal collapse frameworks. If we proceed by assuming the prior $\sigma_8 = 0.8$ we are still only able to constrain $\alpha < 0.75$ at 1σ.

This shows that with todays data catalogues we are unable to rule out DGP and need to either

increase the number of clusters using a survey like the Dark Energy Survey, or reduce the scatter in the cluster mass estimation.

References

Kevork Abazajian et al. The Second Data Release of the Sloan Digital Sky Survey. *AJ.*, 128: 502–512, 2004.

Kevork Abazajian et al. The Third Data Release of the Sloan Digital Sky Survey. *AJ.*, 129: 1755–1759, 2005.

Kevork N. Abazajian et al. The Seventh Data Release of the Sloan Digital Sky Survey. 2008.

Jennifer K. Adelman-McCarthy et al. The Sixth Data Release of the Sloan Digital Sky Survey. *ApJS*, 175:297–313, 2008.

Scott F. Anderson et al. A Large, Uniform Sample of X-ray Emitting AGN: Selection Approach and an Initial Catalog from the ROSAT All-Sky and Sloan Digital Sky Surveys. *AJ.*, 126:2209, 2003.

Christophe Andrieu and Johannes Thoms. A tutorial on adaptive mcmc. *Statistics and Computing*, December 2008. URL `http://dx.doi.org/10.1007/s11222-008-9110-y`.

Raul Angulo, C. M. Baugh, C. S. Frenk, and C. G. Lacey. The detectability of baryonic acoustic oscillations in future galaxy surveys. *MNRAS*, 383:755, 2008.

Monique Arnaud and August E. Evrard. The Lx-T Relation and Intracluster Gas Fractions of X-ray Clusters. *MNRAS*, 305:631, 1999.

Pierre Astier et al. The Supernova Legacy Survey: Measurement of Ω_M, Ω_Λ and w from the First Year Data Set. *A&A*, 447:31–48, 2006.

Steven P. Bamford et al. Galaxy Zoo: the independence of morphology and colour. 2008.

S. Bardeau et al. A Lensing Survey of X-ray Luminous Galaxy Clusters at Redshift z 0.2: II: CFH12k Weak Lensing Analysis and Global Correlations. 2007.

J.M. Bardeen, J.R. Bond, N. Kaiser, and A.S. Szalay. The statistics of peaks of Gaussian random fields. *ApJ*, 304:15–61, May 1986.

M. Bartelmann. Cosmological parameters from angular correlations between QSOs and galaxies. *A&A*, 298:661, June 1995.

Matthias Bartelmann and Peter Schneider. Weak Gravitational Lensing. *Phys. Rev*, 340:291–472, 2001.

C. L. Bennett et al. First Year Wilkinson Microwave Anisotropy Probe (WMAP) Observations: Preliminary Maps and Basic Results. *ApJS*, 148:1, 2003.

M. R. Blanton, J. Dalcanton, D. Eisenstein, J. Loveday, M. A. Strauss, M. SubbaRao, D. H. Weinberg, J. E. Anderson, Jr., J. Annis, N. A. Bahcall, M. Bernardi, J. Brinkmann, R. J. Brunner, S. Burles, L. Carey, F. J. Castander, A. J. Connolly, I. Csabai, M. Doi, D. Finkbeiner, S. Friedman, J. A. Frieman, M. Fukugita, J. E. Gunn, G. S. Hennessy, R. B. Hindsley, D. W. Hogg, T. Ichikawa, Ž. Ivezić, S. Kent, G. R. Knapp, D. Q. Lamb, R. F. Leger, D. C. Long, R. H. Lupton, T. A. McKay, A. Meiksin, A. Merelli, J. A. Munn, V. Narayanan, M. Newcomb, R. C. Nichol, S. Okamura, R. Owen, J. R. Pier, A. Pope, M. Postman, T. Quinn, C. M. Rockosi, D. J. Schlegel, D. P. Schneider, K. Shimasaku, W. A. Siegmund, S. Smee, Y. Snir, C. Stoughton, C. Stubbs, A. S. Szalay, G. P. Szokoly, A. R. Thakar, C. Tremonti, D. L. Tucker, A. Uomoto, D. Vanden Berk, M. S. Vogeley, P. Waddell, B. Yanny, N. Yasuda, and D. G. York. The Luminosity Function of Galaxies in SDSS Commissioning Data. *ApJ*, 121:2358–2380, May 2001.

Michael R. Blanton et al. The Galaxy Luminosity Function and Luminosity Density at Redshift z=0.1. *AJ*, 592:819–838, 2003.

Michael R. Blanton and Sam Roweis. K-corrections and filter transformations in the ultraviolet, optical, and near infrared. *AJ.*, 133:734–754, 2007.

G. R. Blumenthal, S. M. Faber, J. R. Primack, and M. J. Rees. Formation of galaxies and large-scale structure with cold dark matter. *Nature*, 311:517–525, October 1984.

H. Boehringer et al. The ROSAT-ESO Flux Limited X-ray (REFLEX) Galaxy Cluster Survey. V. The cluster catalogue. *A&A*, 425:367–383, 2004.

J.R. Bond, S. Cole, G. Efstathiou, and N. Kaiser. Excursion set mass functions for hierarchical Gaussian fluctuations. *ApJ*, 379:440–460, October 1991.

J.R. Bond and S.T. Myers. The Peak-Patch Picture of Cosmic Catalogs. I. Algorithms. *ApJS*, 103: 1, March 1996.

B. J. Boyle, R. Fong, T. Shanks, and B. A. Peterson. A new faint QSO survey. In G. Giuricin, M. Mezzetti, M. Ramella, and F. Mardirossian, editors, *Structure and Evolution of Active Galactic Nuclei*, volume 121 of *Astrophysics and Space Science Library*, pages 491–498, 1986.

G. Bruzual and S. Charlot. Stellar population synthesis at the resolution of 2003. *MNRAS*, 344: 1000–1028, October 2003.

R. A. Burenin et al. The 400 square degrees rosat pspc galaxy cluster survey: Catalog and statistical calibration. 2006.

R. G. Carlberg, H. K. C. Yee, E. Ellingson, R. Abraham, P. Gravel, S. Morris, and C. J. Pritchet. Galaxy Cluster Virial Masses and Omega. *ApJ*, 462:32, May 1996.

Sante Carloni, Peter K. S. Dunsby, Salvatore Capozziello, and Antonio Troisi. Cosmological dynamics of R^n gravity. *Class. Quant. Grav.*, 22:4839–4868, 2005.

A. Cavaliere and R. Fusco-Femiano. The Distribution of Hot Gas in Clusters of Galaxies. *A&A*, 70:677, November 1978.

Adrian Collister et al. Megaz-lrg: A photometric redshift catalogue of one million sdss luminous red galaxies. *MNRAS*, 375:68–76, 2007.

J. J. Condon, W. D. Cotton, E. W. Greisen, Q. F. Yin, R. A. Perley, G. B. Taylor, and J. J. Broderick. The NRAO VLA Sky Survey. *AJ*, 115:1693–1716, May 1998.

S. M. Croom and T. Shanks. Radio-quiet QSO environments - I. The correlation of QSOs and $b\_J < 23$ galaxies. 303:411–422, February 1999a.

S. M. Croom and T. Shanks. Statistical lensing of faint QSOs by galaxy clusters. 307:L17–L21, August 1999b.

I. Csabai, T. Budavári, A. J. Connolly, A. S. Szalay, Z. Győry, N. Benítez, J. Annis, J. Brinkmann, D. Eisenstein, M. Fukugita, J. Gunn, S. Kent, R. Lupton, R. C. Nichol, and C. Stoughton. The Application of Photometric Redshifts to the SDSS Early Data Release. *AJ*, 125:580–592, February 2003.

I. Csabai, L. Dobos, M. Trencséni, G. Herczegh, P. Józsa, N. Purger, T. Budavári, and A. S. Szalay. Multidimensional indexing tools for the virtual observatory. *Astronomische Nachrichten*, 328:852, September 2007.

Haakon Dahle. A compilation of weak gravitational lensing studies of clusters of galaxies. 2007.

Hakon Dahle. The Cluster Mass Function from Weak Gravitational Lensing.

Xin-Yu Dai, Christopher S. Kochanek, and Nicholas D. Morgan. The x-ray properties of optically-selected galaxy clusters. 2006.

Marc Davis, George Efstathiou, Carlos S. Frenk, and Simon D. M. White. The evolution of large-scale structure in a universe dominated by cold dark matter. *AJ*, 292:371–394, 1985.

K. Dolag and M. Bartelmann. QSO-galaxy correlations induced by weak lensing in arbitrary Friedmann-Lemaitre cosmologies. *MNRAS*, 291:446, November 1997.

A. Dressler. Galaxy morphology in rich clusters - Implications for the formation and evolution of galaxies. *ApJ*, 236:351–365, March 1980.

J. Dunkley, E. Komatsu, M. R. Nolta, D. N. Spergel, D. Larson, G. Hinshaw, L. Page, C. L. Bennett, B. Gold, N. Jarosik, J. L. Weiland, M. Halpern, R. S. Hill, A. Kogut, M. Limon, S. S. Meyer, G. S. Tucker, E. Wollack, and E. L. Wright. Five-Year Wilkinson Microwave Anisotropy Probe (WMAP) Observations: Likelihoods and Parameters from the WMAP data. *ApJS*, 180:306–376, February 2009.

G. R. Dvali, Gregory Gabadadze, and Massimo Porrati. 4D gravity on a brane in 5D Minkowski space. *Phys. Rev. Lett.*, B485:208–214, 2000.

Gia Dvali and Michael S. Turner. Dark energy as a modification of the Friedmann equation. 2003.

H. Ebeling et al. Properties of the X-ray brightest Abell-type clusters of galaxies (XBACs) from ROSAT All-Sky Survey data — I. The sample. *MNRAS*, 281:799–829, 1996.

H. Ebeling et al. The rosat brightest cluster sample (bcs) - i. the compilation of the sample and the cluster log n-log s distribution. *MNRAS*, 301:881–914, 1998.

H. Ebeling et al. The rosat brightest cluster sample (bcs) - iv. the extended sample. *MNRAS*, 318: 333, 2000.

H. Ebeling and G. Wiedenmann. Detecting structure in two dimensions combining Voronoi tessellation and percolation. *Phys. Rev*, E47:704–710, 1993.

Daniel J. Eisenstein et al. Spectroscopic Target Selection for the Sloan Digital Sky Survey: The Luminous Red Galaxy Sample. *AJ.*, 122:2267, 2001.

Daniel J. Eisenstein et al. Detection of the Baryon Acoustic Peak in the Large-Scale Correlation Function of SDSS Luminous Red Galaxies. *AJ*, 633:560–574, 2005.

Anna Kathinka Dalland Evans and Sarah Bridle. A Detection of Dark Matter Halo Ellipticity using Galaxy Cluster Lensing in SDSS. 2008.

Hume A. Feldman, Nick Kaiser, and John A. Peacock. Power spectrum analysis of three-dimensional redshift surveys. *ApJ*, 426:23–37, 1994.

W. L. Freedman, B. F. Madore, B. K. Gibson, L. Ferrarese, D. D. Kelson, S. Sakai, J. R. Mould, R. C. Kennicutt, Jr., H. C. Ford, J. A. Graham, J. P. Huchra, S. M. G. Hughes, G. D. Illingworth, L. M. Macri, and P. B. Stetson. Final Results from the Hubble Space Telescope Key Project to Measure the Hubble Constant. *ApJ*, 553:47–72, May 2001.

L. Fu et al. Very weak lensing in the CFHTLS Wide: Cosmology from cosmic shear in the linear regime. *A&A*, 479:9–25, 2008.

M. Fukugita et al. The Sloan digital sky survey photometric system. *AJ.*, 111:1748, 1996.

N. Gehrels. Confidence limits for small numbers of events in astrophysical data. *ApJ*, 303:"336–346", apr 1986.

Myriam Gitti, Brian R. McNamara, Paul E. J. Nulsen, and Michael W. Wise. Cosmological Effects of Powerful AGN Outbursts in Galaxy Clusters: Insights from an XMM-Newton Observation of MS0735+7421. 2007.

Michael D. Gladders et al. Cosmological constraints from the red-sequence cluster survey. 2006.

Michael D. Gladders and H. K. C. Yee. A New Method For Galaxy Cluster Detection I: The Algorithm. *AJ.*, 120:2148, 2000.

K. M. Gorski et al. HEALPix – a Framework for High Resolution Discretization, and Fast Analysis of Data Distributed on the Sphere. *AJ*, 622:759–771, 2005.

J. E. Gunn et al. The sloan digital sky survey photometric camera. *AJ.*, 116:3040, 1998.

James E. Gunn et al. The 2.5 m telescope of the sloan digital sky survey. *AJ*, 131:2332–2359, 2006.

Alan H. Guth. Was Cosmic Inflation the 'Bang' of the Big Bang? *SLAC Beam Line*, 27N3:14, 1997.

Sarah M. Hansen et al. Photometric Determination of R200 for SDSS Galaxy Clusters. *AJ*, 633: 122–137, 2005.

Henk Hoekstra. Comparison of weak lensing masses and X-ray properties of galaxy clusters. *MNRAS*, 379:317–330, 2007.

David W. Hogg, Ivan K. Baldry, Michael R. Blanton, and Daniel J. Eisenstein. The k correction. 2002.

David W. Hogg et al. The dependence on environment of the color-magnitude relation of galaxies. *AJ*, 601:L29–L32, 2004.

David W. Hogg, Douglas P. Finkbeiner, David J. Schlegel, and James E. Gunn. A photometricity and extinction monitor at the Apache Point Observatory. *AJ.*, 122:2129, 2001.

D. Andrew Howell et al. The type Ia supernova SNLS-03D3bb from a super- Chandrasekhar-mass white dwarf star. *Nature*, 443:308, 2006.

W. Hu and 1 White, Martin J. The cosmic symphony. *ScAm*, 290N2:32–37, 2004.

E. Hubble. A Relation between Distance and Radial Velocity among Extra-Galactic Nebulae. *Proceedings of the National Academy of Science*, 15:168–173, New1929.

Gert Huetsi. Power spectrum of the maxBCG cluster sample: new evidence for the acoustic features. 2007.

A. Jenkins et al. Mass function of dark matter halos. *MNRAS*, 321:372, 2001.

Y. P. Jing. Accurate Determination of the Lagrangian Bias for the Dark Matter Halos. *ApJL*, 515: L45–L48, April 1999.

David E. Johnston et al. Cross-correlation Weak Lensing of SDSS galaxy Clusters II: Cluster Density Profiles and the Mass–Richness Relation. 2007.

Justin Khoury and Mark Wyman. N-Body Simulations of DGP and Degravitation Theories. 2009.

Tsutomu Kobayashi and Hiroyuki Tashiro. Cluster formation and the Sunyaev-Zel'dovich power spectrum in modified gravity: the case of a phenomenologically extended DGP model. 2009.

Benjamin Koester et al. A maxbcg catalog of 13,823 galaxy clusters from the sloan digital sky survey. *AJ*, 660:239–255, 2007a.

Benjamin P. Koester et al. MaxBCG: A Red Sequence Galaxy Cluster Finder. 2007b.

Kazuya Koyama. The cosmological constant and dark energy in braneworlds. *Gen. Rel. Grav.*, 40:421–450, 2008.

Jeffrey M. Kubo et al. The Sloan Nearby Cluster Weak Lensing Survey. 2009.

H. Kuehr, A. Witzel, I. I. K. Pauliny-Toth, and U. Nauber. A catalogue of extragalactic radio sources having flux densities greater than 1 Jy at 5 GHz. *A&AS*, 45:367–430, September 1981.

Cedric G. Lacey and Shaun Cole. Merger rates in hierarchical models of galaxy formation. 2. Comparison with N body simulations. *MNRAS*, 271:676, 1994.

Antony Lewis and Sarah Bridle. Cosmological parameters from CMB and other data: a Monte-Carlo approach. *Phys. Rev*, D66:103511, 2002.

Yen-Ting Lin and Joseph J Mohr. K-band Properties of Galaxy Clusters and Groups: Brightest Cluster Galaxies and Intracluster Light. *AJ*, 617:879, 2004.

Arthur Lue, Román Scoccimarro, and Glenn Starkman. Differentiating between modified gravity and dark energy. *Phys. Rev. D*, 69(4):044005, Feb 2004a.

Arthur Lue, Roman Scoccimarro, and Glenn D. Starkman. Probing Newton's constant on vast scales: DGP gravity, cosmic acceleration and large scale structure. *Phys. Rev*, D69:124015, 2004b.

Robert Lupton, James E. Gunn, and Alex Szalay. A Modified Magnitude System that Produces Well-Behaved Magnitudes, Colors, and Errors Even for Low Signal-to-Noise Ratio Measurements. *AJ.*, 118:1406, 1999.

Claudia Maraston, Gustav Stromback, Daniel Thomas, David A. Wake, and Robert C. Nichol. Modeling the color evolution of luminous red galaxies - improvements with empirical stellar spectra. 2008.

Rachel N. McInnes et al. Lensing measurements of SZ-discovered clusters in the Southern Cosmology Survey. 2009.

Brice Menard, Ryan Scranton, Masataka Fukugita, and Gordon Richards. Measuring the galaxy-mass and galaxy-dust correlations through magnification and reddening. 2009.

Christopher J. Miller et al. The C4 Clustering Algorithm: Clusters of Galaxies in the Sloan Digital Sky Survey. 2005.

Christopher J. Miller, Adrian L. Melott, and Robert C. Nichol. Wavelength Doesn't Matter: Optical vs. X-ray Luminosities of Galaxy Clusters. 1999.

Robert Nichol et al. SDSS-RASS: Next Generation of Cluster-Finding Algorithms. 2000.

D.J. Norman and C.D. Impey. Quasar-Galaxy Correlations: a Search for Amplification Bias. 118: 613–624, August 1999.

Nobuhiro Okabe and Keiichi Umetsu. Observational Constraints on the ICM Temperature Enhancement by Cluster Mergers. 2007.

J.B. Oke. Absolute Spectral Energy Distributions for White Dwarfs. *ApJS*, 27:21, February 1974.

Nikhil Padmanabhan et al. Calibrating photometric redshifts of luminous red galaxies. *MNRAS*, 359:237–250, 2005.

Nikhil Padmanabhan, U. Seljak, and U. L. Pen. Mining Weak Lensing Surveys. *New A*, 8: 581–603, 2003.

Kristian Pedersen and Haakon Dahle. Calibration of the Mass-Temperature Relation for Clusters of Galaxies Using Weak Gravitational Lensing. 2006.

Will J. Percival et al. Measuring the Baryon Acoustic Oscillation scale using the SDSS and 2dFGRS. *MNRAS*, 381:1053–1066, 2007.

S. Perlmutter et al. Measurements of Omega and Lambda from 42 High-Redshift Supernovae. *AJ*, 517:565–586, 1999.

V. Petrosian. Surface brightness and evolution of galaxies. *ApJL*, 209:L1–L5, October 1976.

N. Pogson. Magnitudes of thirty-six of the minor planets for the first day of each month of the year 1857. *MNRAS*, 17:12–15, nov 1856.

W.H. Press and P. Schechter. *ApJ*, 185:716, 1974.

Elena Rasia et al. Systematics in the X-ray Cluster Mass Estimators. *MNRAS*, 369:2013–2024, 2006.

A. Ratcliffe, T. Shanks, Q. A. Parker, and R. Fong. The Durham/UKST Galaxy Redshift Survey - IV. Redshift-space distortions in the two-point correlation function. *MNRAS*, 296:191–205, May 1998.

Gordon T. Richards et al. Spectroscopic Target Selection in the Sloan Digital Sky Survey: The Quasar Sample. *AJ.*, 123:2945, 2002.

Gordon T. Richards et al. Efficient Photometric Selection of Quasars from the Sloan Digital Sky Survey: 100,000 $z < 3$ Quasars from Data Release One. *ApJS*, 155:257–269, 2004.

Gordon T. Richards et al. Efficient Photometric Selection of Quasars from the Sloan Digital Sky Survey: II. $\sim 1,000,000$ Quasars from Data Release Six. 2008.

A. G. Riess, L.-G. Strolger, J. Tonry, S. Casertano, H. C. Ferguson, B. Mobasher, P. Challis, A. V. Filippenko, S. Jha, W. Li, R. Chornock, R. P. Kirshner, B. Leibundgut, M. Dickinson, M. Livio, M. Giavalisco, C. C. Steidel, T. Benítez, and Z. Tsvetanov. Type Ia Supernova Discoveries at z > 1 from the Hubble Space Telescope: Evidence for Past Deceleration and Constraints on Dark Energy Evolution. *ApJ*, 607:665–687, June 2004.

Adam G. Riess et al. Observational Evidence from Supernovae for an Accelerating Universe and a Cosmological Constant. *AJ.*, 116:1009–1038, 1998.

Adam G. Riess et al. A Redetermination of the Hubble Constant with the Hubble Space Telescope from a Differential Distance Ladder. 2009.

A. Kathy Romer, Pedro T. P. Viana, Andrew R. Liddle, and Robert G. Mann. A serendipitous galaxy cluster survey with xmm: Expected catalogue properties and scientific applications. 1999.

Eduardo Rozo et al. Cosmological Constraints from the SDSS maxBCG Cluster Catalog. 2009.

E. S. Rykoff et al. Measuring the mean and scatter of the X-ray luminosity – optical richness relation for maxBCG galaxy clusters. 2007.

R. K. Sachs and A. M. Wolfe. Perturbations of a cosmological model and angular variations of the microwave background. *Astrophys. J.*, 147:73–90, 1967.

Craig L. Sarazin. X-ray emission from clusters of galaxies. *Rev. Mod. Phys.*, 58:1–115, 1986.

Bjoern Malte Schaefer and Kazuya Koyama. Spherical collapse in modified gravity with the Birkhoff-theorem. *MNRAS*, 385:411–422, 2008.

David J. Schlegel, Douglas P. Finkbeiner, and Marc Davis. Maps of Dust IR Emission for Use in Estimation of Reddening and CMBR Foregrounds. *ApJ*, 500:525, 1998.

Fabian Schmidt. Self-Consistent Cosmological Simulations of DGP Braneworld Gravity. 2009.

Ryan Scranton et al. Detection of Cosmic Magnification with the Sloan Digital Sky Survey. *ApJ*, 633:589–602, 2005a.

Ryan Scranton et al. Photometric Covariance in Multi-Band Surveys: Understanding the Photometric Error in the SDSS. 2005b.

Uros Seljak. Analytic model for galaxy and dark matter clustering. *MNRAS*, 318:203, 2000.

Uros Seljak and Michael S. Warren. Large scale bias and stochasticity of halos and dark matter. 2004.

Erin S. Sheldon et al. Cross-correlation Weak Lensing of SDSS Galaxy Clusters I: Measurements. 2007.

Ravi K. Sheth, H. J. Mo, and Giuseppe Tormen. Ellipsoidal collapse and an improved model for the number and spatial distribution of dark matter haloes. *MNRAS*, 323:1, 2001.

Ravi K. Sheth and Giuseppe Tormen. An Excursion set model of hierarchical clustering : Ellipsoidal collapse and the moving barrier. *MNRAS*, 329:61, 2002.

J Allyn Smith et al. The u'g'r'i'z' Standard star system. *AJ.*, 123:2121–2144, 2002.

R. E. Smith et al. Stable clustering, the halo model and nonlinear cosmological power spectra. *MNRAS*, 341:1311, 2003.

G. F. Smoot, C. L. Bennett, A. Kogut, J. Aymon, C. Backus, G. de Amici, K. Galuk, P. D. Jackson, P. Keegstra, L. Rokke, L. Tenorio, S. Torres, S. Gulkis, M. G. Hauser, M. A. Janssen, J. C. Mather, R. Weiss, D. T. Wilkinson, E. L. Wright, N. W. Boggess, E. S. Cheng, T. Kelsall, P. Lubin, S. Meyer, S. H. Moseley, T. L. Murdock, R. A. Shafer, and R. F. Silverberg. Preliminary results from the COBE differential microwave radiometers - Large angular scale isotropy of the cosmic microwave background. *ApJL*, 371:L1–L5, April 1991.

S. L. Snowden et al. ROSAT Survey Diffuse X-Ray Background Maps. II. *AJ*, 485:125, 1997.

Yong-Seon Song and Kazuya Koyama. Consistency test of general relativity from large scale structure of the Universe. *JCAP*, 0901:048, 2009.

Yong-Seon Song, Ignacy Sawicki, and Wayne Hu. Large-Scale Tests of the DGP Model. *Phys. Rev*, D75:064003, 2007.

S. A. Stanford et al. The XMM Cluster Survey: A Massive Galaxy Cluster at z=1.45. *ApJ*, 646: L13–L16, 2006.

F Stoehr. High Resolution Simulations of Underdense Regions, Diploma Thesis, Munich: Technical University. 1999.

Chris Stoughton et al. The sloan digital sky survey: Early data release. *AJ.*, 123:485–548, 2002.

Michael A. Strauss et al. Spectroscopic Target Selection in the Sloan Digital Sky Survey: The Main Galaxy Sample. *AJ.*, 124:1810, 2002.

N. Sugiyama. Cosmic Background Anisotropies in Cold Dark Matter Cosmology. *ApJS*, 100: 281, October 1995.

R. A. Sunyaev and Y. B. Zeldovich. The Spectrum of Primordial Radiation, its Distortions and their Significance. *Comments on Astrophysics and Space Physics*, 2:66, 1970.

Shaun A. Thomas, Filipe B. Abdalla, and Jochen Weller. Constraining Modified Gravity and Growth with Weak Lensing. 2008.

Jeremy L Tinker et al. Toward a halo mass function for precision cosmology: the limits of universality. 2008.

A. Vikhlinin et al. A Catalog of 200 Galaxy Clusters Serendipitously Detected in the ROSAT PSPC Pointed Observations. *AJ*, 502:558, 1998.

A. Vikhlinin et al. Chandra Cluster Cosmology Project III: Cosmological Parameter Constraints. *AJ*, 692:1060–1074, 2009.

Alexey Vikhlinin et al. Chandra sample of nearby relaxed galaxy clusters: mass, gas fraction, and mass-temperature relation. *AJ*, 640:691, 2006.

W. Voges, R. Gruber, J. Paul, and K. Bickert. The rosat standard analysis software system. 1992.

D. Walsh, R. F. Carswell, and R. J. Weymann. 0957 + 561 A, B - Twin quasistellar objects or gravitational lens. *Nature*, 279:381–384, 1979.

R. H. Wechsler. Simulating Galaxy Populations in Clusters. In *Bulletin of the American Astronomical Society*, volume 38 of *Bulletin of the American Astronomical Society*, page 1208, December 2006.

Risa H. Wechsler, Andrew R. Zentner, James S. Bullock, and Andrey V. Kravtsov. The dependence of halo clustering on halo formation history, concentration, and occupation. *AJ*, 652: 71–84, 2006.

Michael A. Weinstein et al. An Empirical Algorithm for Broad-band Photometric Redshifts of Quasars from the Sloan Digital Sky Survey. *ApJS*, 155:243–256, 2004.

S. D. M. White, M. Davis, G. Efstathiou, and C. S. Frenk. Galaxy distribution in a cold dark matter universe. *Nature*, 330:451–453, December 1987.

Xiang-Ping Wu, Tzihong Chiueh, Li-Zhi Fang, and Yan-Jie Xue. A comparison of different cluster mass estimates: consistency or discrepancy? 1998.

Naoki Yasuda et al. Galaxy number counts from the Sloan Digital Sky Survey commissioning data. *AJ.*, 122:1104, 2001.

H. K. C. Yee and E. Ellingson. Correlations of Richness and Global Properties in Galaxy Clusters. *AJ*, 585:215–226, 2003.

Donald G. York et al. The Sloan Digital Sky Survey: technical summary. *AJ.*, 120:1579–1587, 2000.

F. Zwicky. Die Rotverschiebung von extragalaktischen Nebeln. *Helvetica Physica Acta*, 6:110–127, 1933.